TRACING AND QUANTIFYING CONTRIBUTIONS OF PROXIMAL, REGIONAL, AND GLOBAL SOURCES TO PRIMARY PARTICULATE MATTER IN AN URBAN ATMOSPHERE USING RADIOGENIC ISOTOPES, PLATINUM GROUP METALS, AND OTHER TRACE AND MAJOR ELEMENTS

A Dissertation

by

SOURAV DAS

Submitted to the Graduate and Professional School of
Texas A&M University
in partial fulfillment of the requirements for the degree of

DOCTOR OF PHILOSOPHY

Chair of Committee,	Shankararaman Chellam
Committee Members,	Brent V. Miller
	Franco Marcantonio
	Jessica Fitzsimmons
Head of Department,	Zachary Grasley

May 2022

Major Subject: Civil Engineering

ABSTRACT

This research focuses on rare earths, platinum group metals, and Sr, Nd, and Hf isotopes along with a wide spectrum of other trace and major elements to accurately trace and quantify contributions of various source categories to primary ambient airborne particulate matter (PM) in an urban atmosphere. The overarching goal of this research is to establish strong tracers for individual distal and proximal sources and quantify local, regional, and global sources influencing urban aerosols. The work principally focusses on natural mineral dust (from a remote desert and locally resuspended soil), anthropogenic mineral dust from construction activities, anthropogenic emissions from motor vehicles, both natural and anthropogenic biomass burning aerosols, and PM from oil combustion, petroleum refineries, coal combustion, and sea salt. The city of Houston, Texas, a representative urban metroplex which suffers pollution input from both local and distal sources (such as dust from the Saharan-Sahelian region and Central American biomass burning), was chosen as a test bed to prove our hypotheses.

The first part of the research demonstrates the superiority of coupled Sr-Nd-Hf isotopes compared with metal tracers to uniquely trace different natural and anthropogenic mineral dust sources with overlapping elemental composition and accurately isolate various urban PM sources. To achieve this, a novel high-yielding gravity flow column chromatography scheme was developed to separate Sr, Nd, and Hf prior to multi collector – inductively coupled plasma – mass spectrometry (MC-ICP-MS). Thereafter, we fingerprinted several sources including vehicular PM from an underwater tunnel, petroleum refinery PM from fluidized-bed catalytic cracking units,

local soil, concrete/cement dust, and trans-Atlantic North African dust in Barbados. We also measured $^{87}Sr/^{86}Sr$, $^{143}Nd/^{144}Nd$, and $^{176}Hf/^{177}Hf$ ratios along with elemental concentrations in Houston aerosols, which aided in apportioning ambient $PM_{2.5}$ to various sources during two North African dust events in the year 2017. A novel mathematical model was developed to unify elemental and isotopic mass balance equations for sources, which consequently demonstrated the superiority of the selected radiogenic isotopes in tracing and differentiating amongst various mineral sources.

The second part of the research demonstrates platinum group elements (PGEs – Rh, Pd, and Pt) in surface roads to be exclusively emitted from motor vehicles, since their relative abundances were coherent with catalytic converters. Therefore, PGEs were utilized to accurately quantify PM from vehicular emissions. Further, we used the estimates of vehicular contributions to determine the performance of other traffic-related metals as PM tracers for vehicles.

The third part of this research focuses on PM transported to Houston from distal locations and identifies two major sources (i) desert dust from North Africa and (ii) potassium-rich smoke particles linked to forest fires or anthropogenic agricultural burning in Central America, Canada, and southeastern United States. Additionally, the influence of Saharan dust and biomass burning episodes on concentrations of PM_{10}, $PM_{2.5,}$ and anthropogenic metal tracers (rare earths, vanadium, and potassium) were evaluated, demonstrating the need to separate the non-mineral component of these metals.

Finally, we use trace metals to investigate the influence of outdoor PM inside an inner-city high school in the Houston area. Concurrent indoor and outdoor PM samples helped establish the role of infiltration of refinery, oil combustion, motor vehicle, and crustal PM.

DEDICATION

This work is dedicated to my father, mother, and sister for their endless love, support, and encouragement.

ACKNOWLEDGEMENTS

Foremost, I would like to express my sincere gratitude to my advisor, Dr. Shankar Chellam, for giving me an opportunity to pursue doctoral study and helping me prepare this research with tremendous guidance, motivation and patience. I thank him for sharing his expertise, challenging me with hard questions and encouraging thought-provoking discussions that helped in successfully completing this dissertation. I have strengthened "some super important skill" and grown tremendously as a professional researcher under Dr. Chellam's guidance, and I am sincerely thankful to him for supporting me on this journey.

I am deeply grateful to Dr. Brent Miller for introducing me to the MC-ICP-MS and giving me an opportunity to work in the Radiogenic Isotope Geosciences Facility. Dr. Miller has been an integral part of this research and immensely influential in shaping experiment methods and critiquing results for my dissertation. I would also thank other committee members, Dr. Franco Marcantonio and Dr. Jessica Fitzsimmons, for giving me valuable suggestions for laboratory analysis that made quality results possible for this research. I would also thank all the committee members for their valuable time and comments that significantly improved the content of this dissertation.

I can't thank enough my friends and colleagues, Dr. Kunal Gupta, Dr. Kyungho Kim, and Bilal Abada who were present by my side throughout my PhD journey and provided tremendous help, intellectual discussions, and moral support all these years. I would like to acknowledge previous members of Dr. Chellam's group, Dr. Ayse Bozlaker and Dr. Mutiara Ayu Sari, for

guiding me and sharing their knowledge, Darpan Chorghe and Mahith Nadella, for helping in the lab. I would also thank all the undergrads, Kristin Williamson, Hailey Mueller Lavigne, Sarah Christnacht, Aaron Wilson, Andrew McMillin, Garrett Gill, and Jessica Ly, who helped in the field and with laboratory work. Special mention to Steve Paciotti for his help in field sampling and instrument troubleshooting. Jeremy Johnson for helping me with filter weighing and Luz Romero for her continuous assistance with laboratory analysis. Thanks to all faculty whose subject courses helped me gain valuable scientific knowledge.

No words can express my gratitude towards my parents, Sanjukta Das and Ajodhya Nath Das, for their endless love, encouragement, and support. Thanks to my sister, Atula Das, and her family, Rahul Thakur and Shloka Das Thakur, for their emotional support, love, and care. I would also like to thank all my friends, especially the graduate batch of 2017, for the memorable times we had together. Finally, a special thanks to Jai Surabhi Verma for always being by my side lovingly and motivating me to be better every day.

CONTRIBUTORS AND FUNDING SOURCES

Contributors

This work was supervised by a dissertation committee consisting of Professor Shankar Chellam (advisor) and Professor Brent Miller and Professor Franco Marcantonio of the Department of Geology & Geophysics and Professor Jessica Fitzsimmons of the Department of Oceanography.

Literature data for Chapter VI was partly compiled by Kristin Williamson of Department of Civil and Environmental Engineering and were published in 2021. All other work conducted for the dissertation was completed by the student independently.

Funding Sources

This work was made possible in part by grants from the Texas Air Research Center (110TAM0184A), the Center for Advancing Research in Transportation Emissions, Energy, and Health (69A3551747128), the National Institute of Environmental Health Sciences (NIEHS P30ES029067), Texas A&M University's Triads for Transformation (T3) program, and Qatar National Research Fund (NPRP 7-649-2-241). Its contents are solely the responsibility of the authors and do not necessarily represent the official views of the sponsors.

NOMENCLATURE

PM	Particulate matter
PM2.5	Particulate matter greater than 2.5 micrometers
PM10	Particulate matter greater than 10 micrometers
ICP-MS	Inductively Coupled Plasma Mass Spectrometry
MC-ICP-MS	Multi Collector Inductively Coupled Plasma Mass Spectrometry
REE	Rare Earth Element
EF	Enrichment factor
CMB	Chemical Mass Balance
IRCMB	Isotope Resolved Chemical Mass Balance
FCC	Fluidized-bed catalytic cracking
NIST	National Institute of Standards and Technology
BCR	Community Bureau of Reference
CRM	Certified Reference Material
AERONET	Aerosol Robotic Network
NAAPS	Navy Aerosol Analysis and Prediction System
HYSPLIT	Hybrid Single-Particle Lagrangian Integrated Trajectory
EPA	Environmental Protection Agency

TABLE OF CONTENTS

Page

LIST OF FIGURES

Page

LIST OF TABLES

Page

CHAPTER I

INTRODUCTION

Background

Airborne Particulate Matter (PM), a common pollutant in urban atmospheres is a mix of natural (e.g., resuspended local soil and long-range transported dust) and anthropogenic (e.g., industrial and automotive emissions) aerosols [1-3]. There is much interest in identifying PM sources and composition due to its negative impacts on human health [4-7]. To better understand PM exposure and associated effects, it is imperative to quantify the contribution of individual sources to ambient PM concentrations which in turn helps environmental agencies around the world to establish regulate air quality in order to protect human health[8]. Importantly, PM directly emitted from various sources (known as primary PM) along with gaseous precursors interacts both chemically and physically with chemicals in the atmosphere to form more aerosol mass (known as secondary PM) [9, 10]. Therefore, linking primary PM to their respective sources is key to understand the atmospheric chemical processes and secondary aerosol formation, and is the subject of our interest.

Motor vehicle emissions, one of the most common sources of urban PM, has been a subject of interest for many researchers due to reports of its alarming health effects, namely lung cancers, allergies, respiratory and cardiovascular diseases, and even premature death [11-13]. To assist with better quantification of vehicular PM in ambient atmosphere, strong tracers are required that are both conservative (i.e., does not undergo loss or formation in the atmosphere) and are exclusive to

vehicular emission. Current literature has either vastly relied on metals/metalloids such as Fe, Ca, Zn, Mn, Cu, Cd, Pb, As, Ni, Sb, Sn, Ba, Zr, Cr, and Ga for this purpose [14-17]. However, these metals have also been reported to be co-emitted by several other urban sources, especially industrial and road dust [18-20], demonstrating the need to pursue superior tracers. Modern motor vehicles are equipped with catalytic converters, lined with rhodium, palladium, and platinum to reduce gaseous pollutant emissions, and hence emit platinum group elements (PGEs) in ultra-trace amounts from their tailpipes. Consequently, these metals are heavily enriched in vehicular emissions compared to their crustal abundance, more than any other elements [21]. Moreover, PGEs have been reported to be exclusively emitted by motor vehicles in several urban locations [22], making them ideal tracers for vehicular PM. However, these metals have seldom been characterized in urban atmospheres, probably owing to their ultra-trace abundances, and have never before been used to quantify vehicular PM near surface roads.

Urban atmospheres suffer from significant quantities of aerosols from not only local sources but from dust and smoke PM originating from distal locations carried by winds under appropriate meteorological conditions [1, 23-32]. One such source is desert dust resuspension from the Sahara-Sahel region that accounts for ~70% of the total global dust flux emitting an estimated $400 - 2{,}200 \times 10^{12}$ g yr^{-1} [33, 34] and prominently influences particulate matter (PM) concentrations in far-flung populated regions of Europe, North and South America, and sub-Saharan Africa [29, 35-38]. Methods for quantification of sources are primarily based on mass balance equations and rely on unique chemical composition of each relevant source. A major complication in isolating transported desert dust is that it is difficult to chemically differentiate it

from local soil, which is statistically termed as “collinearity” in elemental mass balance equations [39]. Collinearity induces large errors and unreliability in estimating source contributions [39] necessitating approaches to find better tracers. Current methods to isolate long-range desert dust contribution to ambient PM are largely dependent on the selection of suitable background sites [40] and/or number of samples collected at the receptor site [39, 41]. A more promising approach is to employ PM’s isotopic composition to isolate sources of otherwise similar elemental composition [42-46] and accurately estimate their individual contributions without the need to analyze numerous PM samples over a long timeframe (e.g., many months). To relevance of desert dust, we hypothesize that coupled Sr-Nd-Hf would potentially differentiate between various mineral dusts. However, current literature lacks any reports of simultaneous Sr-Nd-Hf analysis in urban PM or its sources. Moreover, analytical methods to accurately characterize urban PM for Sr-Nd-Hf isotopes ratios are not available. In addition to characterization, we need proper mathematical tools to unify and holistically analyze both isotope ratios and elemental concentrations to produce accurate source contribution estimates.

Another reported distal source capable of influencing PM at urban locations is large-scale biomass burning episodes that may arise from either forest fires or agricultural burning [10, 47-50]. These episodes are usually tracked using potassium, which however is co-emitted by several mineral sources, including local soil, deserts, coal combustion, cement kilns, and construction activities/concrete [47, 51, 52]. Therefore, to be effectively used as a tracer for biomass burning, we need to isolate potassium’s non-mineral component demonstrating the need to track mineral sources. The current methodology for separating mineral potassium depends on single elemental

ratios, e.g., K/Al, K/Fe, K/Si, and K/Ca [47-50, 53]. However, this technique may produce unreliable results because elemental ratios are not constant across mineral sources. The need for accurate separation becomes even more crucial during long-range mineral dust storms when these elemental tracers are drastically diluted with crustal signatures, which calls for a need to track and quantify these distal emission episodes.

Due to the relevance of PM exposure on health, especially in children, another topic was pursued that links indoor coarse PM (2.5 – 10 μm sized particles) to outdoor sources via elemental tracers.

Research goal and objectives

The overarching goal of my research is to accurately and precisely trace and quantify source contributions to PM concentrations in ambient air using conservative and unique tracers. Based on an exhaustive literature review, it was hypothesized that Sr-Nd-Hf isotopes, platinum group metals, and the non-mineral component of potassium can enhance accurate quantification of primary PM from mineral dust sources, vehicular emissions, and biomass burning respectively. All ambient aerosols were collected in Houston, Texas, following the reports of desert dust [29, 38] and agricultural smoke [30, 31] episodes, making it an ideal test bed for our research. To prove our hypotheses and achieve our primary goal, several objectives were formulated:

a) Develop a gravity flow chromatography method to precisely and accurately measure isotopic ratios of Sr, Nd, and Hf in low mass urban aerosol samples with multi collector – inductively coupled plasma – mass spectrometry (MC-ICP-MS).

b) Fingerprint various urban and long-range mineral PM sources for Sr-Nd-Hf isotopic ratios that can potentially contribute to Sr, Nd, and Hf in urban PM.

c) Trace and quantify mineral sources by combining Sr-Nd-Hf isotope ratios with several elemental tracers in ambient urban PM samples.

d) Estimate the quantity of vehicular aerosols in urban atmosphere by measuring platinum group elements (Pt, Pd, and Rh) in ambient PM samples.

e) Identify and quantify regional and long-range transported PM in an urban atmosphere and assess their influences on elemental tracers associated with anthropogenic activities.

f) Trace outdoor and indoor PM sources impacting indoor PM and its composition with trace metals and assess elements that could possibly pose health hazards from metal exposures.

Dissertation organization

The main components of this dissertation are five manuscripts (chapters II – VI), three of which have been published, the second chapter has been submitted for peer-review, and the fourth one will be submitted soon. Each of these dissertation chapters is the manuscript and begins with a brief introduction of the work including the objectives, followed by the relevant materials and methods, results and discussion, and the conclusions. The final chapter of the dissertation summarizes the key findings of all these manuscripts and recommends future research directions.

Chapter II discusses a novel laboratory method developed for measurement of $^{87}Sr/^{86}Sr$, $^{143}Nd/^{144}Nd$, $^{176}Hf/^{177}Hf$ that was optimized for low mass (0.3 mg – 25 mg) of urban airborne PM samples. The method was used to characterize isotopic ratios and elemental abundances in four

potential urban sources of Sr, Nd, and Hf, namely Houston soil, concrete dust, motor vehicles, and petroleum refining. Detailed findings can be found in Das, S., Miller, B. V., Prospero, J., & Chellam, S. (2022). Sr-Nd-Hf isotopic analysis of reference materials and natural and anthropogenic particulate matter sources: Implications for accurately tracing North African dust in complex urban atmospheres. *Talanta*, **241**, 123236. [51]

Chapter III quantifies North African dust and other mineral sources in urban atmosphere during mineral dust outbreak events in Houston by concurrently measuring Sr-Nd-Hf isotope ratios in urban PM and incoming North African dust. A novel statistical method was developed to combine isotope ratios and elemental concentrations and estimate source contribution using mass balance principles. This work has just been submitted for peer review. Das, S., Miller, B. V., Prospero, J., Gaston C. J., Royer H. M., Blades E., Sealy P. & Chellam, S. (2022). Coupling Sr-Nd-Hf isotope ratios and elemental analysis to accurately quantify North African dust contributions to $PM_{2.5}$ in a complex urban atmosphere by reducing mineral dust collinearity. [Manuscript submitted for publication]

Chapter IV discusses PGEs (Pt, Pd, and Rh) in urban PM_{10} and $PM_{2.5}$ and demonstrates that these metals originated exclusively from motor vehicle emission, consequently assisting in accurately estimating the vehicular contribution to ambient PM. Additionally, this work evaluates other traffic-related metals for their reliability as a tracer for vehicular PM. This work was published in Das, S., & Chellam, S. (2020). Estimating light-duty vehicles' contributions to ambient $PM_{2.5}$ and PM_{10} at a near-highway urban elementary school via elemental characterization

emphasizing Rhodium, Palladium, and Platinum. *Science of The Total Environment*, **747**, 141268. [54]

Chapter V highlights the impacts of transboundary aerosols from regional and long-range transported PM to the Houston atmosphere. Desert dust outbreaks were found to heavily impair vanadium, lanthanides, and potassium ratios, which otherwise serve as good tracers to anthropogenic emissions, highlighting the importance of separating the mineral component from their ambient concentration. Multiple instances of PM from agricultural and forest fires were detected and quantified with the non-mineral component of potassium, aerosol products, and satellite images. This work will soon be submitted for peer review. Das, S., Prospero J. M. & Chellam, S. (2022). Transboundary aerosol contributions from regional and global sources to primary ambient $PM_{2.5}$ and PM_{10} in a complex metropolitan atmosphere. [Manuscript in preparation for submission]

Additional research work is presented in Chapter VI where elemental tracers were used to link coarse sized (2.5 – 10 μm) PM in an indoor inner city school environment to that of an outdoor PM. Detailed analysis revealed infiltration of PM from refineries PM, motor vehicles, soil, and oil combustion. Additionally, indoor metal concentrations were compared with current indoor air quality standards. These findings were published in Williamson, K., Das, S., Ferro, A. R., & Chellam, S. (2021). Elemental composition of indoor and outdoor coarse particulate matter at an inner-city high school. *Atmospheric Environment*, **261**, 118559. [55]

CHAPTER II

Sr-Nd-Hf ISOTOPIC ANALYSIS OF REFERENCE MATERIALS AND NATURAL AND ANTHROPOGENIC PARTICULATE MATTER SOURCES: IMPLICATIONS FOR ACCURATELY TRACING NORTH AFRICAN DUST IN COMPLEX URBAN ATMOSPHERES[*]

Introduction

The Sahara-Sahel region emits an estimated 400 – 2,200 × 10^{12} g yr^{-1} of dust [33, 38], which travels long distances to prominently affect marine and terrestrial nutrient fluxes, cloud formation, Earth's radiation budget and climate, as well as airborne particulate matter (PM) concentrations in large, industrialized cities in far-flung populated regions of Europe, North and South America, and sub-Saharan Africa [23, 35, 38, 56, 57]. Regulatory compliance with air quality standards in cities and strategies to better protect public health require identifying sources and quantifying their individual contributions to ambient PM. Importantly, governments provide exceptions to "exceptional events" that increase PM levels but are beyond regulatory control making it critical to accurately apportion North African dust in urban atmospheres. To date, North African dust has largely been isolated from urban PM mixtures via (i) receptor modeling using elemental analysis [23, 35, 58] and (ii) subtracting background spikes from PM concentrations at

[*] Reprinted with permission from "Sr-Nd-Hf isotopic analysis of reference materials and natural and anthropogenic particulate matter sources: Implications for accurately tracing North African dust in complex urban atmospheres", S. Das, B. V. Miller, J. Prospero, and S. Chellam (2022), *Talanta*, **241**, 123236, Copyright 2022 by Elsevier

populated receptor sites [1, 40, 58, 59]. The first approach introduces significant uncertainties because long-range transported North African dust (crustal and distal), local resuspended soil and road dust (crustal and local), concrete dust (non-crustal and local), coal fly ash (non-crustal and local), and other urban mineral-rich dust sources are similar in composition in terms of Ca, Si, K, Ti, Al, Fe, and/or rare earth elements [39, 40, 60]. The second approach is also fraught with difficulties since background PM itself can be influenced by local sources, is often highly variable, and may not always represent a true control [58]. Consequently, existing approaches can discriminate North African dust input only approximately and only when it is substantially higher than the background [40] introducing errors when we quantitatively estimate contributions of various sources to PM levels in metropolitan locations.

An alternate and increasingly popular approach to accurately isolate aerosol sources with overlapping elemental characteristics is to employ isotopes, which has been successful in identifying anthropogenic emitters [45, 61-65]. Analogously, we hypothesize herein that limitations posed by using major and rare earth elements to isolate mineral dust sources dust sources (North African dust, local soil, and construction activities) in urban environments can be overcome by measuring coupled Sr-Nd-Hf isotopes [66]. Additionally, isotopic analysis is expected to accurately apportion long-range transported dust even during low impact days (e.g., during leading and trailing edges of North African dust incursions).

To date, Sr, Nd, Pb, and Hf isotopes have been used for fingerprinting and tracking trans-Atlantic dust principally in remote or rural locations [46, 67-72]. While $^{87}Sr/^{86}Sr$ and $^{143}Nd/^{144}Nd$ ratios have been primarily used to trace the potential source areas (PSA) [73] of dust [70, 74, 75],

$^{176}Hf/^{177}Hf$ and $^{143}Nd/^{144}Nd$ have lately evolved as promising tracers for long-range transported dust with higher content of radiogenic Hf, which has been attributed to variations in source bedrock and loss of zircon component of dust during transport [67-69]. Hence, coupling Hf isotopes to Sr and Nd also is likely to enhance the accuracy of isolating long-range transported natural dust sources. However, only a few investigations have measured Sr-Nd-Hf isotopes simultaneously, and those that have were also in remote environments such as ice sheets and offshore sites [66-69, 75-77]. To our knowledge, coupled Sr-Nd-Hf isotopes have never been characterized in a complex urban environment where aerosols emanate from multiple anthropogenic and natural sources and consequently their ability to trace crustal PM in such environments is unclear. Therefore, we focus on $^{87}Sr/^{86}Sr$, $^{143}Nd/^{144}Nd$, and $^{176}Hf/^{177}Hf$, which are strongly influenced by crustal sources [23, 60]. However, since isotopic tracers are only useful if there are measurable discrepancies between local rock/soil and long-range transported dust, quantifying these isotopes in urban soils is also important. Only by demonstrating contrasting isotopic characteristics of urban Sr, Nd, and Hf sources can we establish their isotopes as dust tracers in industrialized environments. However, an optimized analytical method for accurate and precise quantitation of Sr-Nd-Hf isotopes in ambient PM (and some of its sources) is not yet available.

Typically, only sub-milligram masses of aerosols (e.g., $PM_{2.5}$ and PM_{10}) are collected for analysis introducing heterogeneities and analytical uncertainties in laboratory analysis including isotopic ratios, reducing the accuracy of speciation and modeled source contribution estimates necessary to improve air quality [1, 54, 78-80]. It is therefore critical to develop protocols that

maximize elemental and isotope recovery and concurrently remove interferences to the highest extent possible from sub-mg samples.

Existing chromatographic processes employed to extract and separate Sr, Nd, and Hf from dust and geological samples are complex [81, 82]. They typically require a pressurized flow setup and commonly used TODGA resins require elution acid to be maintained at elevated temperatures (60-70°C) to completely recover Hf [83]. Paradoxically, current methods used to extract Sr, Nd, and Hf from dust have been optimized and verified only for rock reference materials (e.g. BHVO-1, BHVO-2 AGV-1, AGV-2, USNM3529, and BCR-2) [82, 84] or loess [84]. However, the low mass coupled with the complex and distinctive matrix of urban PM might shift chromatographic peaks and elution curves [61, 85], necessitating the rigorous documentation of the applicability of new sample preparation and instrumental procedures that target aerosols. Additionally, efficiencies of existing methods have not been reported for sub-mg samples.

The objectives of this research targeting Sr-Nd-Hf isotopic ratios are to (i) develop a convenient gravity flow chromatography method to preconcentrate samples prior to multi collector – inductively coupled plasma – mass spectrometry (MC-ICP-MS), (ii) maximize precision and accuracy by optimizing both chromatography and mass spectrometry for a ~100-fold change in equivalent sample mass (0.3 mg and 25 mg), and (iii) evaluate performance of the novel method against multiple reference materials and environmental samples with a wide range of matrix chemistries relevant to urban PM. In addition, we fingerprint the isotopic ratios of several major urban PM sources by analyzing the Sr-Nd-Hf isotopic composition of collected bulk samples to establish their ability to isolate North African dust. We characterize the isotopic and elemental

abundances of (i) local soil in the vicinity of a large oil refinery that copiously emits Sr, Nd, and Hf, (ii) airborne $PM_{2.5}$ from inside an underwater roadway tunnel representing vehicular contributions, (iii) concrete dust (primarily emitted from construction activities and is enriched in Ca and Sr) from two different commercially available dry mixes, and (iv) four different fluid catalytic cracking (FCC) catalysts that are enriched in all rare earths, especially Nd and represent primary PM emitted from petroleum refineries [86, 87].

Methods

Microwave-assisted sample dissolution

Samples (see Appendix Table A5 for more details including mass employed) were dissolved in a microwave oven (CEM MARS 6, Matthews, North Carolina) in two stages (first with HNO_3 and HF then followed by H_3BO_3) each at 200 °C and 20 minutes [87]. This procedure solubilized 46 elements: 31 from groups 1-16 (Na, Mg, Al, Si, K, Ca, Sc, Ti, V, Cr, Mn, Fe, Co, Ni, Cu, Zn, Ga, As, Se, Rb, Sr, Zr, Mo, Cd, Sn, Sb, Cs, Ba, Pb, Th, and U) and 15 rare earths (Y, La, Ce, Pr, Nd, Sm, Eu, Gd, Tb, Dy, Ho, Er, Tm, Yb, and Lu) without leaving any residue. The resulting solution was divided into two aliquots at 1:15 volume ratio. The smaller aliquot was diluted in ultrapure water to obtain a 2 % nitric acid matrix and directly used for elemental analysis . The larger aliquot was dried down in a Class 100 cleanroom on a hot plate at 80 °C to remove matrix acids, and the solid residue was redissolved in the appropriate acid matrix (3.5 M HNO_3 in this case). The resulting solution was employed for elemental separation prior to isotopic analysis, which is further discussed in the next section. All Certified Reference Material (CRM) samples were duplicated by dividing into five batches of 25 mg each before acid dissolution in different

vessels following the procedure explained in the previous section from which aliquots equivalent to 0.3 mg were pipetted for calibration of low mass samples explained in the following section.

Elemental analysis of aerosol source samples and CRMs with q-ICP-MS

Prior to isotopic analyses by MC-ICP-MS, samples were analyzed by quadrupole ICP-MS equipped with a collision cell pressurized with NH_3 (PerkinElmer® NexION® 300). Instrumental setup and operating parameters are summarized in Appendix Table A1. Internal standardization was achieved using ^{74}Ge (for Na, Mg, K, Mn, and Co), ^{115}In (for Al, Si, Ca, Sc, Ti, V, Cr, Fe, Ni, Cu, Zn, Ga, As, Se, Rb, Sr, Zr, Mo, Cd, Sn, Sb, Cs, Ba, Th, U, and rare earths), and ^{209}Bi (for Pb). Following our earlier aerosol work [87], ^{27}Al, ^{51}V, ^{52}Cr, ^{57}Fe, ^{60}Ni, ^{65}Cu, and ^{66}Zn were analyzed in Dynamic Reaction Cell (DRC) mode using ammonia as the cell gas. The isotopes analyzed with ICP-MS in standard (i.e., with no cell gas) and collision cell mode are summarized in Appendix Table A9. Complete sample dissolution in the microwave oven and quality control in our instrumental analysis was confirmed by obtaining quantitative recoveries of certified elements (84-113%) in National Institute of Standards and Technology (NIST) SRM 1648a (urban particulate matter) and SRM 1633b (coal fly ash) as well as Community Bureau of Reference BCR-723 (road dust) and United States Geological Survey (USGS) BCR-2 (natural basaltic rock standard) as summarized in Appendix Table A2. Recoveries of Sr, Nd, and Hf lie in the range of 86-109%, 92-96% and 89-98% respectively. The choice of these reference materials was driven by their close relevance to our research. SRM 1648a is airborne particulate matter collected in an urban area (near St. Louis, MO) with many certified elements. SRM 1633b represents anthropogenic particles emitted from a typical industrial source with high trace metals and rare earth content. BCR-723 is

a proxy for particles emitted from near-road surfaces through vehicular and aeolian resuspension. BCR-2 is a geological reference material that has certified Sr-Nd-Hf isotopic ratios making it invaluable for this work. Also note that SRM 1648a, SRM 1633b, and BCR-723 have been extensively used in validating the elemental composition of urban PM e.g., [23, 54, 61, 63, 88].

Optimization of sample preparation via liquid chromatography

The four rock/dust reference materials mentioned in the previous section were used to evaluate column performance; BCR-2, SRM 1648a, BCR-723, and SRM 1633b. Elemental elution curves with resin chromatography depend on the sample loading flux [85]. Hence, the column diameter needs to be scaled based on the sample size to obtain comparable elution curves for all sample masses. Since the mass of airborne particulate matter (PM) samples vary based on local aerosol concentrations and there is a lower bound for column diameter to avoid wall effects and short circuiting [89], it is not always feasible to obtain columns of necessary diameter to maintain a constant loading flux. Therefore, we developed a column separation scheme that can be universally applied to maximize recovery and well-separate interfering elements. Column separation behavior was monitored for typically low and high PM masses. The minimum mass was 0.3 mg, chosen to simulate 12 μg m^{-3} of $PM_{2.5}$ (the current United States' primary annual average National Ambient Air Quality Standard) collected over 24 hours period at 1 m^3 h^{-1} (i.e., the Federal Reference Method [1]). The maximum sample mass was arbitrarily chosen at 25 mg representing a nearly 100-fold increase that has been used to measure reference materials [90].

Column separation chemistry was evaluated by eluting suitable reagents based on literature data for the separation of elements of interest and their respective interfering species (Appendix

Table A4). Aliquots of the elutant were collected at intervals determined by the required data resolution. Samples were dried and redissolved in the appropriate reagent before loading onto the columns and after separation, but prior to analysis to remove residual acid matrix from the previous chemical processing step. A detailed description of the column separation process along with column cleaning, reagent purification, and apparatus used has been documented in Appendix section A.2, Table A6 (whole procedure) and Table A7 (reagent description and purity). All procedures were conducted on a Class 100 workbench inside a Class 1000 certified room. The final chromatography process was performed using four columns as mentioned in methods subsections. Elements of interest in liquid chromatography (Rb, Sr, Ti, Hf, Lu, Yb, Nd, Sm) were analyzed in aliquots collected from column separation processes to aid in column optimization using a Thermo Scientific ICP-MS (iCAP RQ ICP-MS).

Sr cleanup with Sr-Spec resin (Column I)

Sr-Spec resin (50-100 μm size, Eichrom Technologies) was used to extract Sr from the sample aliquot and ensure complete separation of Rb which causes isobaric interference on ^{87}Sr. Columns of 0.25 mL volume were made with heat shrink PTFE with 3.5 mm inner diameter, 27.5 mm resin bed height, and 2 mL reservoir volume. Expecting the Sr-Spec resins to selectively retain Sr and Pb in HNO_3 medium [91, 92], a dried sample cut was dissolved overnight in 0.5 mL of 3.5 M HNO_3 solution and passed through the column until Rb was washed out. Sr was eluted with ultrapure water. The Sr cut had Rb/Sr ratio $< 2\times10^{-4}$ in all our samples and ^{87}Rb only contributed $< 0.08\%$ on signal for m/z = 87 (Appendix Table A10). Pb is reported to be eluted by passing ≥ 6 M HCl [83, 91], hence 7 M HCl was passed until complete elution. Sr-Spec resins were discarded

after each use. Cleaning, conditioning and loading procedure for this step is detailed in Appendix Section A.2.1.

50W-X8 Cation exchange resins for Sr-Nd-Hf separation (Column II)

The primary column separation employed Dowex 50W-X8 in its hydrogen form, 200-400 μm mesh size resins [93]. Two types of columns were evaluated because these resins expand in relatively low concentration acids [93]; (i) 3 mL heat shrink PTFE with 6.4 mm inner diameter, 9 cm resin bed height, and 15 mL reservoir volume and (ii) 2.5 mL polyethylene with 7.1 mm inner diameter, 6 cm resin bed height, and 20 mL reservoir volume. The sample was dissolved in 1 M HCl + 0.1 M HF. The acid volume varied from 1.5 mL for low sample mass (< 1 mg) to 5 mL for high sample mass (10 mg – 25 mg). The elution process was optimized with 1 M HCl + 0.1 M HF, 1.5 M HCl, 2.5 M HCl, and 7 M HCl based on the separation efficiency, elution time, and elution volume. Eluted fractions were dried down before proceeding to next chromatography step and 30 mL of acid wash (25 mL of 7 M HCl + 5 mL of 2 M HF) cleaned the resins for each subsequent use.

Nd-cleanup with α-HIBA and AG 50W-X4 resins (Column III)

Since Sm and Nd are not expected to be separated in either of the above two column processes [83, 93], we evaluated AG 50W-X4 (100-200 mesh size, hydrogen form, Bio-Rad) resins and α-hydroxyisobutyric acid (HIBA) as the eluting agent for this purpose. A 1.5 mm inner diameter and 24 cm long glass column was prepared with 0.3 mL resin volume. Resins were equilibrated by submerging in 0.225 M α-HIBA overnight (same value used for elution) and maintaining the pH at 4.7 using NH_4OH. Because rare earths are chelated by negatively charged

ligands generated upon α-HIBA dissociation [94], a 0.200-0.225 M concentration at pH=4.6-4.7 was selected [94-96] wherein > 85% acid will be dissociated. The pH remained constant after passing through the column indicating sufficient buffer capacity. The pH was monitored before and after every column separation as its close control is required to obtain the desired elution pattern [95]. Resins were discarded after each use and columns were cleaned with concentrated HNO_3.

Hf-cleanup with Ln-Spec resins (Column IV)

Isotope ^{176}Hf has direct isobaric interference from ^{176}Lu and ^{176}Yb, both of which have been reported to be removed with 50W-X8 cation resin [93]. However, elements like Ti are likely to enter the Hf-cut [93], which can affect the transmission of Hf into the mass spectrometer [97], so an additional cleaning step was performed with Ln-Spec resins (50-100 mesh size, Eichrom Technologies). Ln-Spec resins retain both Ti and Hf in absence of HF but Ti elutes in presence of H_2O_2 in HNO_3 or HCl [93, 98] Therefore, the dried down Hf cut from the initial cation column step was dissolved in 3 M HCl overnight and loaded onto an Ln-Spec filled column (7.1 mm inner diameter and 3.5 cm resin bed height). An additional 7 M HCl was passed after loading to further remove Na and any traces of Lu and Yb in the Hf cut. Ti removal was tested with 3 M HNO_3 + 1 % H_2O_2. Loss of high field strength elements (HFSE, Ti, Zr, Nb, Hf, and Ta) has been reported when HCl and H_2O_2 mixture was passed through Ln-Spec resins [98]. Hence, the column was washed with 2 mL of ultrapure water twice. Hf was eluted by passing 1 M HNO_3 + 0.3 M HF and 1 M HNO_3 + 0.5 M HF solutions. Columns were cleaned with a 5 mL wash of 2 M HF followed by a 10 mL wash of 7 M HCl. Bubble formation due to H_2O_2 was minimized by pairing it with

HNO_3 instead of HCl and > 7.1 mm diameter columns were used to achieve good separation even in the unlikely case that bubbles appeared.

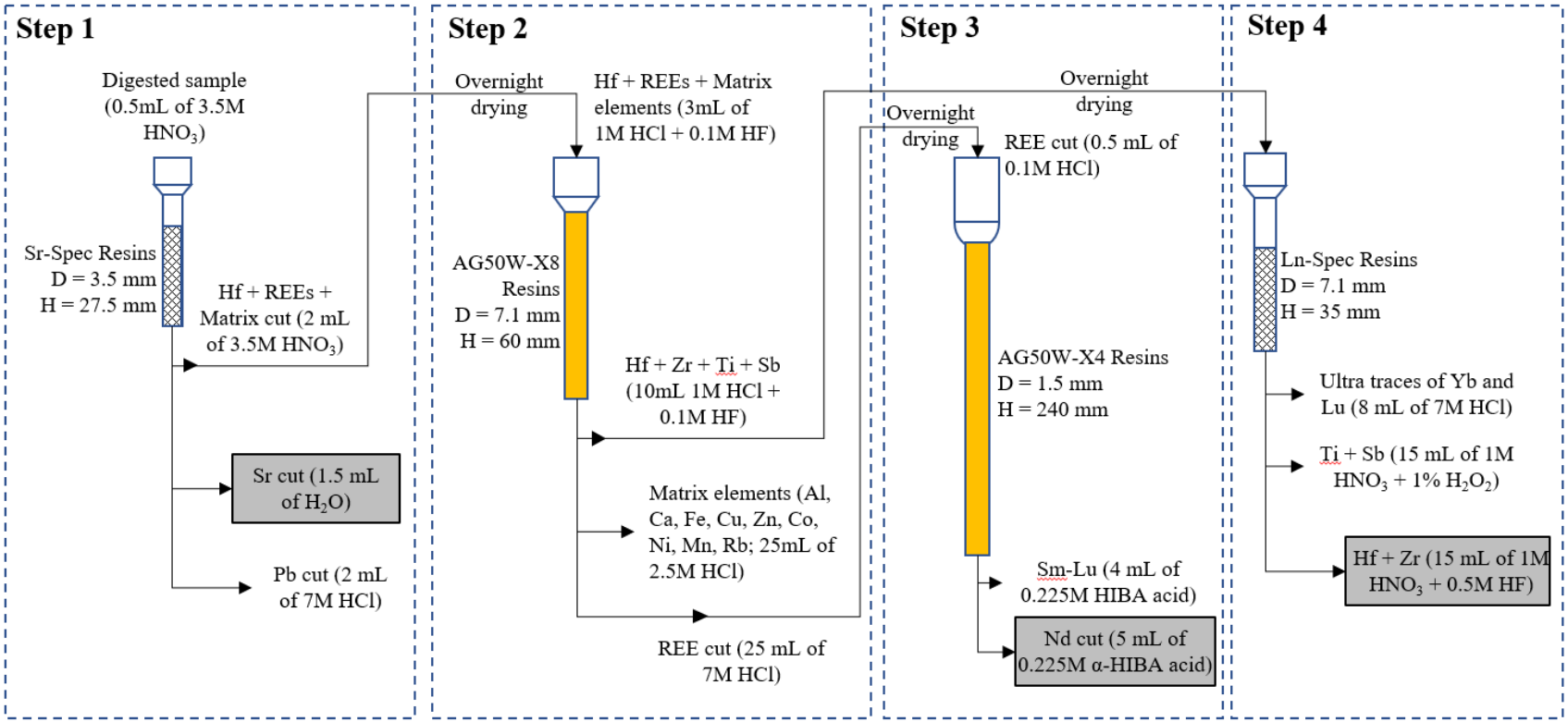

Figure II-1. The complete flow chart demonstrating the proposed column-resin separation scheme to measure isotopic ratios. The column separation characteristics are discussed in results and discussion section. The dimensions of each resin column have been presented with parameters D – inner diameter and H – resin height. The pure elution cuts of Sr, Nd and Hf that are used for isotope ratio analysis are highlighted in grey text boxes. Acid matrix of each eluted cut are presented in parenthesis next to important elements in the respective cut.

MC-ICP-MS setup and data corrections

Purified cuts of Sr, Nd, and Hf were analyzed using a Neptune™ Plus MC-ICP-MS, equipped with nine Faraday cups, each connected to current amplifiers using 10^{11} Ohm resistors. A desolvation sample introduction system (ESI Apex Ω) enhanced sensitivity by 7 to 10 times over the conventional Scott-type spray chamber. For $^{143}Nd/^{144}Nd$ measurement, N_2 gas was introduced in the sample introduction passage to reduce oxide formation and analyte loss. Standard solutions were used for tuning and analyzing MC-ICP-MS performance (Sr isotopic standard SRM 987 for $^{87}Sr/^{86}Sr$ and JNdi-1 for $^{143}Nd/^{144}Nd$). Due to the lack of commercially available solution-based reference material for Hf isotopes, a large batch of in-house reference standard was prepared whose isotopic ratio was measured as $^{176}Hf/^{177}Hf = 0.282141 \pm 0.000015$ (see Appendix Figure A9) calculated from 12 measurements alongside BCR-2 ($^{176}Hf/^{177}Hf = 0.282850 \pm 0.000008$) with identical instrumental settings. These solution-based standards were also used to model uncertainty equations, which were later used to optimize sample volume. BCR-2 (for Sr-Nd-Hf) and BCR-723 (for Sr-Nd) were used to verify the accuracy of our measurements, post column separation. Bias due to fractionation was corrected by normalizing ratios using Russell's law [99, 100]. $^{87}Sr/^{86}Sr$ was normalized with $^{88}Sr/^{86}Sr = 8.375209$, $^{143}Nd/^{144}Nd$ with $^{146}Nd/^{144}Nd = 0.7219$; $^{176}Hf/^{177}Hf$ with $^{179}Hf/^{177}Hf = 0.7325$. Appendix Tables A2 and A3 provides more details of setup and analysis methods. Temporal drifts were corrected by applying the standard-sample bracketing (SSB) method using $^{87}Sr/^{86}Sr = 0.710255$ for SRM 987, $^{143}Nd/^{144}Nd = 0.512102$ for JNdi-1 and $^{176}Hf/^{177}Hf = 0.282141$ for the in-house standard. For better comparison between source samples,

Nd and Hf isotopic ratios are reported as deviation from ratios measured for chondritic uniform reservoir (CHUR, $^{176}Hf/^{177}Hf = 0.282785$ and $^{143}Nd/^{144}Nd = 0.512630$).

Uncertainty modelling and sample volume optimization

Sample dilution after chromatographic chemical separation was carefully considered to maximize precision by balancing MC-ICP-MS signal strength and number of individual measurements for each element. Cumulative error propagation during isotope ratio measurements was mathematically modeled by incorporating three major instrumental uncertainty sources [100-102] in Equation 1; electronic noise and fractionation correction (*f(r)*), blank (P_{bk}), and long term (external) bias (P_{ex}) to obtain total uncertainty in measured ratio (*R*) (see Appendix A.3 for full details):

$$u(R) = u(P_{ex}) + \sqrt{\left(u\left(f(r)\right)\right)^2 + \left(u(P_{bk})\right)^2} \qquad (1)$$

where *u(x)* represents uncertainty associated with *x.* An empirical equation for *u(f(r))* was obtained from multiple measurements (reported in Figure II-2) of reference standard solutions at different concentrations:

$$u\left(f(r)\right) = \sqrt{\left(\frac{k_1}{\sqrt{N}}\right)^2 + \left(\frac{k_2}{N}\right)^2} \qquad (2)$$

where *N* is the signal strength, and k_1 and k_2 are empirical parameters obtained by fitting the above equation for each element (see Figure II-2 for data fitting). Uncertainty due to blank correction and intermediate precision bias were also calculated [101, 102] and detailed in the Appendix (Table A11 and Section A.3). This approach helped in optimizing the final volume and dilution factor for each sample to maximize precision allowing 0.5 mL of sample for uptake, signal

stabilization, and a margin of safety to prevent sample tube drying. Thus, volume $V = \frac{M}{C} = V_0 + F \cdot t$, where F is the sample flow rate (0.1 mL min^{-1}), t is the total analysis time (min), V_0 is the fixed volume (0.5 mL), M is the mass of element of interest (ng), and C is concentration (µg L^{-1}). The voltage signal for a reference isotope was expressed as $N = S \cdot M/V$, where S is sensitivity. The signal variance stabilized after 3 minutes of analysis and the standard error was proportional to $\frac{1}{\sqrt{t}}$ thereafter, which directly governs the uncertainty (u) of a measurement as a function of total sample analysis time (Appendix Equation A11, Figure A10). Since both signal strength N and measurement time t can be described as a function of volume V and uncertainty is a function of N and t (Appendix Equations A3, A8 and A10), we can represent uncertainty (u) as a function of volume V. The optimum volume was then found by setting $\frac{\partial u(V)}{\partial V} = 0$.

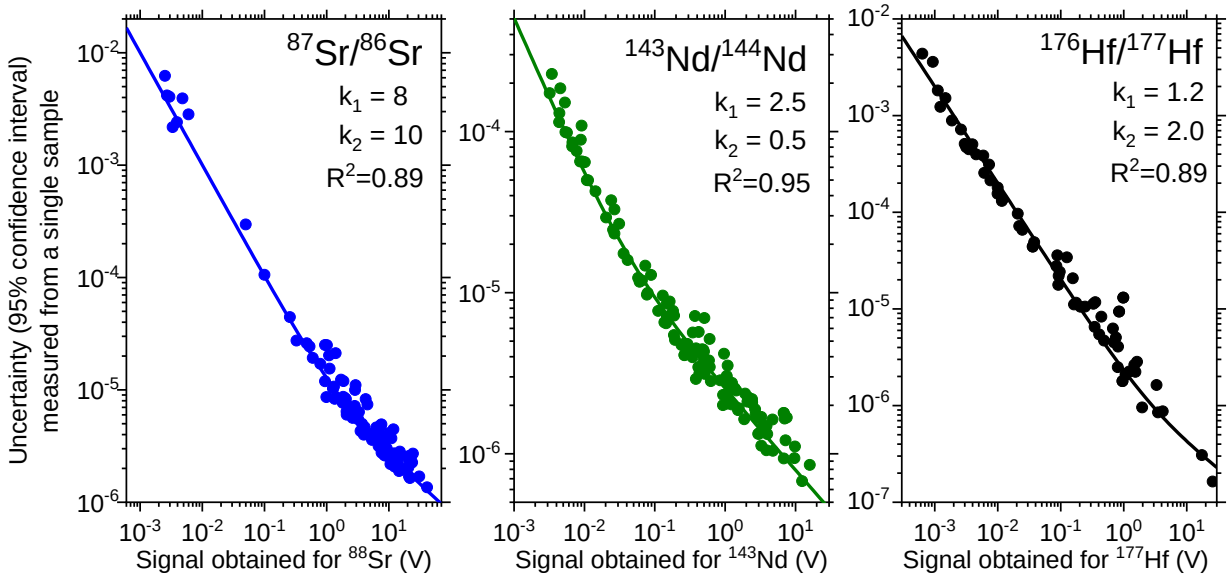

Figure II-2. Measurement uncertainties for $^{87}Sr/^{86}Sr$ (left), $^{143}Nd/^{144}Nd$ (center), and $^{176}Hf/^{177}Hf$ (right) isotope ratios calculated from observed standard deviation. Uncertainty was given by 95% confidence interval (C.I.) = 2×standard deviation/ square root of the number of readings in a single measurement. k_1 and k_2 are empirical constants estimated from best-fit curves and used in Equation 2. Data presented here were generated using analysis of SRM 987 for Sr, JNdi-1 for Nd, and an in-house prepared standard for Hf.

Samples for characterizing PM sources

Based on previous studies on Houston, Texas [23, 54, 86], four major local sources were identified as potential influencers for Sr, Nd and/or Hf in ambient PM – (i) soil and road dust resuspension, (ii) motor vehicle emission, (iii) FCC catalysts emission from petroleum refineries, and (iv) concrete dust from construction activity. Soil samples were collected at Clinton Drive (latitude 29.73372; longitude -95.25759), a hyper-industrialized section of Houston, Texas where the United States Environmental Protection Agency Air Quality Index is often in the unhealthy range, and consequently is the target of many investigations e.g., [23, 87]. We collected the soil samples using plastic spatulas and nylon brushes after digging to ~5 cm depth (to remove contamination from very recent surface activities), oven-dried (105 °C for 24 hours in a loosely

covered Teflon vessel) and sieved with 40 μm mesh (to avoid large clumps and vegetative matter that are unlikely to represent crustal material in ambient PM) [86] before dissolution. No further attempts were made to characterize the soil samples.

Fine PM emitted by the ~20,000 predominantly gasoline-driven light-duty vehicles traversing the Washburn Tunnel (29.72829; -95.21192) daily was collected along with background $PM_{2.5}$ from the ventilation (blower) room [21]. Two sets were obtained (total 4 samples): one from January 3 – February 1, 2013 and the other from February 2 – February 14, 2013 on 47 mm Teflon filters using Rupprecht & Patashnick 2025 Partisol samplers at flow rate of 1 $m^3\ h^{-1}$. Tunnel samplers were placed on a raised catwalk sufficiently away from the north entrance/exit (~44 m) to nearly eliminate sampling of ambient/outside air. Background air was sampled from the ventilation room housing a blower that force-convects air into the tunnel. This approach provided realistic estimates of both tailpipe and non-tailpipe automotive emissions under actual driving conditions accounting for heterogeneities in vehicle/engine types, driving habits, maintenance histories, etc. thereby capturing numerous real-world sources of variability. Concentrations measured inside the tunnel were subtracted from the respective ventilation room values yielding the cumulative emission profile of the vehicular fleet traversing the tunnel over 43-days [21].

Three different fresh zeolite catalysts used in FCC units of petroleum refineries, an important economic activity and pollution source in Houston, were obtained from Grace Davison, Columbia, MD (designated as FCC1–FCC3). Due to possibility of catalyst poisoning during cracking [86], we also analyzed a spent or equilibrium catalyst removed by cyclone separators from the FCC unit's product stream after its prolonged use from a global refining company with

local operations (see also Appendix Table A5). The fresh and spent FCC catalysts are depicted separately due to differences in their elemental composition.

Representative concrete dust was collected from commercially available concrete mix from two different manufacturers (Quikrete and CTS). All bulk samples were sifted through 40 µm polyethylene sieves before dissolution. Aerosol samples were weighed and dissolved as collected on standard 2 µm pore sized Teflon filters commonly used in airborne PM investigations (Whatman Catalog number: 7592-104, $PM_{2.5}$ Air Monitoring PTFE) [21, 23, 35, 45, 54, 86-88].

Results and Discussion

Column chemistry

In contrast to previous cation exchange results with large (≥ 100 mg) rock samples e.g., [93, 103-105], Sr and Nd could not be separated in one step in our environmental samples (Appendix Figure A1). Even though specific reasons for this result are unknown, it could potentially arise from matrix effects and lower mass loading [61]. Nevertheless, it explicitly demonstrates the need for a new analytical method necessitating initial Sr extraction before separating Hf, Nd, and matrix elements. The manuscript only depicts low equivalent mass (0.3 mg) results for SRM 1648a as a representative example since it most closely simulates our target mass of ambient PM. Results for other matrices (BCR-2, BCR-723, and SRM 1633b) and high mass (25 mg) samples are shown in Appendix Figures A2-A5.

Step 1: Sr-Spec columns for initial Sr extraction (Column I)

As shown in Figure II-3(a), Sr and Pb were completely retained on the resin when passed with 3.5 M HNO_3 as expected from previous studies [91, 92] whereas Hf, Ti, Fe, rare earths, Rb, and Ca, and other matrix elements were washed out in the first 2 mL. Sr fully eluted with as little as 1 mL of ultrapure water separating from the Nd-Hf fraction. Ba co-eluted with Sr thereby reducing oxide interference for Nd [103]. Pb did not wash out until 7 M HCl was passed, which was not further pursued herein because it is predominantly of anthropogenic origin [23, 45] and is less likely to be a useful crustal dust tracer in urban environments. However, due to the importance of Pb in urban PM investigations, this fraction can be further analyzed when performing research to distinguish its anthropogenic and crustal origins [23, 45, 63, 74, 83]. Similar results were obtained with other samples (Appendix Figures A2-A5) demonstrating that Sr-Spec resins comprehensively separated Sr in all cases.

Step 2: Cation exchange for Hf, Nd, and matrix separation (Column II)

The first 2 mL eluted in step 1 was subjected to cation exchange to separate Nd and Hf. As shown in Figure II-3(b), the Hf fraction was completely eluted (but along with Ti) in the first 10 mL of passing 1 M HCl + 0.1 M HF without any detectable Lu and Yb. Several trace elements (e.g., Zn, Cu, Co, Ni, Mn), which are tracers for anthropogenic urban PM sources [62, 63] also eluted in the first 10 mL of 2.5 M HCl rinse but were not directly pursued herein. Another 15 mL of 2.5 M HCl ensured the complete removal of Ca and Fe (eliminating its interference for Hf [93]) and > 90 % removal of Rb. The high mass (25 mg) SRM 1633b sample eluted ~ 25 % of Lu, Yb, Tm, and ~18% of other lanthanides in this initial fraction (Appendix Figure A5). For all other samples > 95 % of rare earths were eluted in the next 25 mL of 7 M HCl (see Appendix Figures

A2, A4, and A5). For high mass samples, all rare earths were eluted in no more than 15 mL whereas low mass samples exhibited a wider tailing until a maximum of 25 mL (cumulative 60 mL in Figure II-3(b)). However, in this step, Ti was not separated from Hf, which may bias MC-ICP-MS measurements [93, 106] and Sm co-eluted with Nd necessitating additional steps as described next.

Step 3: α-HIBA chemistry to separate Sm and Nd (Column III)

The isobaric interference of ^{144}Sm on ^{144}Nd can be mathematically corrected during MC-ICP-MS [83, 107]. However, since propagated uncertainties can amplify and significantly reduce accuracy for low concentrations as in our case, a third step to chemically separate Sm from Nd was implemented using the final cut from step 2 (35 – 60 mL range in Figure II-3). All heavy rare earths and Sm were eluted in the first 3 mL of α-HIBA (Figure II-3(c)). Even though the subsequent 4 mL eluted > 99 % of Nd, we collected an additional 1 mL ensuring complete Nd recovery, noting that Pr does not pose any interferences in our measurements. No significant differences were observed in peak locations between different reference materials as no matrix elements were present at this point. Any α-HIBA remaining in the Nd cut was removed by adding A*qua Regia* and heating overnight to 105 °C in a closed Teflon vial [108].

Step 4: Ln-Spec resins to separate Ti and Hf (Column IV)

Both Ti and Fe cause inaccurate ^{176}Hf/^{177}Hf isotope measurements [93, 97]. Since Fe was removed in step 2, the primary focus in this step was to remove Ti from Hf. This step also removes any remaining traces of the main interferents (Lu and Yb), and a few matrix elements (e.g., Na, Mg, and Al) from slipping into the Hf-cut [93], which may induce measurement bias [83, 103]. The Hf-cut from cation exchange (first 10 mL from step 2 and Figure II-3(b)) was initially

dissolved in 3 M HCl, passed through Ln-Spec resins, and followed by 7 M HCl to remove the interfering elements. As shown in Figure II-3(d), Ti and Sb eluted by passing 1% H_2O_2 + 3 M HNO_3. We did not observe typical orange/yellow-colored Ti-peroxide complexes for the low equivalent mass (0.3 mg) sample, which was however prominent in 25 mg samples and has sometimes used as a visual indicator for Ti elution [93, 98]. Washout (1 mL + 1 mL) with ultrapure water is recommended between reagents to prevent Hf elution before passing 1 M HNO_3 + 0.5 M HF. Although 0.3 M HF is sufficient to elute Hf, a sharper curve was achieved with 0.5 M HF. As an aside, Zr was shown to co-elute with Hf in Figure II-3(d), which does not affect Hf isotopes measurements in MC-ICP-MS [93, 106] but severely biases Hf in Thermal Ionization Mass Spectrometry (TIMS) [93, 109].

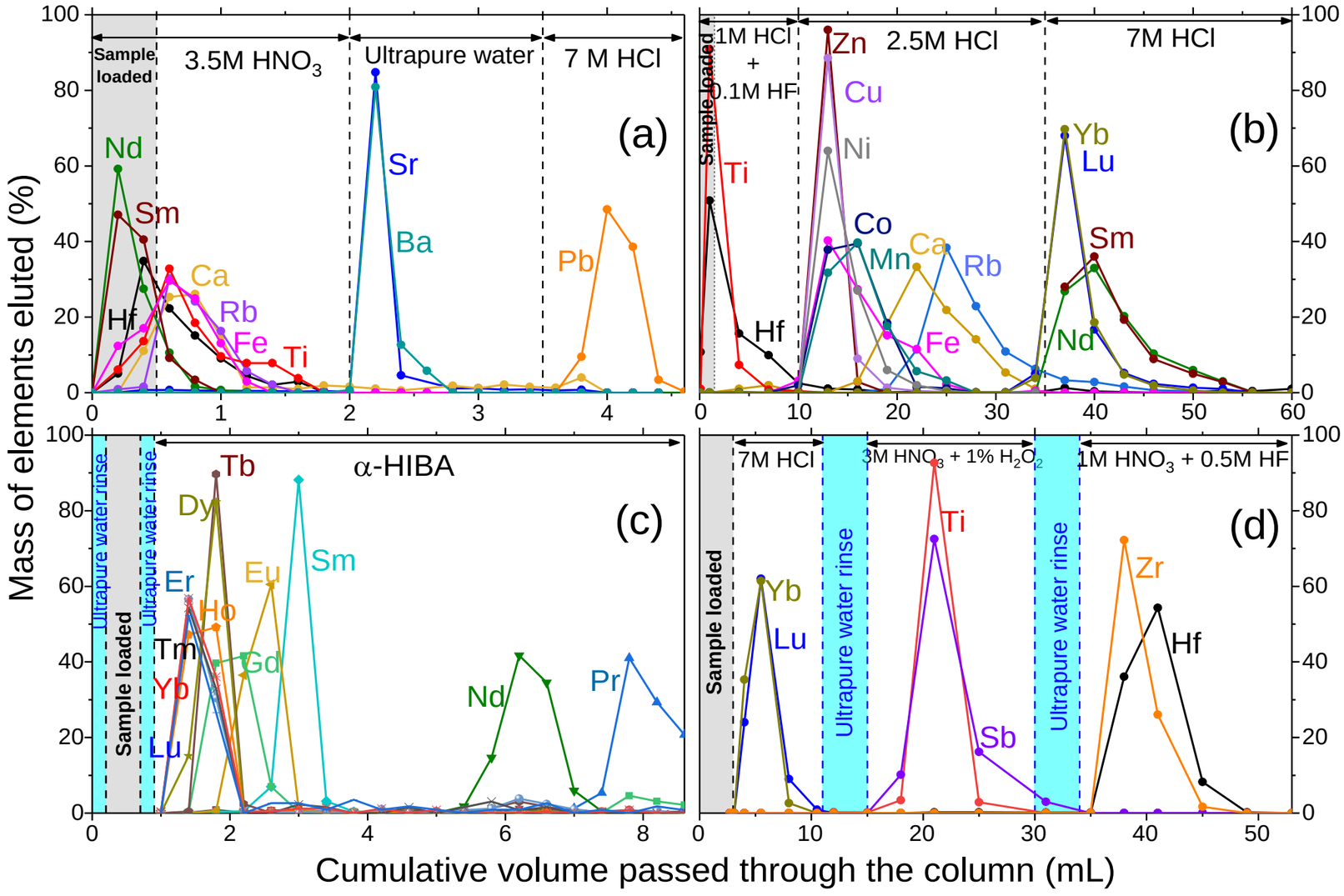

Figure II-3. Elution curves of elements from 0.3 mg equivalent SRM 1648a when passed in sequence through columns (a) Sr- Spec resin, mesh 50-100 µm, (b) 50W-X8 resin, 200-400 µm mesh, hydrogen form, (c) AG 50W-X4 resin, 100-200 µm mesh, hydrogen form with 0.225 M α-HIBA at pH=4.7, and (d) Ln-Spec resin. (See Appendix Figures A2 – A5 for facile chromatographic separation of Sr, Nd , and Hf from all other samples).

The entire scheme for separating Sr, Nd, and Hf fractions based on the above data is shown in Figure II-1 for convenience and described in more detail in Appendix A (Table A6). The measured procedural blanks after passing through columns and the acid blanks (not passed through columns) are summarized in Table II- 1. Blank values in this study are on the lower end of literature reports [46, 61, 77, 81-84, 93, 104, 110] and are 140-1,800 times lower than elemental masses in even the smallest sample mass analyzed (0.3 mg) demonstrating reliable measurements. Analysis of samples post-purification showed significant reduction of isobaric interferences: ^{86}Kr, ^{87}Rb, and ^{144}Sm contributed < 0.2 % of the total signal on ^{86}Sr, ^{87}Sr, and ^{144}Nd respectively (see example of SRM 1648a in Appendix Table A10) and ^{176}Lu and ^{176}Yb interfered < 0.01 % on ^{176}Hf, which was crucial to avoid substantial positive errors in ^{176}Hf/^{177}Hf analysis [93]. Additionally, Ce/Nd ratio was observed to be less than 0.015 in the Nd cut thus ensuring negligible effect of Ce on ^{143}Nd/^{144}Nd measurements. Recovery of Sr, Nd, and Hf for all CRM samples was greater than 94.5%, 82.0% and 91.8% respectively (see Table II- 2 for metals recovery from individual CRMs), demonstrating high efficiency of the proposed scheme. These near quantitative recoveries also demonstrate only minor on-column fractionation effects, which is likely to affect lighter elements like Sr and Nd and was corrected by Russell's correction [111] as discussed in methods section. Elemental analysis of the filter blanks used in PM collection is summarized in Appendix Table A9.

Table II-1 Average (± standard deviation) procedural blank (dissolution + column chemistry) values measured and comparison with our lower bound sample mass. Data from other studies reporting procedural blanks for Sr, Nd, or Hf are also shown for comparison.

Element	Blank values measured only from acids (pg) (n=3)	Procedural blanks measured (pg) (n=3)	Elemental mass in 0.3 mg SRM 1648a (pg)	Literature reported blank range (pg)	References
Sr	5±1	37±5	65,000	29-400	[46, 61, 77, 83, 84, 104, 110]
Nd	1±0.5	17±3	7,500	1-225	[46, 61, 77, 81, 83, 84, 104, 110]
Hf	3±1	11±2	1,500	10-59	[82, 83, 93, 104, 110]

Table II-2. Recovery (in %) of elements measured post chromatography procedure proposed in this study.

Samples	Mass of sample dissolved (mg)	Recovery in %		
		Sr	Nd	Hf
BCR-2	0.3	98.0	95.1	92.2
	25	98.6	96.5	95.1
SRM 1648a	0.3	94.5	96.5	93.9
	25	96.5	96.5	93.1
BCR-723	0.3	95.2	91.3	95.1
	25	99.5	97.0	93.2
SRM 1633b	0.3	98.1	95.9	91.8
	25	99.5	81.5	93.6

Isotope values measured in reference materials

As shown in Figure II-4, isotope ratios measured in BCR-2 were $^{87}Sr/^{86}Sr = 0.705014 \pm 0.000012$, $^{143}Nd/^{144}Nd = 0.512633 \pm 0.000031$, and $^{176}Hf/^{177}Hf = 0.282850 \pm 0.000008$, which agreed with reported values [112] demonstrating the accuracy and precision of the methodology. Note that Sr and Nd isotopic ratios are not certified in BCR-723, but our $^{143}Nd/^{144}Nd$ ratio (0.512223 ± 0.000014) overlapped with a recently published value (0.512222 ± 0.000016) but not $^{87}Sr/^{86}Sr$ [61]. This deviation in Sr ratios cannot be interpreted at this juncture but points to the need for more analyses of BCR-723 to establish an acceptable range of values. Nevertheless, our $^{87}Sr/^{86}Sr$ measurements agree with other reference materials (BCR-2 (Figure II-4) and NIST 987 (Figure A.9)) [112] demonstrating good quality control.

$^{87}Sr/^{86}Sr$, $^{143}Nd/^{144}Nd$, and $^{176}Hf/^{177}Hf$ ratios were also measured for the first time in SRM 1648a and SRM 1633b as 0.712578 ± 0.000010, 0.511740 ± 0.000021, 0.282395 ± 0.000017; and 0.703045 ± 0.0000011, 0.512591 ± 0.000021, 0.282454 ± 0.000015, respectively. Individual measurements for all four reference materials are depicted graphically in Figure II-4 and validate our procedures.

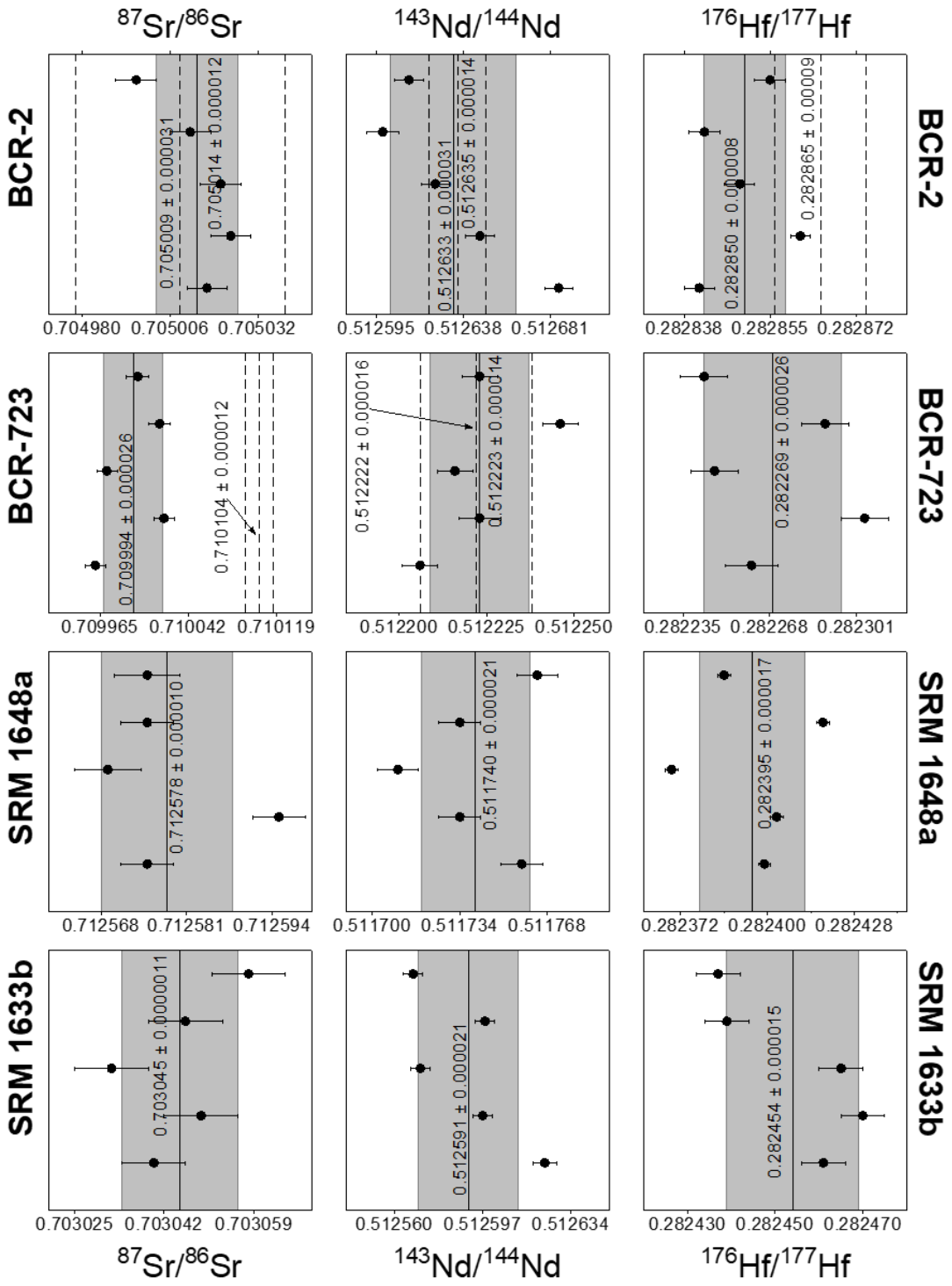

Figure II-4. Compilation of five duplicate measurements of $^{87}Sr/^{86}Sr$ and $^{143}Nd/^{144}Nd$ for all reference materials (BCR-2, BCR-723, SRM 1648a, SRM 1633b) analyzed in this study. The

gray area represents the mean ± 95% confidence interval. Solid vertical lines represent the average depicted in the associated text along with the 95% confidence interval. Dashed vertical lines for BCR-2 represent isotopic data (mean ± standard deviation) from the GeoRem database [112]) and those for BCR-723 are from [61]. These isotopic ratios for 1648a and 1633b and $^{176}Hf/^{177}Hf$ in BCR-723 have not been reported earlier. Difference of means ≤ expanded uncertainties were regarded as not significantly different as per ERM (Application Note 1) [113]. Data for the above graphs are given in Appendix Table A13.

Isotopic ratios to distinguish crustal and anthropogenic sources in urban settings

Measured isotopic ratios for four sources relevant to greater Houston [23, 54, 87] are shown in Figure II-5 (corresponding elemental ratios are in Appendix Table A8). Since this research was motivated by the need to isolate and quantify North African dust in complex urban atmospheres, these matrices are superimposed on North African aerosol signatures in the Caribbean and North Atlantic [68, 69, 74]. As seen in Figure II-5(a), $^{87}Sr/^{86}Sr$ well-distinguished PM from the targeted urban sources; (i) local soil (0.712005 ± 0.000077), (ii) motor vehicles (0.71498 ± 0.00058), (iii) FCC catalysts (0.71104 ± 0.00017) and (iv) concrete (0.708050 ± 0.000016). Importantly, Sr ratios vary widely in long-range transported North African dust (0.711718 – 0.717412) presumably due to differences in potential North African source regions [71], sea spray influences [114], and changes in particle size during transport [67, 68]. Consequently, Sr isotopic ratios in North African dust in Barbados overlapped significantly with vehicular emissions and soil and was close to FCC catalysts pointing to difficulties in separating these four aerosol sources solely via Sr isotopes. In contrast, Sr from concrete dust was easily distinguished because it is extremely non-radiogenic (0.708050 ± 0.000016). Measurements for concrete dust agree with literature data for cement (0.70759 – 0.71034) [45, 115].

Further, as shown in Figure II-5a, the Nd isotopic composition alone is unlikely to distinguish North African dust, soil, concrete, and motor vehicles because they all exhibited relatively similar ε_{Nd}. Other research studies have reported ε_{Nd} in the range of -10.9 to -8.2 for aerosols collected near a densely trafficked site, which bounds our narrower range of -9.5 to 9.0. Similarly, a European study reported a single value of ε_{Nd} in cement (= 7.8) [45], which is within our measured range of -8.2 to -7.7. FCC catalysts' Nd isotopic signature was highly non-radiogenic ($-28 \leq \varepsilon_{Nd} \leq -22$) and substantially different from all other matrices analyzed. Ours are the first reports of Nd isotopic ratios in petroleum refineries' primary emissions, which depict them to be slightly less radiogenic than steel plant emissions ($-20 \leq \varepsilon_{Nd} \leq -18$) [116, 117]. While fresh catalysts ($-28.4 \leq \varepsilon_{Nd} \leq -25.9$) were tightly clustered, the spent catalyst ($\varepsilon_{Nd} = -21.8 \pm 0.7$) migrated towards more radiogenic Nd, attributed to its poisoning [86], which was confirmed by measuring enrichment of V, Co, Ni, Co, Mo, and Sb in comparison to fresh catalysts (see Appendix Figure A11 and Figure A9). This approach demonstrates that Sr and Nd isotopes together can accurately distinguish aerosols emanating from construction (i.e., cement/concrete) and crude oil cracking operations from long-range transported dust, but not North African dust from soil and automobiles. These results motivate the need to monitor another isotope to better separate sources that are enriched in typically crustal elements. We chose Hf for this purpose, which also captures sea spray that tags North African dust as it transports across the Atlantic Ocean, depicted as "seawater array" in blue color on the top left corner of Figure II-5b [118] lying far above the North African dust region.

In contrast to the Sr-Nd relationship in Figure II-5a, concrete dust (ε_{Hf} = -18 to -16.5) and vehicular PM (ε_{Hf} = -20.7 to -20.3) lie closer to one another in Figure II-5b appearing below the zircon-bearing sediment array and separating from FCC catalysts (ε_{Hf} = -14.3 to -12.5). Hf in vehicular aerosols were least radiogenic in comparison to other sources, attributed to its anthropogenic origins from brake linings and autocatalysts as they were also enriched in Zr (26 ± 9 μg g^{-1}), which is strongly chemically associated with Hf [21, 119]. Soil had more radiogenic Hf (ε_{Hf} = -13 to -12) than concrete dust and vehicular PM but overlapped with FCC catalysts. As seen in Figure II-5b, the Nd-Hf combination better distinguishes motor vehicles from North African dust (that scatters around the zircon-free sediment array [67-69]) compared with Sr-Nd in Figure II-5a. The higher content of radiogenic Hf in long-range transported North African dust ($-11 \leq \varepsilon_{Hf} \leq -6$) allows its facile separation from all other sources considered that were less radiogenic ($-21 \leq \varepsilon_{Hf} \leq -13$), indicating its ability to well-trace North African dust in urban settings even in the presence of myriad other sources.

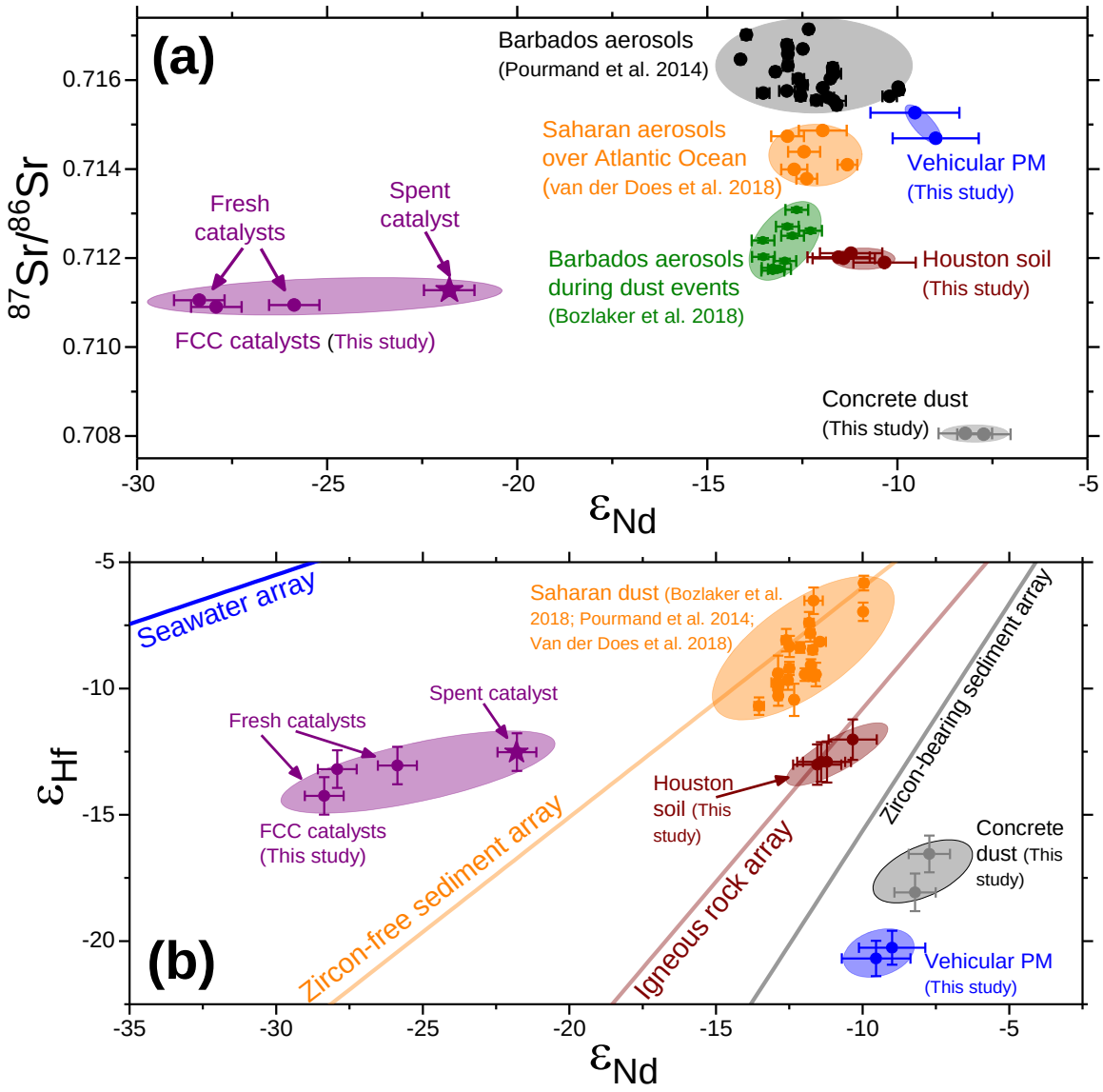

Figure II-5. Sr-Nd variation (top panel, (a)) and Hf-Nd variation (bottom panel, (b)) in several urban source samples measured in this study. Anthropogenic sources (petroleum refining, motor vehicles, and concrete) and soil resuspension are compared with trans-Atlantic North African dust composition obtained from the literature [68, 69, 74]. Hf and Nd variation are expressed in relative deviation with respect to CHUR ($^{176}Hf/^{177}Hf$ = 0.282785 and $^{143}Nd/^{144}Nd$ = 0.512630). Data for the above graph can be found in Appendix Table A12.

Evaluation of elemental tracers supplemental to isotopic ratios for anthropogenic sources

In addition to using isotopic ratios to distinguish dust sources of interest, we fingerprinted PM source samples for their elemental composition and calculated corresponding enrichment factors with respect to the upper continental crust (UCC) with Ti as the reference to assess potential elemental markers for the sources of interest. As seen in Figure II-6, vehicular emissions sampled in the Washburn Tunnel showed enrichment factors > 100 for Cu, Sb, Cd, Mo, Sn, and Se and > 50 for As demonstrating that these seven elements can potentially be used to isolate PM emanating from automobiles. However, Sn has several industrial interferences [54] making it unsuitable as a vehicular tracer and therefore its elemental ratios were not further pursued. Additionally, As and Se were omitted because they are co-emitted by construction activities and coal combustion [54] and hence are not expected to be useful to uniquely track vehicular emissions or concrete dust. This was corroborated using the sample collected in the forced ventilation room i.e., tunnel background representing PM downstream of several industrial sources [21], which was highly enriched in As and Se (enrichment factors > 100 as shown in Figure A.12) demonstrating their non-vehicular anthropogenic sources. In contrast, as summarized in Appendix Table A8, dominant elemental ratios of Cu, Sb, Cd with respect to both Ti (crustal element reference) and Zn (anthropogenic element reference) validate their ability to uniquely track vehicular emissions [54]. Note that although FCC catalysts exhibited a higher Mo/Zn ratio than motor vehicles the Mo/Ti ratio was substantially enriched suggesting Mo could possibly be a good tracer of vehicular $PM_{2.5}$ as we recently reported [54].

Concrete dust was enriched in eight metals Ca, Cu, Zn, As, Se, Sr, Mo, and Cd as seen in Figure II-6. As explained above, Cu, Mo, and Cd were assigned to automobile emissions since they had 10-fold higher enrichment factors in PM collected within the vehicular tunnel (~1,000 compared to ~100 in concrete) and is consistent with other literature reports [21]. Additionally, Zn, As, and Se are emitted by myriad anthropogenic sources negating their use as unique markers for any source [54]. Hence, Ca is the only element that may strongly separate concrete dust and identify anthropogenic Sr from construction activities because Sr is only relatively weakly enriched (~50) in this source.

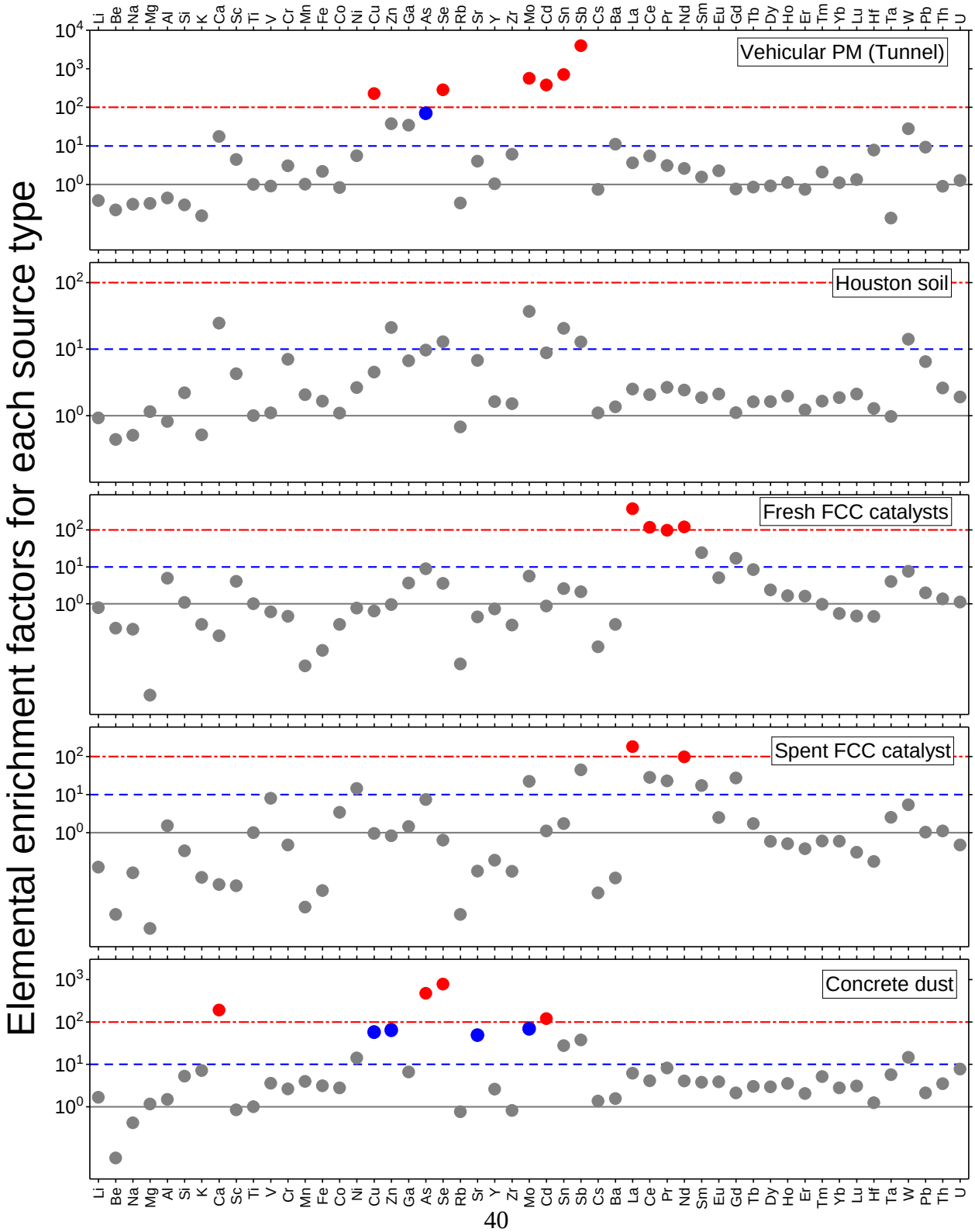
Elemental enrichment factors for each source type
Vehicular PM (Tunnel)
Houston soil
Fresh FCC catalysts
Spent FCC catalyst
Concrete dust
Li Be Na Mg Al Si K Ca Sc Ti V Cr Mn Fe Co Ni Cu Zn Ga As Se Rb Sr Y Zr Mo Cd Sn Sb Cs Ba La Ce Pr Nd Sm Eu Gd Tb Dy Ho Er Tm Yb Lu Hf Ta W Pb Th U

Figure II-6. Average enrichment factors (EFs) of elements measured in this study with respect to average upper continental crust (UCC) [120] with Ti as reference for various PM source samples (Houston soil, n=4; vehicular PM, n=2; fresh FCC catalysts, n=3; used FCC catalyst, n=1; and concrete dust, n=2) with DRC-q-ICP-MS. The solid grey horizontal line represents EF = 1 and dashed horizontal blue line represents EF=10 above which enrichment was considered significant. The blue data points show 50<EF<100 which were tagged as being "moderately enriched" whereas the red data points show EF >100 which were tagged as being "strongly enriched" and consequently potential tracers for the respective sources. Supplementary elemental abundance data for this graph has been plotted in Appendix Figure A6 for reference.

FCC catalysts are enriched lighter lanthanides (La-Sm and Gd), which are typically used to isolate any influence of refining operations on ambient atmospheric rare earth concentrations [86, 87]. Ratios of La to other light rare earths (Appendix Table A8) were highest for FCC validating them as strong tracers of Nd originating from refineries, and when coupled with $^{143}Nd/^{144}Nd$ can effectively remove anthropogenic influences on ambient airborne lanthanoids. The local soil only shows marginal enrichment of vehicular marker metals (Mo, Cd, Pb, Sn, and Sb) and concrete marker metal (Ca) reflective of "contamination" from the 22.7 billion vehicle miles driven by Texans just in November 2019 [121, 122] and the strong construction industry in Houston ($7.3 billion in approved building permits in the year 2019). While Si/Al has been suggested as a potential tracer to isolate local soil from North African dust [23], elemental ratios (Appendix Table A8) show Si/Al is higher in concrete dust than local soil making the ratio ineffective to trace local soil in our case and potentially in other urban/industrialized environments as well. A comparison between Sr-Nd-Hf isotopic characteristics (see Appendix Figure A7) and elemental characteristics of Fe, Al, Si, and Ti (see Appendix Figure A8) of mineral sources (this study) and key potential source areas (PSAs) in Africa additionally show soil is less likely to differentiate itself from other crustal sources solely using elemental measurements. In summary,

even though isotopic ratios are able to separate these sources, including elemental analysis is likely to further differentiate and measure the influence of anthropogenic PM emission.

Table II-3. A comprehensive list of tracers established in this study as well as tracers reported in the literature [21, 23, 68, 69, 86].

Sources	Isotopic tracers			Elemental tracers
	$^{87}Sr/^{86}Sr$	ε_{Nd}	ε_{Hf}	
Houston soil	0.712005 ± 0.000077	-10.3 to -11.5	-13 to -12	Si, Al, Ca, Mg, Ti Fe, K
Motor vehicles†			-20.7 to -20.3	Sb, Cd, Mo, As, Cu
Petroleum refining FCC units		-28 to -22		La, Ce, Pr, Nd, Sm, Gd
Concrete dust	0.708050 ± 0.000016			Ca, Sr, Al, Si, As, Se, Cd
North African dust (literature)	0.711718 – 0.717412	-9 to -13	-11 to -6	Si, Al, Ca, Mg, Ti, Fe, K

† *Note that rhodium, palladium, and platinum are excellent elemental tracers for motor vehicles but have been omitted since they were not measured in this study.*

Conclusions

The newly developed ion-exchange chromatography preconcentration method requires a relatively simple laboratory setup and efficiently extracts Sr, Nd, and Hf from low mass samples displaying its applicability to a range of environmental matrices. This study not only demonstrates a novel chromatography scheme but also measured coupled $^{87}Sr/^{86}Sr$, $^{143}Nd/^{144}Nd$, and $^{176}Hf/^{177}Hf$ isotope ratios for the first time in three reference materials (BCR-723, SRM 1633b and SRM 1648a). Uncertainty equations were modeled with solution-based reference materials to calculate long-term error propagation and establish the volume to which the samples need to be diluted to

maximize precision. Sr-Nd-Hf isotopic characteristics of several urban PM sources including motor vehicles, construction, and petroleum refining were also measured for the first time along with local soil. Isotopic characteristics are demonstrated to well-differentiate long-range transported crustal dust (i.e., from the Sahara-Sahel region of North Africa) from local mineral sources of PM (i.e., construction activity and local soil). For example, concrete/cement materials are highly non-radiogenic in Sr allowing them to be distinguished from North African dust. FCC catalysts are extremely non-radiogenic in Nd separating primary petroleum refining emissions from other aerosol sources. Hf-Nd coupling on the other hand separated North African dust from vehicular sources and soil from FCC catalysts which otherwise had overlapping $^{87}Sr/^{86}Sr$ ratios. Importantly, we show that while the elemental composition of crustal dust sources (North African dust and local soil) is not easily distinguishable, their Sr-Nd-Hf isotopic compositions can be used to explicitly isolate them. However, inclusion of elemental tracers is more likely to distinguish metal rich anthropogenic sources. Thus, we recommend both elemental and isotopic measurements to better isolate myriad natural and anthropogenic sources critical for accurately apportioning primary ambient PM in complex atmospheres.

Reported elution characteristics facilitate quantitation of PM emitters that closely overlap in major and trace elemental composition (e.g., North African dust, construction activities, and local soil that are dominated by Ca, Si, Al, Fe, Mg, and Ti as well as North African dust and soil that share identical rare earth signatures) even during periods of low dust activity. Isotopic analysis enables rigorous differentiation of long-range transported dust from otherwise colinear local sources enabling accurate source apportionment thereby allowing environmental agencies to refine

and implement compliance strategies with respect to air quality standards. For example, regulatory exceptions can be negotiated in case local PM levels exceed federal or state standards under the "exceptional circumstances" category of the United States' Clean Air Act by subtracting apportioned North African dust from measured total PM concentrations (and analogously in Asia and Europe).

CHAPTER III

COUPLING SR-ND-HF ISOTOPE RATIOS AND ELEMENTAL ANALYSIS TO ACCURATELY QUANTIFY NORTH AFRICAN DUST CONTRIBUTIONS TO $PM_{2.5}$ IN A COMPLEX URBAN ATMOSPHERE BY REDUCING MINERAL DUST COLLINEARITY

Introduction

It is imperative to determine the sources and composition of airborne particulate matter (PM) in metropolitan areas to better understand its human health impacts, comply with regulations, and formulate policies and plans to control its concentrations [35, 123-125]. Primary PM in urban atmospheres is typically a complex mixture of aerosols locally emitted by soil and road dust resuspension, industrial and construction activities, and automobiles [1, 2, 9, 19, 42, 45, 54, 126, 127] that can also be seasonally impacted by long-range transport [1, 23, 29, 43, 44, 128]. One example of the latter is dust from the Sahara-Sahel region that, being the largest contributor to global dust flux, can substantially add to the aerosol burden already facing population centers in Europe [40, 124, 128] and the south and southeastern United States [1, 23, 29, 38] exacerbating concerns related to health, regional haze, and regulatory compliance. Importantly, governments allow contributions from exceptional PM events that are not reasonably controllable or preventable to be excluded from regulatory decisions and actions. The overarching goal of this paper is to accurately and quantitatively discriminate distal crustal material from local crustal (natural) and anthropogenic primary PM sources in a complex urban atmosphere.

Significant uncertainties are introduced during source apportionment of primary PM when potential tracers are co-emitted by multiple sources or there is overlap in the composition of potential sources, especially when allocating low mass contributions [23, 29]. For example, it is difficult to separate North African dust and non-African local soil at receptor sites since they both represent crustal material consequently possessing similar elemental composition [35, 40, 41]. Another concern is dust emanating from construction activities, which is comprised largely of mineral material lacking unique markers [39, 51], thereby leading to largely unreliable results when using receptor-based source apportionment models.

Existing methods to isolate North African dust from locally emitted aerosols, e.g., the Spanish-Portuguese reference method (SPR) and Tel Aviv University method (TAU) [40, 129], typically require at least a year's worth of sampling at multiple locations and are heavily dependent on correctly selecting background monitoring, which does not preclude varying influences from local sources [40, 41]. A principal component analysis/multiple linear regression receptor-based model [39] can potentially resolve collinearity of Saharan dust and other mineral PM sources, but again requires a large number of samples (typically $\gtrsim 50$ [41]) to effectively capture variances and isolate mineral dust contributions.

An alternate, more promising approach is to employ PM's isotopic composition to isolate sources of otherwise similar elemental composition [42-46] and accurately estimate their individual contributions to PM mass in a single sample. Of relevance to this manuscript, only limited information is available on using $^{87}Sr/^{86}Sr$ and $^{143}Nd/^{144}Nd$ ratios to trace the geological origins of dust in remote [46, 66, 74, 130] and urban [44, 45] regions of the world. Coupling Hf

isotopes to Sr and/or Nd enhances the accuracy of isolating long-range transported natural dust sources [67, 75, 76] based on differing isotope ratios due to variations in source bedrock (Sr-Nd) and zircon depletion (Hf-Nd) during transport [51, 66-69], which has been studied solely in remote locations.

We hypothesize that including Sr, Nd, and Hf isotopic signatures in source apportionment modeling will reduce collinearity between PM sources of otherwise similar elemental composition and produce accurate source contribution estimates for each receptor sample. Focusing on mineral dust, we fingerprint trans-Atlantic North African dust carried in the Trade Winds at Barbados [131] and ambient $PM_{2.5}$ in Houston, TX (a representative populous and industrialized metroplex) for Sr-Nd-Hf isotopes and elemental abundances before, during, and after Saharan dust intrusions to quantitatively estimate its contributions to airborne fine PM under low and high African aerosol influences. This is the first report of Sr-Nd-Hf isotopic ratios in urban PM and one of the first to do so in Saharan-Sahelian dust. We further develop a novel "Isotope Resolved Chemical Mass Balance" (IRCMB) method that optimally combines isotopic and elemental composition to reduce collinearity and improve accuracy of source contribution estimates. This method, like traditional CMB can be applied for a single sample consequently decreasing the sampling burden necessary to implement existing techniques to separate long-range transported dust from local aerosols.

Methods

Sampling

Trans-Atlantic North African dust was collected from the easternmost point in the Caribbean (Ragged Point, Barbados, 13.165N, 59.432W, www.baco.rsmas.miami.edu) to

minimize anthropogenic influences and where sampling has been conducted for over 50 years.[38] Previous studies of mineral dust elemental composition at this site show that, for most elements, the composition is consistently very similar to that of upper crust abundances and is relatively constant from year-to-year [132]. Representative urban $PM_{2.5}$ was sampled from Clinton Drive, Houston (29.734N, 95.258W), which is surrounded by many industrial campuses, residential neighborhoods, and major roadways and is the site of several previous PM investigations [2, 9, 23, 29]. The sampling campaign was designed to characterize two dust outbreaks in the year 2017 by capturing the same air masses in Barbados and Houston. For episode 1, two samples were collected in Barbados, one was integrated over 3-days to capture an entire outbreak (25 – 28 June) and one daily background sample immediately after the active event (28 – 29 June) and six daily samples at Houston spanning 28 June – 04 July. For episode 2, all samples were collected over 24-hours, one during the active event (23 – 24 July) and one background (24 – 25 July) in Barbados and six samples spanning 25 July – 31 July in Houston. The selected dates represent predictions of when North African dust was expected to reach both sites based on satellite imagery, aerosol modelling (Supporting Information Appendix Figure B2 for HYSPLIT trajectories [133], Appendix Figure B3 for AERONET's AOD Data [134], and Appendix Figure B4 for NAAPS dust model output [135]), and Texas Commission on Environmental Quality (TCEQ) forecasts [136]. Houston $PM_{2.5}$ was collected on PTFE filters using Thermo Fisher 2025i Partisol Air Samplers (16.67 L min^{-1} air flow rate). Total suspended particulate matter (TSP) samples were collected on 20 × 25 cm Whatman-41 filters in Barbados using a high-volume sampler (1 m^3 min^{-1} nominal flow rate), one-eighth of which was utilized for elemental and isotopic characterization [132]. For convenience,

all samples were named by their sampling start date (Appendix Table B1 summarizes sampling duration and aerosol mass concentrations). Procedural blanks were also collected to subtract background material from the filter itself.

African dust characterization from Barbados measurements

The dust composition on low-mass days was subtracted from high mass measurements during the active episode to remove background mixing influences and determine "true" African dust elemental and mass characteristics. Isotopic ratios for high dust samples were calculated by end-member analysis, with background days as one end member and North African dust during the active outbreak as the other [137]:

$$R_{\boldsymbol{AD,i}} = \frac{R_{e,i}.M_{e,i} - R_{b,i}.M_{b,i}}{M_{e,i} - M_{b,i}} \qquad \text{(Equation 1)}$$

where R_i is the i^{th} isotope ratio and subscripts '*AD*' denotes North African dust, '*e*' denotes the event or outbreak, '*b*' is the background, and M_i represents the mass of element *i* in the sample.

Acid dissolution, elemental, and isotopic analysis

Forty-nine elements (Li, Be, Na, Mg, Al, Si, K, Ca, Sc, Ti, V, Cr, Mn, Fe, Co, Ni, Cu, Zn, Ga, As, Se, Rb, Sr, Y, Zr, Mo, Cd, Sn, Sb, Cs, Ba, La, Ce, Pr, Nd, Sm, Eu, Gd, Tb, Dy, Ho, Er, Tm, Yb, Lu, Hf, Pb, Th, and U) were analyzed by quadrupole ICP-MS equipped with a collision cell pressurized with ammonia gas (NH_3) (PerkinElmer® NexION® 300) after solubilization by two-stage microwave digestion [87]. Sr, Nd, and Hf isotopes were analyzed by Multi-Collector ICP-MS (MC-ICP-MS) after column separation chemistry [51]. For ease of comparison and as is the convention, Nd and Hf isotopic ratios were expressed as deviation from chondritic uniform

reservoir (CHUR, $^{176}Hf/^{177}Hf$ = 0.282785 and $^{143}Nd/^{144}Nd$ = 0.512630). Instrumental setup, operating parameters, blank correction, uncertainties, and quality control metrics are summarized in SI Tables S2-S9.

Source Apportionment

Applicable elemental source profiles included soil/road dust[51], concrete dust[20, 51], motor vehicles[21, 51], fluidized-bed cracking catalysts (FCC)/refinery emission[51, 86], oil and coal combustion[20, 138], biomass burning[20, 138], and sea salt[20], based on previous reports in Houston.[2, 9, 19, 23, 54, 87] The trans-Atlantic North African dust profile was established during this work (Appendix Table B15). The IRCMB method balances both elements (Equation 2; conventional CMB[139]) and isotopes (this study; Equation 3):

$$C_i = \sum_{j=1}^{J} F_{ij} \bullet S_j \qquad \text{(Equation 2)}$$

$$\sum_{j=1}^{J} F_{ij} \bullet S_j \bullet \left(R_{ij} - \hat{R}_i\right) = 0 \qquad \text{(Equation 3)}$$

where C_i is the ambient concentration of the i^{th} element, F_{ij} is the abundance of i^{th} element in j^{th} source, S_j is the source contribution j^{th} source to ambient $PM_{2.5}$, R_{ij} is the isotope ratio of the j^{th} source corresponding to isotope i (Sr, Nd, and Hf in our case), and $\hat{R}_i$ is the isotope ratio corresponding to element i. All mass balance equations were weighted with effective variance method.[39]

Collinearity in source profiles was deemed significant when both the condition index (CI) and variance decomposition proposition (VDP) were high (>5 and >0.5, respectively).[39] As expected, the two crustal sources that we focused on, namely local soil and North African dust were collinear (VDP = 0.96 and 0.56, respectively). Also as expected, the other mineral dust source, i.e., concrete dust from construction activity was collinear (VDP = 0.79). Removing these three sources reduced CI from 27 to 4.6, making source profiles statistically non-collinear[39]. To reduce collinearity influences and effectively utilize isotope measurements, source apportionment was conducted in three steps (Appendix Figure B7) as detailed below.

Step 1 (traditional chemical mass balance)

Preliminary estimations of $PM_{2.5}$ and elemental contributions were obtained using a weighted least squares algorithm identical to CMBv8.2.[139] Inclusion of isotope ratios (Equation 3) in the dataset reduced CI from 27 to 21. Here, Na, Mg, Al, Si, K, Ca, Ti, V, Fe, Ni, Cu, Zn, As, Se, Sr, Mo, Cd, La, Ce, Nd, Hf, and Pb were used as fitting species given their importance in tracing PM sources in Houston.[2, 19, 23, 29, 51, 54, 140] The dataset was re-processed to reduce collinearity even further.

Step 2 (data extraction for collinear sources)

$PM_{2.5}$, elemental, and isotopic contributions of non-collinear sources were subtracted to create a dataset representing a $PM_{2.5}$ mix solely of collinear sources.

Step 3 (apportionment of collinear sources)

Finally, source contributions were calculated using the same weighted least square algorithm[139] on the modified dataset and data from three collinear sources. Na, Mg, Al, Si, K,

Ca, Ti, Fe, Sr, Nd, and Hf along with $^{87}Sr/^{86}Sr$, $^{143}Nd/^{144}Nd$, and $^{176}Hf/^{177}Hf$ were used for model fitting to resolve locally emitted aerosols from soil and construction activities and crustal material transported from North Africa[51]. Note that including isotopes in this step decreased CI for all collinear profiles from 21 to 12 compared to a CI of 17 achieved by the previously published statistical technique[39].

Results with statistical parameters $R^2 \geq 0.8$ and $\chi^2 \leq 4.0$ were considered satisfactory.[141-143] MATLAB 2021a was employed to automate linear fitting for all combinations of source categories, which would have been impractical to simulate manually[142]. Negative source contribution estimates were avoided.

Synthetic data and method validation

To validate accuracy improvements by using this 3-step IRCMB method and demonstrate the ability of isotopes to separate near-collinear sources, apportionment was also performed using a synthetic but realistic dataset specially created from earlier reports of Houston area source contribution estimates[23, 54, 87, 140]:

$$C_i = \sum_{j=1}^{J} \widehat{S_J} \bullet (F_{ij} + N_{ij}) \qquad \text{(Equation 4)}$$

where $\widehat{S_J}$ is the actual source contribution of the j^{th} source, incorporated into our synthetic dataset, J is the number of source categories (= 9), and N_{ij} is the noise in the dataset for i^{th} element in the j^{th} source. Noise was calculated by generating a random number between 0 and 1 that follows additive white Gaussian noise (AWGN) algorithm and multiplied by uncertainty of the

corresponding data. The details of the synthetic dataset are given in SI Tables S11 and S12. To validate our method's improved accuracy compared to the traditional CMB algorithm, the standardized root mean squared error (SRMSE) was calculated:

$$SRMSE = \sqrt{\frac{1}{n}\sum_{j=1}^{n}\frac{(\mathrm{S_j} - \hat{S}_\mathrm{j})^2}{\hat{S}_\mathrm{j}^{\,2}}} \qquad \text{(Equation 5)}$$

where *n* is the number of sample points processed.

Results and discussion

Transatlantic North African Dust at Barbados

Aerosols during the outbreak in the Caribbean were substantially more radiogenic in Sr and only marginally less radiogenic in Nd ($0.71297 \leq {}^{87}Sr/{}^{86}Sr \leq 0.71392$ and $-14.4 \leq \varepsilon_{Nd} \leq -10.3$) compared with the background ($0.71065 \leq {}^{87}Sr/{}^{86}Sr \leq 0.71174$ and $-4.1 \leq \varepsilon_{Nd} \leq -10.9$) as depicted in Figure III-1a. These values overlap with results of Pourmand and co-workers,[68, 69] our recent work,[74] and Mali and Senegal transects.[51, 72, 144] While Nd in Saharan dust at Barbados was less radiogenic than most Houston PM sources[51] (namely soil resuspension, motor vehicle emission, and concrete dust), it was significantly higher than Nd from petroleum refining,[51] which can be a prominent source of light rare earths (LREEs) in Houston[86, 87, 145]. Hence, Nd isotopes alone cannot distinguish North African dust from other crustal/mineral sources in urban atmospheres strongly influenced by petroleum refining aerosols such as Texas[86, 87, 140, 145], Illinois[146], Spain[52, 126], etc.

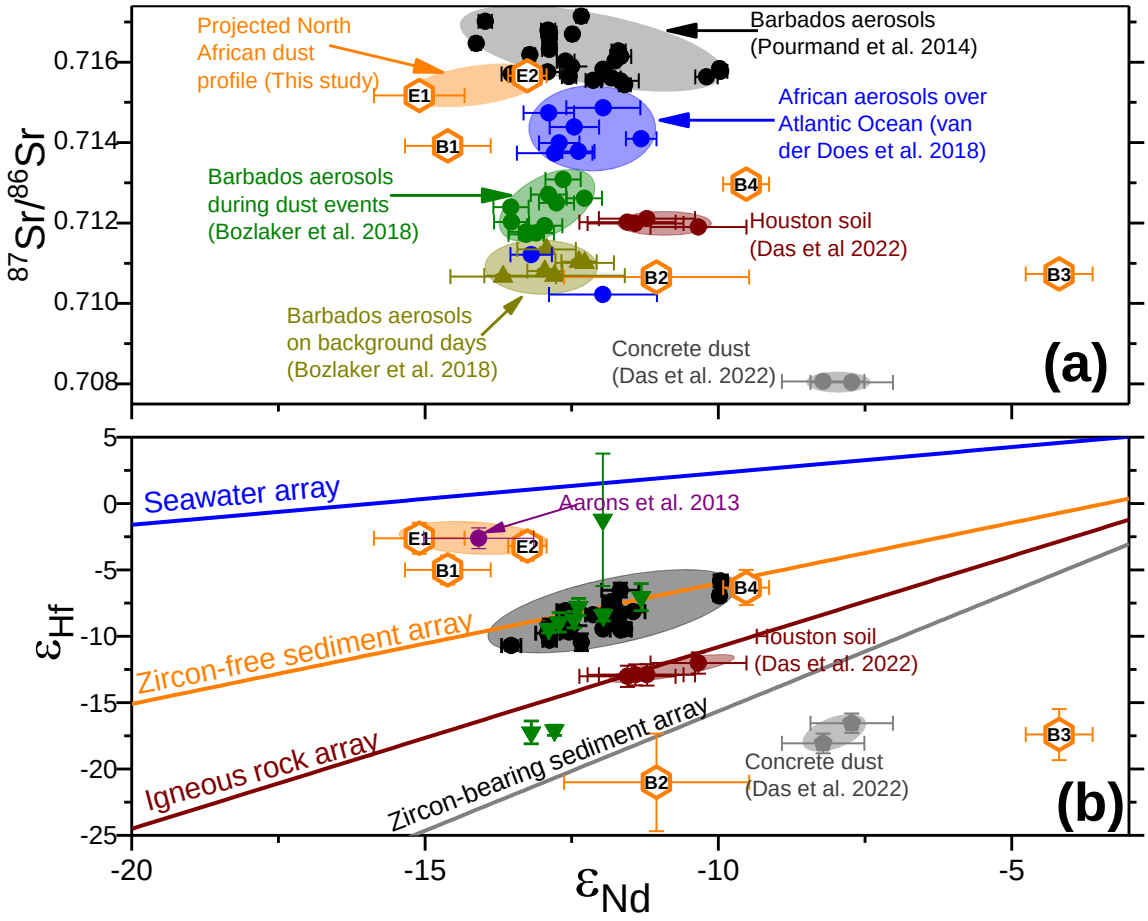

Figure III-1. Top panel (a) Sr-Nd isotopic characteristics of incoming North African dust in Barbados E1 and E2 denote the first and second outbreaks (=B1 – B2 and B4 – B3, respectively)). They are similar to literature reports of trans-Atlantic Saharan dust and distinguish themselves from local mineral dust sources (i.e., soil and construction dust). Bottom panel (b) Nd-Hf isotopic characteristics, showing more radiogenic Hf than some literature data [68, 69] from the mid-Atlantic indicating dependency of $^{176}Hf/^{177}Hf$ on transport distance possibly due to the "zircon effect" [67]. The number labels inside the hexagonal points represent the sample number (e.g., "B1" represents the sample dates June 25-28 and "B4" represents the sample taken on July 22-23 as summarized in Appendix Table B1). Note: Increase in $^{87}Sr/^{86}Sr$, ε_{Nd}, and ε_{Hf} values represents more radiogenic components of the corresponding element.

During the dust outbreak in Barbados, Hf isotopes became more radiogenic ($-6.9 \leq \varepsilon_{Hf} \leq -4.1$) compared with background days ($-21.4 \leq \varepsilon_{Hf} \leq -17.9$) agreeing with literature reports [51, 67-69, 72]. Unlike the Sr-Nd isotope couple, which clearly overlapped with North African source

regions, ε_{Hf} during the outbreak in Barbados was higher than any corresponding reports in the Sahara-Sahel region. This suggests the gravitational settling and loss of the denser and less radiogenic zircon component in dust during long-range transport, which is termed the "zircon effect" [67-69]. Importantly, Sr-Nd-Hf isotopes in Saharan dust measured in Barbados overlapped with another sample collected 5,800 km away from the West African coast in a remote region of the Atlantic Ocean [67], validating our results.

Elemental ratios and corresponding enrichment factors of North African dust in Barbados with respect to crustal Ti are summarized in Appendix Table B10 and Appendix Figure B7. The lack of elemental enrichment (except Co, Mo, and Sn) but contrasting isotopic ratios from local sources demonstrate the value of isotopic measurements to track North African dust in the Houston metroplex.

$PM_{2.5}$ isotopic variations during North African dust storm in Houston

$PM_{2.5}$ concentrations at Clinton Drive increased steeply from 9.3 μg m^{-3} on 28 June to 31.7 μg m^{-3} on 30 June during the first Saharan-Sahelian outbreak and from 10.2 μg m^{-3} on 22nd July to 32 μg m^{-3} on 24th July during the second event (Figure III-2) consistent with North African dust influences evidenced by satellite observations, ground monitoring and TCEQ air quality forecasts, and back trajectories (SI Figures S2 – S4). To facilitate discussion, days with ambient $PM_{2.5}$ concentrations > 25 μg m^{-3} (June 30, July 1, 26, and 27) were classified as "high dust days," those between 12 and 25 μg m^{-3} (June 29, July 2, 28, and 30) were tagged as "medium dust days," and the rest that were < 12 μg m^{-3} (June 28, July 3, 25, and 29) were labelled as regular days (Appendix Table B1). During both the dust events, $^{87}Sr/^{86}Sr$ and ε_{Hf} were in-phase with $PM_{2.5}$ mass

concentrations (R^2 = 0.72 and 0.81, SI Figures S9a and S9c respectively). These variations agree with our finding in Figure 1 that Sr and Hf are more radiogenic in African dust than local PM). While Sr and Hf were significantly more radiogenic during the active outbreak in Houston, ε_{Nd} was negatively correlated (R^2 = 0.72 in Figure B9b), as expected from the lower Nd radiogenicity in North African dust than local sources (Figure III-1). More radiogenic Sr and Hf coupled with less radiogenic Nd in $PM_{2.5}$ support satellite imagery and synoptic-scale models of North African dust transport and its influences on Houston ambient aerosols during the sampling campaign.

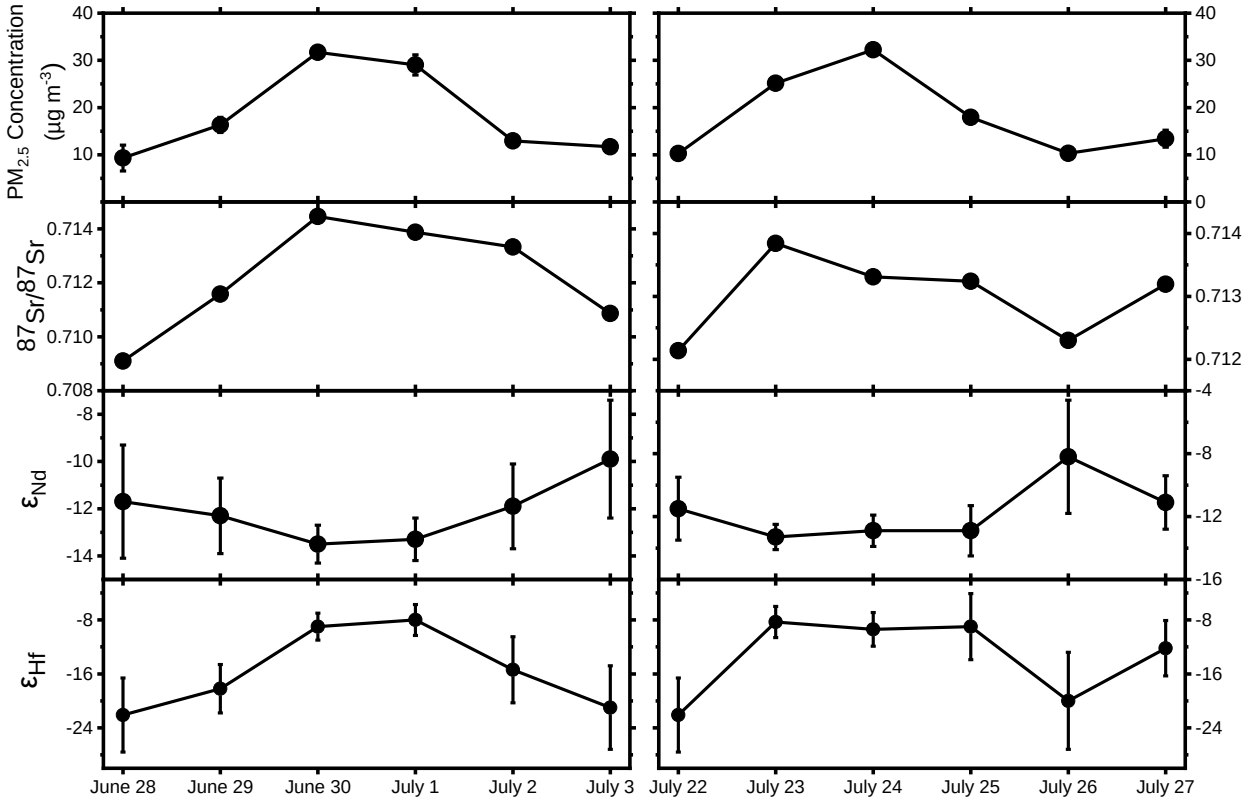

Figure III-2. Simultaneous variations in ambient $PM_{2.5}$ mass concentrations (top row) and isotopic characteristics for both outbreaks. As seen in the second and fourth rows, $^{87}Sr/^{86}Sr$ and ε_{Hf} were in-phase with PM levels whereas as seen in the third row ε_{Nd} was out-of-phase with PM indicating the high sensitivity of these isotopes to detect mixing of North African dust with local urban $PM_{2.5}$. Note that error bars in Sr ratios (second row) are smaller than

the symbol size. Our daily PM measurements are compared with TCEQ's data in Appendix Figure B5 as a quality control check. Variation of isotopic ratios with $PM_{2.5}$ mass concentration is further analyzed in Appendix Figure B9.

Isotopic end member analysis coupled with elemental ratios

End member analysis of Sr, Nd, and Hf characteristics on an isotope mixing plane (enclosed by isotope mixing lines) in combination with elemental ratios were used to further investigate aerosol sources and qualitatively resolve the apportionment of sources rich in mineral material (Figure III-3). Typically, mixing lines between end members are represented by plotting isotope ratios against the inverse of elemental abundance [137]. However, this procedure cannot be directly implemented to ambient urban PM influenced by secondary organic aerosols and black carbon particles that are highly depleted in metals [9, 147, 148]. The presence of metal-poor aerosols reduces elemental abundances and shifts data away from the mixing line, which we accounted for by using elemental ratios that are largely unaffected by metal-depleted aerosols instead of elemental abundances. We chose Ca to normalize Sr, samarium (Sm) for Nd, and lutetium (Lu) for Hf to complement isotopes and explicitly differentiate individual sources. To clearly distinguish concrete dust, which is depleted in radiogenic Sr, Ca was chosen as a reference since it is enriched in both concrete and soil compared to Saharan dust, therefore, we are able to explicitly separate them. Since ratios of different LREEs to Sm can distinguish FCC (petroleum refining) from mineral sources [23, 29, 52, 140, 146], Nd was normalized by Sm to clearly demarcate FCC influences on $^{143}Nd/^{144}Nd$. Hf is relatively depleted in concrete and soil compared to vehicular PM and Saharan dust, however, HREE (heavy rare earth elements) abundances are relatively invariant in these sources [51]. Thus, Lu was chosen to normalize Hf.

Sr and Hf isotopic mixing

Figure III-3a shows the influence of North African dust on Sr isotope ratios in Houston. High dust days (June 30, July 1, July 23, and July 24) move closer to the Barbados North African dust profile in comparison to regular or background days (June 28, July 3, July 22, and July 26), which either lie near Houston soil or concrete dust. Thus, in the absence of Saharan-Sahelian dust, the two dominant sources of Sr in ambient Houston $PM_{2.5}$ are local soil and construction activity. The influence of vehicular emission is potentially masked by concrete dust, which tends to lower the overall $^{87}Sr/^{86}Sr$ ratio and dampen radiogenic Sr emitted by vehicles and move Sr isotope ratios in ambient PM away from vehicular sources. Medium dust days (June 29, July 2, July 25, and July 27) exhibited variability in the $^{87}Sr/^{86}Sr$ ratio, indicating mixing of multiple sources such as Saharan-Sahelian and concrete dust (for June 29, July 2, and July 25) and local soil (for July 27). The two days immediately following the peak outbreak (July 2 and 25), tended closer to North African indicating its continued presence post dust outbreak on regular or background days (a phenomenon that we have reported earlier [29]) and significantly affecting Sr.

Unlike Sr, Hf isotope ratios show that its mixing primarily arises from vehicular PM and Saharan dust (Figure III-3b). Although there is an overlap between Lu/Hf ratios in local soil and North African dust, the $^{176}Hf/^{177}Hf$ ratio effectively separates them. We recently reported ~10-fold Hf enrichment in PM collected from a vehicular tunnel compared with local soil and concrete dust [51]. Additionally, vehicular PM was marginally enriched in zirconium (Zr) [21, 51], an element strongly associated with Hf [149], indicating motor vehicles may dominate as a Hf source during regular days. This was confirmed by clustering of ambient PM on regular days (June 28, July 3,

22, and 26) around the motor vehicle profile, which clearly shift towards African dust along the mixing lines of the two sources during episodic intrusions of Saharan dust. This indicates that $^{176}Hf/^{177}Hf$ is a strong tracer of North African dust in urban atmospheres despite Hf being present only at ultra-trace (i.e., sub ng m^{-3}) concentrations.

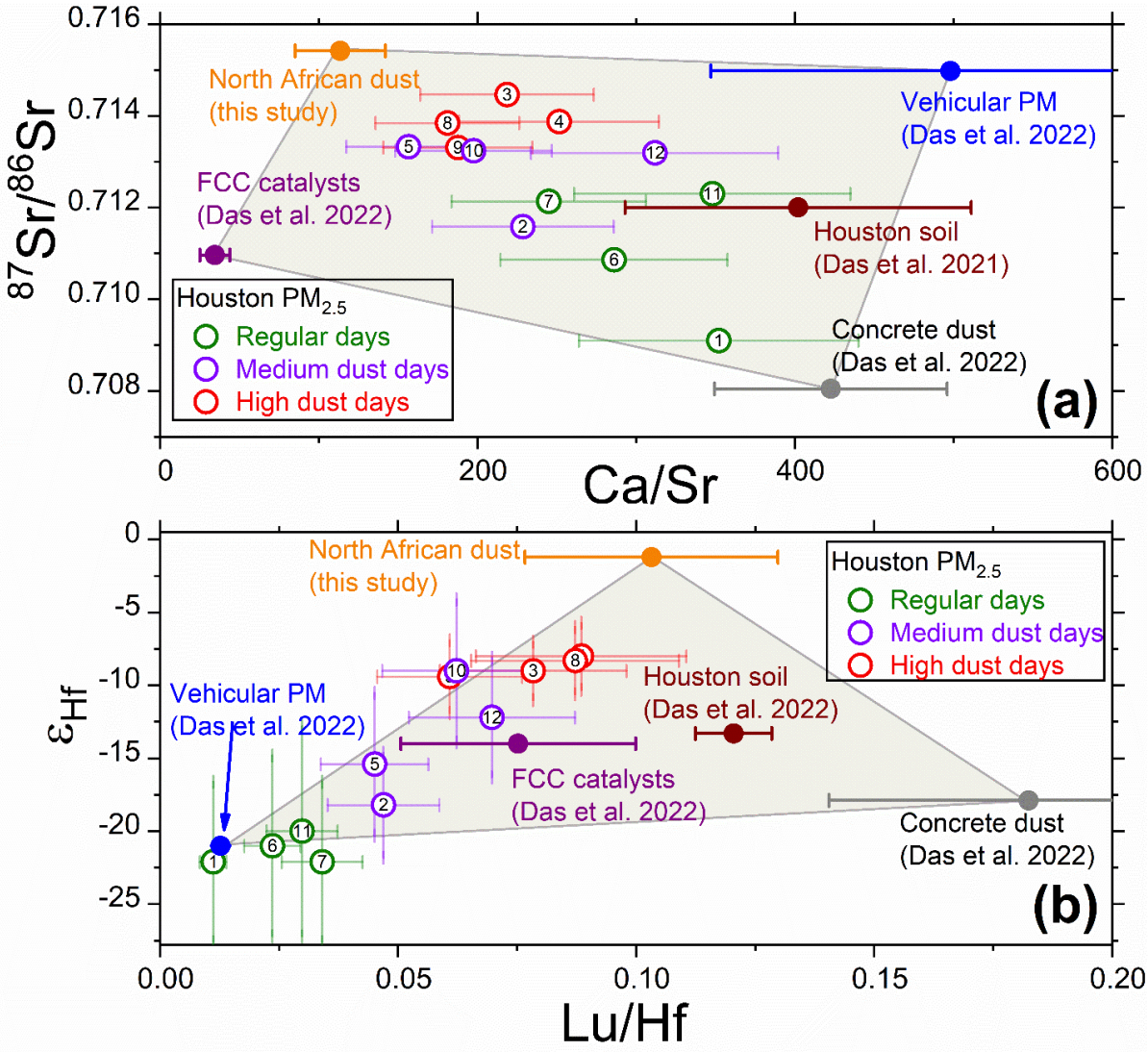

Figure III-3. Top panel (a) A plot of $^{87}Sr/^{86}Sr$ vs Ca/Sr to analyze the source of Sr in ambient Houston $PM_{2.5}$. The gray area encompassing the quadrilateral shows the mixing region for all four likely sources of Sr (North African dust, vehicular PM, local soil, and concrete

dust)[51]. Samples during regular days lie near soil or concrete dust profiles and tend to shift toward African dust during high dust days. Bottom panel (b) A plot of ε_{Hf} vs Lu/Hf to analyze the source of Hf in Houston $PM_{2.5}$. The gray triangular area shows the mixing region for all three likely sources of Hf (North African dust, vehicular PM, local soil, and concrete dust). Samples during regular days lie near vehicular PM, and tend to shift toward African dust, similar to $^{87}Sr/^{86}Sr$. High dust days are plotted in red, medium dust in purple, and regular days in green to better visualize the influence of African dust. The number labels on the PM2.5 datapoints represent the sample number (e.g., "1" represents the first sample date June 28 and "12" represents the final sample taken on July 27 as summarized in Appendix Table B1).

Nd isotopic mixing in Houston and lack of petroleum refinery influence

Ambient $PM_{2.5}$ at Clinton Drive clustered near the North African dust, local soil, and vehicular PM apices in Figure III-4a where its mixing is evaluated by plotting ε_{Nd} versus Sm/Nd. Significant separation from the FCC end member (near the southeast corner of the graph) reveals the lack of influence from petroleum refining. Consequently, emissions from numerous FCC units in Houston were deemed insignificant during or just prior to North African dust intrusions thereby not contaminating urban air with anthropogenic REEs having different signatures than crustal REEs [87, 126, 145, 146]. Switching between refining-dominated and crustal-dominated atmospheric light rare earth elements (LREEs) is typical in Houston [23, 29, 87, 140, 145] and Figure III-4a suggests that Nd predominantly originated from crustal sources during this research. This was confirmed via a three-component plot of LREE elemental tracers (i.e., lanthanum-cerium-samarium (La-Ce-Sm) in Figure III-4b) wherein all ambient $PM_{2.5}$ samples grouped near the average upper continental crust [120] at the centroid [29, 52, 140]. Migration away from the FCC catalysts profile (i.e., the La vertex) in the ternary diagram affirms inferences from Figure III-4a that petroleum refining had limited influence on atmospheric lanthanoid enrichment during both the North African dust events analyzed herein. Importantly, even though Nd was strongly

influenced by mineral/crustal sources of similar elemental composition, the $^{143}Nd/^{144}Nd$ ratio (or ε_{Nd}) effectively differentiated North African dust from local soil in all cases, i.e., during high, medium, and regular dust days. Hence, a combination of elemental and isotopic analysis not only successfully separated local anthropogenic and natural PM from long-range transported dust, but also efficiently distinguished collinear crustal sources (local soil and Saharan-Sahelian dust) validating the importance of analyzing isotopes in addition to elements.

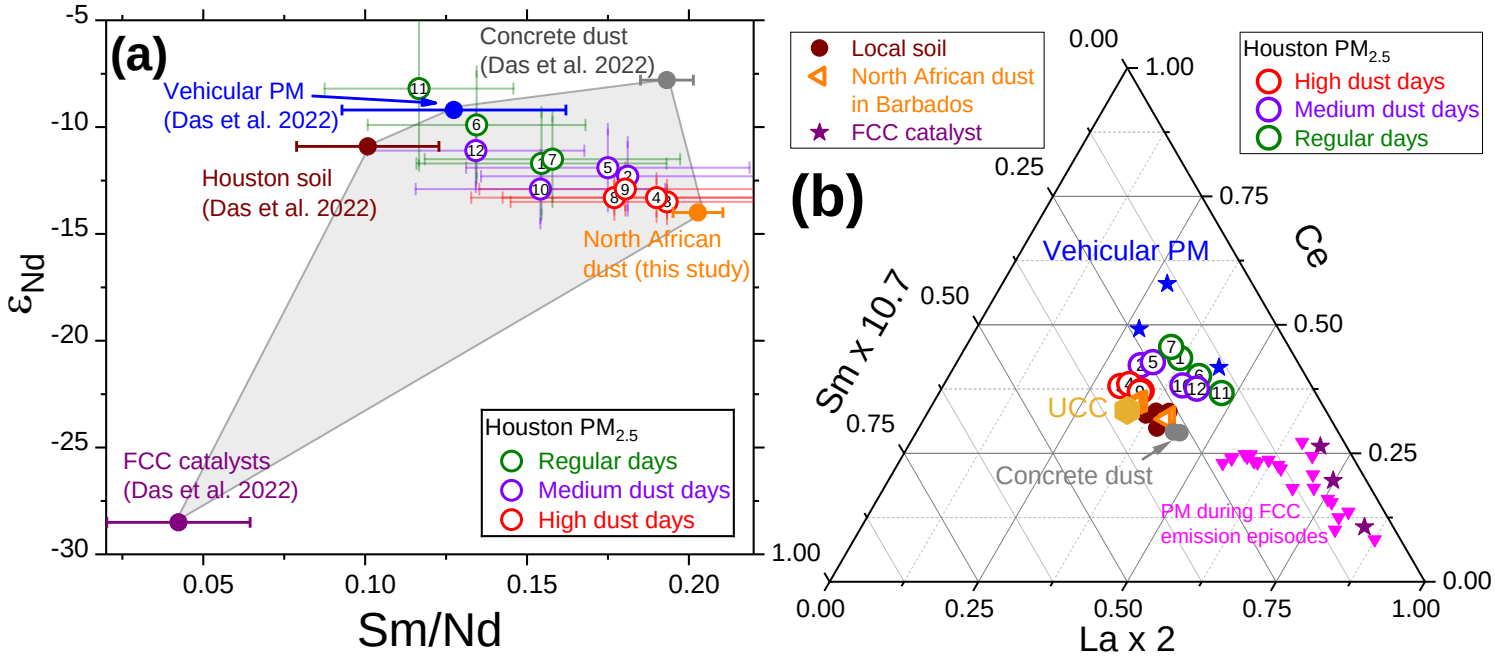

Figure III-4. Left panel (a). A plot of ε_{Nd} versus Sm/Nd to analyze the source of Sr in ambient Houston $PM_{2.5}$. The pentagonal gray area shows the mixing region for all the five possible sources (North African dust, FCC, Houston soil, motor vehicles, and construction activities) [51]. Aerosols during regular days lie near soil or vehicular dust and tend to shift toward African dust during the outbreak. No significant influence of FCC catalyst was observed on our samples suggesting the absence of refinery FCC emissions during the sampling campaign. Right panel (b). Ternary plot of La-Ce-Sm showing lack of influence from FCC catalyst and supports the argument made from ε_{Nd} vs Sm/Nd graph of no refinery emissions. Literature datapoints include Vehicular PM [21, 51], FCC [51], concrete dust [51], soil [51], and PM during FCC emission episode in Houston [140]. The ternary plot was normalized so that the upper continental crust (UCC) [120] appears at the centroid. High dust days are plotted in red, medium dust in purple, and regular days in green for a better visualization. The number labels on the $PM_{2.5}$ datapoints represent the sample number (e.g., "1" represents the first sample date (June 28) and "12" represents the final sample taken on July 27 as summarized in Appendix Table B1).

An initial attempt at quantitative apportionment of Sr, Nd, and Hf solely based on end member mixing analysis [43] is presented in Appendix Figure B12, which revealed North African dust contributions of 28 – 65% for Sr, 32 – 65% for Nd, and 6 – 46% for Hf during medium dust days, which appeared reasonable. However, this procedure calculated 25-34% of strontium to originate from North Africa on regular days in Houston (June 28 and July 22), which is a vast overestimation (see Figure III-6 where African dust contributions are negligible on both these days and explained later). Therefore, end member mixing analysis alone is not a reliable method for quantitatively estimating Saharan influences, potentially due to a low degree of freedom arising from the limited number of simultaneous mass balance equations. This necessitates combining isotopic ratios with elemental tracers to increase the number of equations to obtain more accurate results (step 3 of IRCMB).

Improved apportionment via isotope ratios to reduce collinearity in elemental source profiles using a synthetic dataset

Figure III-5 compares IRCMB and CMB errors as a function of the contributions of the two collinear crustal sources to ambient PM demonstrating more accurate apportionment with IRCMB in all cases. The left panel (a, c, and e) shows an increase in standardized errors for local soil and concrete dust but a decrease for North African dust. Similar trends were observed in the right panel (b, d, and f) when local soil decreased the standardized error for itself while deteriorating the estimation accuracy for the other two mineral sources (African dust and concrete dust). This implies that increasing the proportion of one of the mineral mass contents is likely to affect quantifying other mineral sources. Therefore, apportioning African dust is likely less reliable

during low dust days. In general, during dust episodes where crustal material dominates, estimating mass contributions from local mineral sources can get less reliable.

Applying the IRCMB model to the synthetic Houston PM dataset reduced the average standard root mean squared error (SRMSE) for North African dust, local soil, and concrete dust from 0.21 to 0.17 (19%), 0.57 to 0.27 (53%), and 0.82 to 0.17 (79%), respectively as summarized in Appendix Table B13. In Figures 5a and 5b, both traditional CMB and IRCMB had low error (< 0.18) when North African dust was 12 µg m^{-3} (Figure III-5a) or local soil was 0.5 µg m^{-3} (Figure III-5b). This error however, increased to > 0.3 for traditional CMB when African dust decreased in proportion but was relatively low in IRCMB (< 0.25) in Figure III-5a. Similarly, for local soil when error increased to ~0.8 with CMB, IRCMB suppressed the error significantly (< 0.45) during higher African dust days (up to 12 µg m^{-3}) in Figures 5c and 5d. The most improvement was observed with concrete dust when error increased up to 1.2 with CMB, IRCMB was able to suppress it below 0.3 at all mass variations (Figures 5e and 5f). This implies that the IRCMB model is significantly helpful when estimating low mass proportions of collinear sources (the three mineral sources in this study).

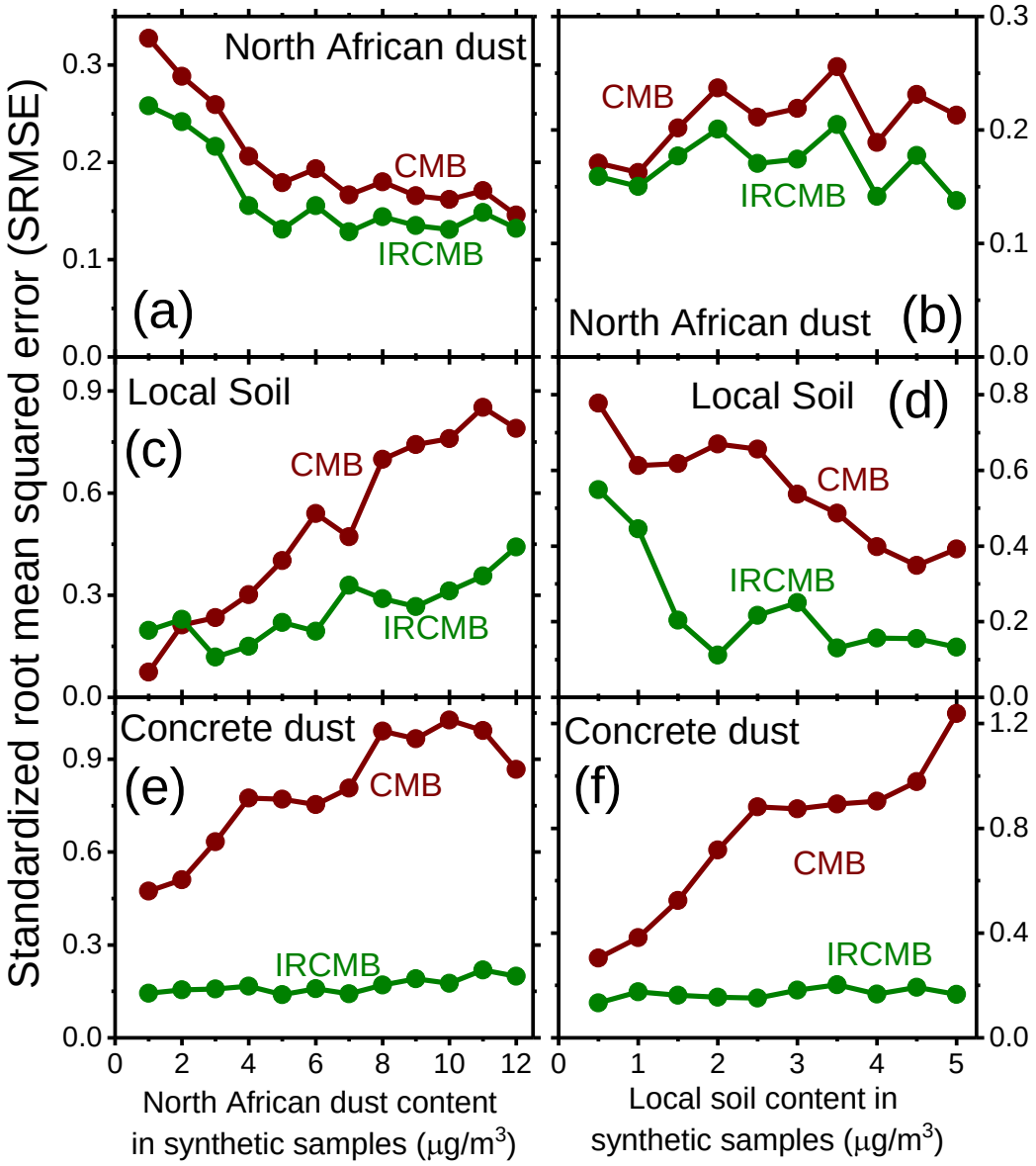

Figure III-5. A comparison of the standardized root mean squared error (SRMSE) obtained with the synthetic dataset for the three mineral dust sources. The new IRCMB model (green symbols and lines) incorporating isotope ratios and the traditional chemical mass balance model (brown symbols and lines) solely with elemental data are depicted. The left panel represents variation of SRMSE when North African dust varied from 1 to 12 μg m^{-3} (each symbol is calculated from 10 datapoints) and right panel represents variation with of RMSE when local soil varied from 0.5 to 5 μg m^{-3} (each symbol is calculated from 12 datapoints).

The IRCMB model also improved the accuracy of apportioning biomass burning by reducing its average SRMSE to 0.48 from 0.63 obtained by traditional CMB performed with elemental concentrations alone (Appendix Table B13). Hence, IRCMB appears to have better separated potassium (the sole elemental tracer for biomass combustion) from mineral sources when isotope ratios were included in the mass balance equation. All other sources (apportioned in Step 1 of the IRCMB model) did not improve significantly. Improvements in predictions by ~20 – 80% for the three collinear sources in this synthetic dataset along with more accurate estimates of biomass burning demonstrates the value of incorporating Sr, Nd, and Hf isotopes along with elemental analysis for source apportionment, which is next applied to $PM_{2.5}$ concentrations measured during the two Saharan dust episodes in Houston.

Source apportionment of Houston $PM_{2.5}$ via IRCMB

Figure III-6 shows the IRCMB apportioned mass for each source category. Excellent fits were evidenced by high R^2 values (0.87 – 0.96) and low χ^2 (1.4 – 2.8), and 78 – 89% of the $PM_{2.5}$ mass was apportioned to various source categories, the remaining attributed to secondary PM that has been shown to be a significant summertime component in Houston [9, 127, 148]. The reconstructed measured mineral mass [23, 29] (RMMM, calculated as the sum of oxide forms of major crustal elements Al, Si, Ca, Ti, Mg, and Fe) equaled the total apportioned mineral mass (African dust + soil + concrete dust) validating the robustness of IRCMB estimates (slope = 1.03 ± 0.03 in Appendix Figure B13). North African dust was estimated to contribute 12–16 μg m^{-3} of $PM_{2.5}$ during high dust days (41 – 50% of total mass), 2.6–4.1 μg m^{-3} of $PM_{2.5}$ during medium dust days (50 – 26%) and 0 – 1.1 μg m^{-3} of $PM_{2.5}$ during regular days (0 – 9%). Calculating an average

of 0.6 ± 0.5 μg m^{-3} on regular days demonstrates that long-range transported dust lingered in Houston as background PM beyond the peak outbreak, a phenomenon which is typically undetected by meteorological models and satellite products, but consistent with our conceptual understanding of Saharan dust transport to the Caribbean and continental United States [29, 150]. Accounting for background contributions of African dust in addition to peak values will better assist in categorizing exceptional events and compliance with Clean Air Act regulations.

To further demonstrate the effectiveness of the IRCMB method, we show apportionment results with traditional CMB using only elemental concentrations in Appendix Figure B13. As observed, this procedure separated local soil from North African dust only on two days (June 30 and July 1) corresponding to peak PM concentrations, unlike the IRCMB method that could accurately apportion local soil in all cases. As expected, IRCMB estimated local soil contributions remained relatively constant throughout the sampling campaign averaging 1.5 ± 0.5 μg m^{-3} for high dust days (0.8 – 2.1 μg m^{-3}), 1.21 ± 0.7 μg m^{-3} for medium dust days, and 0.8 ± 0.4 μg m^{-3} for regular days since local Aeolian soil resuspension is likely independent of North African dust intrusions. Traditional CMB overestimated mass contributions from concrete dust (2.3 ± 0.4 μg m^{-3}; 1.2 – 3.1 μg m^{-3}) compared with IRCMB that apportioned only 1.4 ± 0.7 μg m^{-3} (0.6 – 2.8 μg m^{-3}) to construction activity. Additionally, CMB estimated less variability of concrete dust's contributions (only 15% coefficient of variation) over the entire sampling period compared with IRCMB's estimations that exhibited 50% coefficient of variation. Note that Clinton Drive is proximal to cement manufacturers and gypsum users, which has been reported to cause substantial fluctuations in daily contributions to ambient PM [23, 29, 140] lending further credibility to

IRCMB predictions. Significant overestimation (> 60% on average) of the influence of concrete dust on PM levels by traditional CMB further points to the need for isotopic measurements to accurately apportion measured aerosol mass to local and distal sources. Further, traditional CMB under-apportioned total mineral mass (African dust + soil + concrete dust) by ~11%, compared with more accurate IRCMB results (see Appendix Figure B14).

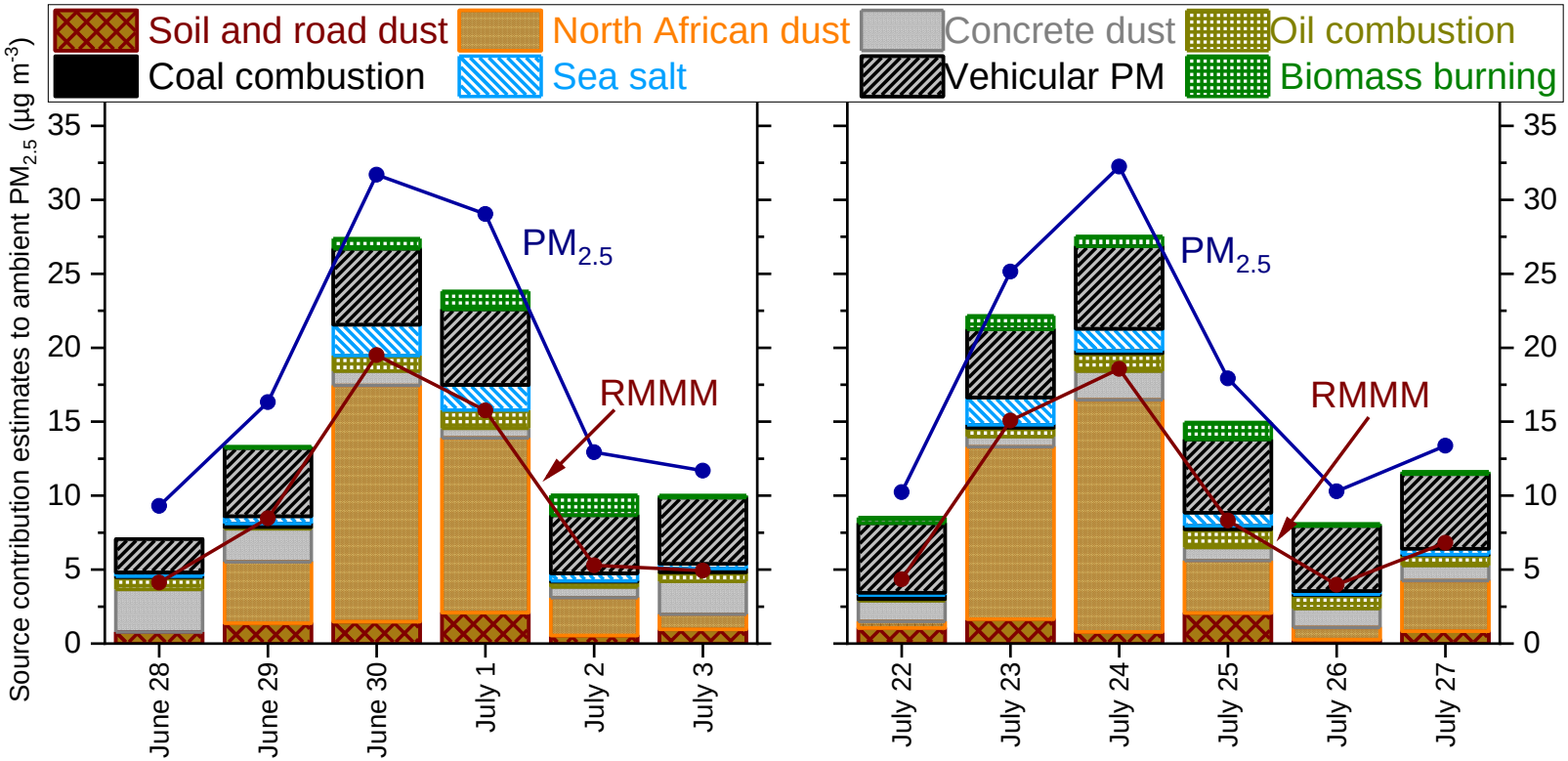

Figure III-6. Source apportionment results for Houston $PM_{2.5}$ calculated by the IRCMB method. The time-series of ambient $PM_{2.5}$ is superposed (in blue color) on individual source contribution estimates along with the reconstructed measured mineral mass [29] (RMMM in brown color). Non-trivial amounts of North African dust were estimated even on days not associated with the active outbreak exhibiting low PM mass concentrations (e.g., July 3, 26, and 27). Low concentrations of Saharan dust at ground level mixed with ambient PM may be undetected in satellite images [151] and large-scale aerosol transport models. The FCC source is not shown because it did not contribute to any our samples.

Vehicular emissions contributed substantially to measured $PM_{2.5}$ mass, averaging 4.6 ± 0.8 μg m^{-3} (and ranging between 2.3 and 5.6 μg m^{-3}), consistent with earlier investigations at and near this site [23, 54]. Sea salt was estimated to contribute more on high and medium dust days (1.8 ± 0.3 μg m^{-3}) compared to regular days (0.3 ± 0.4 μg m^{-3}), attributed to it being carried along with North African dust during its transport over the Atlantic Ocean and the Gulf of Mexico before reaching Houston. Importantly, traditional CMB failed to apportion biomass burning for two samples (June 30 and July 27), which was however resolved via IRCMB. Biomass burning contributions were independent of North African dust and estimated to contribute as high as 1.4 μg m^{-3} or 10.4% of PM mass. Appendix Table B14 summarizes other relevant sources.

Conclusion

Accurately resolving locally emitted and long-range transported collinear mineral aerosols and their quantitative apportionment in this work demonstrates the importance of isotopic and elemental measurements for urban aerosol investigations. The IRCMB technique substantially improved source contribution estimates for North African dust, local soil, and local construction activities not only during the active outbreak when PM levels were high but also on regular or background days when PM levels were low. Rigorously characterizing Saharan intrusions and improved source apportionment are particularly valuable during negotiations with governments that allow exceptional events “not reasonably controllable or preventable” to be excluded from regulatory decisions, i.e., isolating and subtracting mass of long-range transported aerosols from samples to comply with ever-tightening air quality legislations. Interestingly, although our principal focus was discriminating African and local sources, Sr-Nd-Hf isotopes in conjunction

with elemental analysis successfully identified biomass burning that in two cases were completely unresolved by traditional CMB. This is particularly relevant because regional anthropogenic biomass burning aerosols from agricultural activities in Central America also contribute significantly to Houston PM during the spring season, necessitating its careful examination under the exceptional event categorization [30]. Additionally, although we demonstrated the IRCMB method only in Houston, Texas, the same approach can be implemented without loss of generality to better assess PM burden facing other metroplexes in North America, Europe, and Asia under the influence of desert aerosols [40, 43, 128-130, 152]. Importantly, measuring the combined isotopic and elemental composition of PM significantly alleviates the need to collect and analyze lots of samples to assess relative contributions of distal crustal dust and locally emitted mineral dust (current methods require $\gtrsim 50$ samples whereas the new method needs only one), but also substantially improves accuracy of source contribution estimates.

Further, even though our research was motivated by ambient PM in urban settings tackling health and regulatory implications, Sr-Nd-Hf isotopes can successfully discriminate long-range transported and locally emitted crustal aerosols in rural and remote areas where their impacts on haze, climate dynamics, heterogenous chemistry, and nutrient cycling are of more immediate concern [1, 66-69, 72, 75]. Finally, successful tracking of the provenance of mineral matter in ambient PM in complex atmospheres of urban/industrialized regions by Sr-Nd-Hf isotopes motivates future research in other isotope systems such as copper [63, 153], osmium [154], and zinc [63, 153] to uniquely identify anthropogenic sources.

CHAPTER IV

ESTIMATING LIGHT-DUTY VEHICLES' CONTRIBUTIONS TO AMBIENT $PM_{2.5}$ AND PM_{10} AT A NEAR-HIGHWAY URBAN ELEMENTARY SCHOOL VIA ELEMENTAL CHARACTERIZATION EMPHASIZING RHODIUM, PALLADIUM, AND PLATINUM[†]

Introduction

Populations living adjacent to highways and busy roadways have an increased risk for morbidity and premature mortality [12, 155-157], a portion of which has been assigned to airborne particulate matter (PM) and its metals content [11, 12]. This necessitates accurate identification and apportionment of ambient PM arising from motor vehicles. To date, the vast majority of investigations into vehicular PM elemental emissions have relied on metals such as Fe, Ca, Zn, Mn, Cu, Cd, Pb, As, Ni, Sb, Sn, Ba, Zr, Cr, and Ga for this purpose [14-17]. Since these metals are co-emitted by several other natural and anthropogenic sources, solely relying on non-platinum group elements (non-PGEs) introduces substantial uncertainties into quantitative estimates of mobile source contributions to PM, especially in urban and industrialized environments. On the other hand, measuring Rh, Pd, and Pt (i.e. PGEs), which are incorporated in 3-way catalytic converters of light-duty vehicles (LDVs) can improve estimations of PM emissions by gasoline-driven motor vehicles because there are only very few other environmental sources of PGEs [22].

[†] Reprinted with permission from "Estimating light-duty vehicles' contributions to ambient $PM_{2.5}$ and PM_{10} at a near-highway urban elementary school via elemental characterization emphasizing Rhodium, Palladium, and Platinum", S. Das and S. Chellam, *Science of The Total Environment*, **747**, 141268, Copyright 2020 by Elsevier

(The United States Environmental Protection Agency defines LDVs as those with a gross vehicle weight rating up to 4500 kg (10,000 pounds).) However, only a very limited number of measurements of PGEs in ambient PM are available in the United States [19, 154, 158-162], although more data have been reported for European surface roads [158, 163-171]. Paradoxically, none of these earlier studies used their PGE measurements to quantitatively estimate LDVs' contributions to ambient PM mass concentrations (i.e. perform source apportionment).

The overarching focus of this manuscript is on LDV PM emissions. To accomplish this, we target numerous metals, including PGEs in ambient $PM_{2.5}$ and PM_{10} within the property line of an elementary school located in close proximity of several heavily trafficked roads because this is representative of many United States schools [172] and children are particularly vulnerable to traffic related air pollution [173, 174]. Although metals measurements allow epidemiological assessments of specific health outcomes to outdoor PM [175], our main goal herein is to use them for quantitative source apportionment in order to accurately estimate LDV contributions to PM_{10} and $PM_{2.5}$. We also address environmental justice concerns [176, 177] since this school serves predominantly African American and Hispanic (97%), low-income (100% qualifying for the Department of Education's Title I program), and academically high-risk (84%) students.

Another consideration is that anthropogenic PGE releases, largely from LDVs' catalytic converters, have substantially altered the biogeochemical cycling of these extreme siderophiles allowing them to accumulate in surficial urban soils [22, 165, 178-181] thereby becoming bioavailable to humans, plants, and animals [182-184] necessitating measurements of their environmental concentrations even though current evidence does not suggest human toxicity at these low levels [185].

Our primary objective is to measure the detailed elemental composition of ambient $PM_{2.5}$ and PM_{10} with particular emphasis on Rh, Pd, and Pt in order to accurately estimate LDVs' PM emissions. We also focus on other trace elements that are typically assigned to motor vehicles (Sb, Cu, Zn, As, Pb, Cd, Mo, Sn, W, Ba, and Ga) to systematically and rigorously identify non-PGE LDV tracers for both PM size classes on surface roads. These were accomplished by analyzing 52 major, trace, and ultra-trace elements in ambient PM inside the fence line of an urban school located on the feeder road of a major national highway over the course of a year and applying the Chemical Mass Balance (CMB) model using our unique vehicular source profile incorporating PGEs [21].

Materials and methods

Sampling and Site Description

Ambient PM samples (19 $PM_{2.5}$ and 19 PM_{10}) were collected at the Texas Commission on Environmental Quality's Continuous Air Monitoring Station 1 in Houston (+29.7679965, -95.2205822) between July 31, 2014 and August 10, 2015 on 47 mm PTFE filters (Rupprecht & Patashnick 2025 Partisol; 1 m^3/h). Each sample was collected over 12 to 22 days to facilitate detection of most elements, especially PGEs, which are present only in pg m^{-3} levels in the ambient atmosphere. Sampling over the course of 12-months captured any potential seasonal variations due to operational/ambient temperature and driving patterns [14, 186].

This sampling site is within the property line of Roland P. Harris Elementary School within the Houston Independent School District (Appendix, Figure C1). A total of 650 students attended kindergarten-5^{th} grades at this school largely from the communities of Jacinto City and Cloverleaf, which have an extremely high poverty rate of ~25% and low median per-capita annual incomes of

only $19,260 and $16,390 respectively. This school is located on the eastbound frontage road of Interstate Highway 10, which had an annual average daily traffic (AADT) count of 194,945 vehicles (95% light-duty cars/pickups and 5% heavy-duty trucks (HDTs)) during the sampling campaign. It is also close to several other highly trafficked roads, just 2,500 feet west of FM 526 (AADT 27,504 vehicles/day), 2.5 miles east of Interstate 610 (AADT 134,864 vehicles/day), and 4.1 miles west of Beltway 8 (AADT 103,441 vehicles/day) as seen in Figure IV-1 left panel. Representative hourly NOx and $PM_{2.5}$ profiles (Appendix C.5) validate our site selection since they depict a strong vehicular influence inferred from the morning peaks coinciding with rush-hour traffic [187, 188]. PM measurements reported herein represent lower estimates of LDVs' contributions since permission was granted to install samplers only at the rear of the school, ~250 m away from the interstate (Figure IV-1 right panel) and thus likely to receive lower amount of vehicular PM [157, 165, 178, 180, 189].

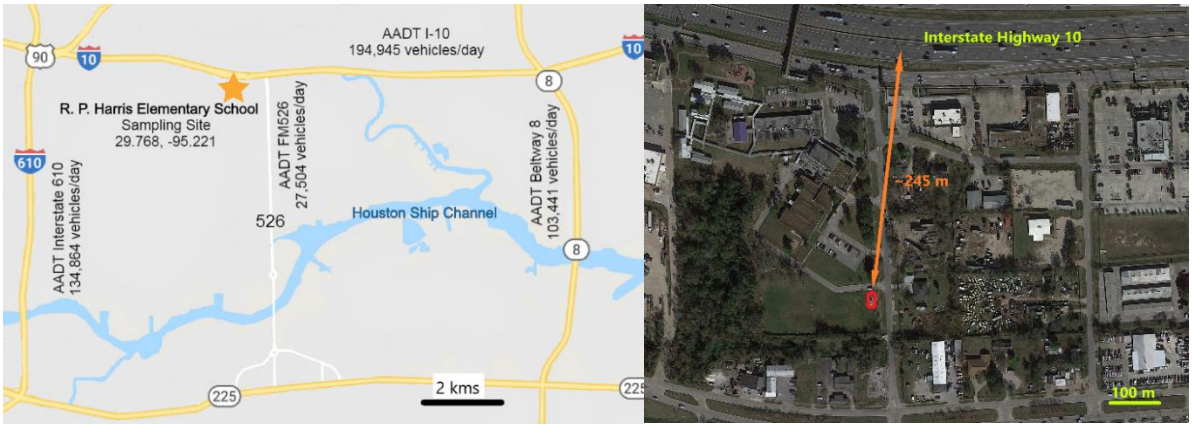

Figure IV-1. Left panel: map of the school showing its proximity to major roadways along with annual average daily traffic (AADT) values obtained from the City of Houston [190] and Texas Department of Transportation [191]. Right panel: map showing samplers that were allowed to be placed only at the rear end of the school at a distance ~800 feet or 245 meters from Interstate Highway 10. Graphics were created using google products. Image credits: Google Maps.

Sample Preparation and Analysis

Our previously developed multi-step digestion procedure was employed to analyze Rh, Pd, Pt separately from 49 other elements using inductively coupled plasma – mass spectrometry (ICP-MS) [18]. In short, after cleaning all plasticware and Teflonware, filters were first placed in 8 mL concentrated aqua regia (6 mL 32-35% w/w Optima grade HCl : 2mL 65% w/w Suprapur grade HNO_3) and digested (CEM Mars 5) three times, each at 200 °C and 200 psig with 20 minute dwell time [18]. The digestate was separated into two equal parts (4 mL each) – one for PGE analysis and another for all other elements. Samples for PGE analyses were prepared by heating (80 °C) one part of the aliquot to dryness in a loosely capped vessel. Polyatomic interferences were removed by cation exchange, diluted with 0.5 M HCl, and analyzed by magnetic sector field ICP-MS (ThermoScientific ELEMENT) after internal standardization with ^{115}In and ^{209}Bi.

Concentrated (48%, 0.5 mL) HF was added to the second aliquot and digested (200 °C, 200 psig, 20 minute) three more times to dissolve the siliceous matrix. Next, 4 mL H_3BO_3 (5% w/v) was added and the resultant solution diluted to 2% HNO_3 and analyzed for 18 representative elements (Li, Be, Na, Mg, Al, Si, K, Ca, Ga, As, Se, Rb, Sr, Sn, Sb, Cs, Ba, Pb), 15 transition metals (Sc, Ti, V, Cr, Mn, Fe, Co, Ni, Cu, Zn, Y, Zr, Mo, Cd, W), 14 lanthanides (La, Ce, Pr, Nd, Sm, Eu, Gd, Tb, Dy, Ho, Er, Tm, Yb, Lu) and 2 actinides (Th, U) using dynamic reaction cell-quadrupole-inductively coupled plasma-mass spectrometry. V, Fe, Ni, Cd were analyzed using NH_3 as a cell gas [87]. More details are in Appendix C.3.

Three reference materials; BCR-723 (European Commission road dust), SRM-2556 (National Institute of Standards and Technology used auto catalyst), and SRM-1648a (National Institute of Standards and Technology urban particulate matter) were employed for quality

assurance and quality control (QA/QC). PGE recoveries from BCR 723 and SRM 2556 (the only ones bearing Rh, Pt, and Pd) were in the range 88-115% and all other elements from these reference materials were recovered between 85% and 118%. More QA/QC details are in Appendix C4.

Source Apportionment

PM masses were apportioned by the CMB model (EPA CMB8.2) using elemental source profiles for LDVs [21] and other local and regional sources; soil and road dust [18], North African dust [29], petroleum refinery fluid catalytic cracking activities [86], coal combustion [138], oil combustion, and shipping activities [192-194], biomass burning and municipal incineration [138, 194], and cement manufacturing [193, 195]. Note that our LDV source profile incorporates PGEs [21] unlike other published ones [138, 196] and was developed in an adjacent underwater tunnel where diesel driven HDTs are banned. Our soil-road dust profile [18] also includes PGEs along with numerous other elements (Appendix C.6).

Note that since we did not measure elemental carbon or volatile organic carbon species [197-200], CMB estimates also probably include contributions from HDTs as their elemental source profiles are collinear with LDVs [14, 160, 201, 202] (see Appendix C.9).

Results and Discussion

PM Mass Concentrations

$PM_{2.5}$ ranged from 6.5-15.5 μg m^{-3} (average 9.7±2.1) and PM_{10} varied between 12.2-29.1 μg m^{-3} (average 19.7±5.0) as shown in Appendix Figure C6. The Texas Commission on Environmental Quality monitors hourly $PM_{2.5}$ at this site using a Tapered Element Oscillating Microbalance, which correlated strongly (R^2=0.98) when averaged over our sampling periods with

slope → 1 (0.95±0.04) demonstrating the accuracy of our gravimetric filter-based measurements (Appendix Figure C3).

PGE Concentrations

Ambient Pd concentrations (2.03-5.88 pg m^{-3} in $PM_{2.5}$ and 4.26-19.63 pg m^{-3} in PM_{10}) were the highest followed by Pt (0.69-1.84 pg m^{-3} in $PM_{2.5}$ and 1.55-6.27 pg m^{-3} in PM_{10}) and Rh (0.28-0.80 pg m^{-3} in $PM_{2.5}$ and 0.43-2.91 pg m^{-3} in PM_{10}) (Appendix Figure C7). These are in the lower range of values reported in urban areas and other surface roads over the world [19, 22, 154, 160, 163, 168, 169, 203] (see Appendix C1), even though traffic counts were very high near our site (see Figure IV-1). This is attributed to the depletion of vehicular PM before it was sampled at the rear section of the school that was farthest from the highway [157, 165, 178, 180, 189]. Average Rh, Pd, and Pt concentrations in $PM_{2.5}$ were 0.52, 3.95, and 1.28 pg m^{-3} respectively, which were ~1/3rd of the corresponding PM_{10} values of 1.48, 10.64, and 3.28 pg m^{-3} respectively. Rh, Pd, and Pt average PM_{10} mass fractions (0.078, 0.571, and 0.174 µg g^{-1} respectively) were 25-40% higher than corresponding $PM_{2.5}$ values (0.056, 0.426, and 0.137 µg g^{-1} respectively). This is consistent with higher PGE abundances in coarser aerosols [19, 158, 181, 204].

PGE characteristics

The average $PM_{2.5}$ and PM_{10} Pt/Pd ratios were statistically indistinguishable both being 0.30±0.01 (Figure IV-2a), which overlapped with our measurements in a nearby tunnel that is closed to HDTs (0.31±0.02) [21]. Higher Pd concentrations compared with Pt (i.e. Pt/Pd < 1) measured herein are consistent with other United States studies [21, 154, 158, 160, 162]. However, some European measurements report Pt/Pd > 1[158, 163-167] while others show Pt/Pd < 1 [168-171] in PM depending on when and where the studies were performed and what size fractions

were analyzed. The Pt/Pd ratio in ambient PM also varies widely in other parts of the world [203, 205-207] even though there is a relatively consistent trend of Pt/Pd < 1 over the last decade or so. These observations demonstrate spatiotemporal variations in catalyst formulation, which are attributed to differences in vehicle fleet characteristics, environmental regulations, economic drivers (e.g. declining Pd prices in the late 1990s and corresponding increase in consumption) [22, 179] and the recognition that Pd better diminishes emissions of hydrocarbons, nitrogen oxides, and carbon monoxide from gasoline-driven vehicles under real-world driving situations compared with Pt [22, 208, 209]. The Pt/Rh ratio of ambient aerosols in this study (2.17 ± 0.07) also overlapped with tunnel PM (2.08 ± 0.38) [21] (see Figure IV-2b, further pointing to LDVs as the predominant PGE source in the school.

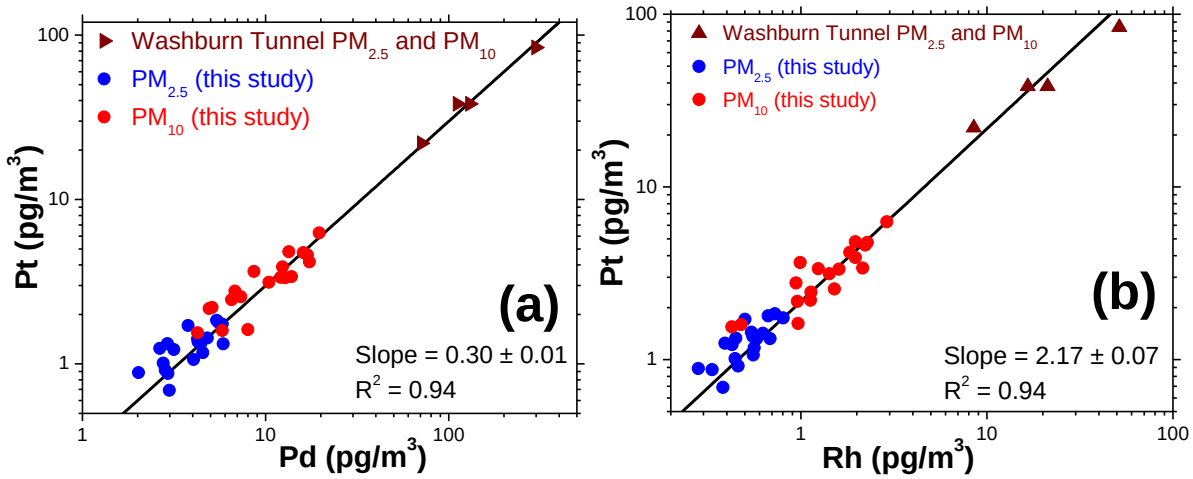

Figure IV-2. Strong, positive correlations between Rh, Pd, and Pt concentrations in $PM_{2.5}$ and PM_{10}. A log-log scale is employed to accommodate the ~2.5-orders of magnitude variations in values. Linear regression was performed using pooled $PM_{2.5}$ and PM_{10} results only from this study (i.e. excluding Washburn Tunnel values) in arithmetic scale. Statistically similar slopes (95% confidence) between measurements in this study and an adjacent underwater tunnel [21] suggested LDVs as dominant PGE emitters.

Three-component Rh-Pd-Pt variations in PM_{10} and $PM_{2.5}$ collected in this study, earlier in the nearby tunnel [21], and a composite autocatalyst [21] sample are shown in Figure IV-3a after

normalization with respect to their average upper continental crust (UCC) abundances [210]. Displacement of aerosols away from the UCC centroid towards the Rh apex signifies their extreme Rh enrichment and their distinct anthropogenic origins. This was substantiated by remarkably high PGE enrichment factors with respect to crustal Ti (median values 26,930, 7650, and 2,000, respectively in $PM_{2.5}$ and 17,870, 4,760, and 1,190, respectively in PM_{10} for Rh, Pd, and Pt; Figure IV-3b). Additionally, all PM_{10} and $PM_{2.5}$ tightly clustered amongst each other superposing on our measurements in a proximal underwater tunnel just 18-months prior to the start of this campaign [21]. Crucially, they all coincided with a mixed-lot recycled autocatalysts sample representative of the entire United States automotive fleet provided to us by BASF with Rh, Pd and Pt concentrations of 184, 1,148 and 814 μg g^{-1}, respectively [21]. Excellent coherence between PGEs in these matrices provides strong evidence that LDVs were their primary source and validates Rh, Pd, and Pt to be unique LDV tracers [154, 158, 165, 168, 179, 211].

Further, since Rh was enriched to the greatest extent in the nearby tunnel [21], it was also used as a reference to calculate enrichment factors and shown in Figure IV-4. With this normalization, enrichment factors for Pd and Pt $\rightarrow$ 1 (median 1.02 and 1.07, respectively) validating LDVs as their common source and the absence of other PGE sources e.g. [165, 203].

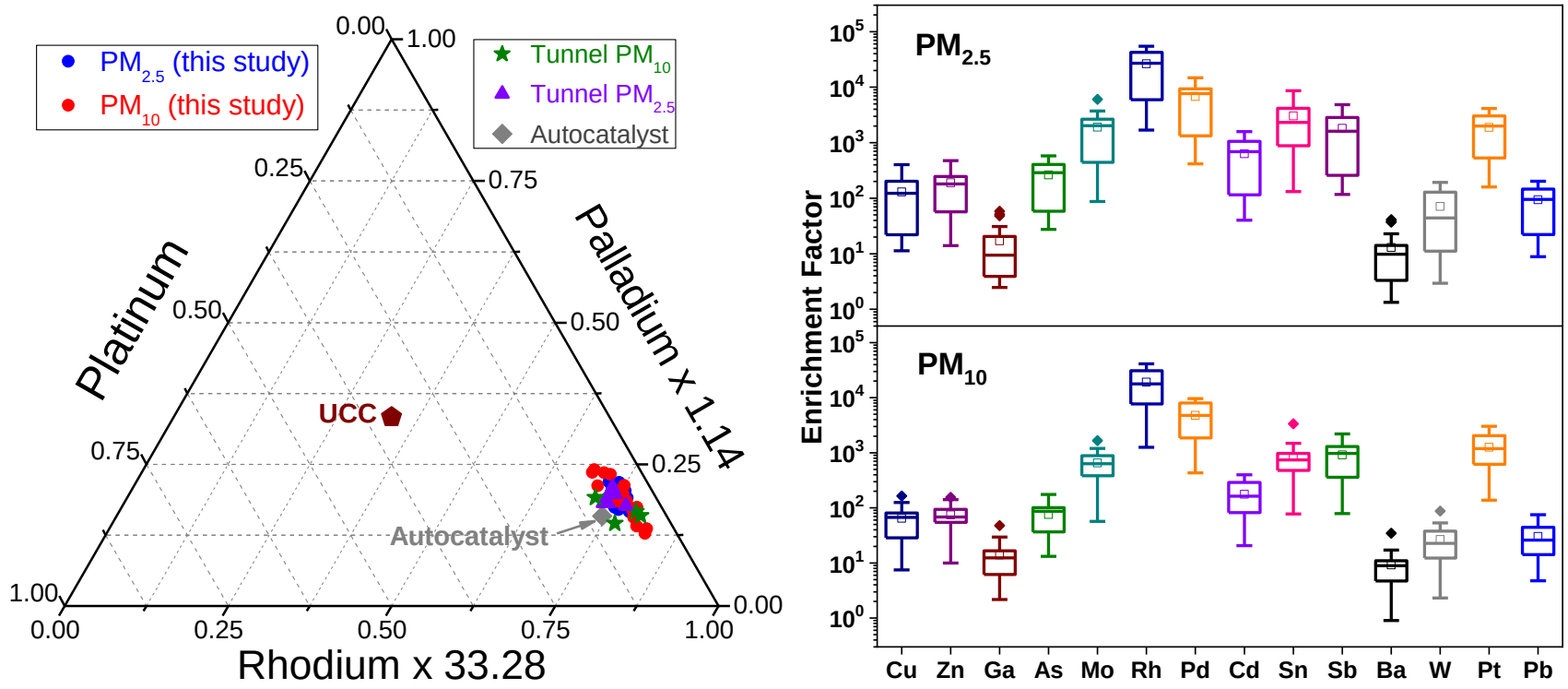

Figure IV-3. (a) Ternary Rh-Pd-Pt representation for all PM collected in this study. Our earlier measurements from a nearby underwater vehicle tunnel [21] and a mixed-lot recycled autocatalyst (from Englehard/BASF) are also included. Data have been normalized so that the UCC profile [210] appears at the centroid. (b) Enrichment factors with respect to the upper continental crust (UCC) for all elements typically attributed to vehicular emissions. Ti was chosen as the reference element as it has lower anthropogenic interferences in Houston. Note that both Fe and Al are released in copious quantities from industries lining the Houston Ship Channel. In this representation, high enrichment factors denote elements arising from anthropogenic activity (i.e. different from natural or crustal sources).

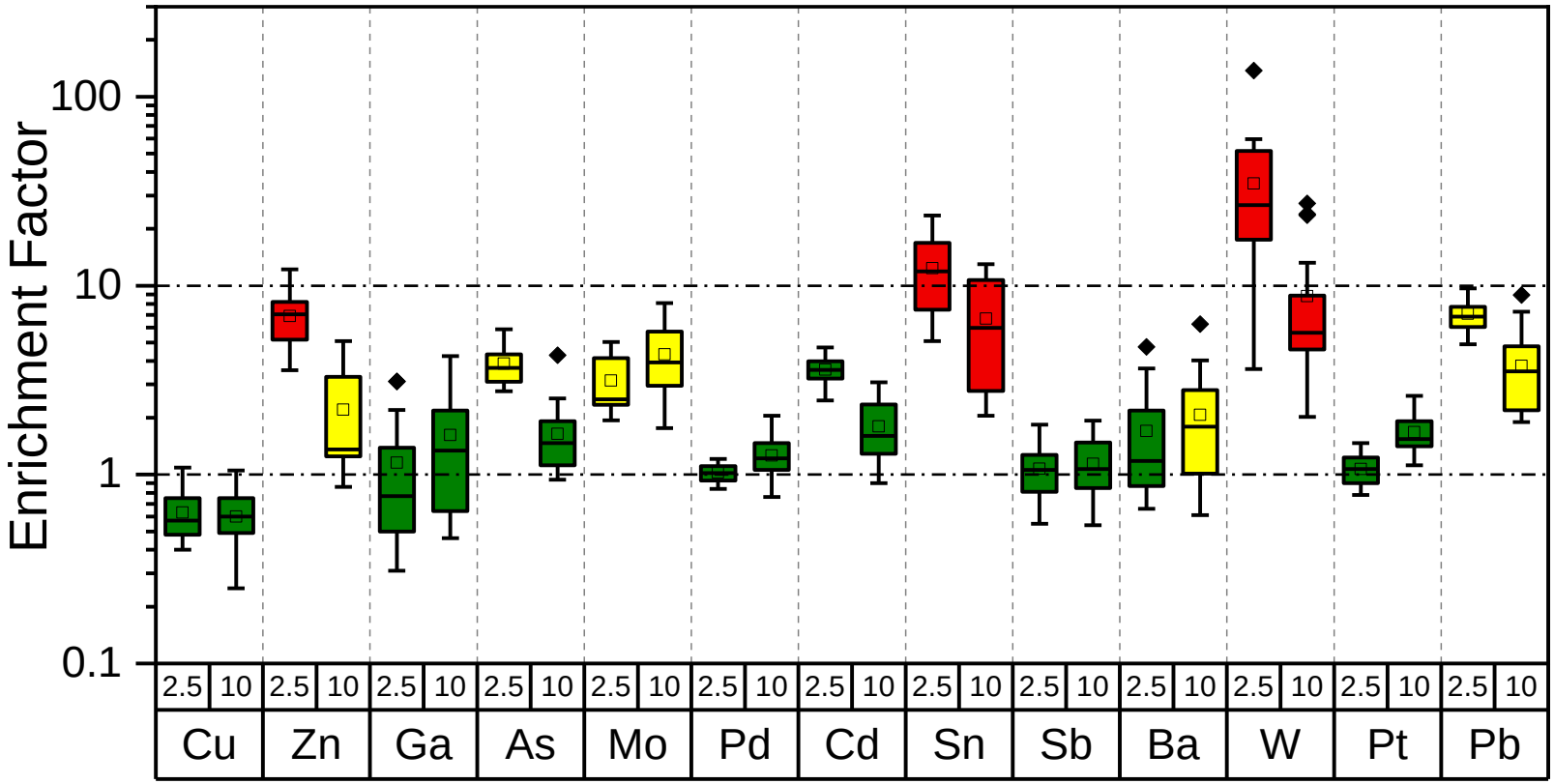

Figure IV-4. Enrichment factors of elements typically attributed to vehicular emissions with respect Rh in the Washburn Tunnel [21]. Rh was chosen as the reference element because vehicular tailpipe emission is the only known environmental source of Rh in ambient air and it had the highest enrichment factor in Figure IV-3b, strongly demonstrating its LDV origins. Note that both size fractions are included with $PM_{2.5}$ and PM_{10} abbreviated as "2.5" and "10," respectively just above the element symbol. In this representation, low enrichment factors denote elements arising from vehicles. In this case, high enrichment factors represent "interferences" from non-vehicular sources or inconsistencies in abundance compared to tunnel measurements. Green boxes represent non/low-enriched metals, yellow boxes represent medium-enriched metals and red boxes represent highly-enriched metals. Metals having enrichment factors > 5 were arbitrarily categorized as "moderately enriched" and those with > 10 were tagged as "highly enriched."

Other non-PGE trace elements

Simultaneous variations in Sb-Cu-Zn were analyzed since these metals are abundant in brakes [14, 212-215], even though other vehicular sources of Zn exist [19, 216], after normalization to the UCC [120] (Figure IV-5a). These three metals were all highly enriched with respect to crustal Ti (median enrichment factors of 1610, 123, and 181 in $PM_{2.5}$ and 980, 67, and 68, in PM_{10} for Sb, Cu, and Zn respectively; see Figure IV-3b) and extremely high Sb enrichment shifts aerosols towards the corresponding apex proving their anthropogenic origins. Importantly, in Figure IV-5a, all $PM_{2.5}$ and PM_{10} clustered around the composition of aerosols derived from brake wear [214, 217], vehicle tunnels [14, 21, 218], and near-highway sites [160, 219-223]. Additionally, ambient PM was distinct from tire abrasion [215, 217], direct dynamometer tailpipe emissions [217], and crustal material [120]. Further, the Cu/Sb ratio in $PM_{2.5}$ and PM_{10} averaged 3.77 ± 0.85 and 3.6 ± 0.86 respectively, which are in the same range as roadside urban aerosols [14, 21, 160, 217, 219, 221, 224] and overlaps with brake wear emissions [214, 217] (Appendix Table C4). Note that the Cu/Zn ratio in PM diverged from the tunnel, near-roadways, and brakes (Appendix Table C4) suggesting other anthropogenic Zn sources in Houston [19]. Hence, brake wear was inferred to be the predominant Sb and Cu source whereas Zn originated from LDVs as well as other local sources.

Aerosols also moved away from the crustal centroid in the As-Pb-Cd ternary plot (Figure IV-5b) towards the As axis and closer to the Cd apex overlapping with PM from the Washburn Tunnel [21] and dynamometer emissions [217]. Note that all PM are strongly depleted in Pb relative to As and Cd lying close to the Pb=0 (bottom) axis. Both gasoline [225] and a combined LDV/HDT emission factor profile [225] positioned near the Cd apex given their relative Cd-

enrichment. On the other hand, since brake/tire wear [217] are As-rich, they migrated towards the corresponding apex. All PM collected in this study were located between the As and Cd apexes indicating their mixed influences from both tailpipe and non-tailpipe LDV sources. Low As/Pb ratios of all PM in this study also suggests limited influence of coal combustion [16, 226] at this site, consistent with an earlier report [19]. High enrichment factors of these metals relative to crustal Ti (median values of 288, 95, and 692 in $PM_{2.5}$ and 87, 26, and 163, in PM_{10} for As, Pb, and Cd respectively; see Figure IV-3b) further validated their anthropogenic nature.

Additionally, enrichment factors of Sb, Cu, As, and Cd with respect to tunnel Rh were near unity in both $PM_{2.5}$ and PM_{10} further validating their likely predominant LDV origins even on surface roads (see Figure IV-4). In contrast, Zn and Pb were moderately enriched when referenced to tunnel Rh in Figure IV-4 (median values of ~5) showing the influence of non-LDV sources for these metals.

Mo was distinctly anthropogenic with very high enrichment factors in Figure IV-3b (median 2,030 for $PM_{2.5}$ and 633 for PM_{10} with respect to crustal Ti). This coupled with its lack of enrichment when referenced to tunnel Rh strongly evidenced its LDV origins [19] (see Figure IV-4). Mo possibly arises from engine wear [227], lubricating oil [228], and autocatalysts [19] for $PM_{2.5}$ and from brake wear for PM_{10} [227]. Sn was also highly enriched compared to the Earth's crust in Figure IV-3b (median values of 2,320 for $PM_{2.5}$ and 740 for PM_{10}). However, Sn was also relatively enriched with respect to tunnel Rh in Figure IV-4 (median values of 12 for $PM_{2.5}$ and 6 for PM_{10}). Similar observations were also made for W and Pb. Hence, Sn, W, and Pb likely had mixed origins from LDVs and other anthropogenic sources (e.g. coal/oil combustion [19, 138], high temperature operations [19, 229], and road dust [18, 224]).

Ba and Ga were only moderately enriched with respect to crustal Ti (median enrichment factors of only ~10 for both metals in both size fractions) not suggesting definitive links to anthropogenic sources, including LDVs.

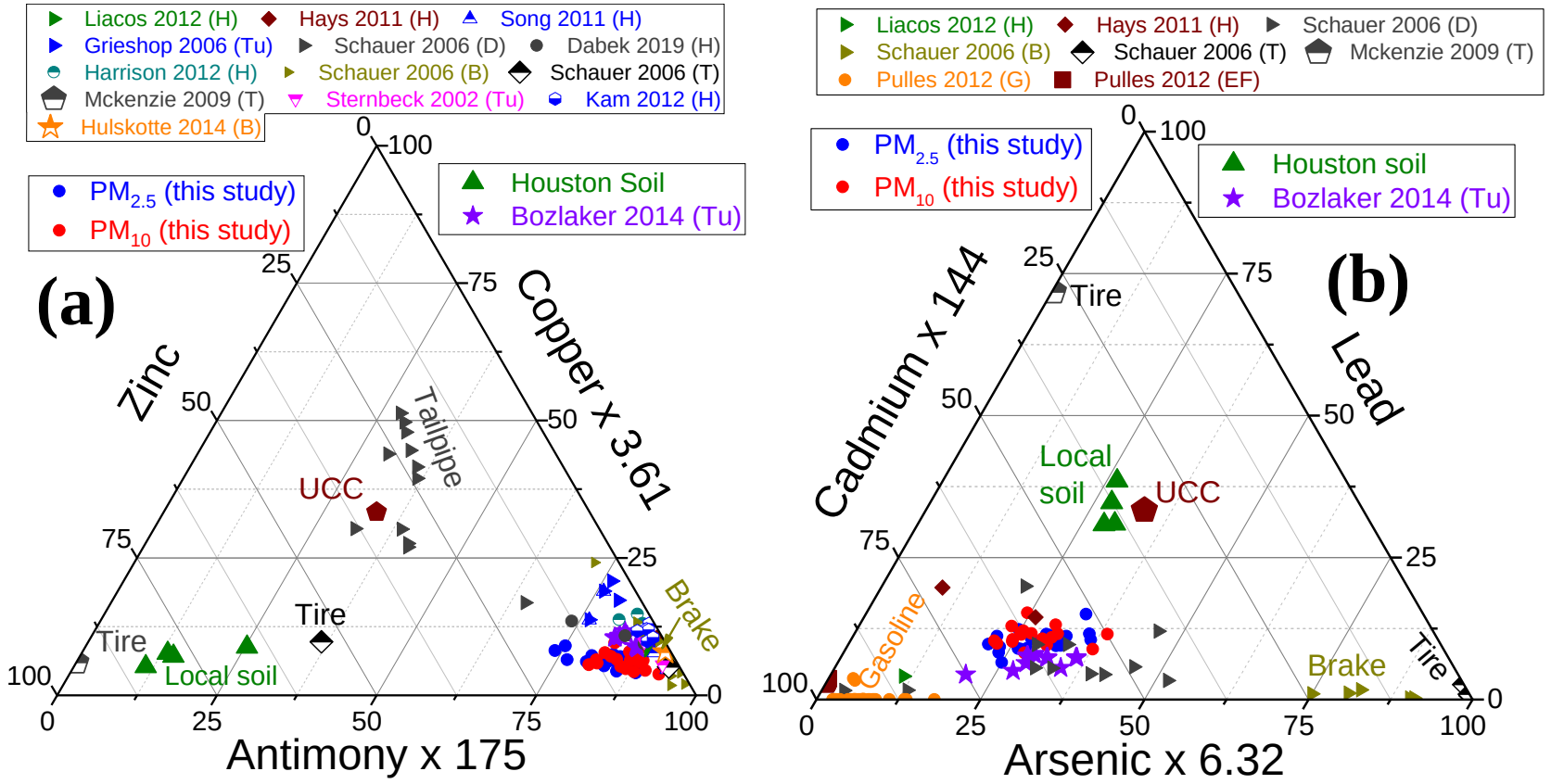

Figure IV-5. (a) Sb-Cu-Zn are associated with brake wear emissions showing enormous Sb enrichment relative to Zn and Cu and typifies all samples in this manuscript demonstrating their strong vehicular influence (left panel). (b) Pb-Cd-As, which are also associated with vehicular PM, do not strictly show only vehicular characteristics indicating that these metals have not been exclusively emitted by motor vehicles (right panel). Data from several previous studies of vehicular emissions are superposed to better understand metals' origins. The following abbreviations are used in the legend: (H) for near highways [160, 219-223] (Tu) for tunnel studies,[14, 218], (D) for dynamometer or tailpipe[217], (B) for brake wear [214, 217], (T) for tire wear [215, 217], (G) for gasoline samples [225], and (EF) for combined LDV and HDT emission factors[225]. The local soil profile was taken from our earlier publication [18].

Enrichment factors and ternary variations provide strong but only qualitative evidence that LDV emissions can be well-tracked by Rh, Pd, Pt, Sb, Cu, As, Cd, and Mo. These analyses signal that LDVs also emitted other trace metals (Zn, Ga, Sn, Ba, W, and Pb) to varying extents. Next, LDV contributions to PM mass are quantitatively estimated.

LDV source contribution estimates

Excellent CMB model statistical measures of fit ($0.82 \leq R^2 \leq 0.99$ and $0.09 \leq \chi^2 \leq 1.84$ for $PM_{2.5}$; $0.85 \leq R^2 \leq 0.98$ and $0.14 \leq \chi^2 \leq 2.27$ for PM_{10}) demonstrated robust source contribution estimations (see Appendix C.10). Model fits for vehicular contributions were also precise (low uncertainties, $t_{stat}>5$) demonstrating stable and reliable estimates. On average, 78% of $PM_{2.5}$ mass and 84% of PM_{10} mass were apportioned to eight different sources of which only LDVs are discussed herein based on the manuscript's focus (see Appendix Figure C9). As expected from the study design and site location, LDVs were the single most dominant source contributing an average of 4.7 μg m^{-3} to $PM_{2.5}$ (2.7 – 7.7 μg m^{-3}) and an average of 6.9 μg m^{-3} to PM_{10} (3.2 – 11.6 μg m^{-3}). In other words, automobiles accounted for nearly half (48.7%) of $PM_{2.5}$ mass and more than 1/3rd (37.2%) of PM_{10} mass on average. Higher relative LDV contributions to $PM_{2.5}$ than $PM_{2.5-10}$ is consistent with earlier research [16, 198, 230] and with greater enrichment of vehicle-derived elements in fine PM summarized above (see Figure IV-3b). Our estimates show that on an average $PM_{2.5}$ contributed to 68 ± 16% of PM_{10} mass attributable to motor vehicles.

Validation of potential LDV tracer metals using CMB source contribution estimates

We further analyzed the effectiveness of each potential automobile marker metal by relating its presence in PM to CMB estimates of LDV contributions [199]. Metals concentrations were normalized by corresponding PM masses to reduce potential bias introduced by differences

in total PM amount effectively correlating elemental abundances to the mass fraction apportioned to vehicular emissions. As seen, Rh, Pd, and Pt strongly correlated ($0.71 \leq R^2 \leq 0.89$) and their intercepts $\rightarrow 0$ for both PM size classes, establishing them as excellent LDV tracers with negligible "interferences" from other sources, e.g. [203]. This validates PGEs' ability to accurately apportion LDVs via CMB modeling. Note that even though PGEs are emitted via the tailpipe, their mass fraction (abundance) has been reported to be higher in coarse PM [204, 231] leading to their higher slopes in PM_{10} compared with $PM_{2.5}$ in Figure IV-6 (also see Appendix Table C5).

Also shown in Figure IV-6 is that Sb, Cu, Cd, As, and Mo were reasonably well correlated ($0.51 \leq R^2 \leq 0.67$) for both size classes supporting above assertions of their predominant emissions by LDVs (see previous section). Preponderant association of As and Cd with LDVs rather than coal combustion is also consistent with their links to gasoline in general [225] and fuel oil combustion specifically in Houston [19]. The reasonably good correlation for $PM_{2.5}$ Pb in Figure IV-6 appears to be fortuitous given its relative depletion compared with As and Cd (Figure IV-5b) and its numerous other fine PM sources in the Houston Ship Channel area [19, 232]. Weaker PM_{10} correlations for Cd, Mo, As, and Pb compared with $PM_{2.5}$ was attributed to "interferences" from local soil/road dust, which is relatively abundant in these metals [18, 183, 233] and is known to contribute preferentially to the coarse fraction [21, 164, 224, 227].

Poor correlations for Zn in Figure IV-6 are potentially caused by its substantial industrial emissions [19, 216, 232] (and even soil/road dust [18, 233]) in the Houston Ship Channel area as revealed in Figure IV-5a. Sn and W were also poorly correlated with CMB estimates demonstrating they are not applicable markers for LDVs even though they compose various vehicular components such as catalysts, brakes, and tires [14, 200, 234, 235]. Weak statistical

associations of Ba and Ga in Figure IV-6 are consistent with enrichment factor analysis above confirming that they are also unsuitable as LDV markers.

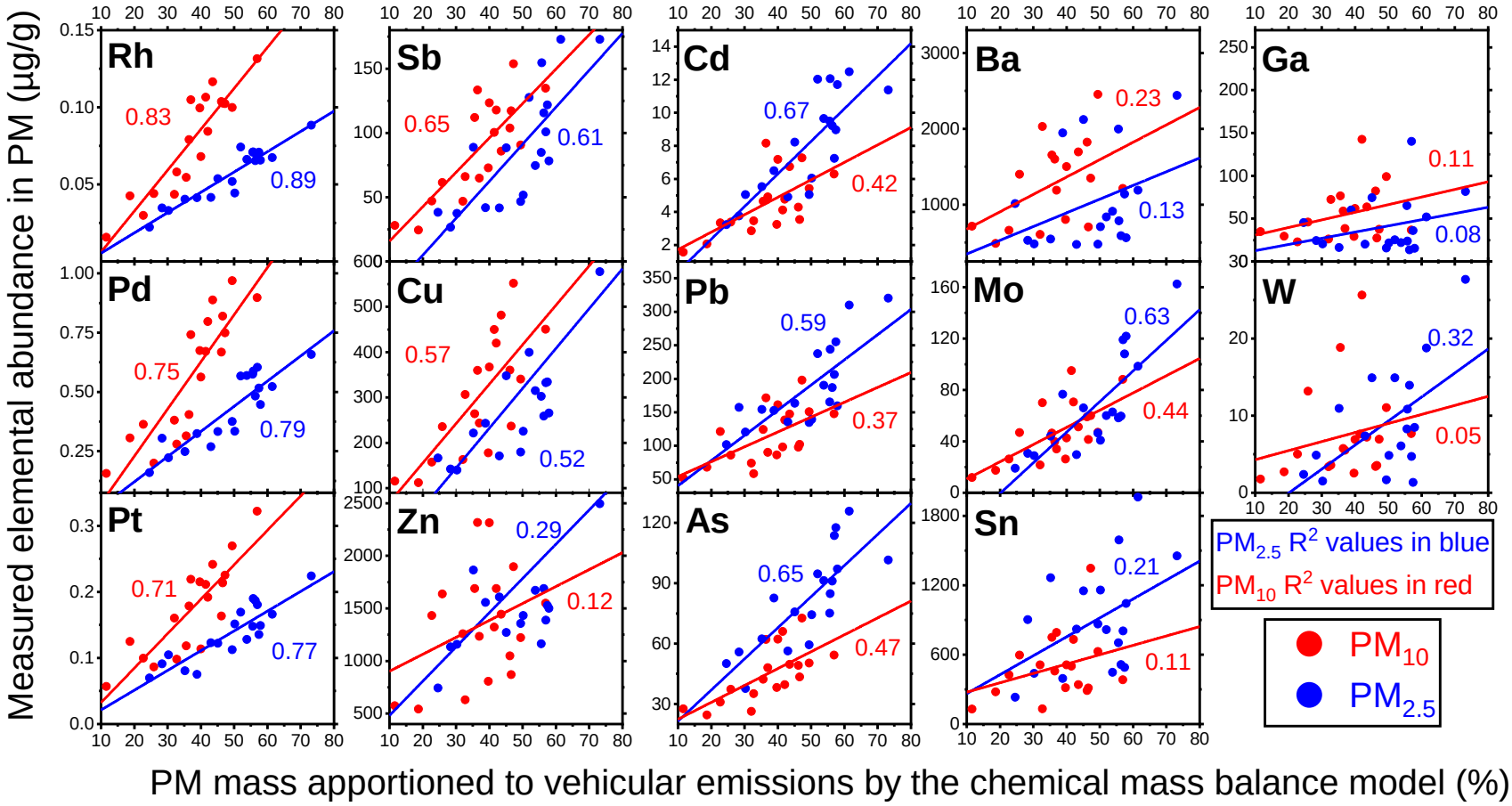

Figure IV-6. Scatter plots of all commonly vehicular related metals expressed as abundances (µg element/g PM) with quantitative CMB estimations of LDV contributions illustrating their individual effectiveness as potential tracers. Blue color depicts $PM_{2.5}$ and red color depicts PM_{10} along with their corresponding linear regression correlation coefficients. The correlation coefficients for $PM_{2.5}$ and PM_{10} are also shown in blue and red color respectively. Additional statistics for the above plots are given in (Appendix Table C5).

Conclusions

This is the first report of all three vehicular PGEs from United States' surface roads in about a decade [160] or more [19, 154] with others largely focusing on non-PGEs, Pt, and Rh [161, 219]. CMB calculated motor vehicles to account for about half of ambient $PM_{2.5}$ (2.7 – 7.7 μg m^{-3} out of a total of 6.5 – 15.5 μg m^{-3}) and for more than a third to PM_{10} (3.2 – 11.6 μg m^{-3} out of a total of 12.2 – 29.1 μg m^{-3}) even though samples were collected ~250 meters from the highway. Multiple lines of evidence strongly linked Rh, Pd, Pt, Sb, Cu, As, Cd, and Mo to motor vehicle emissions. Other trace metals often assigned to motor vehicles such as Zn, Ga, Sn, Ba, W, and Pb did not suitably trace LDVs. These observations point to the importance of incorporating PGEs in motor vehicles' elemental source profiles to accurately estimate their source contributions via CMB modelling especially in urban and heavily industrialized environments. Because numerous United States' schools are located in close proximity of heavily trafficked roads [172, 177] and a portion of ambient outdoor PM infiltrates indoors [17, 236], results reported herein point to elevated children's exposure to traffic related air pollution (and associated health impacts) even while inside the school. Hence, monitoring the detailed elemental composition of PM, including PGEs, also facilitates better estimating human exposure from the transportation sector in near-road environments. We emphasize cautious extrapolation of outdoor ambient PM LDV source appointment to assess indoor exposure to students and school staff where they spend most of their time, warranting additional research on infiltration/ventilation of outdoor aerosols into the indoor environment.

CHAPTER V

TRANSBOUNDARY AEROSOL CONTRIBUTIONS FROM REGIONAL AND GLOBAL SOURCES TO PRIMARY AMBIENT PM2.5 AND PM10 IN A COMPLEX METROPOLITAN ATMOSPHERE

Introduction

Non-urban particulate matter (PM) transport has been long known to affect air quality across many cities in the United States [1, 2, 32, 237], Europe [26, 27, 238], Asia [28, 43, 239], and elsewhere [240]. Two important non-local sources that commonly impact PM in many metropolitan areas of the world are desert dust [23-29] and biomass burning, namely agricultural and forest fires [30, 31, 241]. Texas is no exception being strongly influenced by Aeolian dust from the Sahara-Sahel region and biomass burning aerosols from Central America and neighboring states [1, 29-32]. Episodic intrusions of mineral dust from the Sahara Desert have been reported to increase emergency room visits, immunotoxicological risks, and even mortality [5, 124, 242, 243]. Smoke from agricultural and forest fires reportedly causes respiratory and cardiovascular problems and even mortality [244, 245]. In addition to acutely impacting human health, episodic transboundary aerosol transport can also potentially result in non-compliance with PM regulations especially considering increasingly stringent standards over time [8, 246]. Of particular relevance to this work is the presence of these non-local aerosols in Houston, Texas that are often a result of intentionally set agricultural fires in Central America [30], forest fires outside its borders [31], or windblown dust from North Africa [23, 29]. Hence, they fall under the "exceptional events that are not reasonably controlled/preventable" category under the United States' Clean Air Act

allowing the exclusion of their contributions from regulatory decisions and actions [247] necessitating their accurate quantification.

Vanadium and rare earth metals, which are strong tracers for primary PM locally emitted from oil combustion and refineries respectively [19, 52, 86, 87, 140, 146, 248, 249] are confounded by mineral dust intrusions into urban atmospheres that contribute to the same metals [29, 51, 140, 146, 242]. Hence, when excessive mineral dust is present in urban air, e.g., during Saharan dust intrusions in Houston, these metals may not be effective in uniquely tracing locally emitted anthropogenic PM. Another element of interest is potassium, which is an important marker for primary PM from biomass burning [10, 47-50]. However, potassium is not exclusive to vegetative combustion PM and is co-emitted by mineral dust sources such as local soil, deserts, coal combustion, cement kilns, and construction activities/concrete [47, 51, 52]. Nevertheless, mineral sources can be traced with major elements such as Al, Si, Ca, Mg, and Fe [23, 29, 47, 48, 52, 239]. However, previous studies have attempted to isolate potassium from biomass burning with reference to only one other element with the hypothesis that elemental ratios are stable across sources [47-50, 53], which is not the case with Houston [51]. Therefore, we adopt a multi-elemental approach that can isolate the non-mineral fraction of relevant tracer elements can be isolated from its mineral fraction enhancing their effectiveness to accurately identify and quantitate sources of primary PM. Note that large-scale biomass burning also generates significant quantities of secondary aerosols [9, 241, 250], which cannot be detected by elemental analysis and therefore are insensitive to techniques employed/developed in this manuscript.

Although episodic intrusions of North African dust and regional vegetative combustion events into Texas occur on multiple occasions annually [23, 29, 136, 250], earlier studies have

predominantly focused on individual episodes and PM issues over short time-frames [3, 23, 29, 251]. For this reason, a year-long sampling campaign was conducted to obtain clues to annual variations in PM mass concentration, composition, and contributions from transboundary and proximal sources. Although our work was largely motivated by urban air quality issues, it also has implications for studying biogeochemical cycling of macro-and micro-nutrients, and other metals in the earth ecosystem, which is strongly impacted by synoptic-scale dust transport [38, 237, 252].

The manuscript is designed to address the following objectives that were formulated to assess the effects of regional and long-range transported primary aerosols on ambient $PM_{2.5}$ and PM_{10}: (i) accurately detect intrusion of transboundary PM and potentially identify their corresponding source areas, (ii) analyze impacts of non-local aerosols on ambient PM mass and elemental concentrations and implications for tracing PM from local, regional, and global sources, (iii) isolate the non-mineral fraction of La, V, and K to effectively trace primary PM from refineries, oil combustion, and biomass burning respectively, and (iv) perform source apportionment to accurately and quantitatively estimate contributions of transboundary aerosols and locally emitted PM over the course of one year. Samples were collected over a 12-month period within the fence line of an elementary school in Houston, TX. Environmental justice concerns are also indirectly addressed since this school serves ethnic minority and low-income students almost exclusively.

Materials and methods

Sampling

Samples were collected in eastern Houston, TX (+29.76800, −95.22058) inside the perimeter of R. P. Harris Elementary School that was attended by 97% African American and

Hispanic students of whom 82% were academically "at risk," 92% were "economically disadvantaged," and 57% had only limited English proficiency. Additionally, the 2010 census (relevant for our sampling period) revealed a 25% poverty rate in the surrounding community allowing 100% of the students to qualify for the Department of Education Title I program for low-income families raising significant environmental justice issues at this location. The sampling site is in the proximity of the ultra-industrialized Houston Ship Channel and surrounded by heavily trafficked roadways (total daily vehicular count of ~620,000), petroleum refineries and petrochemical operations, and other manufacturing and recycling industries. Hence, it is a representative example of a complex atmosphere associated with a highly industrialized and urbanized metropolitan region. Nineteen $PM_{2.5}$ and 19 PM_{10} time-integrated samples were collected on PTFE filters using sequential air samplers (Partisol-Plus 2025 Rupprecht and Patashnick) from July 31, 2014 to August 10, 2015, labeled S1 – S19 for convenience as summarized in Table V-1. Each sample was integrated over 12 to 22 days to collect more aerosol mass and detect ultra-trace elements such as platinum, palladium, and rhodium, which are present only in pg m^{-3} levels in ambient air [22]. Note that results pertaining to platinum group metals were recently published [54] and this manuscript focuses on other elements and sources germane to synoptic-scale aerosols. $PM_{2.5}$ mass concentrations over the study period ranged from 6.5–15.5 μg m^{-3} (average 9.7 ± 2.1) and PM_{10} varied between 12.2 and 29.1 μg m^{-3} (average 19.7 ± 5.0) as reported in detail in Table V-1.

Table V-1. Summary of samples collected over a 1-year period during this investigation.

Sample ID	Start date	End date	PM_{10} concentration ($\mu g\ m^{-3}$)	$PM_{2.5}$ concentration ($\mu g\ m^{-3}$)
S1	31 July 2014	14 August 2014	25.6	11.4
S2	14 August 2014	04 September 2014	26.2	9.2
S3	05 September 2014	21 September 2014	18.5	8.0
S4	23 September 2014	08 October 2014	20.8	7.8
S5	11 October 2014	24 October 2014	20.8	8.2
S6	29 October 2014	15 November 2014	14.2	7.8
S7	16 November 2014	07 December 2014	12.2	7.9
S8	11 December 2014	31 December 2014	12.5	8.3
S9	02 January 2015	17 January 2015	13.9	9.4
S10	19 January 2015	05 February 2015	21.8	8.2
S11	05 February 2015	17 February 2015	19.1	10.3
S12	25 February 2015	11 March 2015	14.9	9.5
S13	20 March 2015	07 April 2015	15.6	6.5
S14	07 April 2015	25 April 2015	21.7	11.3
S15	28 April 2015	15 May 2015	22.8	10.8
S16	18 May 2015	30 May 2015	29.1	15.5
S17	08 June 2015	24 June 2015	22.2	9.6
S18	29 June 2015	21 July 2015	27.2	12.7
S19	21 July 2015	10 August 2015	16.0	11.9

Elemental analysis

Fifty-two elements (Li, Be, Na, Mg, Al, Si, K, Ca, Sc, Ti, V, Cr, Mn, Fe, Co, Ni, Cu, Zn, Ga, As, Se, Rb, Sr, Y, Zr, Mo, Rh, Pd, Cd, Sn, Sb, Cs, Ba, La, Ce, Pr, Nd, Sm, Eu, Gd, Tb, Dy, Ho, Er, Tm, Yb, Lu, Hf, Pt, Pb, Th, and U) were analyzed using our previously developed method [18, 21, 54]. PM dissolution was accomplished over multiple steps; first heating with ultrapure concentrated *Aqua Regia*, then dividing the resulting aliquot into two fractions and heating one part with additional 48% hydrofluoric acid and 5% v/w boric acid in sequence to dissolve all metals except platinum group elements (PGEs; Pt, Pd, and Rh). The dissolved non-PGE fraction was analyzed for metals using Dynamic Reaction Cell Quadrupole Inductively Coupled Plasma – Mass Spectrometry (DRC-q-ICP-MS; PerkinElmer® NexION® 300). The second fraction was dried and redissolved in 0.5M hydrochloric acid matrix before passing it through cation exchange resins (Dowex 50WX8 200-400 mesh, Sigma–Aldrich, Saint Louis, MO) to chemically separate PGEs from interfering elements (Zn, Cu, Rb, Sr, Zr, Hf, Pb). The purified fraction was analyzed for Pt, Pd, and Rh in Sector Field Inductively Coupled Plasma – Mass Spectrometry (SF-ICP-MS). The platinum group metals data was analyzed and published in our previous publication to trace vehicular PM [54]. Information on the quality control measures for these measurements are in Appendix Table D2 (blank filter analysis and detection limits) and Table A3 (elemental recoveries from Standard Reference Material SRM 1648a and European Commission standard BCR-723). Enrichment factors (EF) of individual elements (X) in $PM_{2.5}$ and PM_{10} were calculated with reference to titanium in the upper continental crust (UCC) [120]: $EF_X = [X/Ti]_{Sample}/[X/Ti]_{UCC}$.

Source Apportionment

The Chemical Mass Balance model (CMB) was used to quantify each source contribution[9, 23, 140]. Source profiles used on this data set included transatlantic North African dust collected at Barbados [29, 74], local soil [18, 51], motor vehicles [21], biomass burning [20, 138], fluid cracking catalysts (FCC) [86], oil combustion [138, 194, 253], coal combustion [138], cement and concrete dust [20, 51], and sea salt [20]. Na, Mg, Al, Si, K, Ca, Ti, V, Fe, Ni, Cu, Zn, As, Se, Sr, Rh, Pd, Cd, Sb, Ba, light rare earths, and Pb were chosen as fitting species owing to their importance in tracing sources of our interest. CMB modeling statistically measured were excellent ($0.82 \leq R^2 \leq 0.99$ and $\chi^2 < 1.84$ for both $PM_{2.5}$ and PM_{10}) validating accurate source contribution estimates. Since one of our foci was tracing biomass burning with potassium, priority was given to results that achieved minimum residual potassium, following EPA protocol [139].

Result and discussion

Long-range transported PM from North Africa to Houston

Identification of samples for long-range transported mineral dust

HYSPLIT back trajectories [133] track air masses to the western Sahara-Sahel region for samples S1, S2, S5, S15, S17, S18, and S19 (Appendix Figures D8, D9, and D11). Appendix Figure D12 shows the NAAPS aerosol optical depth (AOD) modelling output [254] over the North Atlantic Ocean indicating the presence of dust clouds during the corresponding sampling periods. AOD data combined with wind rose diagrams (Appendix Figure D6), TCEQ predictions [136], and HYSPLIT back trajectories, provide strong qualitative evidence of the presence of North African dust in Houston during the corresponding sampling periods. Interestingly, although it is untimely for North African dust to reach Texas in October, a relatively small amount (1.6 μg m^{-3}

for PM_{10} and 0.5 μg m^{-3} for $PM_{2.5}$) of North African dust was detected in sample S5 (October 11-24). This was verified by via NAAPS images (Appendix Figure D12b) showing an aerosol plume stretching over the North Atlantic ocean, AERONET's AOD data (Appendix Figure D28) from an oil rig platform in the Gulf of Mexico upstream of the dust storm (+28.86667, −90.48333) also showing PM spikes at ground level, and TCEQ's air quality forecasts [136]. To our knowledge, this is the first report of Saharan dust in Texas beyond September suggesting the need to monitor this phenomenon beyond the May – August timeframe. Fugitive dust likely dominates PM_{10} concentrations, however, for North African dust a preferential loss of larger particles during long-range transport reduces the $PM_{10}/PM_{2.5}$ ratio and proportionately increases both size fractions [255]. Simultaneous spikes in both PM_{10} and $PM_{2.5}$ data obtained from the AERONET database (Appendix Figure D22) and from the background site at the Gulf of Mexico oil rig platform further validates classifying these samples as episodic for North African dust. All dust episodes identified herein during May – August, (i.e., non-October timeframe) have been reported with in the literature [23, 255] providing additional validation of our assignment.

Rare earth elements and vanadium during episodes

Lanthanide signature ratios (La/Ce, La/Nd, and La/Sm) are key to differentiate rare earths emitted from FCC units of petroleum refineries and crustal material [140, 146, 248, 256]. A significant decrease in La/Ce for $PM_{2.5}$ (Appendix Figure D4a) during Saharan episodes (1.08 ± 0.44), compared with regular days (2.6 ± 1.4) when refinery emissions dominate lanthanum enrichment [23, 87, 145, 146, 256]. However, changes in La/Ce are less prominent in PM_{10} (Appendix Figure D4a; 0.79 ± 0.22 during Saharan episodes as compared to 1.39 ± 0.74 on regular days). This behavior is expected as fugitive mineral dust (soil and cement/concrete dust) dominate

the coarse fraction on regular days diluting any lanthanum enrichment brought about by refinery FCC emissions. Similar changes were calculated in La/Na and La/Sm ratios as well (Appendix Figure D4b and Figure D4c) affirming lanthanide dilution due to mineral dust intrusion. Three-component variations in La-Ce-Sm (Figure 1b), with concentrations normalized so that the average UCC values [120] appear at the centroid, additionally verified intrusion of crustal matter from the Sahara Desert into Houston's atmosphere. Predictably, North African dust and local Houston soil plotted very close to the UCC centroid in Figure V-1b symptomatic of their crustal origins. In contrast, FCC catalysts migrated towards the La-apex in the bottom-right corner symptomatic of their strong La-enrichment and anthropogenic nature. The near-linear spread of PM samples spanning the entire distance between the La-apex and the UCC-centroid strongly indicates that the light lanthanoids content of ambient $PM_{2.5}$ and PM_{10} was solely a mixture of emissions from petroleum refineries' FCC units and crustal resuspension. Importantly, the May-August timeframe samples remained on this line but moved closer to the UCC centroid (represented by the grey ellipse area in Figure V-1a) signifying greater North African dust contributions. In samples containing mineral dust from Saharan episodes (Figure V-1c), the average La concentration increased from 0.35 to 0.45 ng m^{-3} in $PM_{2.5}$ and 0.67 to 0.86 ng m^{-3} in PM_{10}. However, its enrichment factor relative to UCC-average titanium (Appendix Figure D26a) decreased 66% (from 9.6 to 3.3) in $PM_{2.5}$ and 39% (from 4.4 to 2.7) in PM_{10}. In addition to ternary plots, rare earth abundance patterns (Appendix Figure D3), and their abundance correlation (Appendix Figure D5) indicated a shift of ambient PM towards mineral characteristics, reaffirming major lanthanide inferences from North African dust in these samples of ambient Houston $PM_{2.5}$ and PM_{10}.

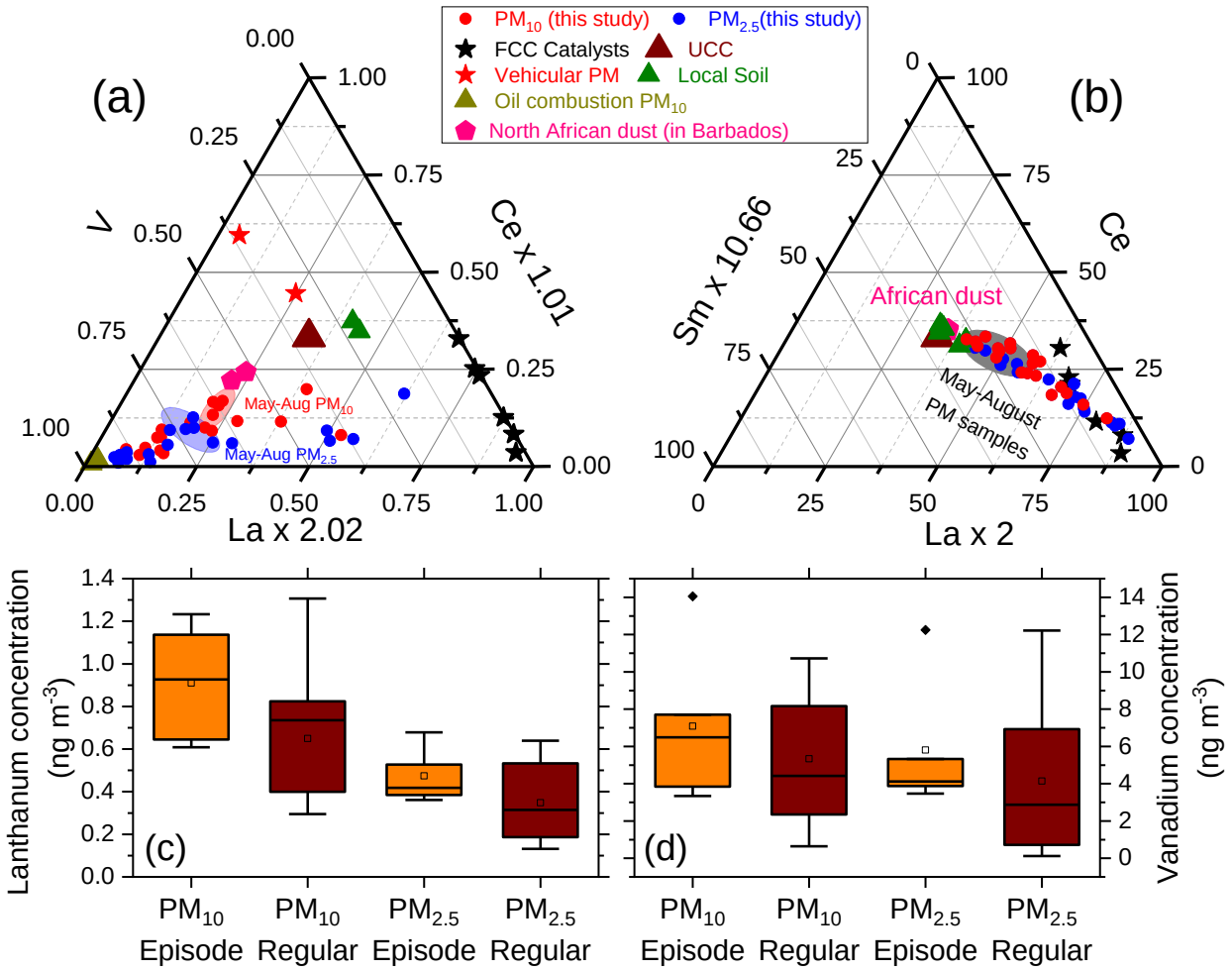

Figure V-1. Top left panel (a): La-Ce-V ternary plot showing vanadium enrichment from oil combustion. However, during high Saharan dust influenced months (May to August) samples tend to move towards North African dust profile similar to La-Ce-Sm behavior in the top right panel (b), indicating a significant vanadium contribution from crustal sources. Ternary La-Ce-Sm diagram in (b) depicts mixing of lanthanides from FCC emission (clustered near the La apex) and crustal matter (at the centroid). As seen, PM samples in both size classes moved closer to the center during high African dust months (May to August) enclosed in a gray oval. The concentration of (c) lanthanum and (d) vanadium substantially increased during episodes in both size classes indicating significant contributions from mineral dust.

Vanadium is a strong tracer for oil combustion and is typically enriched in urban PM on regular days [140, 248], which is symptomatic of industrial activities. Three-component variations in La-Ce-V (Figure V-1a) show that vanadium and light lanthanides in $PM_{2.5}$ and PM_{10} were

heavily influenced by crustal matter during May-August, which is the period of mineral dust surges. During dust episodes average vanadium concentration increased 59% in $PM_{2.5}$ (from 3.97 to 6.30 ng m^{-3}) and 57% in PM_{10} (from 5.04 to 7.91 ng m^{-3}) as shown in Figure V-1d. However, its enrichment factor decreased 66% in $PM_{2.5}$ (from 61 to 21) and 21% in PM_{10} (from 16.1 to 12.7) as shown in Appendix Figure D26. Hence, large-scale mineral dust intrusions weaken the effectiveness of vanadium as a tracer for oil combustion PM.

Impact on Potassium

Since biomass burning emits potassium-rich aerosols while being relatively depleted in all other metals [20, 138], it has been used as a tracer in many investigations, sometimes through K/Al, K/Si, K/Fe, and K/Ca ratios e.g., [47-50, 53]. Since airborne iron arises from many vehicular and industrial sources in urban environments [47, 54], we chose K/Al over K/Fe. However, in the current dataset K/Al, K/Si, and K/Ca ratios lie much closer to mineral dust profiles, viz., North African dust, local soil, and cement/concrete rather than biomass profiles that appear on the top right corners of Figures V-2A and V-2B [20, 138]. This indicates that the major potassium fraction arose from mineral dust thus making this element unsuitable to trace primary PM from vegetative combustion during our investigation. Note that $PM_{2.5}$ exhibited more influence of biomass burning appearing closer to the corresponding profiles and moving away from the mineral dust. In contrast, PM_{10} primarily overlapped with mineral dust since they are likely to dominate the coarser sizes whereas biomass combustion is likely to dominate the finer sizes (reported mean particle diameter less than 700 nm [257]).

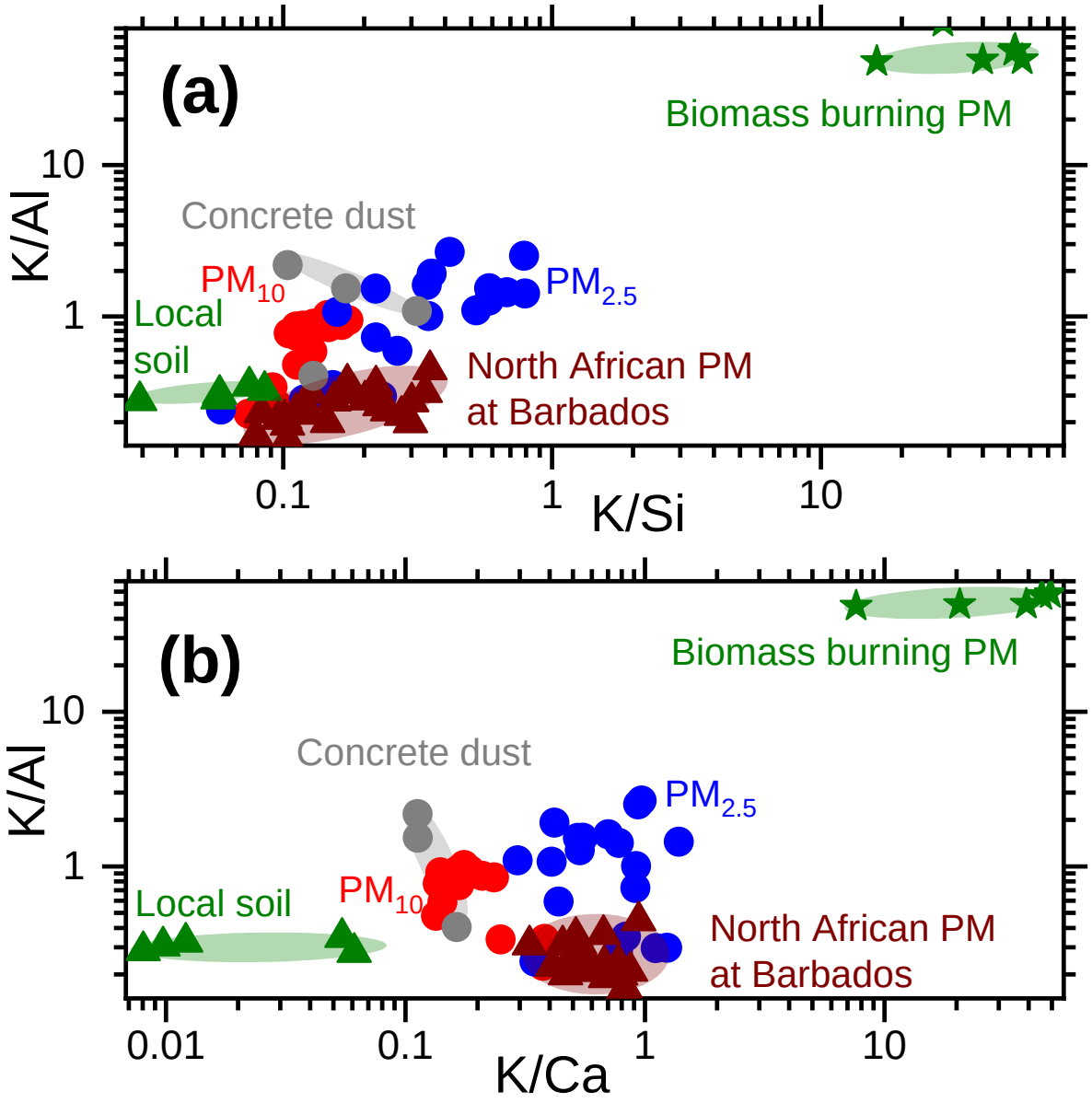

Figure V-2. PM_{10} and $PM_{2.5}$ in this study (shown as red and blue circles) drift away from mineral sources such as local soil (shown as green triangles), trans-Atlantic Saharan dust at Barbados (shown as brown triangles), and concrete/cement dust from construction activities (shown as grey circles in both the top panel, (a) that depicts K/Al versus K/Si and the bottom panel (b) that depicts K/Al versus K/Ca graphs. Note that both plots are in log-scale to better visualize the orders of magnitude variations in individual ratios. $PM_{2.5}$ exhibited higher potassium enrichment compared to PM_{10} indicating the higher influence of mineral materials towards coarser aerosols. Source characteristics for this graph are adapted from the literature [20, 51, 74].

Reconstructed Measured Mineral Material and Apportioning Mineral Sources

The Reconstructed Measured Mineral Material (RMMM) is a good surrogate to estimate the quantity of mineral mass in ambient PM [23, 29, 193, 258] by capturing oxide forms of all major crustal metals (Appendix Section D.3). Estimates of the total mineral dust component (North African dust + local soil + cement + concrete) quantified by CMB strongly correlated with RMMM for both PM_{10} (slope = 0.92 ± 0.10; R^2 = 0.95) and $PM_{2.5}$ (slope = 1.03 ± 0.08; R^2 = 0.98), validating our source apportionment results. African dust was estimated to be a major contributor to both PM sizes (Table A5). On episodic days it contributed nearly 30% (average 3.5 μg m^{-3}) to $PM_{2.5}$ and 33% to PM_{10} (average 7.9 μg m^{-3}). At the same time, a 24% surge in net $PM_{2.5}$ (average 2.8 μg m^{-3}) and 25% increase in PM_{10} (average 3.1 μg m^{-3}) was measured, pointing to African dust as the chief underlying reason for the increase in PM mass concentration. The ratio of North African dust estimated in $PM_{2.5}$ to PM_{10} during episodic days was in the range 0.35 – 0.47 (average 0.44 ± 0.05), which overlapped with earlier reports from our group in Houston [29], validating the current estimates.

Distinguishing North African dust from local soil

Due to their similar elemental composition, Houston soil that is locally resuspended and African dust cannot be directly discriminated using rare earth elements and RMMM. However, size fractions of the RMMM are likely to differ between the two sources due to the loss of coarse particles from Saharan dust during trans-Atlantic transport [255]. Local fugitive mineral dust sources will dominate the coarser sizes [259]. RMMM in $PM_{2.5}$ to PM_{10} ratio for soil is likely to lie between 0.15-0.25 (Cowherd and Ono, 2006; Tong et al., 2012). This ratio for North African dust in the southeastern United States is expected to be $\gtrsim$ 0.36 [29] due to the relative loss of larger

particles during its long journey before reaching the receptor site. As expected from these arguments, the ratio of RMMM in $PM_{2.5}$ to RMMM in PM_{10} in this study increased from 0.19 ± 0.06 on regular days to 0.46 ± 0.07 during North African dust events (Appendix Figure D24), providing further evidence of North African impacts. Al/Si and Al/Ca have also been used to differentiate mineral sources with African dust reportedly having $0.3 \leq Al/Si \leq 0.7$ and $1.1 \leq Al/Ca \leq 3.5$ [25, 74]. Hence, African dust is relatively enriched in Al than Si and depleted in Ca in comparison to elemental characteristics reported for Houston soil ($0.07 \leq Al/Si \leq 0.11$ and $0.15 \leq Al/Ca \leq 0.5$) [51, 74]. During Saharan intrusions in Texas, the PM_{10} Al/Si ratio prominently increased and doubled from 0.16 ± 0.03 to 0.32 ± 0.07. The $PM_{2.5}$ Al/Si ratio also increased but only by 40% (from 0.33 ± 0.14 to 0.47 ± 0.20). In contrast, changes in Al/Ca were equally prominent for $PM_{2.5}$ (increasing 5.5-fold from 0.54 ± 0.31 on regular days to 2.89 ± 1.09 during episodes) and PM_{10} (increasing 6-fold from 0.20 ± 0.03 on regular days to 1.23 ± 0.81 during episodes). This implies that Al/Si is not a good tracer for fine particles and Al/Ca is not a good tracer for PM_{10}, which suggests interferences from industrial sources to $PM_{2.5}$ and cement/concrete dust from construction activities to larger particles. These observations highlight the necessity of measuring both size fractions to differentiate North African dust from local mineral aerosol sources.

Regionally transported primary PM from large scale biomass burning

Identification of regional biomass burning aerosols

NASA's fire maps from the FIRMS database (Appendix Figure D23) and HYSPLIT back trajectories (Figure V-3 and Appendix Figures D7 and D10) revealed several instances of PM from large-scale biomass burning events entering Houston influencing samples S1, S4, S5, S11, S14,

and S16. The most dominant incidents of biomass burning aerosols in Houston were during April and May of 2015 (samples S14 and S16) when large quantities of smoke were predicted by the United States Navy NAAPS global aerosol model [254] and evident from satellite images (see Appendix Figure D17). It has been recognized for over 40-years that anthropogenic biomass burning as an agricultural activity in Central America beginning with the Northern Hemisphere tropical dry season (i.e., March) and ending with the rainy season (i.e., early June) [260] adds substantial quantities of aerosols to the troposphere [261]. Figure V-3 (i.e., FIRMS' fire maps) confirms several intense, large-scale fires during this timeframe in Central America, which directly inject smoke above the boundary layer allowing it to travel long distances under the control of moist oceanic airflow, crossing over the Gulf of Mexico into the southeastern United States [30, 262, 263]. These paths were validated by HYSPLIT back trajectories that depicted their transport from central American source regions to the receptor site. Primary and secondary aerosols arising from these vegetation combustion events marginally spiked ambient $PM_{2.5}$ and PM_{10} concentrations from 9.2 to 10.6 μg m^{-3} and 19.2 to 20.7 μg m^{-3} respectively.

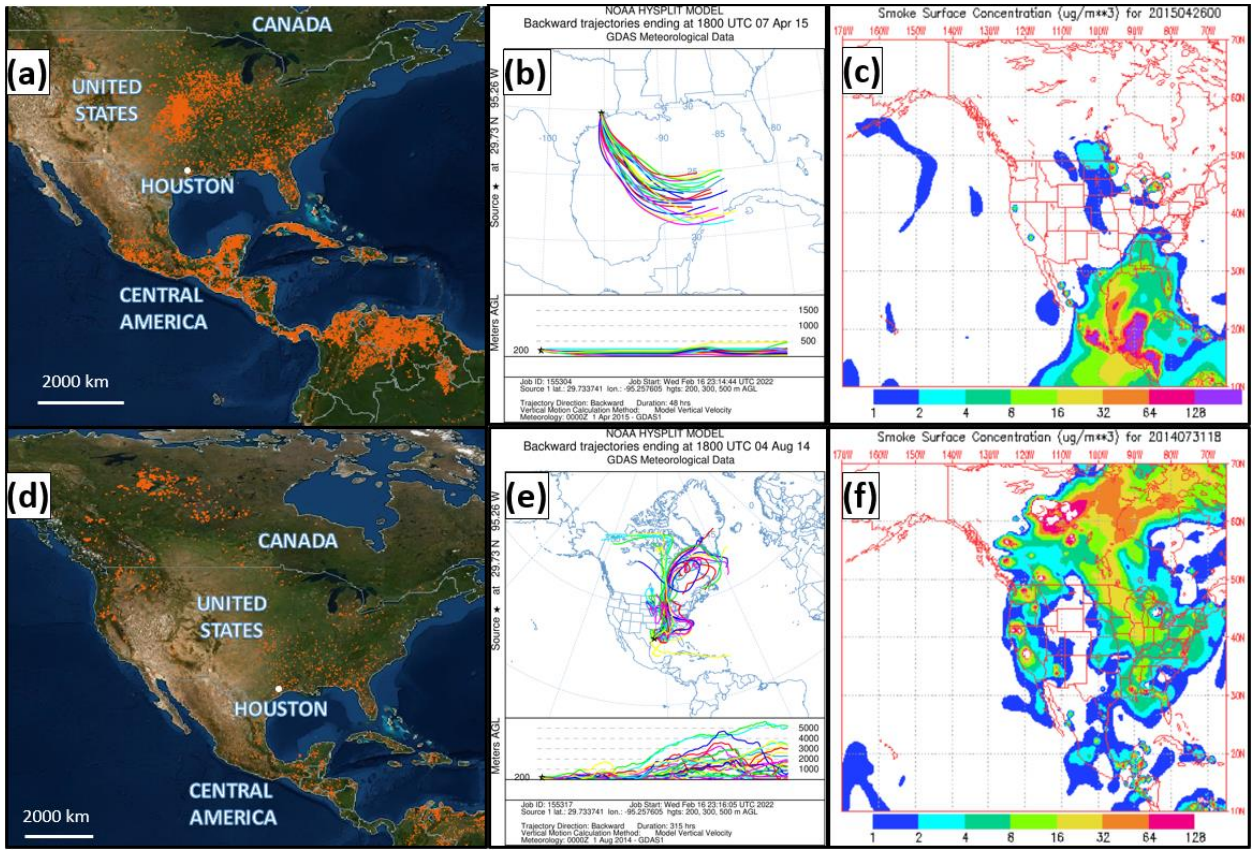

Figure V-3. International biomass burning events that impacted Houston during the study period. The top row (a – c) shows large-scale smoke events originating from Central America in spring/summer 2015. See also satellite imagery in Appendix Figure D17 that pinpoints the origin of this event in Honduras. The bottom panel (d – f) describes a particular fire event in Canada, which originated from Northwest Territories and British Columbia [264], in August 2014. The two leftmost panels show respective NASA's fire maps to spot large-scale American combustion events (orange dots). The top and bottom middle panels show cumulative HYSPLIT back trajectories of wind integrated over the corresponding sampling duration. The rightmost panel shows smoke concentrations simulated by the NAAPS model confirming the transport of biomass burning smoke from Central America (top panel (c)) and Canada (bottom panel (f)), respectively.

Outside the Central American biomass burning season, PM from a Canadian forest fire reportedly originating from Northwest Territories and British Columbia [264], traveled all the way south to Houston in August 2014 as shown in Figure V-3 that was captured in sample S1. Separately, agricultural residues are sometimes burnt in October in southeastern states in the USA [265], which was confirmed by fire maps in Appendix Figure D23 that episodically affected samples S4 and S5. Wind roses from mid-September to October show prevailing winds from the northeast facilitating PM transport to Houston (Appendix Figure D6). Forest fires in the southeastern United States were detected in February 2015 (Appendix Figure D16 and sample S11 in Appendix Figure D23) and confirmed via TCEQ's air quality predictions [136].

Non-mineral potassium for tracing biomass burning PM

Iron has been proposed to isolate potassium from biomass burning [48], which does not apply in our case due to differing K/Fe ratios for motor vehicles ($0.04 \leq K/Fe \leq 0.07$) and mineral mass ($0.3 \leq K/Fe \leq 1.8$) as well significantly higher iron contributions from motor vehicles (3.8 – 5.2 %) [21, 54] compared with mineral mass (0.5 – 2.3 %) [51]. Silicon has also been used [50], but K/Si in North African dust (= 0.19) is different from local soil (K/Si = 0.03). The K/Ca ratio, which has a higher value in North African dust (0.45) compared to only 0.08 in local soil and 0.11 in concrete dust can be used [47, 49]. Coal combustion also releases copious amounts of potassium consequently making it difficult to segregate biomass burning PM in cities that are heavily dependent on coal-fired power plants [47]. However, because Houston has only a single power plant that only partially uses coal (W.A. Parish) and is ~50 km southwest from our site and another coal combustion marker selenium was very low in ambient PM (< 1 ng m^{-3}), we can infer that coal did not contribute significantly to airborne potassium during our sampling campaign. In any case,

trace contributions of potassium from coal combustion were separated using the K/Se ratio (1.27) [20].

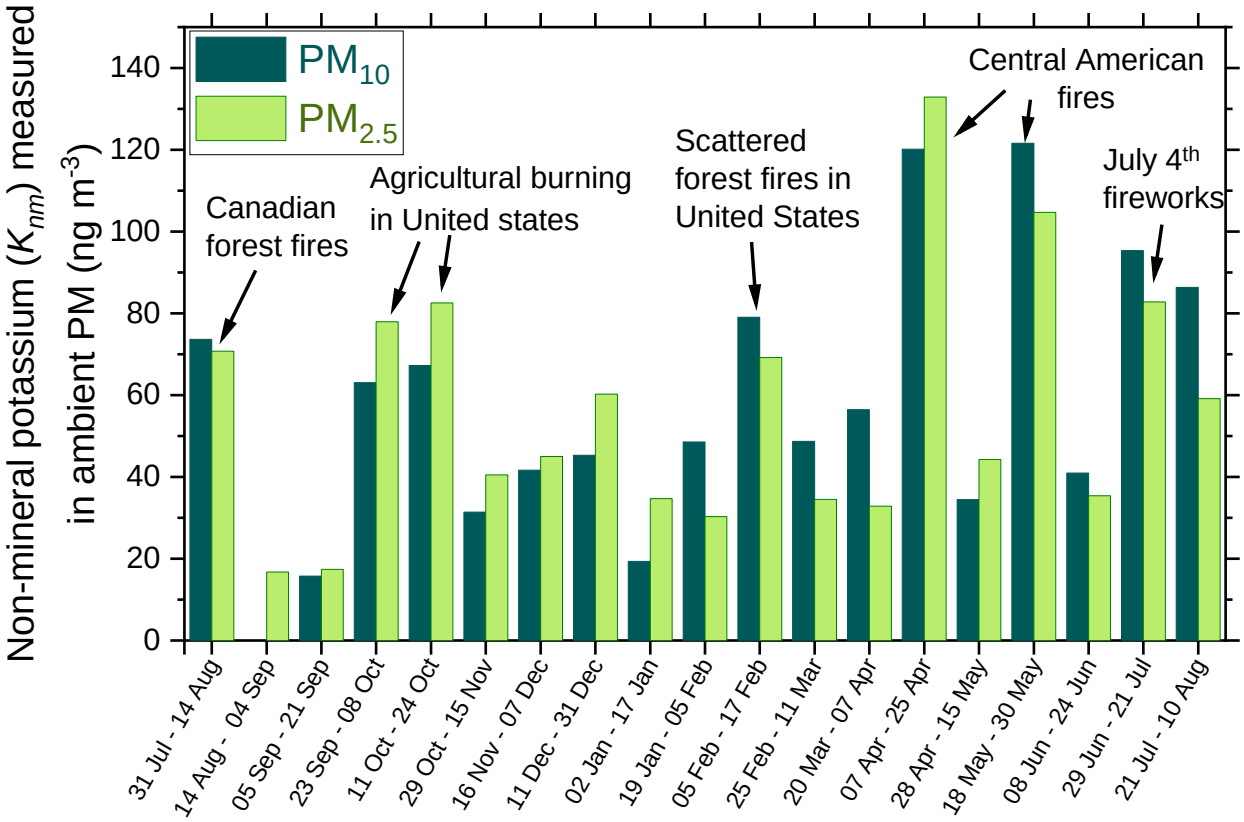

Figure V-4. Peaks in the temporal profile of non-mineral potassium (K_{nm}) in our samples coincide with large-scale episodes of biomass burning identified by other approaches. Note that "July 4 fireworks" correspond to American Independence Day celebrations.

We tackle limitations posed by single tracers explained in the previous paragraph with a multi-elemental approach to isolate potassium from biomass burning, in turn creating a "non-mineral potassium" parameter to directly track PM from vegetative combustion. Crustal potassium was traced by aluminum because both local soil and long-range transported dust had a stable mean K/Al of 0.22 ± 0.06. Anthropogenic potassium is enriched in construction activity/concrete dust but depleted in aluminum (K/Al = 1.85 ± 0.50) and is not separated using Al but can be tracked because of its calcium enrichment (K/Ca = 0.13). However, calcium needs to be carefully

implemented as it can be co-contributed from crustal sources, and in this study, we used the Ca/Si ratio to separate crustal calcium from concrete dust calcium (Appendix Section D.4). Overall, an equation was derived to calculate non-mineral potassium (Knm, Equation 1) with detailed information given in Appendix Section D.10 page 27. The calculated non-mineral potassium over the entire study duration is presented in Figure V-4. Importantly, the peaks in non-mineral K coincided with identified biomass burning episodes identified by other approaches using satellite products and aerosol models (Figure V-4) validating our Knm estimations and its direct association with primary PM from vegetative combustion.

$$K_{nm} = K - 0.22 \times Al - 0.11 \times Ca + 0.032 \times Si - 1.27 \times Se \qquad \text{(Equation 1)}$$

Quantitative apportionment of the non-mineral potassium component including biomass burning

The non-mineral potassium (K_{nm}) and CMB-apportioned biomass burning PM were strongly correlated in both size classes (R^2 = 0.83 for $PM_{2.5}$ and 0.70 for PM_{10}, Figure V-5) validating our approach to apportion biomass burning PM. A comprehensive apportionment of all relevant sources reveals that biomass burning contributed to all our samples except one (sample S2 between August 14 and September 4, 2014 in Appendix Figure D27). Hence, our approach also captured smaller and local biomass burning events that emit potassium even on regular days but are not large enough to be captured by satellites e.g., [10]. Since the increase in potassium levels in early July has been traced to fireworks celebrating American Independence Day [2], it was not classified as a biomass burning episode herein. More detailed source characterization and higher time resolution during sampling are required to identify PM from fireworks. As shown in Appendix Table D6, contributions more than doubled averaging 0.6 μg m^{-3} in PM_{10} and 0.5 μg m^{-3} in $PM_{2.5}$ on regular days to 1.4 μg m^{-3} in PM_{10} and 1.3 μg m^{-3} in $PM_{2.5}$ during transborder fire

episodes. Appendix Table D6 also shows the average total potassium on episodic days increased by 27% to 241 ng m^{-3} from 191 ng m^{-3} on regular days in PM_{10} and by 46% to 122 ng m^{-3} from 84 ng m^{-3}. Further, average non-mineral potassium (K_{nm}) increased 106% to 92 ng m^{-3} from 45 ng m^{-3} in PM_{10} and 111% to 92 ng m^{-3} from 44 ng m^{-3} in $PM_{2.5}$ under identical circumstances confirming the effectiveness of using non-mineral potassium (Equation 1) instead of total potassium to track biomass burning.

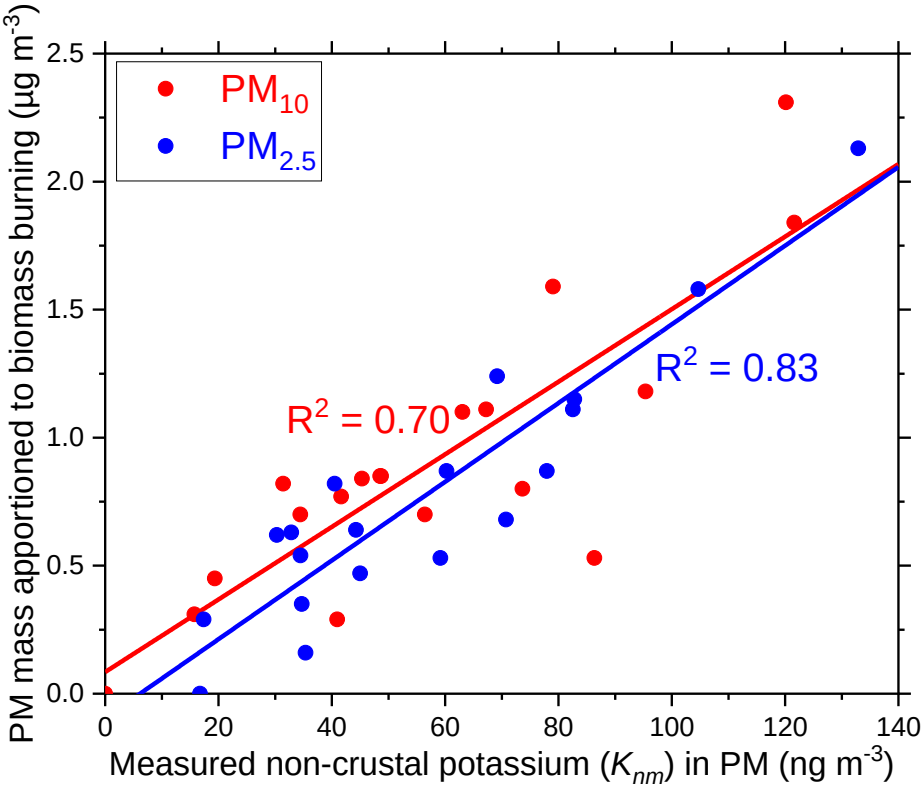

Figure V-5. Strong correlations between non-mineral potassium (K_{nm}) and $PM_{2.5}$ (in blue) and PM_{10} (in red) qualitatively validate CMB source apportionment results.

Locally emitted PM from proximal Houston-area sources

Figure V-6c shows a good correlation of platinum group metals, i.e., Rh + Pd + Pt (R^2 = 0.85 for $PM_{2.5}$ and 0.80 for PM_{10}) with CMB estimated vehicular PM contributions. Other trace elements (Cu, As, Mo, Cd, Sb, and Pb), which are also primarily associated with vehicular PM

were well-correlated with CMB estimations (R^2= 0.65 and 0.71 for $PM_{2.5}$ and R^2=0.57 and 0.68 for PM_{10} in Figures V-6a and V-6b). The Cu/Sb ratio varied between 2.2–5.8 for $PM_{2.5}$ and 2.0–5.6 for PM_{10}, (Appendix Figure D25) overlapping with the range we reported [21, 54]. These results demonstrate that Sb, Cu, Cd, As, Mo, Pb, Rh, Pd, and Pt were all excellent tracers for vehicular PM and were minimally interfered by other sources even during African dust episodes.

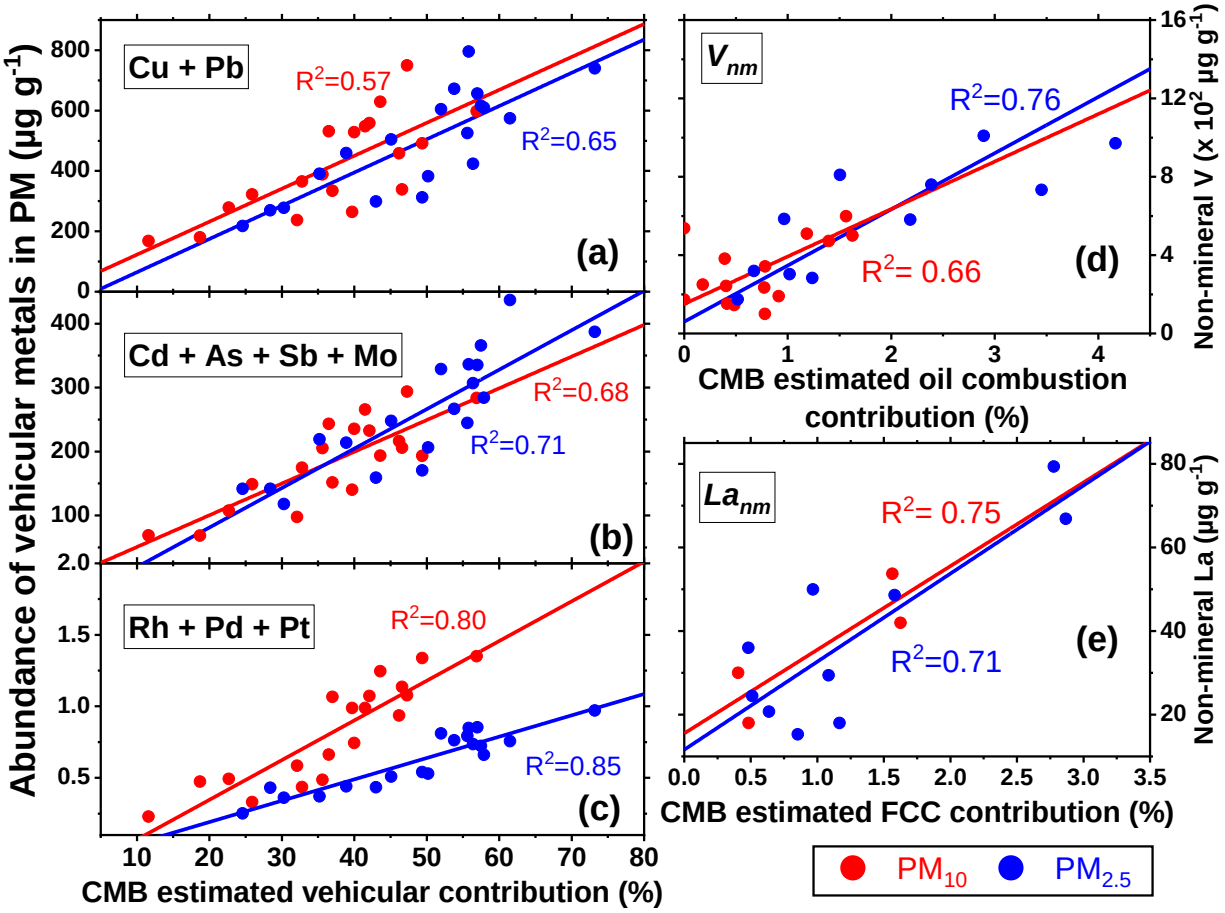

Figure V-6. Correlations of tracers or signature elements abundances with their respective source contributions to PM_{10} (shown in red color) and $PM_{2.5}$ (shown in blue color) for three local sources, namely automobiles (a, b, and c), oil combustion (d), and petroleum refinery FCC units (e). Based on their abundances in ambient PM, vehicular metals were grouped into three categories (a) Cu and Pb, (b) Sb, Cd, As, and Mo, and (c) Rh, Pd, and Pt. Subfigure (d) depicts non-mineral vanadium (V_{nm}) and (e) shows non-mineral lanthanum (La_{nm}), both of which well-correlated with CMB source contribution estimates qualitatively validating our approach.

We also validated mineral mass in this study and separation of North African dust with Al and Si, axiomatically validating our estimates for local soil. Oil combustion PM was traced with non-mineral vanadium instead of total vanadium as typically used [52, 140]. As discussed in North African discussion section, natural vanadium was separated using the V/RMMM ratio (= 9×10^{-5}) given its uniform abundance in crustal mass [51]. A good correlation was obtained for non-mineral vanadium (V_{nm}) with oil combustion contributions for $PM_{2.5}$ (R^2 = 0.76) and PM_{10} (R^2 =0.66). Similar to vanadium, crustal lanthanum was separated with the help of yttrium, because the ratio corresponding to natural La/Y (= 1.6) [51] was obtained in all mineral samples differentiating itself from refinery PM that has a very high La/Y ratio (> 500) [51, 86]. Unlike vanadium, non-mineral lanthanum (La_{nm}) was not detected in several PM_{10} and $PM_{2.5}$ samples (thirteen and nine, respectively) indicating strong mineral influences but only occasional refinery emissions. It is noted that the time-integration of our samples may have diluted anthropogenically-emitted La because refinery emissions are relatively short-lived [87, 145, 146]. Nevertheless, non-mineral La (La_{nm}) correlated with CMB estimates of refinery/FCC contribution to $PM_{2.5}$ (R^2 = 0.71) and PM_{10} (R^2 = 0.75) validating our results. Calculations of non-mineral vanadium (V_{nm}) and lanthanum (La_{nm}) are given in Appendix Section D.11 and correlations with relevant sources are presented in Figure V-6d and V-6e.

Cement/concrete dust from construction activities was the third major mineral dust material and it is strongly enriched in Ca exhibiting $14 \leq Ca/Al \leq 19$ [20, 51]. During the entire course of this study, Ca was not enriched (Appendix Figure D25 for Ca/Al ratios) in any of our samples (Ca/Al = 0.4 – 6.5 for PM_{10} and 0.4 – 4.6 for $PM_{2.5}$) justifying its low apportionment (averaging 0.03 – 0.46 μg m^{-3} to PM_{10} and negligible in $PM_{2.5}$). The greater contribution to PM_{10} (0 – 8%)

than $PM_{2.5}$ (0 – 2%) agrees with the fugitive nature of this PM source in Houston[29], qualitatively validating our estimates. As seen in Appendix Table D7, the overall contribution of local anthropogenic sources remained relatively constant throughout the 12-months, ranging only between 3.9 to 5.5 μg m^{-3} in $PM_{2.5}$ and 6.8 to 9.0 μg m^{-3} in PM_{10}. As shown in Appendix Figure D1, the sampling site is surrounded by numerous anthropogenic sources and dominated by traffic emissions, which emit PM year-round and are less likely to vary with seasons and change in wind directions, again consistent with CMB estimations.

Summary of estimated primary PM contributions from distal and local sources

CMB apportioned 84 ± 10% of PM_{10} and 78 ± 9 % of $PM_{2.5}$ mass to several sources and the unapportioned mass is attributed to secondary aerosols, which is a known PM component in Houston [9, 10, 23] as summarized in Appendix Figure D27. The Sahara-Sahel region was the dominant distal source contributing > 30% of Aeolian dust to PM mass during May – August (Figures V-7a and V-7d). Averaged over 12-months its annual contribution was ~13% to both size classes, amounting to 2.7 μg m^{-3} to PM_{10} and 1.1 μg m^{-3} to $PM_{2.5}$ (Figure V-7g and V-7h). Large-scale regional anthropogenic and natural biomass burning events (i.e., forest and agricultural fires) in Canada, Central America, and neighboring southeastern states were also recognized as a distal source using satellite products and aerosol models during various periods over the study duration. International and out-of-state biomass burning accounted for 6.4% of PM_{10} and 12% of $PM_{2.5}$ when it episodically contributed to ambient PM in Houston (Figures V-7b and V-7e), amounting to 0.46 μg m^{-3} (2.3%) in PM_{10} and 0.40 μg^{-3} (4.1%) in $PM_{2.5}$ when averaged over the entire year of sampling (Figures V-7g and V-7h). Local biomass burning sources include wood burning, meat cooking, waste incinerator, and smaller-scale agricultural fires [10], which were classified as such

in the lack of evidence from satellite products and synoptic-scale aerosol models. These in state sources were estimated to contribute ~0.40 µg m^{-3} to both PM size classes shown as blue sectors in Figures V-7a, V-7c, V-7d, and V-7f. Cumulatively, distal sources annually contributed 1.5 µg m^{-3} (16%) to $PM_{2.5}$ and 3.2 µg m^{-3} (16%) to PM_{10} as summarized in Figure V-7g and V-7h. As expected, locally derived PM (from motor vehicles, resuspended soil, and industries) were dominant > 62% of apportioned PM_{10} and $PM_{2.5}$. A detailed breakdown of the local sources with seasonal categorization is given in Appendix Table D7.

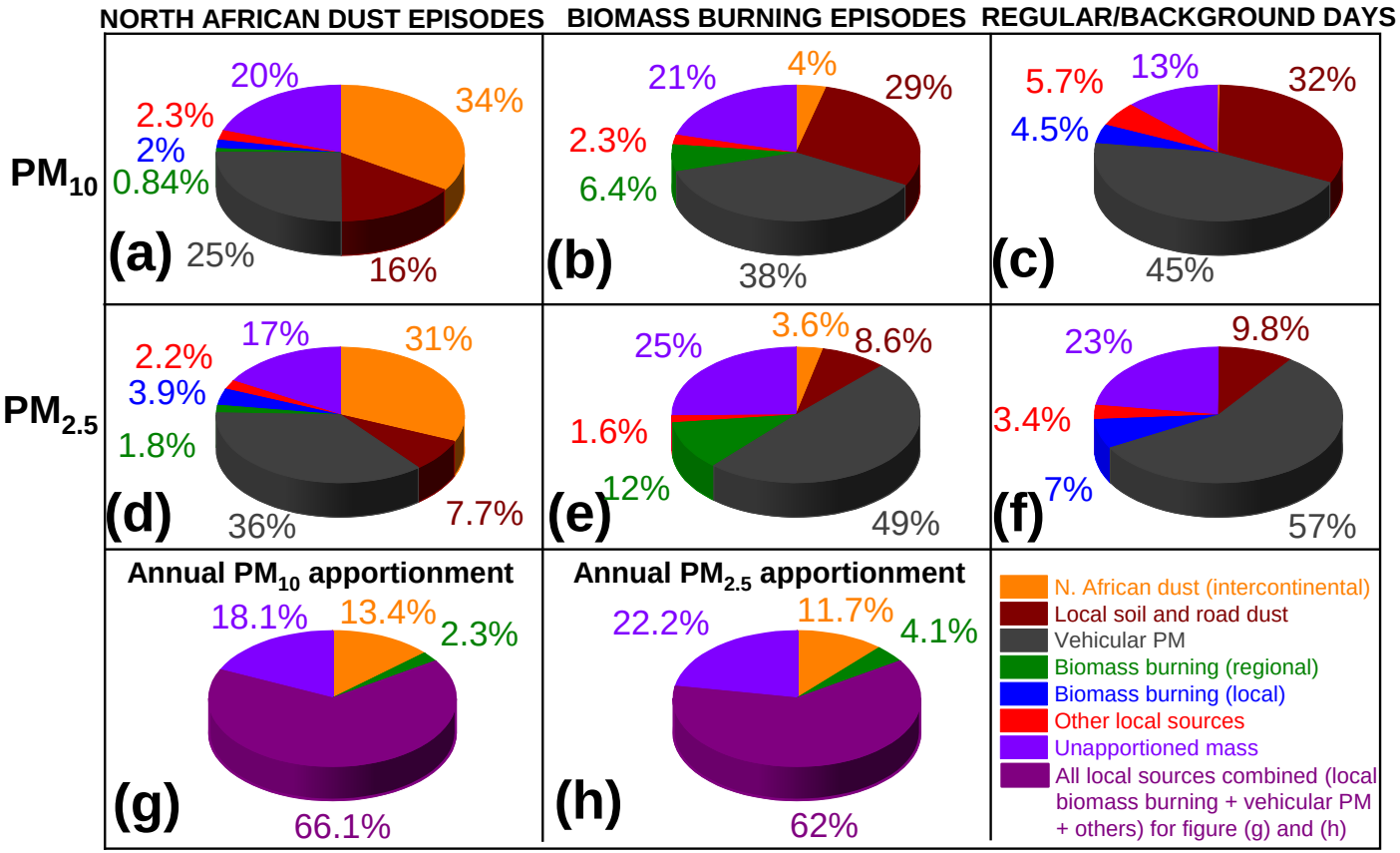

Figure V-7. Summary of contributions from major sources to ambient PM_{10} (top row, a – c) and $PM_{2.5}$ (bottom row d – f). CMB estimated North African dust, local soil, motor vehicles, and biomass burning as major sources of primary ambient $PM_{2.5}$ and PM_{10} in Houston. North African mineral dust episodes (S2, S5, S15, S17, S18, S19) are highlighted in (a) and (d), regional agricultural and forest fire episodes (S1, S4, S5, S11, S14, S16) are highlighted in (b) and (e), and regular/background days (S3, S6, S7, S8, S9, S10, S12, S13) dominated by proximal sources correspond to (c) and (f). The annual average contribution of intercontinental (North African dust), regional (large-scale biomass burning identified as fire episodes outside of Texas), and local sources to (g) PM_{10} and (h) $PM_{2.5}$ (bottom).

3. CONCLUSIONS

We quantified the episodic influences of transboundary long-range (trans-Atlantic Saharan) and regional (biomass burning) sources on ambient primary PM levels in Houston and their effects on the chemistry of rare earths, vanadium, and potassium over the course of 12-months. Our results point to the need to isolate the non-mineral component of these elemental tracers (La_{nm}, V_{nm}, and K_{nm}) to accurately distinguish, track, and apportion international, out-of-state, and local emissions that contribute to primary PM. North African influences were prominent between May and August contributing 30% of $PM_{2.5}$ and 33% of PM_{10} during the respective intrusions increasing fine and coarse PM concentrations by ~25% (with another minor event in October). Biomass burning episodes significantly affected aerosol levels from mid-September to November (agricultural burning in eastern United States) and between April to June (biomass burning in Central America). During the periods when out-of-state and cross-border fire episodes were detected, primary PM from biomass burning was estimated to be 10% of $PM_{2.5}$ and 6% for PM_{10}. For the first time, the non-mineral portion of potassium was calculated using multiple elements, which was more robust and stable in tracking biomass PM than using single elements as is currently done. Analogously, non-mineral components of lanthanum and vanadium were also calculated, which correlated well with source contribution estimates of refinery emission and oil combustion respectively. Overall, distal sources (intercontinental + regional) contributed an average of 1.5 μg m^{-3} to $PM_{2.5}$ and 3.7 μg m^{-3} to PM_{10} over the course of this 12-month study, which may prove critical in the future when more stringent federal PM regulations designed to better protect human health may be promulgated [8, 246]. In any case, techniques developed in this manuscript can better identify exceptional events originating internationally, out-of-state, and

inside Texas and estimate their contributions to ambient primary aerosol levels compared to existing methodologies demonstrating the importance of this work. Finally, coupling these procedures with organic markers (e.g., levoglucosan [10]) will improve quantitative estimates of total (i.e., primary + secondary) PM arising from exceptional biomass burning events assisting with regulatory compliance, policy making, and health effects investigations.

CHAPTER VI

ELEMENTAL COMPOSITION OF INDOOR AND OUTDOOR COARSE PARTICULATE MATTER AT AN INNER-CITY HIGH SCHOOL‡

Introduction

It has been estimated that we spend as much as 90% of our time indoors; making the quality of indoor air a vital public health concern, especially for more vulnerable groups such as children [266-268]. Since children spend substantial time indoors while attending schools, their exposure to airborne particulate matter (PM) in this environment is a pathway of particular concern as it can lead to diminished lung function growth, increase suceptibility to acute respiratory illness and asthma, and even increase violent neighborhood crime [267, 269-271]. This is crucial for schools located in highly industrialized regions where outdoor air pollution may transport indoors via the ventilation (HVAC) system and/or infiltrate through cracks in the building envelope, thereby exposing children to elevated levels of anthropogenic pollutants [272, 273].

Houston, Texas provides a unique location to analyze indoor and outdoor air pollution. The United States Environmental Protection Agency's Toxics Release Inventory (TRI) Program ranks Houston 4th out of 893 urban areas based on the amount of toxic chemicals released per square mile. With a population of almost 7 million people, greater Houston ranks as the fifth largest metropolitan region in the United States. Contained in this region is the Ship Channel, which encompasses numerous industries, including United States' largest (and world's second largest)

‡ ‡ Reprinted with permission from "Elemental composition of indoor and outdoor coarse particulate matter at an inner-city high school", K. Williamson, S. Das, A.R. Ferro, and S. Chellam, *Atmospheric Environment*, **261**, 118559, Copyright 2021 by Elsevier

petrochemical complex. We identified a school in the city of Galena Park, which is adjacent to the Ship Channel, as our test site. Air pollution at this location is heavily influenced by industrial sources and tailpipe and non-tailpipe emissions, including road dust resuspension, from automobiles traversing nearby heavily-trafficked highways. Outdoor particulate matter and airborne metals measured in this region have been linked to health risks [189, 274-277].

Galena Park is primarily populated by Hispanics, African Americans, and Native Americans with a median per capita income of $17,255 (in 2020 dollars) and 29.4% of the population living below the poverty level [278]. Additionally, ~ 28% of students in Galena Park Independent School District belong to poverty-stricken families and receive Food Stamp/Snap benefits [279] raising environmental justice concerns [176, 280].

Most previous investigations of paired indoor and outdoor particulate matter have analyzed only a limited number of metals with many of them being conducted outside the United States [272, 281-289]. We have recently reported a wide suite of metals in outdoor and indoor $PM_{2.5}$ [290] in a United States school, which we extend in this manuscript by targeting nearly 50 elements in indoor and outdoor coarse PM ($PM_{10-2.5}$). Even though the coarse fraction enters the thoracic part of the airways, it is generally retained in the upper respiratory tract, representing an inhalable size range that exacerbates cardiovascular, asthma, and other health problems in children and adults [291]. Measurements herein are further motivated by the "metals hypothesis", which assigns a portion of human health effects to respirable metals [175].

The primary objective of this research is to characterize the elemental composition of indoor and outdoor coarse PM in a school. Paired indoor and outdoor $PM_{2.5}$ and PM_{10} samples were collected over a two-month period at a high school in the Galena Park Independent School District, which were analyzed to derive coarse PM concentrations for a multitude of representative

elements, rare earth elements (REEs), and transition metals. Outdoor and indoor relationships for $PM_{10-2.5}$ were evaluated by comparing mass concentrations, elemental abundance patterns, indoor/outdoor (I/O) PM mass and elemental abundance ratios, enrichment factors, tracer element ratios, and ternary diagrams, which also provided clues to metals' sources. Findings from this study primarily contribute to understanding PM infiltration/ventilation and provide a potential lower-bound for resulting exposure in schools for coarse PM metals. The work is particularly important because studies reporting compositional analysis for PM inside school buildings is limited, and the school is located in a highly industrialized, underserved, and marginalized community with high risk for adverse effects due to the exposure.

Methods

Sampling and site location

Aerosols were collected on 47 mm PTFE filters using Rupprecht & Patashnick Partisol-Plus 2025 samplers, operated at 1.0 m3/h at the North Shore Senior High School Ninth Grade Center (29.7875, -95.1828) as shown in Figure VI-1. Permission was not granted to install samplers in an occupied classroom because their noise would hinder teaching, the perception that students' safety might be compromised, and they could interfere with the sampling. Hence, two indoor samplers (one for PM2.5 and one for PM10) were installed on a 3 foot high countertop in a closed, unoccupied, ventilated (via the school HVAC system) storage room adjoining two classrooms on the second floor of the building. Therefore, our results potentially represent a lower bound contribution from outdoor sources to the indoor concentrations measured inside the school. Outdoor samplers were installed on the west side roof on the same floor. A total of 26 samples were collected (13 PM2.5 and 13 PM10 (one of which was lost)), each integrated over 2 – 6 days

over a period of two months from March 11 – May 11, 2011 (Supporting Information (SI) Table SI-1). The longer (2-6 day) sampling periods allowed the collection of sufficient PM mass for elemental analysis and accommodated scheduled access to the school. Extended sampling durations do not impact our findings since only concentrations (e.g. μg m^{-3}) and abundances (e.g. μg g^{-1}) were interpreted. Four blank filters were analyzed and concentrations were corrected using their average concentrations [290]. The limited number of samples precluded quantitative source apportionment and synchronous indoor/outdoor measurements provided information on infiltration and/or ventilation.

Approximately 4,500 students were enrolled in this nearly 60-year old school (constructed in the year 1962), which is surrounded by very busy highways including Interstate-610 (annual average daily traffic (AADT) 130,000 vehicles/day), Interstate-10 (AADT 168,000 vehicles/day), Beltway 8 (AADT 96,000 vehicles/day), State Highway 90 (18,000 vehicles/day), and State road 526 (AADT 23,000 vehicles/day). All windows and doors of the school are always kept closed given its proximity to the myriad Ship Channel PM sources, several heavily trafficked roads, and the typically hot and humid local weather. Consequently, the HVAC system, which is fitted with a Minimum Efficiency Reporting Value (MERV) 9 filter is continuously operated (at a 15% fresh air and 85% return air setting). A MERV 9 filter is nominally ~85% efficient in removing 3-10 μm aerosols and < 50% efficient in removing 1-3 μm particles [292] and has been estimated to be only 30-35% efficient for removing PM2.5 [293].

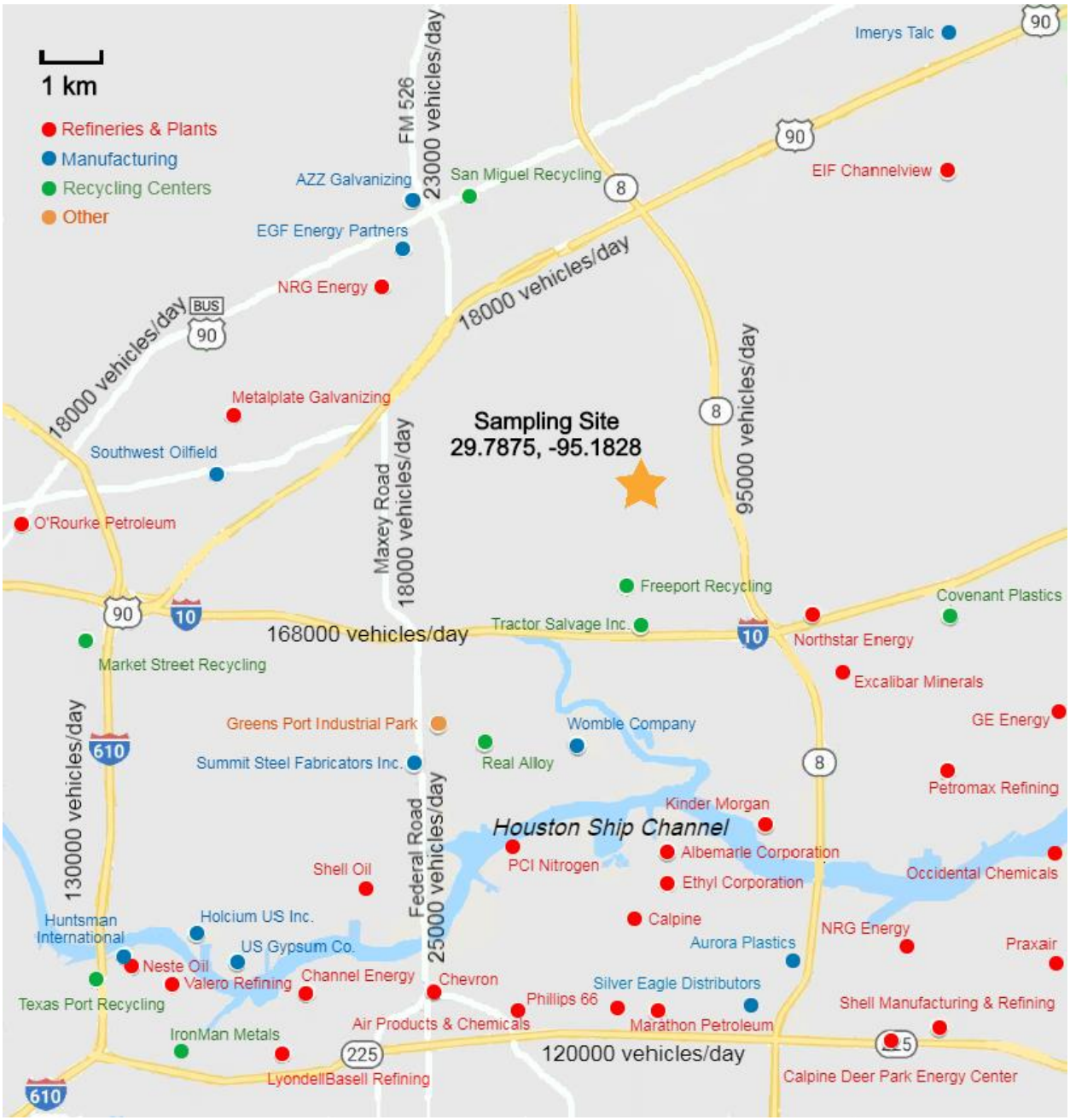

Figure VI-1. Location of sampling site (created using a Google product. Map data: Google Earth) showing its proximity to several heavily trafficked roads and numerous industrial (petrochemical, refining, manufacturing, and recycling operations). Prevailing winds were from the south to southeast (see Supplementary Information (SI) Appendix Figure E1).

Elemental analysis

PM samples were digested in two stages in a microwave oven (MARS 5, CEM Corp., Matthews, NC), first by adding 3 mL HNO3 (14.3 M) and 10 □L HF (48%) and heating to 200 °C

at a pressure set point of 1.55 MPa (225 psig) for 20 minutes dwell time. In the second stage, any remaining HF was masked and fluoride precipitates redissolved by adding 80 □L of 5% (m v^{-1}) H3BO3 and reheating with the same settings. A total of 50 elements including 18 from the main groups (Li, Be, Na, Mg, Al, Si, K, Ca, Ga, As, Se, Rb, Sr, Sn, Sb, Cs, Ba, Pb), 16 transition metals (Sc, Ti, V, Cr, Mn, Fe, Co, Ni, Cu, Zn, Y, Zr, Mo, Cd, Hf, W), and 16 inner transition metals (La, Ce, Pr, Nd, Sm, Eu, Gd, Tb, Dy, Ho, Er, Tm, Yb, Lu, Th, U) were analyzed by quadrupole inductively coupled plasma-mass spectrometry (q-ICP-MS; ELAN DRC II, PerkinElmer SCIEX). Improved measurements of several elements (Al, Ca, V, Cr, Mn, Fe, Ni, Co, Cu, Zn, As, Se, and Cd) were facilitated by exploiting ion-molecule reactions in a reaction cell with NH3 as the cell gas at 1 mL min-1 flow rate. Quality control and assurance details can be found in our earlier publications [87, 290]. Our ICP-MS measurements yielded a maximum of 15% uncertainty resulting in 30% uncertainty propagated in REE ratios. Even with 30% uncertainty, REEs clearly distinguished separation betweem crustal and petroleum refining sources (e.g. in Figure VI-6).

Results and Discussion

Indoor and Outdoor $PM_{10-2.5}$ and $PM_{2.5}$ Mass Concentrations

Figure VI-2 illustrates a time series of indoor and outdoor $PM_{10-2.5}$ mass concentrations (see also Table SI-1). Indoor coarse PM mass concentrations were very low, always < 1 μg m^{-3} and were not statistically correlated with outdoor levels (R^2 = 0.020 and p-value > 0.050), as shown in Figure VI-2c. Poor correlations between indoor and outdoor coarse PM agree with earlier results [283, 294, 295] and may be attributed to the transient nature of outdoor sources of coarse PM as well as its larger size, greater deposition rate, and filtration efficiency as opposed to fine PM [1, 236, 296]. Fine and coarse PM were also poorly correlated both indoors (R^2 = 0.010) and outdoors

(R^2 = 0.070) similar to earlier reports [291]. In contrast, indoor fine PM mass concentrations varied from 2.3 to 4.1 μg m^{-3} (Figure VI-2b) and were well-correlated to outdoor $PM_{2.5}$ values (R^2 = 0.73 and p-value < 0.010; Figure VI-2d) illustrating that outdoor sources primarily determined indoor fine PM concentrations in the storage room [290].

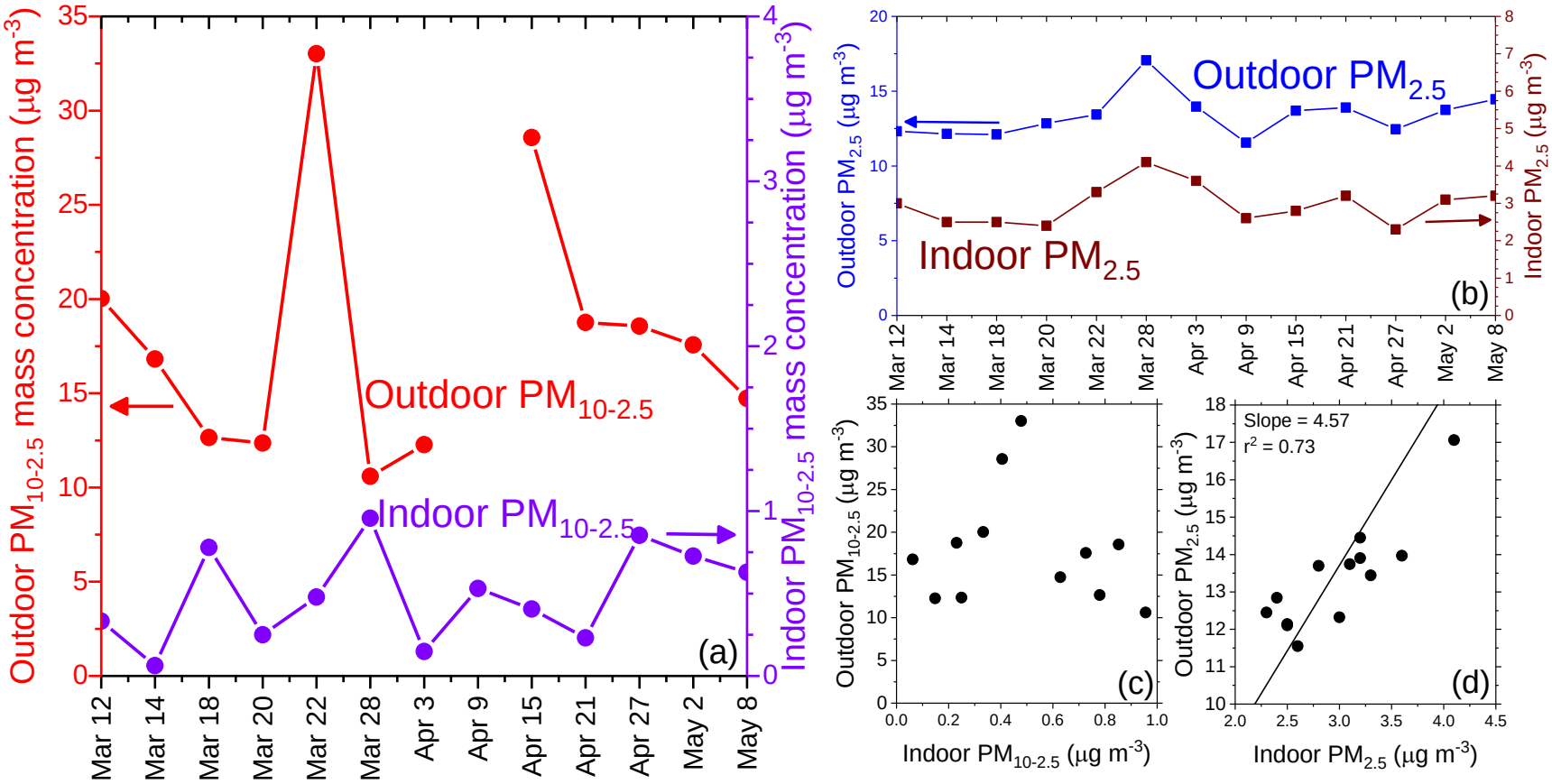

Figure VI-2. The left panel (a) and the top right panel (b) are time series of indoor and outdoor mass concentrations for coarse and fine PM, respectively. Note that one outdoor PM_{10} (April 6 – April 12) sample was lost during analysis. The bottom right panels (c and d) depict paired indoor/outdoor coarse PM and fine PM, respectively showing that indoor/outdoor $PM_{10-2.5}$ are uncorrelated but indoor $PM_{2.5}$ concentrations are correlated well with outdoor values.

Measured indoor coarse PM mass concentrations were significantly lower than several other studies in schools and domestic environments that reported $6.4 \leq PM10\text{-}2.5 \leq 73$ μg m-3 [282, 283, 287, 297-299], likely due to the low infiltration of outdoor air and our placement of the indoor sampler in an unoccupied room. Indoor coarse PM is often the result of activities such as cleaning and particle resuspension due to human occupation with limited contributions from cooking [300-304]. In places where such sources are present, coarse PM mass concentrations are typically much higher than fine PM [282, 300]. In occupied environments, indoor PM is typically dominated by indoor sources, especially when the outdoor PM concentration and the infiltration rate are relatively low [305-312].

Indoor coarse PM levels (0.49 ± 0.28 μg m-3) were 11-270 times lower than corresponding outdoor levels (18.0 ± 6.8 μg m-3) leading to an exceedingly low average I/O mass concentration ratio of only 0.033 ± 0.027. Measured PM levels were lower than previous reports [17, 272, 298, 305] and attributed to the site-specific factors detailed in methods section. While measurements in the classroom would better represent student exposure, the distraction and risks associated with running the sampling equipment in the occupied classrooms were deemed unacceptable by the collaboration partners. The samples collected in the storage room provide a means of comparison of outdoor and indoor measurements without the usual high peaks associated with close proximity to resuspension events from human activity [313, 314] and represent a lower bound contribution from the outdoor sources to the indoor concentrations measured inside the school.

Airborne Elemental Concentrations and their Potential Health Implications

Metals quantified herein were compared with 23 elements that have associated health standards and classified either as a hazardous air pollutant (HAP) or toxic air contaminant (TAC). Figure VI-3 illustrates comparisons between elemental concentrations and several health standards

similar to an earlier publication [315] as detailed in Appendix Table E2. These include the Texas Commission on Environmental Quality Long-Term Air Monitoring Comparison Value (TCEQ AMCV) [316], the Occupational Safety and Health Administration reference concentration for workplace exposure (OSHA 8 h) [317], the U.S. Environmental Protection Agency (USEPA) chronic noncancer reference concentration (EPA RfC) [318], the USEPA and Agency for Toxic Substances and Disease Registry RfCs for chronic exposure (EPA/ATSDR) [318], the cancer exposure level derived from the California Environmental Protection Agency (CalEPA) cancer unit risk estimate (CAL cancer) [315], the CalEPA non-cancer reference exposure levels (CAL Non-Cancer REL), and the CalEPA 8 hour reference exposure level (CAL 8 h) [319]. All cancer, RfC, and REL standards are for chronic long-term exposure (70 years), and the OSHA standards are for workday exposure for an expected fraction of a lifetime. Notably, the OSHA regulations are intended to protect adult workers of average health, and their allowable concentrations are therefore much higher than those set by other regulating entities. The standards of CalEPA are generally more strict than those of the U.S. EPA and represents a more cautious metric for assessing exposure to sensitive receptors, such as schools, hospitals, and day care facilities.

Indoor concentrations of cobalt exceeded the TCEQ AMCV, which are set to evaluate ambient air and the potential for specific chemicals to adversely impact human health or welfare. For this reason, this value is most directly applicable to outdoor air quality. However, it can be argued that, due to the increased amount of time a person spends indoors and the attenuation of the pollutants as the outdoor air moves indoors due to particle deposition and filtration, indoor air quality should be at least, if not more stringent than outdoor air quality. This increase in indoor cobalt concentrations needs to be evaluated further to determine how often it occurs so that associated risks and sources can be better established.

Of the targeted metals with relevant health standards, Cr might be the only one to potentially pose a hazard. It is emphasized that we only measured total Cr without speciation, whereas standards specifically address Cr(VI). However, since hexavalent chromium dominates airborne PM emissions from combustion and other high temperature processes, the Cr oxidation state in particulate matter is often assumed to be Cr(VI) [320, 321]. All measured concentrations exceeded the designated value [315] (6.67×10^{-2} ng m^{-3}) for cancer exposure standard, derived from the CalEPA unit risk estimate (1.5×10^{-2} μg m^{-3}). Cr(VI) is classified as a Class 1 carcinogenic element by the International Agency for Research on Cancer (IARC), and its exposure is correlated with cancer of the nose and sinuses [322]. Chromium is associated with road dust and may originate from nearby heavily trafficked roads and highways as shown in Figure VI-1 [140]. It might also have originated from the W.A. Parish Generating Station, which is the United States' second largest fossil fuel power plant located 55 km southwest of the school [323], transporting indoors through cracks in the building envelope or via the ventilation (HVAC) system. Chromium has also been linked to petroleum refining emissions [87]. It may also leach from stainless steel materials, such as those used in cooking processes at significantly high temperatures (e.g. from the school cafetaria), contributing to its presence indoors [324]. Other researchers have also implicated Cr exposure as a potential carcinogenic health risk in indoor environments via fine PM [315, 324-326] and even comprising the largest health risk of measured elements in some cases [287, 327, 328]. It is well understood that coarse PM is generally retained in the upper parts of the breathing system (nasopharynx) and, therefore, may pose lower risks to lung health and development than fine PM [287]. However, because Cr is often associated with cancers relating to the upper respiratory tract, its coarse fraction may pose significant cancer risks that have yet to be rigorously quantified.

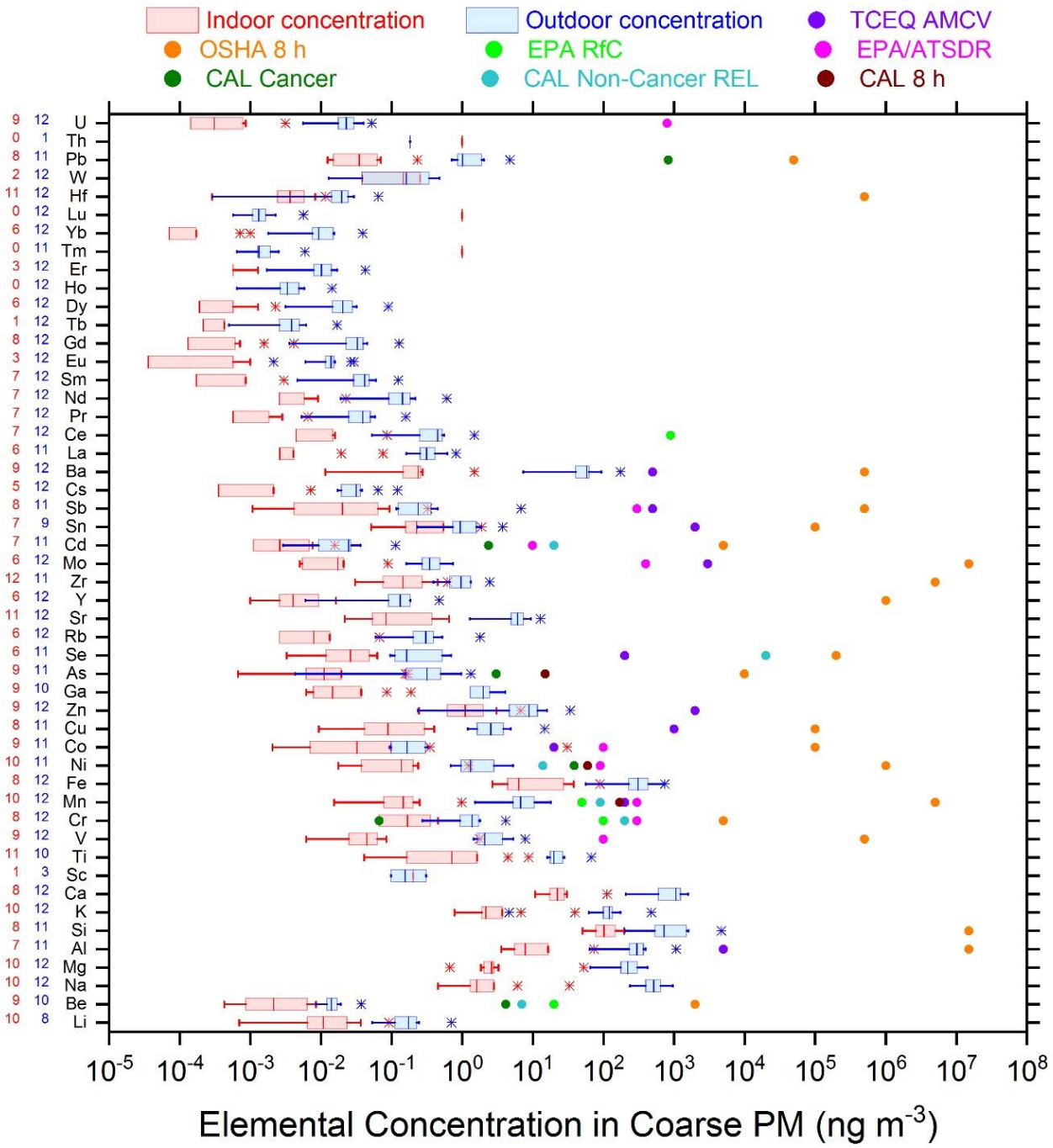

Figure VI-3. Coarse PM indoor and outdoor elemental concentrations compared to metal HAP/TAC health standards. The red and blue colored boxplots indicate indoor and outdoor air concentrations, respectively. The box covers the interquartile range, the median represented as a solid line within the box, and outliers are depicted as asterisks with this color code. The number of samples above detection limit are shown directly to the left of each element (blue color for outdoor and red color for indoor). The colored circles indicate associated regulatory or health-based standards designated by various governing bodies as denoted in the legend.

Airborne Elemental Abundances and Their Indoor/Outdoor Relationships

Mass abundances (μg element/g PM) for indoor and outdoor coarse PM elemental concentrations are shown in Figure VI-4 where the black line represents perfect equality (45° slope). Unsurprisingly, highest elemental abundances were measured for crustal and sea salt elements such as Na, Mg, Al, Si, Ca, Ti, Mn, and Fe both indoors and outdoors, suggesting outdoor origins of these elements. Note that Sc, Cs, Eu, Tb, Ho, Er, Tm, Lu, W, and Th were excluded in this analysis because they were not detected in nearly half (6 of out 13 or > 46%) of indoor samples. This may be attributed to the relatively low crustal abundances of odd numbered heavy lanthanoids, i.e. the Oddo-Harkin rule [329] and also in local anthropogenic sources such as fluid catalytic cracking, oil combustion, and automobiles [21, 86, 330]. Notably, a single sample (April 8 – 24, 2011) exhibited extremely elevated indoor abundances for 39 of the 50 metals with I/O elemental mass ratios $\left(= \frac{\left(\frac{ng\ element}{mg\ PM\ mass}\right)_{indoor}}{\left(\frac{ng\ element}{mg\ PM\ mass}\right)_{outdoor}} \right)$ ranging from a low of 2.0 for Cs and a high of 430 for Mo with an average of 52 ± 84. This included some metals (Sc, Cs, Eu, and Er) that were below the detection limit in over half (n=7) of the samples, demonstrating that this sample was a statistical outlier and was therefore excluded in subequent analysis. Conspicuously, outdoor PM10-2.5 during the same time period did not show any anomalies suggesting a unique indoor coarse PM source (e.g. disturbance of previously settled dust). More time resolved sampling (e.g. hourly) and sampling in an occupied classroom may be needed to determine the frequency, intensity, and identity of such indoor sources.

Figure VI-4a displays elements whose coarse and fine PM abundances were nearly identical indoors and outdoors. This was the case for all detected lanthanoids (with the exception of La), Al, K, Ca, V, Mn, Fe, Cu, Rb, Sr, Y, Mo, Cs, and U. All REEs were individually well-

correlated with each other in both indoor and outdoor coarse PM (indoor: $r = 0.97 \pm 0.020$; outdoor: $r = 0.98 \pm 0.020$) reflecting common sources. Additionally, the average I/O abundance ratios approach 1 (0.85 ± 0.44) for these elements. Hence, each of these elements most likely infiltrated across the building and/or transported indoors via the HVAC system from the outside and did not appear to have significant indoor sources.

Figure VI-4b summarizes elements with relatively high I/O abundance ratios (average 5.0 ± 2.4, ranging from a low of 2.1 for Pb and a high of 10.0 for Cr). Notable examples include Sn (6.1), Cr (10.), Zn (6.5), and Ni (2.7), suggesting potential indoor coarse PM sources of these metals such as resuspension of indoor dust that originated outside, construction materials, paint, and cleaning products [287, 300, 303, 309]. Only Co was remarkably more abundant indoors (average I/O ratio of 820 ± 2100), indicative of indoor sources such as paints or dyes [298]. Associated PM10-2.5 bearing these metals likely entered the sampling room through the HVAC system, penetrated the doorway, and/or was transported into the sampling area when occasionally someone entered the room.

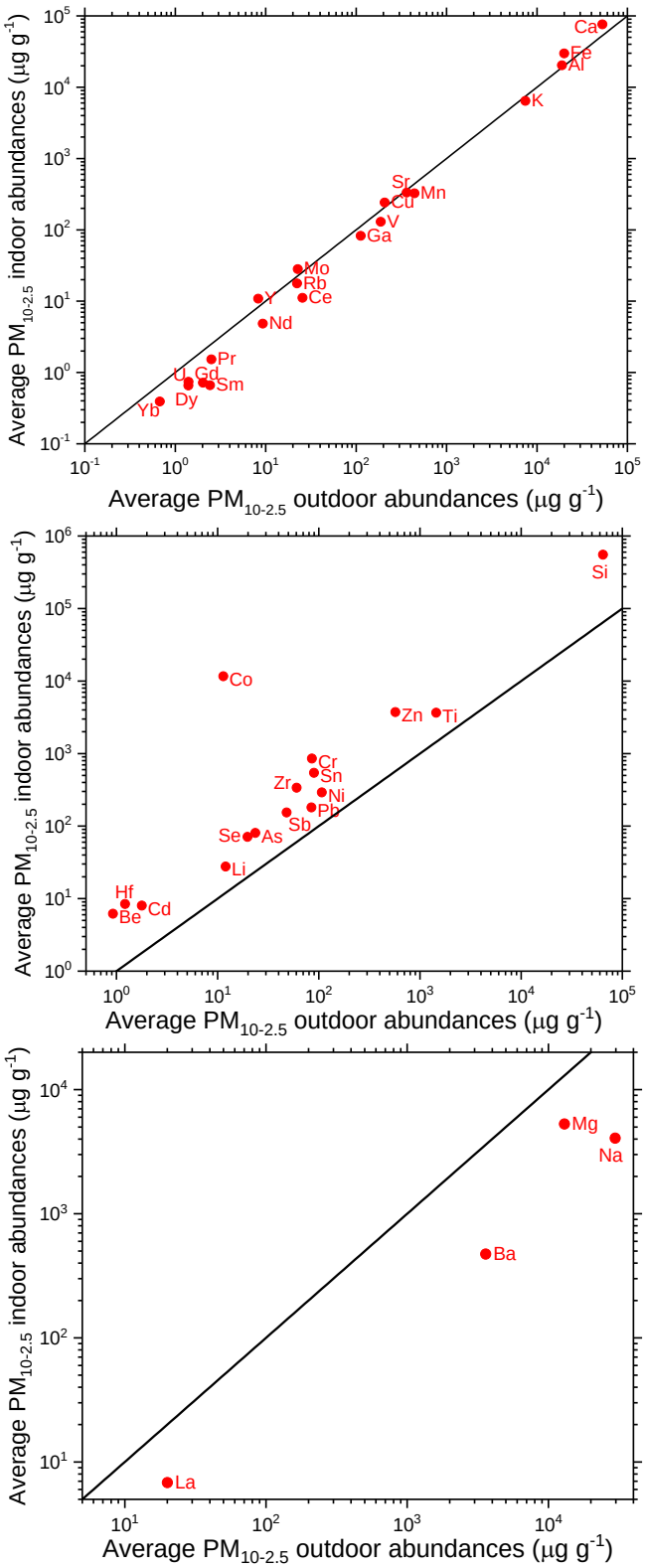

Figure VI-4. Comparison of average elemental abundances in indoor and outdoor coarse PM. The left panel shows near identical I/O abundances for 20 metals (Al, K, Ca, V, Mn, Fe,

Cu, Ga, Rb, Sr, Y, Mo, Ce, Pr, Nd, Sm, Gd, Dy, Yb, and U). The middle panel shows 16 elements (Li, Be, Si, Ti, Cr, Co, Ni, Zn, As, Se, Zr, Cd, Sn, Sb, Hf, and Pb) that are significantly elevated indoors. The right panel shows that Na, Mg, Ba, and La are significantly depleted indoors.

Na, Mg, Ba, and La in PM10-2.5 were significantly depleted indoors (Figure VI-4c), exhibiting average I/O abundances ratios < 1 (0.16 ± 0.090, 0.40 ± 0.29, 0.13 ± 0.17 and 0.34 ± 0.18, respectively).

Elemental Characteristics and Origins of Indoor PM

Since numerous indoor elements were strongly influenced by outdoor PM infiltrating through the building envelope and/or transporting across the HVAC system, clues to their potential outdoor sources were pursued. We focused on petroleum refining, oil combustion, motor vehicles, and crustal sources, which have been shown to be major PM influencers at this general location [21, 86, 140, 145] and seen in Figure VI-1. Fluctuations between periods influenced by refining operations and those dominated by crustal emissions were identified using REEs as markers, specifically targeting light lanthanoid ratios particularly La/Ce, enrichment factors (see SI Figures SI 17-20), and abundance sequences in fluidized-bed catalytic cracking (FCC) catalysts and local soil [86, 126, 145, 146, 232, 248]. Left hand side panels in Figure VI-5 (a and c) display correlations between rare earths in indoor and outdoor PM and FCC catalysts consistent with episodic FCC catalyst emissions. Analogously, right hand side panels on Figure VI-5 (b and d) represent routine or background indoor and outdoor samples where REEs in PM are primarily governed by natural crustal emissions. A complete catalog of the samples with their designation oscillating between these two sources are shown in SI-Figure 3 to SI-Figure 14 further validating our earlier results that the lanthanoid atmospheric chemistry in Houston is primarily controlled by petroleum refining and wind-blown dust.

Note that in Figure VI-5a and 5c, La > Ce in all cases (i.e. La/Ce > 1), like in FCC catalysts. Notably, all other light rare earth ratios, i.e. La/Pr, La/Nd, and La/Sm ratios also aligned closely with those of FCC catalysts and PM sampled during FCC unit emission events near this site [87, 140, 145, 290] (e.g. average La/Sm = 29, = 55 in FCC catalysts, and = 37 in outdoor PM during FCC emission events). Also, REE abundance sequences were identical to FCC catalysts (La>Ce>Nd>Pr>Gd>Sm>Dy) [145]. Additionally, REE concentrations were strongly correlated ($0.90 \leq r \leq 0.96$) with corresponding FCC catalysts' values in Figure VI-5a and 5c. Hence, it can be concluded that lanthanides on these six days (April 24-30) were largely derived from direct anthropogenic releases from petroleum refining operations, dominating their lanthanoid composition. Similar results were obtained for another sample (March 13-15).

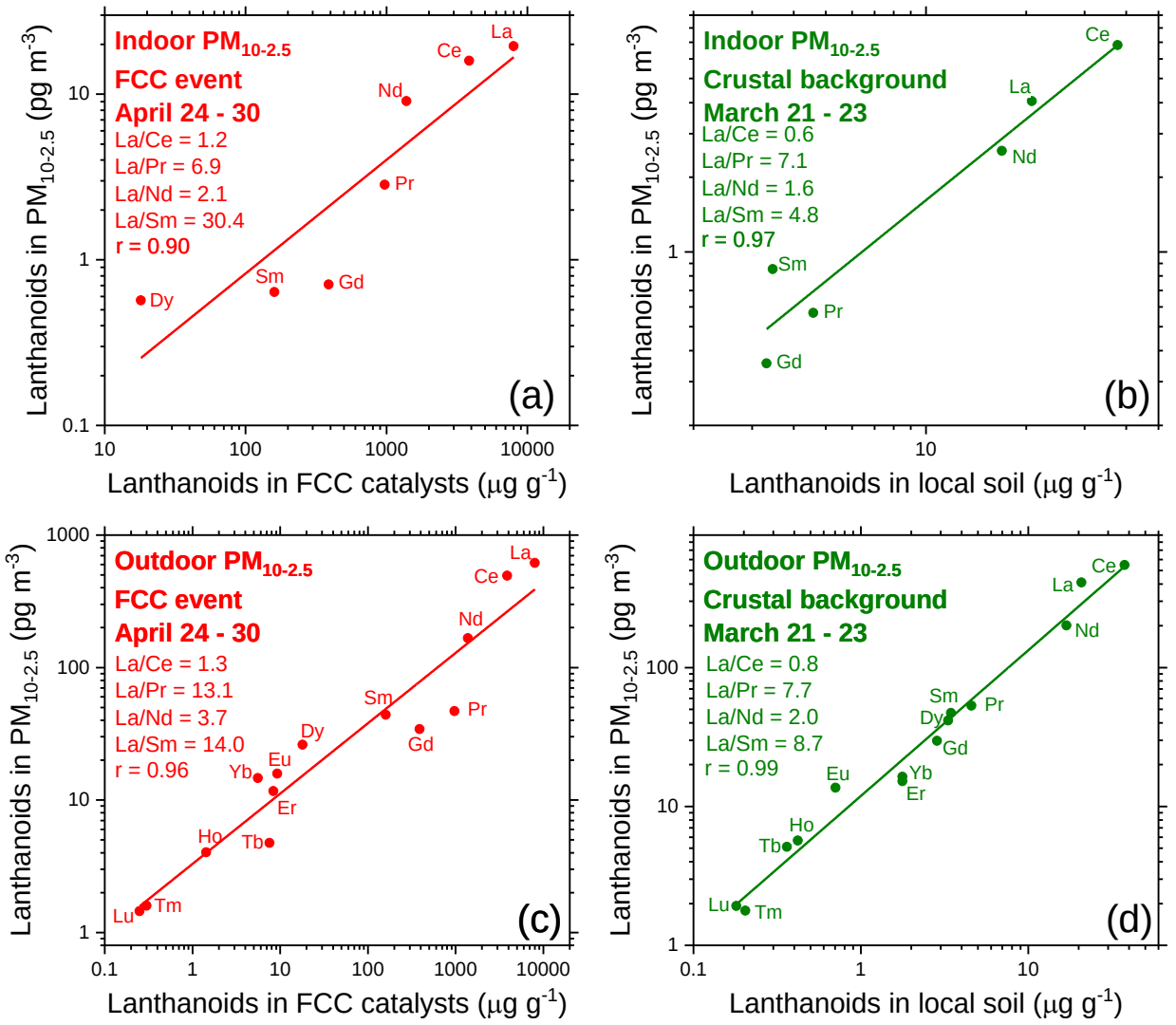

Figure VI-5. Rare earth correlations used to identify petroleum refining FCC emission events and windblown local soil dust. The top panels represent indoor coarse PM with heavy rare earths below detection limits in both cases. Bottom panels represent outdoor coarse PM with all 14 rare earths present above detection limits. The left panels (a and c) are for a representative sample (April 24-30) that is highly influenced by petroleum refining. The right panels (b and d) are for a representative sample (March 21-23) where REEs originated from crustal material.

As shown in Figure VI-5b and VI-5d, PM rare earth concentrations were strongly correlated ($0.97 \leq r \leq 0.99$) with corresponding values in local soil for the March 21-23 sample. Additionally, Ce > La (i.e. La/Ce < 1) like in the upper continental crust and local soil (and unlike in FCC catalysts). Notably, all light rare earth ratios, i.e. La/Ce, La/Pr, La/Nd, and La/Sm ratios

also aligned closely with those of soil and PM sampled when aerosols are dominated by natural sources in Houston (e.g. average La/Sm = 8.4 in Figure VI-5b and VI-5d, = 4.0 in local soil, = 6.6 in upper continental crust, and 7.3 during strong natural dust episodes [23, 329]). Further, the rare earth sequence was different than in FCC catalysts but idential to local soils, i.e. Ce>La>Nd>Pr>Sm>Gd [18]. Hence, ambient PM on these two days (March 21-23) was largely derived via routine wind-blown dust from local soil, rather than industrial activity. Using this approach, ten PM10-2.5 samples were inferred to be associated with natural processes that resuspend soil, also reinforcing the notion that the coarse fraction dominates crustal resuspension [324].

While Figure VI-5 depicts detailed information on single samples (see supporting information for others), the entire dataset is summarized in Figures 6 and 7 and Appendix Figure E16, E21, E22, and E23 displaying numerous elemental ratios, which provide additional clues to likely sources of ambient PM at this location. Because they are the only known potential contributors of lanthanides and vanadium, we focus on FCC catalysts [86, 87], crustal matter [18], motor vehicles [21], and oil combustion [52, 256, 331, 332].

Figure VI-6 employs La to light lanthanoid ratios (La/Ce, La/Sm, La/Nd, and La/Pr) to provide additional evidence for the role of petroleum refining in determining REE composition. Crustal-dominated PM appear on the lower left region (low La ratios) which migrated towards the top right corner (high La ratios) when petroleum refining dominated Houston's atmospheric rare earth chemistry. Similar results have been reported in Spain [52, 126, 248]. The extent of anomalies depends on proportion of anthropogenic REEs and FCC-impacted fine PM typically is influenced more than the coarse fraction [86, 145, 290]. In contrast, rare earths traced the majority of outdoor coarse PM (n = 10) to local soil confirming that windblown dust is typically larger in

size. Notably, coarse PM did not easily enter into the school, reducing the number of samples with detectable rare earth levels (only 1 during FCC event and 4 corresponding to crustal resuspension).

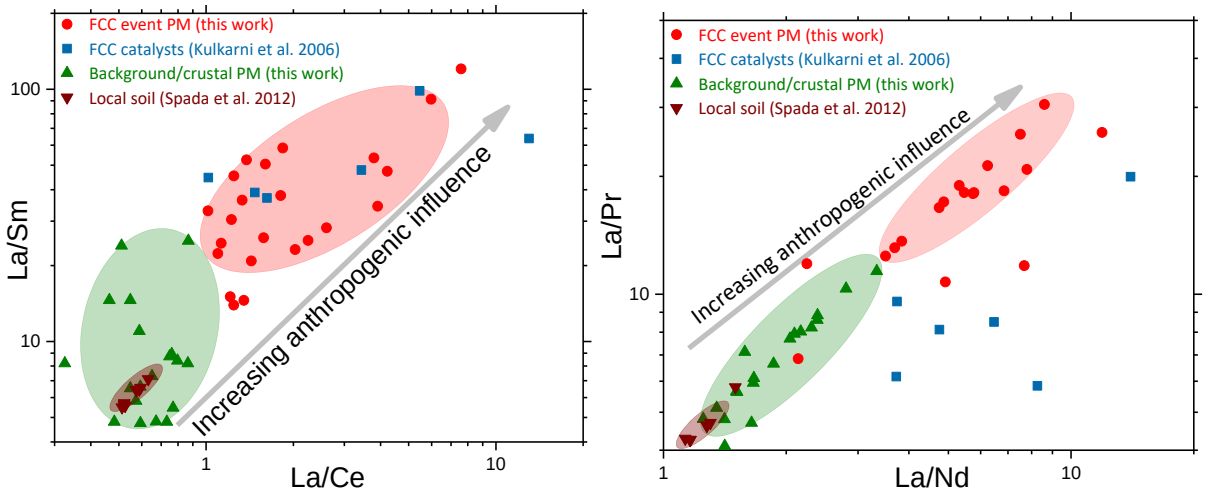

Figure VI-6. Light rare earth ratios to identify PM impacted by petroleum refining FCC emission events and windblown local soil dust. The left panel depicts La/Ce versus La/Sm whereas the right panel depicts La/Nd versus La/Pr. Fine and coarse and indoor and outdoor PM have not been separated to increase readability. PM in this study are superposed on measurements of local soil (Spada et al. 2012) and FCC catalysts (Kulkarni et al. 2006). Local soil and background PM plot on the lower left corner and overlap each other (green and maroon regions) denoting crustal dominance. Increasing ratios of La to other light REEs (red region) demonstrate stronger influence of primary emissions from petroleum refining.

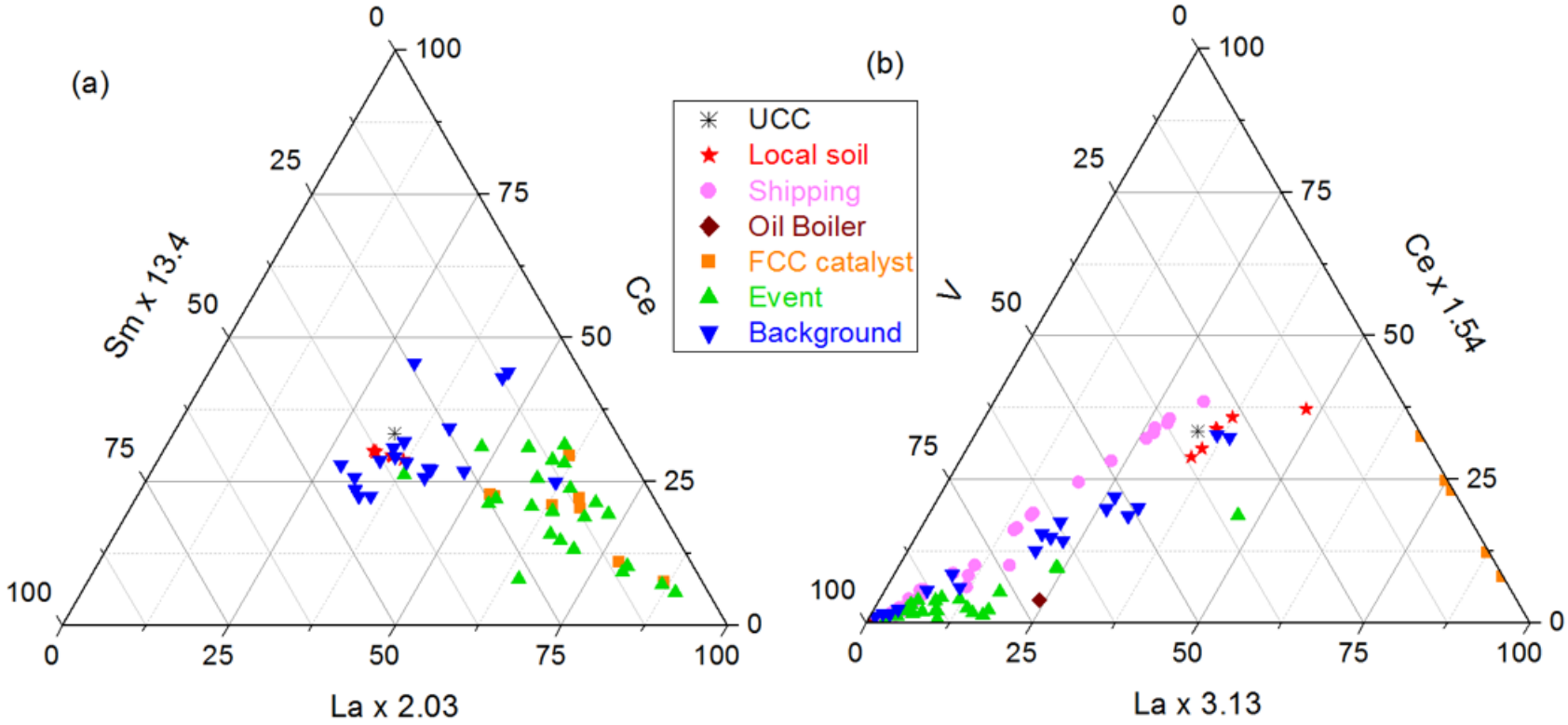

Figure VI-7. La-Ce-Sm (left panel, (a)) and La-Ce-V (right panel, (b)) ternary plots for indoor/outdoor PM and samples from various probable sources (crustal, shipping/oil combustion [52, 256, 331, 332], FCC catalysts [86, 87]) after normalization such that the upper continental crust (UCC) [329] appears at the centroid of the triangle. Note PM associated FCC events appear between the La-apex (bottom right corner) and the UCC centroid in the left panel denoting La enrichment relative to Ce and Sm. In contrast, PM during background days are generally scattered around the UCC centroid denoting predominant crustal origins. The same FCC event PM typically appear closer to the V-apex (bottom left corner) than the UCC centroid in the right panel denoting V enrichment associated with oil combustion. In contrast, the background samples span the entire distance between the V-apex and UCC centroid denoting oil combustion and local soil typically contribute to PM in Houston's air.

The influence of FCC episodic emissions was further interpreted using ternary diagrams by analyzing simultaneous La-Ce-Sm variations in Figure VI-7a after normalization such that the upper continental crust (UCC) appears at the centroid. In such a representation, deviation from the centroid signifies anthropogenic alterations to the relative REE composition. Predictably, the local soil appears in the close vicinity of the UCC centroid given similarities in its composition and the Earth's crust. Background samples (i.e. windblown dust) also mostly hovered around the centroid, denoting their similarities with local soil as discussed in SI Figures S3-S15 and Figure VI-6. Since FCC catalysts are highly enriched in La in relation to Ce and Sm, they migrated away from the centroid moving closer to the La apex unambiguously demonstrating their anthropogenic nature. Samples associated with FCC emission events positioned themselves between the La-apex and the UCC centroid and overlap on the catalysts. Their positioning implies that these three REEs in the Houston atmosphere originated predominantly from the mixing of petroleum refining and crustal-derived aerosols as demonstrated earlier [23, 29, 290].

Simultaneous La-Ce-V variations were also analyzed (Figure VI-7b) since shipping and oil combustion enormously enrich V making it a strong marker for such activities [87, 301, 305, 333] similar to La/V ratio depicted in Appendix Figure E23. Similar to Figure VI-7a, local soil clustered around the centroid due to its similar composition as the UCC. As expected, combustion sources positioned near the V-apex distinguishing them from FCC catalysts that continue to align near the La-apex. Ambient background PM followed a highly linear trend spanning the entire distance between the V-apex and and the UCC centroid signifying that V almost solely arose from the mixing of anthropogenic oil combustion, and natural crustal emissions [256, 332], regardless of refining operation. Further, aerosols collected during FCC events generally clustered near the V-apex, perhaps due to their simultaneous V-enrichment when catalysts are episodically released to

the local atmosphere [87]. Nevertheless, FCC operations are the primary contributor to La at this location [86, 145, 232].

Another important PM source at this location is motor vehicles, especially since 435,000 vehicles daily traverse major roadways surrounding the school on average, which was evaluated using Cu/Sb, Pb/Cu, Sb/Cd, and Mo/Cd ratios in Appendix Figure E22 [21, 52, 54]. Trace metal ratios for indoor/outdoor PM sampled in this study overlapped with FCC catalysts, PM in a proximal vehicular tunnel, and local soil (see Appendix Figure E22) suggesting ambient aerosols arose from a combination of industrial (refining), vehicular, and crustal sources similar to retirement communities in California [334].

Conclusions

It is emphasized that logistical constraints limited the number of samples, the collection of time-integrated samples, and sampler placement. More realistic estimates of children's exposure to PM would be obtained by collecting samples in a classroom rather than in a largely unoccupied room. Additional and more frequent (e.g. daily) samples will allow rigorous source apportionment. Nevertheless, our results lead to the following inferences that are relevant to understanding PM infiltration and/or ventilation in schools and childrens' PM exposure in this environment.

Indoor coarse PM concentrations in this study were relatively low ($\leq$ 1 μg m-3) demonstrating their low infiltration through the entire building envelope (since the windows and doors were kept closed), the outdoor air changes were relatively low, the HVAC system filters the air, and the samplers were isolated from the occupants. Several coarse PM elements approached an I/O mass abundance ratio of one (Al, K, Ca, V, Mn, Fe, Cu, Ga, Rb, Sr, Y, Mo, Ce, Pr, Nd, Sm, Gd, Dy, Yb, and U) demonstrating that corresponding indoor metal-bearing PM predominantly

infiltrated through the building envelope and/or ventilated via the HVAC system from the outside. Elevated I/O mass ratios for many other metals in coarse PM (Li, Be, Si, Ti, Cr, Ni, Zn, As, Se, Zr, Cd, Sn, Sb, Hf, and Pb) suggested their indoor sources. Cobalt was remarkably enriched indoors probably emitted from paints used in art classes. Co, Cu, Mo, Cd, Sb, and Pb were most enriched compared with their crustal abundances confirming their anthropogenic nature and influence of several outdoor sources. Furthermore, hazardous air metallic pollutants were measured inside the school, albiet at significantly lower concentrations than outdoors and not posing substantial human health risks with the sole exception of chromium.

CHAPTER VII

CONCLUSIONS AND RECOMMENDATIONS FOR FUTURE WORK

Conclusions

The analytical procedure developed using simple gravity flow techniques was highly effective in extracting purified cuts of Sr, Nd, and Hf with minimum loss (recovery >85%) that improved the accuracy and precision of measuring their isotope ratios. Moreover, the procedure was optimal for low mass samples (0.3 mg – 25 mg) of several environmental matrices relevant to primary urban PM. The Sr-Nd-Hf content amongst different mineral dust sources revealed contrasting isotopic ratios establishing them as strong tracers for differentiating various natural and anthropogenic sources rich in mineral material.

Sr-Nd-Hf isotope ratios in ambient Houston PM samples were sensitive to North African dust intrusion. Isotope mixing analysis with isotopic and elemental ratios revealed that primary end members of strontium, neodymium, and hafnium were concrete dust and soil, soil and motor vehicles, and motor vehicles and North African dust, respectively. Our novel mathematical model, IRCMB, demonstrated how isotope ratios can be combined with elemental concentration to reduce collinearity between mineral sources. Evaluating with a synthetic dataset, IRCMB was able to reduce error in the estimation of North Africa (~20%), local soil (~55%), concrete dust (~80%), and biomass burning (~25%), demonstrating the superiority of using isotopes over elemental signatures for mineral dust apportionment. In addition, accuracy in estimation of biomass burning was shown to improve by ~24%, which was attributed to the more robust isolation of mineral potassium with isotopes. Importantly, it was able to differentiate local mineral sources from North

African dust, which was not achieved with traditional CMB methods in the majority of our samples.

Elemental ratios and enrichment factors confirmed that PGEs were exclusively originating from light-duty vehicles. Consequently, chemical mass balance modeling with PGEs was able to accurately quantify contributions from tailpipe and non-tailpipe motor vehicle emissions. In the investigation at a near highway location in Houston, CMB estimated that vehicles contributed 37% on average (12–67%) to PM_{10} and 49% on average (25–73%) to $PM_{2.5}$. Importantly, correlation analysis provided evidence for a subset of other trace metals; i.e. Cu, As, Mo, Cd, and Sb to also be relatively strong LDV tracers.

Analyzing trace metals along with aerosol and meteorological products (NAAPS, HYPLIT, fire maps, and satellite imagery) helped us identify multiple instances of PM intrusion from large-scale regional biomass burning and long-range desert dust. The impacts of these dust outbreaks on lanthanum, vanadium, and potassium concentrations demonstrates the necessity to isolate the mineral component of these tracers to effectively use them to track anthropogenic sources. The impacts of these "exceptional events that are not reasonably controllable or preventable" on compliance with PM regulations designed to protect human health demonstrates the need to precisely quantify distal sources.

Finally, fingerprinting indoor PM with trace metal markers shows evidence of PM from outdoor sources, namely vehicular PM, FCC, oil combustion, and soil, that infiltrated indoors. Importantly, indoor/outdoor ratios of Li, Be, Si, Ti, Cr, Co, Ni, Zn, As, Se, Zr, Cd, Sn, Sb, Hf, and Pb imply their potential indoor sources. Cr was found to exceed indoor air quality standards posing potential health hazards.

Although, the measurements were made targeting Houston, Texas as a representative industrial/urban metroplex, the novel methods and techniques developed for this dissertation can be applied to other parts of the world that experience aerosol burden from deserts in Africa, Asia, Australia, South America, South Africa, and others [33] without loss of generality.

Recommendations for future work

Based on the results of this research, the following ideas can be pursued in the future:

With the availability of superior faraday cup amplifiers for MC-ICP-MS (~100 time more sensitivity than this study), future studies could focus on analyzing low abundance elements, e.g. Hf, in PM samples. Of relevance to this dissertation, reducing the uncertainty in $^{176}Hf/^{177}Hf$ is expected to further enhance the isolation of long-range transported mineral dust. Moreover, the current literature is limited to a few major urban samples, therefore more extensive study on the potential sources of Sr-Nd-Hf, such as steel plant and coal combustion, is required.

More advanced methods (such as high-pressure flow system and multi-layered resin columns) for chromatographic separation of Sr-Nd-Hf from urban PM, need to be explored to reduce the sample preparation time. The methodology developed in this study may take 3 – 4 days to complete before samples can be analyzed with MC-ICP-MS., therefore limiting the capacity of a laboratory to process a large number of samples.

Due to the large-scale effect of distal sources, it may benefit to analyze the spatio-temporal variations of respective tracers, focusing on both upstream and downstream of PM transport directions.

REFERENCES

[1] J.L. Hand, T.E. Gill, and B.A. Schichtel, Urban and rural coarse aerosol mass across the United States: Spatial and seasonal variability and long-term trends, Atmospheric Environment 218 (2019) 117025.

[2] D.W. Sullivan, J.H. Price, B. Lambeth, K.A. Sheedy, K. Savanich, and R.J. Tropp, Field study and source attribution for $PM_{2.5}$ and PM_{10} with resulting reduction in concentrations in the neighborhood north of the Houston Ship Channel based on voluntary efforts, Journal of the Air & Waste Management Association 63(9) (2013) 1070-1082.

[3] M.A. Venecek, X. Yu, and M.J. Kleeman, Predicted ultrafine particulate matter source contribution across the continental United States during summertime air pollution events, Atmospheric Chemistry and Physics 19(14) (2019) 9399-9412.

[4] D.P. Croft, W.J. Zhang, S. Lin, S.W. Thurston, P.K. Hopke, E. van Wijngaarden, S. Squizzato, M. Masiol, M.J. Utell, and D.Q. Rich, Associations between source-specific particulate matter and respiratory infections in New York State adults, Environmental Science & Technology 54(2) (2020) 975-984.

[5] S.A. Morman and G.S. Plumlee, Dust and human health, in: P. Knippertz, J.-B.W. Stuut (Eds.), Mineral dust: A key player in the earth system, Springer Netherlands, Dordrecht, 2014, pp. 385-409.

[6] T.A. Cahill, D.E. Barnes, N.J. Spada, J.A. Lawton, and T.M. Cahill, Very fine and ultrafine metals and ischemic heart disease in the California Central Valley 1: 2003-2007, Aerosol Science and Technology 45(9) (2011) 1123-1134.

[7] S.H. Gavett, N. Haykal-Coates, L.B. Copeland, J. Heinrich, and M.I. Gilmour, Metal composition of ambient $PM_{2.5}$ influences severity of allergic airways disease in mice, Environmental Health Perspectives 111(12) (2003) 1471-1477.

[8] EPA to reexamine health standards for harmful soot that previous administration left unchanged. https://www.epa.gov/newsreleases/epa-reexamine-health-standards-harmful-soot-previous-administration-left-unchanged. (Accessed 12 February 2022).

[9] I.M. Al-Naiema, A.P.S. Hettiyadura, H.W. Wallace, N.P. Sanchez, C.J. Madler, B.K. Cevik, A.A.T. Bui, J. Kettler, R.J. Griffin, and E.A. Stone, Source apportionment of fine particulate matter in Houston, Texas: insights to secondary organic aerosols, Atmospheric Chemistry and Physics 18(21) (2018) 15601-15622.

[10] U. Nopmongcol, W. Khamwichit, M.P. Fraser, and D.T. Allen, Estimates of heterogeneous formation of secondary organic aerosol during a wood smoke episode in Houston, Texas, Atmospheric Environment 41(14) (2007) 3057-3070.

[11] L. Pererz, M. Medina-Ramon, N. Kunzli, A. Alastuey, J. Pey, N. Perez, R. Garcia, A. Tobias, X. Querol, and J. Sunyer, Size fractionate particulate matter, vehicle traffic, and case-specific daily mortality in Barcelona, Spain, Environmental Science & Technology 43(13) (2009) 4707-4714.

[12] I. Kheirbek, J. Haney, S. Douglas, K. Ito, and T. Matte, The contribution of motor vehicle emissions to ambient fine particulate matter public health impacts in New York City: a health burden assessment, Environmental Health 15(1) (2016) 89.

[13] D. Brugge, K. Lane, L.T. Padró-Martínez, A. Stewart, K. Hoesterey, D. Weiss, D.D. Wang, J.I. Levy, A.P. Patton, W. Zamore, and M. Mwamburi, Highway proximity associated with cardiovascular disease risk: the influence of individual-level confounders and exposure misclassification, Environmental Health 12(1) (2013) 84.

[14] A.P. Grieshop, E.M. Lipsky, N.J. Pekney, S. Takahama, and A.L. Robinson, Fine particle emission factors from vehicles in a highway tunnel: Effects of fleet composition and season, Atmospheric Environment 40 (2006) S287-S298.

[15] L.Y. He, M. Hu, Y.H. Zhang, X.F. Huang, and T.T. Yao, Fine particle emissions from on-road vehicles in the Zhujiang Tunnel, China, Environmental Science & Technology 42(12) (2008) 4461-4466.

[16] F. Amato, A. Alastuey, A. Karanasiou, F. Lucarelli, S. Nava, G. Calzolai, M. Severi, S. Becagli, V.L. Gianelle, C. Colombi, C. Alves, D. Custodio, T. Nunes, M. Cerqueira, C. Pio, K. Eleftheriadis, E. Diapouli, C. Reche, M.C. Minguillon, M.I. Manousakas, T. Maggos, S. Vratolis, R.M. Harrison, and X. Querol, AIRUSE-LIFE plus : A harmonized PM speciation and source apportionment in five southern european cities, Atmospheric Chemistry and Physics 16(5) (2016) 3289-3309.

[17] F. Amato, I. Rivas, M. Viana, T. Moreno, L. Bouso, C. Reche, M. Àlvarez-Pedrerol, A. Alastuey, J. Sunyer, and X. Querol, Sources of indoor and outdoor $PM_{2.5}$ concentrations in primary schools, Science of The Total Environment 490 (2014) 757-765.

[18] N. Spada, A. Bozlaker, and S. Chellam, Multi-elemental characterization of tunnel and road dusts in Houston, Texas using dynamic reaction cell-quadrupole-inductively coupled plasma–mass spectrometry: evidence for the release of Platinum group and anthropogenic metals from motor vehicles, Analytica Chimica Acta 735 (2012) 1-8.

[19] A.M. Dillner, J.J. Schauer, W.F. Christensen, and G.R. Cass, A quantitative method for clustering size distributions of elements., Atmospheric Environment 39(8) (2005) 1525-1537.

[20] A. Reff, P.V. Bhave, H. Simon, T.G. Pace, G.A. Pouliot, J.D. Mobley, and M. Houyoux, Emissions inventory of $PM_{2.5}$ trace elements across the United States, Environmental Science & Technology 43(15) (2009) 5790-5796.

[21] A. Bozlaker, N.J. Spada, M.P. Fraser, and S. Chellam, Elemental characterization of $PM_{2.5}$ and PM_{10} emitted from light duty vehicles in the Washburn tunnel of Houston, Texas: Release of rhodium, palladium, and platinum, Environmental Science & Technology 48(1) (2014) 54-62.

[22] F. Zereini and C. Wiseman, Platinum metals in the environment, Springer Berlin Heidelberg2015.

[23] A. Bozlaker, J.M. Prospero, J. Price, and S. Chellam, Identifying and quantifying the impacts of advected North African dust on the concentration and composition of airborne fine particulate matter in Houston and Galveston, Texas, Journal of Geophysical Research: Atmospheres 124(22) (2019) 12282-12300.

[24] K.D. Perry, T.A. Cahill, R.A. Eldred, D.D. Dutcher, and T.E. Gill, Long-range transport of North African dust to the eastern United States, Journal of Geophysical Research: Atmospheres 102(D10) (1997) 11225-11238.

[25] A.M. Aldhaif, D.H. Lopez, H. Dadashazar, and A. Sorooshian, Sources, frequency, and chemical nature of dust events impacting the United States East Coast, Atmospheric Environment 231 (2020) 117456.

[26] X. Querol, J. Pey, M. Pandolfi, A. Alastuey, M. Cusack, N. Perez, T. Moreno, M. Viana, N. Mihalopoulos, G. Kallos, and S. Kleanthous, African dust contributions to mean ambient PM10 mass-levels across the Mediterranean Basin, Atmospheric Environment 43(28) (2009) 4266-4277.

[27] X. Querol, N. Perez, C. Reche, M. Ealo, A. Ripoll, J. Tur, M. Pandolfi, J. Pey, P. Salvador, T. Moreno, and A. Alastuey, African dust and air quality over Spain: Is it only dust that matters?, Science of The Total Environment 686 (2019) 737-752.

[28] N. Dewan, B.J. Majestic, M.E. Ketterer, J.P. Miller-Schulze, M.M. Shafer, J.J. Schauer, P.A. Solomon, M. Artamonova, B.B. Chen, S.A. Imashev, and G.R. Carmichael, Stable isotopes of lead and strontium as tracers of sources of airborne particulate matter in Kyrgyzstan, Atmospheric Environment 120(Supplement C) (2015) 438-446.

[29] A. Bozlaker, J.M. Prospero, M.P. Fraser, and S. Chellam, Quantifying the contribution of long-range Saharan Dust transport on particulate matter concentrations in Houston, Texas, using detailed elemental analysis, Environmental Science & Technology 47(18) (2013) 10179-10187.

[30] S.-C. Wang, Y. Wang, M. Estes, R. Lei, R. Talbot, L. Zhu, and P. Hou, Transport of Central American fire emissions to the U.S. Gulf coast: Climatological pathways and impacts on

ozone and $PM_{2.5}$, Journal of Geophysical Research: Atmospheres 123(15) (2018) 8344-8361.

[31] D.A. Westenbarger and G.A. Morris, Identifying biomass burning impacts on air quality in Southeast Texas 26–29 August 2011 using satellites, models and surface data, Atmospheric Chemistry and Physics Discussion 2018 (2018) 1-21.

[32] J.L. Hand, T.E. Gill, and B.A. Schichtel, Spatial and seasonal variability in fine mineral dust and coarse aerosol mass at remote sites across the United States, Journal of Geophysical Research: Atmospheres 122(5) (2017) 3080-3097.

[33] N. Huneeus, M. Schulz, Y. Balkanski, J. Griesfeller, J. Prospero, S. Kinne, S. Bauer, O. Boucher, M. Chin, F. Dentener, T. Diehl, R. Easter, D. Fillmore, S. Ghan, P. Ginoux, A. Grini, L. Horowitz, D. Koch, M.C. Krol, W. Landing, X. Liu, N. Mahowald, R. Miller, J.J. Morcrette, G. Myhre, J. Penner, J. Perlwitz, P. Stier, T. Takemura, and C.S. Zender, Global dust model intercomparison in AeroCom phase I, Atmospheric Chemistry and Physics 11(15) (2011) 7781-7816.

[34] J.M. Prospero, F.-X. Collard, J. Molinié, and A. Jeannot, Characterizing the annual cycle of African dust transport to the Caribbean basin and South America and its impact on the environment and air quality, Global Biogeochemical Cycles 28(7) (2014) 757-773.

[35] X. Querol, A. Tobías, N. Pérez, A. Karanasiou, F. Amato, M. Stafoggia, C. Pérez García-Pando, P. Ginoux, F. Forastiere, S. Gumy, P. Mudu, and A. Alastuey, Monitoring the impact of desert dust outbreaks for air quality for health studies, Environment International 130 (2019) 104867.

[36] S. Mallone, M. Stafoggia, A. Faustini, G.P. Gobbi, A. Marconi, and F. Forastiere, Saharan dust and associations between particulate matter and daily mortality in Rome, Italy, Environmental Health Perspectives 119(10) (2011) 1409-1414.

[37] S. Heft-Neal, J. Burney, E. Bendavid, K.K. Voss, and M. Burke, Dust pollution from the Sahara and African infant mortality, Nature Sustainability 3(10) (2020) 863-871.

[38] J.M. Prospero, A.C. Delany, A.C. Delany, and T.N. Carlson, The discovery of African dust transport to the western hemisphere and the Saharan air layer: A history, Bulletin of the American Meteorological Society 102(6) (2021) E1239-E1260.

[39] G.L. Shi, Y.C. Feng, F. Zeng, X. Li, Y.F. Zhang, Y.Q. Wang, and T. Zhu, Use of a nonnegative constrained principal component regression chemical mass balance model to study the contributions of nearly collinear sources, Environmental Science & Technology 43(23) (2009) 8867-8873.

[40] M. Viana, P. Salvador, B. Artinano, X. Querol, A. Alastuey, J. Pey, A.J. Latz, M. Cabanas, T. Moreno, S.G. Dos Santos, M.D. Herce, P.D. Hernandez, D.R. Garcia, and R. Fernandez-

Patier, Assessing the performance of methods to detect and quantify African dust in airborne particulates, Environmental Science & Technology 44(23) (2010) 8814–8820.

[41] M.M. Scerri, K. Kandler, and S. Weinbruch, Disentangling the contribution of Saharan dust and marine aerosol to PM_{10} levels in the Central Mediterranean, Atmospheric Environment 147 (2016) 395-408.

[42] L.S. Zhao, G.R. Hu, Y. Yan, R.L. Yu, J.Y. Cui, X.M. Wang, and Y. Yan, Source apportionment of heavy metals in urban road dust in a continental city of eastern China: Using Pb and Sr isotopes combined with multivariate statistical analysis, Atmospheric Environment 201 (2019) 201-211.

[43] S. Kanayama, S. Yabuki, F. Yanagisawa, and R. Motoyama, The chemical and strontium isotope composition of atmospheric aerosols over Japan: the contribution of long-range-transported Asian dust (Kosa), Atmospheric Environment 36(33) (2002) 5159-5175.

[44] Y. Yan, Q. Zheng, R.L. Yu, G.R. Hu, H.B. Huang, C.Q. Lin, J.Y. Cui, and Y. Yan, Characteristics and provenance implications of rare earth elements and Sr-Nd isotopes in $PM_{2.5}$ aerosols and $PM_{2.5}$ fugitive dusts from an inland city of southeastern China, Atmospheric Environment 220 (2020) 117069.

[45] M.L. Geagea, P. Stille, F. Gauthier-Lafaye, and M. Millet, Tracing of industrial aerosol sources in an urban environment using Pb, Sr, and Nd isotopes, Environmental Science & Technology 42(3) (2008) 692-698.

[46] A. Kumar, W. Abouchami, S.J.G. Galer, V.H. Garrison, E. Williams, and M.O. Andreae, A radiogenic isotope tracer study of transatlantic dust transport from Africa to the Caribbean, Atmospheric Environment 82 (2014) 130-143.

[47] J. Yu, C. Yan, Y. Liu, X. Li, T. Zhou, and M. Zheng, Potassium: A tracer for biomass burning in Beijing?, Aerosol and Air Quality Research 18(9) (2018) 2447-2459.

[48] J.E. Pachon, R.J. Weber, X. Zhang, J.A. Mulholland, and A.G. Russell, Revising the use of potassium (K) in the source apportionment of $PM_{2.5}$, Atmospheric Pollution Research 4(1) (2013) 14-21.

[49] C.A. Pio, M. Legrand, C.A. Alves, T. Oliveira, J. Afonso, A. Caseiro, H. Puxbaum, A. Sanchez-Ochoa, and A. Gelencsér, Chemical composition of atmospheric aerosols during the 2003 summer intense forest fire period, Atmospheric Environment 42(32) (2008) 7530-7543.

[50] C.W. Lewis, G.A. Norris, T.L. Conner, and R.C. Henry, Source Apportionment of Phoenix $PM_{2.5}$ Aerosol with the Unmix Receptor Model, Journal of the Air & Waste Management Association 53(3) (2003) 325-338.

[51] S. Das, B.V. Miller, J. Prospero, and S. Chellam, Sr-Nd-Hf isotopic analysis of reference materials and natural and anthropogenic particulate matter sources: Implications for

accurately tracing North African dust in complex urban atmospheres, Talanta 241 (2022) 123236.

[52] T. Moreno, X. Querol, A. Alastuey, J. de la Rosa, A.M. Sánchez de la Campa, M. Minguillón, M. Pandolfi, Y. González-Castanedo, E. Monfort, and W. Gibbons, Variations in vanadium, nickel and lanthanoid element concentrations in urban air, Science of The Total Environment 408(20) (2010) 4569-4579.

[53] A. Alastuey, X. Querol, W. Aas, F. Lucarelli, N. Perez, T. Moreno, F. Cavalli, H. Areskoug, V. Balan, M. Catrambone, D. Ceburnis, J.C. Cerro, S. Conil, L. Gevorgyan, C. Hueglin, K. Imre, J.L. Jaffrezo, S.R. Leeson, N. Mihalopoulos, M. Mitosinkova, C.D. O'Dowd, J. Pey, J.P. Putaud, V. Riffault, A. Ripoll, J. Sciare, K. Sellegri, G. Spindler, and K.E. Yttri, Geochemistry of PM_{10} over Europe during the EMEP intensive measurement periods in summer 2012 and winter 2013, Atmospheric Chemistry and Physics 16(10) (2016) 6107-6129.

[54] S. Das and S. Chellam, Estimating light-duty vehicles' contributions to ambient $PM_{2.5}$ and PM_{10} at a near-highway urban elementary school via elemental characterization emphasizing Rhodium, Palladium, and Platinum, Science of The Total Environment 747 (2020) 141268.

[55] K. Williamson, S. Das, A.R. Ferro, and S. Chellam, Elemental composition of indoor and outdoor coarse particulate matter at an inner-city high school, Atmospheric Environment 261 (2021) 118559.

[56] S. Nowak, S. Lafon, S. Caquineau, E. Journet, and B. Laurent, Quantitative study of the mineralogical composition of mineral dust aerosols by X-ray diffraction, Talanta 186 (2018) 133-139.

[57] M.M.G. Perron, M. Strzelec, M. Gault-Ringold, B.C. Proemse, P.W. Boyd, and A.R. Bowie, Assessment of leaching protocols to determine the solubility of trace metals in aerosols, Talanta 208 (2020) 120377.

[58] R.E. Hester, R.M. Harrison, and X. Querol, Airborne particulate matter: Sources, atmospheric processes and health, first ed., Royal Society of Chemistry, Cambridge, 2016.

[59] M. Escudero, X. Querol, J. Pey, A. Alastuey, N. Perez, F. Ferreira, S. Alonso, S. Rodriguez, and E. Cuevas, A methodology for the quantification of the net African dust load in air quality monitoring networks, Atmospheric Environment 41(26) (2007) 5516-5524.

[60] P.S. Fedotov, M.S. Ermolin, V.K. Karandashev, and D.V. Ladonin, Characterization of size, morphology and elemental composition of nano-, submicron, and micron particles of street dust separated using field-flow fractionation in a rotating coiled column, Talanta 130 (2014) 1-7.

[61] A. Vanderstraeten, S. Bonneville, S. Gili, J. de Jong, W. Debouge, P. Claeys, and N. Mattielli, First multi-isotopic (Pb-Nd-Sr-Zn-Cu-Fe) characterisation of dust reference materials (ATD and BCR-723): A multi-column chromatographic method optimised to trace mineral and anthropogenic dust sources, Geostandards and Geoanalytical Research 44(2) (2020) 307-329.

[62] C.E. Souto-Oliveira, M. Babinski, D.F. Araújo, D.J. Weiss, and I.R. Ruiz, Multi-isotope approach of Pb, Cu and Zn in urban aerosols and anthropogenic sources improves tracing of the atmospheric pollutant sources in megacities, Atmospheric Environment 198 (2019) 427-437.

[63] S. Dong, R. Ochoa Gonzalez, R.M. Harrison, D. Green, R. North, G. Fowler, and D. Weiss, Isotopic signatures suggest important contributions from recycled gasoline, road dust and non-exhaust traffic sources for copper, zinc and lead in PM_{10} in London, United Kingdom, Atmospheric Environment 165 (2017) 88-98.

[64] S. Dong, D.J. Weiss, S. Strekopytov, K. Kreissig, Y. Sun, A.R. Baker, and P. Formenti, Stable isotope ratio measurements of Cu and Zn in mineral dust (bulk and size fractions) from the Taklimakan Desert and the Sahel and in aerosols from the eastern tropical North Atlantic Ocean, Talanta 114(Supplement C) (2013) 103-109.

[65] G. Le Roux, N. Fagel, F. De Vleeschouwer, M. Krachler, V. Debaille, P. Stille, N. Mattielli, W.O. van der Knaap, J.F.N. van Leeuwen, and W. Shotyk, Volcano- and climate-driven changes in atmospheric dust sources and fluxes since the Late Glacial in Central Europe, Geology 40(4) (2012) 335-338.

[66] T. Wei, J. Brahney, Z. Dong, S. Kang, C. Zong, J. Guo, L. Yang, and X. Qin, Hf–Nd–Sr isotopic composition of the Tibetan Plateau dust as a fingerprint for regional to hemispherical transport, Environmental Science & Technology (2021) 10121–10132.

[67] S.M. Aarons, S.M. Aciego, and J.D. Gleason, Variable Hf-Sr-Nd radiogenic isotopic compositions in a Saharan dust storm over the Atlantic: Implications for dust flux to oceans, ice sheets and the terrestrial biosphere, Chemical Geology 349-350 (2013) 18-26.

[68] M. Van der Does, A. Pourmand, A. Sharifi, and J.-B.W. Stuut, North African mineral dust across the tropical Atlantic Ocean: Insights from dust particle size, radiogenic Sr-Nd-Hf isotopes and rare earth elements (REE), Aeolian Research 33 (2018) 106-116.

[69] A. Pourmand, J.M. Prospero, and A. Sharifi, Geochemical fingerprinting of trans-Atlantic African dust based on radiogenic Sr-Nd-Hf isotopes and rare earth element anomalies, Geology 42(8) (2014) 675-678.

[70] F.E. Grousset and P.E. Biscaye, Tracing dust sources and transport patterns using Sr, Nd and Pb isotopes, Chemical Geology 222(3) (2005) 149-167.

[71] W. Abouchami, K. Nathe, A. Kumar, S.J.G. Galer, K.P. Jochum, E. Williams, A.M.C. Horbe, J.W.C. Rosa, W. Balsam, D. Adams, K. Mezger, and M.O. Andreae, Geochemical and isotopic characterization of the Bodele Depression dust source and implications for transatlantic dust transport to the Amazon Basin, Earth and Planetary Science Letters 380 (2013) 112-123.

[72] W. Zhao, W. Balsam, E. Williams, X. Long, and J. Ji, Sr–Nd–Hf isotopic fingerprinting of transatlantic dust derived from North Africa, Earth and Planetary Science Letters 486 (2018) 23-31.

[73] B. Delmonte, J.R. Petit, K.K. Andersen, I. Basile-Doelsch, V. Maggi, and V. Ya Lipenkov, Dust size evidence for opposite regional atmospheric circulation changes over east Antarctica during the last climatic transition, Climate Dynamics 23(3) (2004) 427-438.

[74] A. Bozlaker, J.M. Prospero, J. Price, and S. Chellam, Linking Barbados mineral dust aerosols to North African sources using elemental composition and radiogenic Sr, Nd, and Pb Isotope signatures, Journal of Geophysical Research: Atmospheres 123(2) (2018) 1384-1400.

[75] S.M. Aarons, M.A. Blakowski, S.M. Aciego, E.I. Stevenson, K.W.W. Sims, S.R. Scott, and C. Aarons, Geochemical characterization of critical dust source regions in the American West, Geochimica Et Cosmochimica Acta 215 (2017) 141-161.

[76] Z. Dong, Y. Shao, D. Qin, S. Kang, T. Wei, X. Wang, and S. Wang, Hf-Nd-Sr isotopic composition as fingerprint for long-range transported eolian dust deposition in glacier snowpack of eastern Tibetan plateau, Journal of Geophysical Research: Atmospheres 123(13) (2018) 7013-7023.

[77] G. Újvári, W. Wegner, U. Klötzli, M. Horschinegg, and D. Hippler, Sr-Nd-Hf isotopic analysis of <10 mg dust samples: implications for ice core dust source fingerprinting, Geochemistry, Geophysics, Geosystems 19(1) (2018) 60-72.

[78] E.J. dos Santos Souza, C. Zapata Mora, B.H. Aristizábal Zuluaga, C.D. Britto do Amaral, and M.T. Grassi, Multi-elemental analysis of particulate matter $PM_{2.5}$ and PM_{10} by ICP OES, Talanta 221 (2021) 121457.

[79] R. Clough, M.C. Lohan, S.J. Ussher, M. Nimmo, and P.J. Worsfold, Uncertainty associated with the leaching of aerosol filters for the determination of metals in aerosol particulate matter using collision/reaction cell ICP-MS detection, Talanta 199 (2019) 425-430.

[80] M. Ogrizek, R. Jaćimović, M. Šala, and A. Kroflič, No more waste at the elemental analysis of airborne particulate matter on quartz fibre filters, Talanta 226 (2021) 122110.

[81] A. Pourmand, N. Dauphas, and T.J. Ireland, A novel extraction chromatography and MC-ICP-MS technique for rapid analysis of REE, Sc and Y: Revising CI-chondrite and Post-Archean Australian Shale (PAAS) abundances, Chemical Geology 291 (2012) 38-54.

[82] A. Pourmand and N. Dauphas, Distribution coefficients of 60 elements on TODGA resin: Application to Ca, Lu, Hf, U and Th isotope geochemistry, Talanta 81(3) (2010) 741-753.

[83] C.-F. Li, X.-C. Wang, J.-H. Guo, Z.-Y. Chu, and L.-J. Feng, Rapid separation scheme of Sr, Nd, Pb, and Hf from a single rock digest using a tandem chromatography column prior to isotope ratio measurements by mass spectrometry, Journal of Analytical Atomic Spectrometry 31(5) (2016) 1150-1159.

[84] S.M. Aciego, B. Bourdon, M. Lupker, and J. Rickli, A new procedure for separating and measuring radiogenic isotopes (U, Th, Pa, Ra, Sr, Nd, Hf) in ice cores, Chemical Geology 266(3-4) (2009) 194-204.

[85] I.A. Haidar Ahmad, Necessary analytical skills and knowledge for identifying, understanding, and performing HPLC troubleshooting, Chromatographia 80(5) (2017) 705-730.

[86] P. Kulkarni, S. Chellam, and M.P. Fraser, Lanthanum and lanthanides in atmospheric fine particles and their apportionment to refinery and petrochemical operations in Houston, TX, Atmospheric Environment 40(3) (2006) 508-520.

[87] K.S.K. Danadurai, S. Chellam, C.T. Lee, and M.P. Fraser, Trace elemental analysis of airborne particulate matter using dynamic reaction cell inductively coupled plasma - mass spectrometry: application to monitoring episodic industrial emission events, Analytica Chimica Acta 686(1-2) (2011) 40-49.

[88] A. Arı, P.E. Arı, and E.O. Gaga, Chemical characterization of size-segregated particulate matter (PM) by inductively coupled plasma – Tandem mass spectrometry (ICP-MS/MS), Talanta 208 (2020) 120350.

[89] J. Prentice, S.T. Evans, D. Robbins, and G. Ferreira, Pressure-Flow experiments, packing, and modeling for scale-up of a mixed mode chromatography column for biopharmaceutical manufacturing, Journal of Chromatography A 1625 (2020) 461117.

[90] S. Datta, A.M. Rule, J.N. Mihalic, S.N. Chillrud, B.C. Bostick, J.P. Ramos-Bonilla, I. Han, L.M. Polyak, A.S. Geyh, and P.N. Breysse, Use of X-ray absorption spectroscopy to speciate manganese in airborne particulate matter from five counties across the United States, Environmental Science & Technology 46(6) (2012) 3101-3109.

[91] C. Pin, A. Gannoun, and A. Dupont, Rapid, simultaneous separation of Sr, Pb, and Nd by extraction chromatography prior to isotope ratios determination by TIMS and MC-ICP-MS, Journal of Analytical Atomic Spectrometry 29(10) (2014) 1858-1870.

[92] K. Kołacińska, E. Chajduk, J. Dudek, Z. Samczyński, E. Łokas, A. Bojanowska-Czajka, and M. Trojanowicz, Automation of sample processing for ICP-MS determination of ^{90}Sr radionuclide at ppq level for nuclear technology and environmental purposes, Talanta 169 (2017) 216-226.

[93] R. Bast, E.E. Scherer, P. Sprung, M. Fischer-Gödde, A. Stracke, and K. Mezger, A rapid and efficient ion-exchange chromatography for Lu–Hf, Sm–Nd, and Rb–Sr geochronology and the routine isotope analysis of sub-ng amounts of Hf by MC-ICP-MS, Journal of Analytical Atomic Spectrometry 30(11) (2015) 2323-2333.

[94] H. Li, F.L.H. Tissot, S.-G. Lee, E. Hyung, and N. Dauphas, Distribution coefficients of the REEs, Sr, Y, Ba, Th, and U between α-HIBA and AG50W-X8 resin, Acs Earth and Space Chemistry 5(1) (2020) 55-65.

[95] J. Harvey and E.F. Baxter, An improved method for TIMS high precision neodymium isotope analysis of very small aliquots (1–10 ng), Chemical Geology 258(3-4) (2009) 251-257.

[96] G. Olszewski, P. Lindahl, P. Frisk, M. Eriksson, and H.B.L. Pettersson, Development of ^{148}Gd analysis method using stable Gd, Talanta 229 (2021) 122295.

[97] S. Weyer, C. Münker, M. Rehkämper, and K. Mezger, Determination of ultra-low Nb, Ta, Zr and Hf concentrations and the chondritic Zr/Hf and Nb/Ta ratios by isotope dilution analyses with multiple collector ICP-MS, Chemical Geology 187(3) (2002) 295-313.

[98] C. Münker, S. Weyer, E. Scherer, and K. Mezger, Separation of high field strength elements (Nb, Ta, Zr, Hf) and Lu from rock samples for MC-ICPMS measurements, Geochemistry, Geophysics, Geosystems 2(12) (2001) 2001GC000183.

[99] L. Yang, S. Tong, L. Zhou, Z. Hu, Z. Mester, and J. Meija, A critical review on isotopic fractionation correction methods for accurate isotope amount ratio measurements by MC-ICP-MS, Journal of Analytical Atomic Spectrometry 33(11) (2018) 1849-1861.

[100] M. Horsky, J. Irrgeher, and T. Prohaska, Evaluation strategies and uncertainty calculation of isotope amount ratios measured by MC ICP-MS on the example of Sr, Analytical and Bioanalytical Chemistry 408(2) (2016) 351-367.

[101] M.A. Elburg, P. Vroon, and A. Scherstén, An empirical method for determining the error introduced by blank corrections on MC-ICP-MS measurements, Journal of Analytical Atomic Spectrometry 20(12) (2005) 1389-1391.

[102] L. Yang, Accurate and precise determination of isotopic ratios by MC-ICP-MS: A review, Mass Spectrometry Reviews 28(6) (2009) 990-1011.

[103] H.-L. Lei, T. Yang, S.-Y. Jiang, and W. Pu, A simple two-stage column chromatographic separation scheme for strontium, lead, neodymium and hafnium isotope analyses in geological samples by thermal ionization mass spectrometry or multi-collector inductively coupled plasma mass spectrometry, Journal of Separation Science 42(20) (2019) 3261-3275.

[104] E.K. Mullen and D. Weis, Sr-Nd-Hf-Pb isotope and trace element evidence for the origin of alkalic basalts in the Garibaldi Belt, northern Cascade arc, Geochemistry, Geophysics, Geosystems 14(8) (2013) 3126-3155.

[105] D. Weis, B. Kieffer, C. Maerschalk, J. Barling, J. de Jong, G.A. Williams, D. Hanano, W. Pretorius, N. Mattielli, J.S. Scoates, A. Goolaerts, R.M. Friedman, and J.B. Mahoney, High-precision isotopic characterization of USGS reference materials by TIMS and MC-ICP-MS, Geochemistry, Geophysics, Geosystems 7(8) (2006).

[106] Y. Lu, A. Makishima, and E. Nakamura, Purification of Hf in silicate materials using extraction chromatographic resin, and its application to precise determination of $^{176}Hf/^{177}Hf$ by MC-ICP-MS with ^{179}Hf spike, Journal of Analytical Atomic Spectrometry 22(1) (2007) 69-76.

[107] Y. Yang, F. Wu, L. Xie, and Y. Zhang, High-precision measurements of the $^{143}Nd/^{144}Nd$ isotope rtio in crtified reference materials without Nd and Sm Separation by multiple collector inductively coupled plasma mass spectrometry, Analytical Letters 43(1) (2010) 142-150.

[108] N. Sharp, B.W. Ticknor, M. Bronikowski, T. Nichols, W.F. McDonough, A. Mignerey, and D. Beals, Nd and Sm isotopic composition of spent nuclear fuels from three material test reactors, Journal of Radioanalytical and Nuclear Chemistry 311(1) (2017) 801-808.

[109] X.-J. Yang and C. Pin, Separation of hafnium and zirconium from Ti- and Fe-rich geological materials by extraction chromatography, Analytical Chemistry 71(9) (1999) 1706-1711.

[110] C.-F. Li, J.-H. Guo, Y.-H. Yang, Z.-Y. Chu, and X.-C. Wang, Single-step separation scheme and high-precision isotopic ratios analysis of Sr–Nd–Hf in silicate materials, Journal of Analytical Atomic Spectrometry 29(8) (2014) 1467-1476.

[111] T. Nakano, Potential uses of stable isotope ratios of Sr, Nd, and Pb in geological materials for environmental studies, Proceedings of the Japan Academy. Series B, Physical and Biological Sciences 92(6) (2016) 167-184.

[112] K.P. Jochum, U. Nohl, K. Herwig, E. Lammel, B. Stoll, and A.W. Hofmann, GeoReM: A new geochemical database for reference materials and isotopic standards, Geostandards and Geoanalytical Research 29(3) (2005) 333-338.

[113] European Reference Materials (ERM) - Application note 1. https://ec.europa.eu/jrc/sites/default/files/erm_application_note_1_en.pdf. (Accessed 19 October 2021).

[114] R. Frei and K.M. Frei, The geographic distribution of Sr isotopes from surface waters and soil extracts over the island of Bornholm (Denmark) – A base for provenance studies in archaeology and agriculture, Applied Geochemistry 38 (2013) 147-160.

[115] L.N. Christian, J.L. Banner, and L.E. Mack, Sr isotopes as tracers of anthropogenic influences on stream water in the Austin, Texas, area, Chemical Geology 282(3) (2011) 84-97.

[116] Y. Yan, R.-l. Yu, G.-r. Hu, S.-s. Wang, H.-b. Huang, J.-y. Cui, and Y. Yan, Characteristics and provenances of rare earth elements in the atmospheric particles of a coastal city with large-scale optoelectronic industries, Atmospheric Environment 214 (2019) 116836.

[117] G. Hu, S. Wang, R. Yu, Z. Zhang, and X. Wang, Source apportionment of rare earth elements in $PM_{2.5}$ in a southeast coastal city of China, Aerosol and Air Quality Research 19(1) (2019) 92-102.

[118] G. Bayon, K.W. Burton, G. Soulet, N. Vigier, B. Dennielou, J. Etoubleau, E. Ponzevera, C.R. German, and R.W. Nesbitt, Hf and Nd isotopes in marine sediments: Constraints on global silicate weathering, Earth and Planetary Science Letters 277(3) (2009) 318-326.

[119] Q. Wang, B. Zhao, G. Li, and R. Zhou, Application of rare earth modified Zr-based ceria-zirconia solid solution in three-way catalyst for automotive emission control, Environmental Science & Technology 44(10) (2010) 3870-3875.

[120] R.M. Gaschnig, R.L. Rudnick, W.F. McDonough, A.J. Kaufman, J.W. Valley, Z. Hu, S. Gao, and M.L. Beck, Compositional evolution of the upper continental crust through time, as constrained by ancient glacial diamictites, Geochimica Et Cosmochimica Acta 186 (2016) 316-343.

[121] The Federal Highway Administration (FHWA), U.S. Department of Transportation, Traffic volume trends. https://www.fhwa.dot.gov/policyinformation/travel_monitoring/tvt.cfm, 2019 (accessed 25 Dec 2021).

[122] Greater Houston Partnership, Houston facts. https://www.houston.org/sites/default/files/2020-08/houston%20facts%202020_final.pdf. (Accessed 25 December 2021).

[123] C.A. Pope and D.W. Dockery, Health effects of fine particulate air pollution: Lines that connect, Journal of the Air & Waste Management Association 56(6) (2006) 709-742.

[124] M. Stafoggia, S. Zauli-Sajani, J. Pey, E. Samoli, E. Alessandrini, X. Basagaña, A. Cernigliaro, M. Chiusolo, M. Demaria, J. Díaz, A. Faustini, K. Katsouyanni, A.G. Kelessis, C. Linares, S. Marchesi, S. Medina, P. Pandolfi, N. Pérez, X. Querol, G. Randi, A. Ranzi, A. Tobias, and F. Forastiere, Desert dust outbreaks in southern Europe: Contribution to daily PM_{10} concentrations and short-term associations with mortality and hospital admissions, Environmental Health Perspectives 124(4) (2016) 413-419.

[125] A.G. Russell and B. Brunekreef, A Focus on particulate matter and health, Environmental Science & Technology 43(13) (2009) 4620-4625.

[126] T. Moreno, X. Querol, A. Alastuey, J. Pey, M.C. Minguillon, N. Perez, R.M. Bernabe, S. Blanco, B. Cardenas, and W. Gibbons, Lanthanoid geochemistry of urban atmospheric particulate matter, Environmental Science & Technology 42(17) (2008) 6502-6507.

[127] S. Yoon, S.M. Ortiz, A.E. Clark, T.E. Barrett, S. Usenko, R.M. Duvall, L.H. Ruiz, J.K. Bean, C.B. Faxon, J.H. Flynn, B.L. Lefer, Y.J. Leong, R.J. Griffin, and R.J. Sheesley, Apportioned primary and secondary organic aerosol during pollution events of DISCOVER-AQ Houston, Atmospheric Environment 244 (2021) 117954.

[128] X. Querol, A. Alastuey, T. Moreno, M.M. Viana, S. Castillo, J. Pey, S. Rodríguez, B. Artiñano, P. Salvador, M. Sánchez, S. Garcia Dos Santos, M.D. Herce Garraleta, R. Fernandez-Patier, S. Moreno-Grau, L. Negral, M.C. Minguillón, E. Monfort, M.J. Sanz, R. Palomo-Marín, E. Pinilla-Gil, E. Cuevas, J. de la Rosa, and A. Sánchez de la Campa, Spatial and temporal variations in airborne particulate matter (PM_{10} and $PM_{2.5}$) across Spain 1999–2005, Atmospheric Environment 42(17) (2008) 3964-3979.

[129] J. Nicolás, M. Chiari, J. Crespo, I.G. Orellana, F. Lucarelli, S. Nava, C. Pastor, and E. Yubero, Quantification of Saharan and local dust impact in an arid Mediterranean area by the positive matrix factorization (PMF) technique, Atmospheric Environment 42(39) (2008) 8872-8882.

[130] M.K. Lee, Y.I. Lee, and H.-I. Yi, Provenances of atmospheric dust over Korea from Sr–Nd isotopes and rare earth elements in early 2006, Atmospheric Environment 44(20) (2010) 2401-2414.

[131] J.M. Prospero and P.J. Lamb, African droughts and dust transport to the Caribbean: climate change implications, Science 302(5647) (2003) 1024-7.

[132] J.M. Trapp, F.J. Millero, and J.M. Prospero, Temporal variability of the elemental composition of African dust measured in trade wind aerosols at Barbados and Miami, Marine Chemistry 120(1-4) (2010) 71-82.

[133] A.F. Stein, R.R. Draxler, G.D. Rolph, B.J.B. Stunder, M.D. Cohen, and F. Ngan, NOAA's HYSPLIT atmospheric transport and dispersion modeling system, Bulletin of the American Meteorological Society 96(12) (2015) 2059-2077.

[134] B.N. Holben, T.F. Eck, I. Slutsker, D. Tanré, J.P. Buis, A. Setzer, E. Vermote, J.A. Reagan, Y.J. Kaufman, T. Nakajima, F. Lavenu, I. Jankowiak, and A. Smirnov, AERONET—A federated instrument network and data archive for aerosol characterization, Remote Sensing of Environment 66(1) (1998) 1-16.

[135] P. Lynch, J.S. Reid, D.L. Westphal, J. Zhang, T.F. Hogan, E.J. Hyer, C.A. Curtis, D.A. Hegg, Y. Shi, J.R. Campbell, J.I. Rubin, W.R. Sessions, F.J. Turk, and A.L. Walker, An 11-year global gridded aerosol optical thickness reanalysis (v1.0) for atmospheric and climate sciences, Geoscientific Model Development 9(4) (2016) 1489-1522.

[136] TCEQ daily air quality forecast. https://www.tceq.texas.gov/airquality/monops/forecast_today.html (Accessed 30 January 2022).

[137] G. Faure, Principles of isotope geology, 2nd ed., John Wiley & Sons, United States, 1986.

[138] J.C. Chow, J.G. Watson, H. Kuhns, V. Etyemezian, D.H. Lowenthal, D. Crow, S.D. Kohl, J.P. Engelbrecht, and M.C. Green, Source profiles for industrial, mobile, and area sources in the Big Bend Regional Aerosol Visibility and Observational study, Chemosphere 54(2) (2004) 185-208.

[139] EPA-CMB8.2 Users Manual. https://www3.epa.gov/ttn/scram/models/receptor/EPA-CMB82Manual.pdf. (Accessed 05 Feb 2022).

[140] A. Bozlaker, B. Buzcu-Guven, M.P. Fraser, and S. Chellam, Insights into PM_{10} sources in Houston, Texas: Role of petroleum refineries in enriching lanthanoid metals during episodic emission events, Atmospheric Environment 69 (2013) 109-117.

[141] J.G. Watson, N.F. Robinson, J.C. Chow, R.C. Henry, B.M. Kim, T.G. Pace, E.L. Meyer, and Q. Nguyen, The USEPA/DRI chemical mass balance receptor model, CMB 7.0, Environmental Software 5(1) (1990) 38-49.

[142] G. Argyropoulos and C. Samara, Development and application of a robotic chemical mass balance model for source apportionment of atmospheric particulate matter, Environmental Modelling & Software 26(4) (2011) 469-481.

[143] G.-L. Shi, F. Zeng, X. Li, Y.-C. Feng, Y.-Q. Wang, G.-X. Liu, and T. Zhu, Estimated contributions and uncertainties of PCA/MLR–CMB results: Source apportionment for synthetic and ambient datasets, Atmospheric Environment 45(17) (2011) 2811-2819.

[144] F.E. Grousset, M. Parra, A. Bory, P. Martinez, P. Bertrand, G. Shimmield, and R.M. Ellam, Saharan wind regimes traced by the Sr-Nd isotopic composition of subtropical Atlantic sediments: Last Glacial maximum vs today, Quaternary Science Reviews 17(4-5) (1998) 395-409.

[145] P. Kulkarni, S. Chellam, and M.P. Fraser, Tracking petroleum refinery emission events using Lanthanum and Lanthanides as elemental markers for $PM_{2.5}$, Environmental Science & Technology 41(19) (2007) 6748-6754.

[146] L. Du and J. Turner, Using $PM_{2.5}$ lanthanoid elements and nonparametric wind regression to track petroleum refinery FCC emissions, Science of The Total Environment 529 (2015) 65-71.

[147] S. Hasheminassab, N. Daher, A. Saffari, D. Wang, B.D. Ostro, and C. Sioutas, Spatial and temporal variability of sources of ambient fine particulate matter ($PM_{2.5}$) in California, Atmospheric Chemistry and Physics 14(22) (2014) 12085-12097.

[148] B. Yan, M. Zheng, Y. Hu, X. Ding, A.P. Sullivan, R.J. Weber, J. Baek, E.S. Edgerton, and A.G. Russell, Roadside, urban, and rural comparison of primary and secondary organic molecular markers in ambient $PM_{2.5}$, Environmental Science & Technology 43(12) (2009) 4287-4293.

[149] K.J. Orians and C.L. Merrin, Refractory metals, in: J.H. Steele (Ed.), Encyclopedia of Ocean Sciences, Academic Press, Oxford, 2001, pp. 687-698.

[150] J.M. Prospero and O.L. Mayol-Bracero, Understanding the transport and impact of African dust on the Caribbean basin, Bulletin of the American Meteorological Society 94(9) (2013) 1329-1337.

[151] J. Li, B.E. Carlson, and A.A. Lacis, How well do satellite AOD observations represent the spatial and temporal variability of $PM_{2.5}$ concentration for the United States?, Atmospheric Environment 102 (2015) 260-273.

[152] C. Milford, E. Cuevas, C.L. Marrero, J.J. Bustos, V. Gallo, S. Rodríguez, P.M. Romero-Campos, and C. Torres, Impacts of desert dust outbreaks on air quality in urban areas, Atmosphere 11(1) (2020) 23.

[153] R.O. Gonzalez, S. Strekopytov, F. Amato, X. Querol, C. Reche, and D. Weiss, New insights from zinc and copper isotopic compositions into the sources of atmospheric particulate matter from two major European cities, Environmental Science & Technology 50(18) (2016) 9816-9824.

[154] S. Rauch, H.F. Hemond, B. Peucker-Ehrenbrink, K.H. Ek, and G.M. Morrison, Platinum group element concentrations and osmium isotopic composition in urban airborne particles from Boston, Massachusetts, Environmental Science & Technology 39(24) (2005) 9464-9470.

[155] R. Ghosh, F. Lurmann, L. Perez, B. Penfold, S. Brandt, J. Wilson, M. Milet, N. Künzli, and R. McConnell, Near-roadway air pollution and coronary heart disease: burden of disease and potential impact of a greenhouse gas reduction strategy in southern California, Environmental Health Perspectives 124(2) (2016) 193-200.

[156] K. Zhang and S. Batterman, Air pollution and health risks due to vehicle traffic, Science of The Total Environment 450-451 (2013) 307-316.

[157] S. Pateraki, M. Manousakas, K. Bairachtari, V. Kantarelou, K. Eleftheriadis, C. Vasilakos, V.D. Assimakopoulos, and T. Maggos, The traffic signature on the vertical PM profile: Environmental and health risks within an urban roadside environmen, Science of The Total Environment 646 (2019) 448-459.

[158] S. Rauch, H.F. Hemond, C. Barbante, M. Owari, G.M. Morrison, B. Peucker-Ehrenbrink, and U. Wass, Importance of automobile exhaust catalyst emissions for the deposition of platinum, palladium, and rhodium in the northern hemisphere, Environmental Science & Technology 39(21) (2005) 8156-62.

[159] I.S. Sen, B. Peucker-Ehrenbrink, and N. Geboy, Complex anthropogenic sources of platinum group elements in aerosols on Cape Cod, USA, Environmental Science & Technology 47(18) (2013) 10188-10196.

[160] J.W. Liacos, W. Kam, R.J. Delfino, J.J. Schauer, and C. Sioutas, Characterization of organic, metal and trace element $PM_{2.5}$ species and derivation of freeway-based emission rates in Los Angeles, CA, Science of The Total Environment 435-436(Supplement C) (2012) 159-166.

[161] P. Pakbin, Z. Ning, M.M. Shafer, J.J. Schauer, and C. Sioutas, Seasonal and spatial coarse particle elemental concentrations in the Los Angeles area, Aerosol Science and Technology 45(8) (2011) 949-963.

[162] Y. Zhang, J.J. Schauer, M.M. Shafer, M.P. Hannigan, and S.J. Dutton, Source apportionment of in vitro reactive oxygen species bioassay activity from atmospheric particulate matter, Environmental Science & Technology 42(19) (2008) 7502-7509.

[163] S. Rauch, M. Lu, and G.M. Morrison, Heterogeneity of platinum group metals in airborne particles, Environmental Science & Technology 35(3) (2001) 595-9.

[164] A. Limbeck, C. Puls, and M. Handler, Platinum and palladium emissions from on-road vehicles in the Kaisermühlen Tunnel (Vienna, Austria), Environmental Science & Technology 41(14) (2007) 4938-4945.

[165] H. Wichmann, G.A.K. Anquandah, C. Schmidt, D. Zachmann, and M.A. Bahadir, Increase of platinum group element concentrations in soils and airborne dust in an urban area in Germany, Science of The Total Environment 388(1) (2007) 121-127.

[166] K. Kanitsar, G. Koellensperger, S. Hann, A. Limbeck, H. Puxbaum, and G. Stingeder, Determination of Pt, Pd and Rh by inductively coupled plasma sector field mass spectrometry (ICP-SFMS) in size-classified urban aerosol samples, Journal of Analytical Atomic Spectrometry 18(3) (2003) 239-246.

[167] M.B. Gomez, M.M. Gomez, and M.A. Palacios, ICP-MS determination of Pt, Pd and Rh in airborne and road dust after tellurium coprecipitation, Journal of Analytical Atomic Spectrometry 18(1) (2003) 80-83.

[168] F. Zereini, H. Alsenz, C.L.S. Wiseman, W. Püttmann, E. Reimer, R. Schleyer, E. Bieber, and M. Wallasch, Platinum group elements (Pt, Pd, Rh) in airborne particulate matter in rural Vs. urban areas of Germany: Concentrations and spatial patterns of distribution, Science of The Total Environment 416 (2012) 261-8.

[169] F. Zereini, F. Alt, J. Messerschmidt, A. von Bohlen, K. Liebl, and W. Puttmann, Concentration and distribution of platinum group elements (Pt, Pd, Rh) in airborne particulate matter in Frankfurt am Main, Germany, Environmental Science & Technology 38(6) (2004) 1686-92.

[170] J. Rinkovec, G. Pehnec, R. Godec, S. Davila, and I. Bešlić, Spatial and temporal distribution of platinum, palladium and rhodium in Zagreb air, Science of The Total Environment 636 (2018) 456-463.

[171] C. Puls, A. Limbeck, and S. Hann, Bioaccessibility of palladium and platinum in urban aerosol particulates, Atmosppheric Environment 55 (2012) 213-219.

[172] S.L. Kingsley, M.N. Eliot, L. Carlson, J. Finn, D.L. MacIntosh, H.H. Suh, and G.A. Wellenius, Proximity of US schools to major roadways: a nationwide assessment, Journal of Exposure Science & Environmental Epidemiology 24(3) (2014) 253-259.

[173] E. Danysh Heather, E. Mitchell Laura, K. Zhang, E. Scheurer Michael, and J. Lupo Philip, Traffic-related air pollution and the incidence of childhood central nervous system tumors: Texas, 2001–2009, Pediatric Blood & Cancer 62(9) (2015) 1572-1578.

[174] C. Jephcote and H. Chen, Environmental injustices of children's exposure to air pollution from road-transport within the model British multicultural city of Leicester: 2000–09, Science of The Total Environment 414 (2012) 140-151.

[175] C.S. Claiborn, T. Larson, and L. Sheppard, Testing the metals hypothesis in Spokane, Washington, Environmental Health Perspectives 110 Suppl 4 (2002) 547-552.

[176] S.E. Grineski and T.W. Collins, Geographic and social disparities in exposure to air neurotoxicants at U.S. public schools, Environmental Research 161 (2018) 580-587.

[177] P. Gaffron and D. Niemeier, School locations and traffic emissions — Environmental (in)justice findings using a new screening method, International Journal of Environmental Research and Public Health 12(2) (2015) 2009-2025.

[178] C.L.S. Wiseman, Z. Hassan Pour, and F. Zereini, Platinum group element and cerium concentrations in roadside environments in Toronto, Canada, Chemosphere 145 (2016) 61-67.

[179] F. Zereini, C. Wiseman, and W. Püttmann, Changes in palladium, platinum, and rhodium concentrations, and their spatial distribution in soils along a major highway in Germany from 1994 to 2004, Environmental Science & Technology 41(2) (2007) 451-456.

[180] J.C. Ely, C.R. Neal, C.F. Kulpa, M.A. Schneegurt, J.A. Seidler, and J.C. Jain, Implications of platinum-group element accumulation along U.S. Roads from catalytic-converter attrition, Environmental Science & Technology 35(19) (2001) 3816-22.

[181] H.M. Prichard and P.C. Fisher, Identification of platinum and palladium particles emitted from vehicles and dispersed into the surface environment, Environmental Science & Technology 46(6) (2012) 3149-3154.

[182] C.L.S. Wiseman, J. Niu, C. Levesque, M. Chénier, and P.E. Rasmussen, An assessment of the inhalation bioaccessibility of platinum group elements in road dust using a simulated lung fluid, Environmental Pollution 241 (2018) 1009-1017.

[183] C.L.S. Wiseman, F. Zereini, and W. Püttmann, Traffic-related trace element fate and uptake by plants cultivated in roadside soils in Toronto, Canada, Science of The Total Environment 442 (2013) 86-95.

[184] M.A. Palacios, M. Gómez, M. Moldovan, and B. Gómez, Assessment of environmental contamination risk by Pt, Rh and Pd from automobile catalyst, Microchemical Journal 67(1) (2000) 105-113.

[185] Y. Wang and X. Li, Health risk of platinum group elements from automobile catalysts, Procedia Engineering 45 (2012) 1004-1009.

[186] L. Morawska, Z. Ristovski, E.R. Jayaratne, D.U. Keogh, and X. Ling, Ambient nano and ultrafine particles from motor vehicle emissions: Characteristics, ambient processing and implications on human exposure, Atmospheric Environment 42(35) (2008) 8113-8138.

[187] M. Russell, D.T. Allen, D.R. Collins, and M.P. Fraser, Daily, seasonal, and spatial trends in $PM_{2.5}$ mass and composition in southeast Texas special issue of Aerosol Science and Technology on findings from the fine particulate matter supersites program, Aerosol Science and Technology 38(sup1) (2004) 14-26.

[188] J.P. Pancras, M.S. Landis, G.A. Norris, R. Vedantham, and J.T. Dvonch, Source apportionment of ambient fine particulate matter in Dearborn, Michigan, using hourly resolved PM chemical composition data, Science of The Total Environment 448 (2013) 2-13.

[189] X. Zhang, E. Craft, and K. Zhang, Characterizing spatial variability of air pollution from vehicle traffic around the Houston Ship Channel area, Atmospheric Environment 161(Supplement C) (2017) 167-175.

[190] The city of Houston. http://www.gims.houstontx.gov/trafficcounts/Reports.aspx. (Accessed 01 July 2019).

[191] Texas Department of Transportation, 2015. https://www.txdot.gov/inside-txdot/division/transportation-planning/maps.html (Accessed April 22, 2018).

[192] EPA, SPECIATE Version 4.5 (Profile IDs: 135052.5 and 1350510), Research Triangle Park, NC, Washington, DC, 2016.

[193] L.W.A. Chen, J.G. Watson, J.C. Chow, D.W. DuBois, and L. Herschberger, Chemical mass balance source apportionment for combined $PM_{2.5}$ measurements from US non-urban and urban long-term networks, Atmospheric Environment 44(38) (2010) 4908-4918.

[194] I. Olmez, A.E. Sheffield, G.E. Gordon, J.E. Houck, L.C. Pritchett, J.A. Cooper, T.G. Dzubay, and R.L. Bennett, Compositions of particles from selected sources in Philadelphia for receptor modeling applications, JAPCA 38(11) (1988) 1392-1402.

[195] E. Vega, V. Mugica, E. Reyes, G. Sanchez, J.C. Chow, and J.G. Watson, Chemical composition of fugitive dust emitters in Mexico City, Atmospheric Environment 35(23) (2001) 4033-4039.

[196] L.M. Hildemann, G.R. Markowski, and G.R. Cass, Chemical-Composition of Emissions from Urban Sources of Fine Organic Aerosol, Environmental Science & Technology 25(4) (1991) 744-759.

[197] M.P. Fraser, B. Buzcu, Z.W. Yue, G.R. McGaughey, N.R. Desai, D.T. Allen, R.L. Seila, W.A. Lonneman, and R.A. Harley, Separation of fine particulate matter emitted from gasoline and diesel vehicles using chemical mass balancing techniques, Environmental Science & Technology 37(17) (2003) 3904-3909.

[198] M.D. Geller, S.B. Sardar, H. Phuleria, P.M. Fine, and C. Sioutas, Measurements of particle number and mass concentrations and size distributions in a tunnel environment, Environmental Science & Technology 39(22) (2005) 8653-8663.

[199] S. Balachandran, H.H. Chang, J.E. Pachon, H.A. Holmes, J.A. Mulholland, and A.G. Russell, Bayesian-based ensemble source apportionment of $PM_{2.5}$, Environmental Science & Technology 47(23) (2013) 13511-13518.

[200] A. Charron, L. Polo-Rehn, J.L. Besombes, B. Golly, C. Buisson, H. Chanut, N. Marchand, G. Guillaud, and J.L. Jaffrezo, Identification and quantification of particulate tracers of exhaust and non-exhaust vehicle emissions, Atmospheric Chemistry and Physics 19(7) (2019) 5187-5207.

[201] M.S. Landis, C.W. Lewis, R.K. Stevens, G.J. Keeler, J.T. Dvonch, and R.T. Tremblay, Ft. McHenry tunnel study: Source profiles and mercury emissions from diesel and gasoline powered vehicles, Atmospheric Environment 41(38) (2007) 8711-8724.

[202] S. Hasheminassab, N. Daher, J.J. Schauer, and C. Sioutas, Source apportionment and organic compound characterization of ambient ultrafine particulate matter (PM) in the Los Angeles Basin, Atmospheric Environment 79 (2013) 529-539.

[203] S. Rauch, B. Peucker-Ehrenbrink, L.T. Molina, M.J. Molina, R. Ramos, and H.F. Hemond, Platinum group elements in airborne particles in mexico city, Environmental Science & Technology 40(24) (2006) 7554-60.

[204] S. Artelt, H. Kock, H.P. König, K. Levsen, and G. Rosner, Engine dynamometer experiments: platinum emissions from differently aged three-way catalytic converters, Atmospheric Environment 33(21) (1999) 3559-3567.

[205] H.T. Diong, R. Das, B. Khezri, B. Srivastava, X. Wang, P.K. Sikdar, and R.D. Webster, Anthropogenic platinum group element (Pt, Pd, Rh) concentrations in PM_{10} and $PM_{2.5}$ from Kolkata, India, SpringerPlus 5(1) (2016) 1242.

[206] L. Zhang, Y. Wang, Y. Liu, Z. Li, and X. Li, Variation of platinum group elements (PGE) in airborne particulate matter (PM2.5) in the Beijing urban area, China: A case study of the 2014 APEC summit, Atmospheric Environment 198 (2019) 70-76.

[207] Y. Liu, B. Fu, Y. Shen, Y. Yu, H. Liu, Z. Zhao, and L. Zhang, Seasonal properties on PM_1 and PGEs (Rh, Pd, and Pt) in PM_1, Atmospheric Pollution Research 9(6) (2018) 1032-1037.

[208] F. Zereini and F. Alt, Palladium emissions in the environment: Analytical methods, environmental assessment and health effects, 1st ed., Springer, Berlin, Heidelberg, 2006.

[209] R.J. Brisley, G.R. Chandler, H.R. Jones, P.J. Anderson, and P.J. Shady, The Use of palladium in advanced catalysts, SAE Technical Paper Series, SAE International, 1995.

[210] J.W. Park, Z.C. Hu, S. Gao, I.H. Campbell, and H.J. Gong, Platinum Group Element Abundances in the Upper Continental Crust Revisited - New Constraints from Analyses of Chinese Loess, Geochimica Et Cosmochimica Acta 93 (2012) 63-76.

[211] S. Rauch, H.F. Hemond, and B. Peucker-Ehrenbrink, Source characterisation of atmospheric platinum group element deposition into an ombrotrophic peat bog, Journal of Environmental Monitoring 6(4) (2004) 335-343.

[212] T. Grigoratos and G. Martini, Brake wear particle emissions: A review, Environmental Science and Pollution Research International 22 (2015) 2491-2504.

[213] A. Thorpe and R.M. Harrison, Sources and properties of non-exhaust particulate matter from road traffic: A review, Science of The Total Environment 400(1) (2008) 270-282.

[214] J.H.J. Hulskotte, G.D. Roskam, and H.A.C. Denier van der Gon, Elemental composition of current automotive braking materials and derived air emission factors, Atmospheric Environment 99 (2014) 436-445.

[215] E.R. McKenzie, J.E. Money, P.G. Green, and T.M. Young, Metals associated with stormwater-relevant brake and tire samples, Science of The Total Environment 407(22) (2009) 5855-5860.

[216] B. Baensch-Baltruschat, B. Kocher, F. Stock, and G. Reifferscheid, Tyre and roadwear particles (TRWP) - A review ofgeneration, properties, emissions, human health risk, ecotoxicity, and fate in the environment, Science of The Total Environment 733 (2020) 137823.

[217] J.J. Schauer, G.C. Lough, M.M. Shafer, W.F. Christensen, M.F. Arndt, J.T. DeMinter, and J.S. Park, Characterization of metals emitted from motor vehicles, Research report (Health Effects Institute), Boston, MA, 2006, pp. 1-76.

[218] J. Sternbeck, A. Sjodin, and K. Andreasson, Metal emissions from road traffic and the influence of resuspension—results from two tunnel studies, Atmospheric Environment 36(30) (2002) 4735-4744.

[219] M.D. Hays, S.-H. Cho, R. Baldauf, J.J. Schauer, and M. Shafer, Particle size distributions of metal and non-metal elements in an urban near-highway environment, Atmospheric Environment 45(4) (2011) 925-934.

[220] R.M. Harrison, A.M. Jones, J. Gietl, J. Yin, and D.C. Green, Estimation of the contributions of brake dust, tire wear, and resuspension to nonexhaust traffic particles derived from atmospheric measurements, Environmental Science & Technology 46(12) (2012) 6523-6529.

[221] E. Dabek-Zlotorzynska, V. Celo, L.Y. Ding, D. Herod, C.H. Jeong, G. Evans, and N. Hilker, Characteristics and sources of $PM_{2.5}$ and reactive gases near roadways in two metropolitan areas in Canada, Atmospheric Environment 218 (2019) 13.

[222] W. Kam, J.W. Liacos, J.J. Schauer, R.J. Delfino, and C. Sioutas, On-road emission factors of PM pollutants for light-duty vehicles (LDVs) based on urban street driving conditions, Atmospheric Environment 61 (2012) 378-386.

[223] F. Song and Y. Gao, Size distributions of trace elements associated with ambient particular matter in the affinity of a major highway in the New Jersey–New York metropolitan area, Atmospheric Environment 45(37) (2011) 6714-6723.

[224] G.C. Lough, J.J. Schauer, J.-S. Park, M.M. Shafer, J.T. DeMinter, and J.P. Weinstein, Emissions of metals associated with motor vehicle roadways, Environmental Science & Technology 39(3) (2005) 826-836.

[225] T. Pulles, H. Denier van der Gon, W. Appelman, and M. Verheul, Emission factors for heavy metals from diesel and petrol used in European vehicles, Atmospheric Environment 61 (2012) 641-651.

[226] C.A. Alves, E.D. Vicente, A.M.P. Vicente, I.C. Rienda, M. Tomé, X. Querol, and F. Amato, Loadings, chemical patterns and risks of inhalable road dust particles in an Atlantic city in the north of Portugal, Science of The Total Environment 737 (2020) 139596.

[227] T. Gonet and B.A. Maher, Airborne, vehicle-derived Fe-bearing nanoparticles in the urban environment - A review, Environmental Science & Technology 53(17) (2019) 9970-9991.

[228] C.A. Alves, J. Gomes, T. Nunes, M. Duarte, A. Calvo, D. Custodio, C. Pio, A. Karanasiou, and X. Querol, Size-segregated particulate matter and gaseous emissions from motor vehicles in a road tunnel, Atmospheric Research 153 (2015) 134-144.

[229] E. Kelepertzis, A. Argyraki, V. Chrastný, F. Botsou, K. Skordas, M. Komárek, and A. Fouskas, Metal(loid) and isotopic tracing of Pb in soils, road and house dusts from the

industrial area of Volos (Central Greece), Science of The Total Environment 725 (2020) 138300.

[230] A.W. Gertler, Diesel vs. gasoline emissions: Does PM from diesel or gasoline vehicles dominate in the US?, Atmospheric Environment 39(13) (2005) 2349-2355.

[231] R.A. Sutherland, D. Graham Pearson, and C.J. Ottley, Grain size partitioning of platinum-group elements in road-deposited sediments : implications for anthropogenic flux estimates from autocatalysts, Environmental Pollution 151(3) (2008) 503-15.

[232] P. Kulkarni, S. Chellam, J.B. Flanagan, and R.K.M. Jayanty, Microwave digestion - ICP-MS for elemental analysis in ambient airborne fine particulate matter: Rare earth elements and validation using a filter borne fine particle certified reference material, Analytica Chimica Acta 599(2) (2007) 170-176.

[233] F. Amato, A. Alastuey, J. de la Rosa, Y. Gonzalez Castanedo, A.M. Sánchez de la Campa, M. Pandolfi, A. Lozano, J. Contreras González, and X. Querol, Trends of road dust emissions contributions on ambient air particulate levels at rural, urban and industrial sites in southern Spain, Atmospheric Chemistry and Physics 14(7) (2014) 3533-3544.

[234] M. Giuliano, G. Ricchiardi, A. Damin, M. Sgroi, G. Nicol, and F. Parussa, Thermal ageing effects in a commercial three-way catalyst: physical characterization of washcoat and active metal evolution, International Journal of Automotive Technology 21(2) (2020) 329-337.

[235] J.K. Gietl, R. Lawrence, A.J. Thorpe, and R.M. Harrison, Identification of brake wear particles and derivation of a quantitative tracer for brake dust at a major road, Atmospheric Environment 44(2) (2010) 141-146.

[236] Z. El Orch, B. Stephens, and M.S. Waring, Predictions and determinants of size-resolved particle infiltration factors in single-family homes in the US, Building and Environment 74 (2014) 106-118.

[237] D.D. Parrish, H.B. Singh, L. Molina, and S. Madronich, Air quality progress in North American megacities: A review, Atmospheric Environment 45(39) (2011) 7015-7025.

[238] O. Masson, D. Piga, R. Gurriaran, and D. D'Amico, Impact of an exceptional Saharan dust outbreak in France: PM_{10} and artificial radionuclides concentrations in air and in dust deposit, Atmospheric Environment 44(20) (2010) 2478-2486.

[239] Y.C. Lee, X. Yang, and M. Wenig, Transport of dusts from East Asian and non-East Asian sources to Hong Kong during dust storm related events 1996–2007, Atmospheric Environment 44(30) (2010) 3728-3738.

[240] J. Huang, C. Zhang, and J.M. Prospero, African dust outbreaks: A satellite perspective of temporal and spatial variability over the tropical Atlantic Ocean, Journal of Geophysical Research: Atmospheres 115(D5) (2010) D05202.

[241] Y. Wu, A. Arapi, J. Huang, B. Gross, and F. Moshary, Intra-continental wildfire smoke transport and impact on local air quality observed by ground-based and satellite remote sensing in New York City, Atmospheric Environment 187 (2018) 266-281.

[242] D.E. Keil, B. Buck, D. Goossens, Y. Teng, J. Pollard, B. McLaurin, R. Gerads, and J. DeWitt, Health effects from exposure to atmospheric mineral dust near Las Vegas, NV, USA, Toxicology reports 3 (2016) 785-795.

[243] E. Herrera-Molina, T.E. Gill, G. Ibarra-Mejia, and S. Jeon, Associations between dust exposure and hospitalizations in El Paso, Texas, USA, Atmosphere 12(11) (2021) 1413.

[244] C.J. Matz, M. Egyed, G. Xi, J. Racine, R. Pavlovic, R. Rittmaster, S.B. Henderson, and D.M. Stieb, Health impact analysis of $PM_{2.5}$ from wildfire smoke in Canada (2013–2015, 2017–2018), Science of The Total Environment 725 (2020) 138506.

[245] H. Youssouf, C. Liousse, L. Roblou, E.M. Assamoi, R.O. Salonen, C. Maesano, S. Banerjee, and I. Annesi-Maesano, Quantifying wildfires exposure for investigating health-related effects, Atmospheric Environment 97 (2014) 239-251.

[246] T. Holloway, A. Fiore, and M.G. Hastings, Intercontinental transport of air pollution: Will emerging science lead to a new hemispheric treaty?, Environmental Science & Technology 37(20) (2003) 4535-4542.

[247] Treatment of air quality data influenced by exceptional events. https://www.federalregister.gov/documents/2016/10/03/2016-22983/treatment-of-data-influenced-by-exceptional-events. (Accessed 03 February 2022).

[248] T. Moreno, X. Querol, A. Alastuey, and W. Gibbons, Identification of FCC refinery atmospheric pollution events using lanthanoid- and vanadium-bearing aerosols, Atmospheric Environment 42(34) (2008) 7851-7861.

[249] P. Salvador, S.M. Almeida, J. Cardoso, M. Almeida-Silva, T. Nunes, M. Cerqueira, C. Alves, M.A. Reis, P.C. Chaves, B. Artíñano, and C. Pio, Composition and origin of PM_{10} in Cape Verde: Characterization of long-range transport episodes, Atmospheric Environment 127 (2016) 326-339.

[250] H.L. Zhang and Q. Ying, Source apportionment of airborne particulate matter in southeast Texas using a source-oriented 3D air quality model, Atmospheric Environment 44(29) (2010) 3547-3557.

[251] A.N. Myers-Pigg, R.J. Griffin, P. Louchouarn, M.J. Norwood, A. Sterne, and B.K. Cevik, Signatures of biomass burning aerosols in the plume of a saltmarsh wildfire in south Texas, Environmental Science & Technology 50(17) (2016) 9308-9314.

[252] D.S. Hamilton, M.M.G. Perron, T.C. Bond, A.R. Bowie, R.R. Buchholz, C. Guieu, A. Ito, W. Maenhaut, S. Myriokefalitakis, N. Olgun, S.D. Rathod, K. Schepanski, A. Tagliabue, R. Wagner, and N.M. Mahowald, Earth, wind, fire, and pollution: Aerosol nutrient sources

and impacts on ocean biogeochemistry, Annual Review of Marine Science 14(1) (2022) 303-330.

[253] M.D. Hays, L. Beck, P. Barfield, R.D. Willis, M.S. Landis, R.K. Stevens, W. Preston, and Y. Dong, Physical and chemical characterization of residual oil-fired power plant emissions, Energy & Fuels 23(5) (2009) 2544-2551.

[254] T.F. Hogan and T.E. Rosmond, The description of the Navy Operational Global Atmospheric Prediction System's spectral forecast model, Monthly Weather Review 119(8) (1991) 1786-1815.

[255] S.J. Kramer, C. Alvarez, A.E. Barkley, P.R. Colarco, L. Custals, R. Delgadillo, C.J. Gaston, R. Govindaraju, and P. Zuidema, Apparent dust size discrepancy in aerosol reanalysis in north African dust after long-range transport, Atmospheric Chemistry and Physics 20(16) (2020) 10047-10062.

[256] T. Moreno, N. Perez, X. Querol, F. Amato, A. Alastuey, R. Bhatia, B. Spiro, M. Hanvey, and W. Gibbons, Physicochemical variations in atmospheric aerosols recorded at sea onboard the Atlantic-Mediterranean 2008 Scholar Ship cruise (Part II): Natural versus anthropogenic influences revealed by PM_{10} trace element geochemistry, Atmospheric Environment 44(21-22) (2010) 2563-2576.

[257] H. Lamberg, K. Nuutinen, J. Tissari, J. Ruusunen, P. Yli-Pirilä, O. Sippula, M. Tapanainen, P. Jalava, U. Makkonen, K. Teinilä, K. Saarnio, R. Hillamo, M.-R. Hirvonen, and J. Jokiniemi, Physicochemical characterization of fine particles from small-scale wood combustion, Atmospheric Environment 45(40) (2011) 7635-7643.

[258] M. Marconi, D.M. Sferlazzo, S. Becagli, C. Bommarito, G. Calzolai, M. Chiari, A. di Sarra, C. Ghedini, J.L. Gómez-Amo, F. Lucarelli, D. Meloni, F. Monteleone, S. Nava, G. Pace, S. Piacentino, F. Rugi, M. Severi, R. Traversi, and R. Udisti, Saharan dust aerosol over the central Mediterranean Sea: PM_{10} chemical composition and concentration versus optical columnar measurements, Atmospheric Chemistry and Physics 14(4) (2014) 2039-2054.

[259] C. Cowherd and D. Ono, Proposed revisions to fine fraction ratios used for AP-42 fugitive dust emission factors, 15th International Emission Inventory Conference, Midwest Research Institute, New Orleans, USA, 2006.

[260] P.J. Crutzen, L.E. Heidt, J.P. Krasnec, W.H. Pollock, and W. Seiler, Biomass burning as a source of atmospheric gases CO, H_2, N_2O, NO, CH_3Cl and COS, Nature 282(5736) (1979) 253-256.

[261] P.J. Crutzen and M.O. Andreae, Biomass burning in the tropics: Impact on atmospheric chemistry and biogeochemical cycles, Science 250(4988) (1990) 1669-1678.

[262] A. Mendoza, M.R. Garcia, P. Vela, D.F. Lozano, and D. Allen, Trace gases and particulate matter emissions from wildfires and agricultural burning in northeastern Mexico during the

2000 fire season, Journal of the Air & Waste Management Association 55(12) (2005) 1797-1808.

[263] P.E. Saide, S.N. Spak, R.B. Pierce, J.A. Otkin, T.K. Schaack, A.K. Heidinger, A.M. da Silva, M. Kacenelenbogen, J. Redemann, and G.R. Carmichael, Central American biomass burning smoke can increase tornado severity in the U.S, Geophysical Research Letters 42(3) (2015) 956-965.

[264] Acres burned in Canada in 2014 were three times the average. https://wildfiretoday.com/2014/12/24/acres-burned-in-canada-in-2014-was-three-times-the-average/. (Accessed 20 Feb 2022).

[265] J.L. McCarty, S. Korontzi, C.O. Justice, and T. Loboda, The spatial and temporal distribution of crop residue burning in the contiguous United States, Science of The Total Environment 407(21) (2009) 5701-5712.

[266] P. Jenkins, T. Phillips, E. Mulberg, and S. Hui, Activity patterns of Californians - use of and proximity to indoor pollutant sources, Atmospheric Environment 26(12) (1992) 2141-2148.

[267] T.F. Bateson and J. Schwartz, Children's Response to Air Pollutants, Journal of Toxicology and Environmental Health, Part A 71(3) (2008) 238-43.

[268] N.E. Klepeis, W.C. Nelson, W.R. Ott, J.P. Robinson, A.M. Tsang, P. Switzer, J.V. Behar, S.C. Hern, and W.H. Engelmann, The National Human Activity Pattern Survey (NHAPS): a resource for assessing exposure to environmental pollutants, Journal of Exposure Analysis and Environmental Epidemiology 11(3) (2001) 231-252.

[269] W.J. Gauderman, E. Avol, F. Gilliland, H. Vora, D. Thomas, K. Berhane, R. McConnell, N. Kuenzli, F. Lurmann, E. Rappaport, H. Margolis, D. Bates, and J. Peters, The effect of air pollution on lung development from 10 to 18 years of age, N. Engl. J. Med. 351(11) (2004) 1057.

[270] J. Burkhardt, J. Bayham, A. Wilson, E. Carter, J.D. Berman, K. O'Dell, B. Ford, E.V. Fischer, and J.R. Pierce, The effect of pollution on crime: evidence from data on particulate matter and ozone, J. Environ. Econ. Manage. 98 (2019).

[271] L. Yu, Y. Dai, Z. Yuan, and J. Li, Effects of rare earth elements on telomerase activity and apoptosis of human peripheral blood mononuclear cells, Biological Trace Element Research 116(1) (2007) 53-59.

[272] G. de Gennaro, P.R. Dambruoso, A.D. Loiotile, A.D. Gilio, P. Giungato, M. Tutino, A. Marzocca, A. Mazzone, J. Palmisani, and F. Porcelli, Indoor air quality in schools, Environmental Chemistry Letters 12 (2014) 467.

[273] J.F. Mejia, S.L. Choy, K. Mengersen, and L. Morawska, Methodology for assessing exposure and impacts of air pollutants in school children: Data collection, analysis and health effects - A literature review, Atmospheric Environment 45 (2011) 813-823.

[274] A. Rammah, K.W. Whitworth, I. Han, W. Chan, and E. Symanski, $PM_{2.5}$ metal constituent exposure and stillbirth risk in Harris County, Texas, Environmental Research (2019).

[275] K. Sexton, S.H. Linder, D. Marko, H. Bethel, and P.J. Lupo, Comparative assessment of air pollution-related health risks in Houston, Environmental Health Perspectives 115(10) (2007) 1388.

[276] S. Liu, C.M. Ganduglia, X. Li, G.L. Delclos, L. Franzini, and K. Zhang, Short-term associations of fine particulate matter components and emergency hospital admissions among a privately insured population in Greater Houston, Atmospheric Environment 147 (2016) 369-375.

[277] I.Y. Han, D. Richner, H.A. Han, L. Hopkins, D. James, and E. Symanski, Evaluation of metal aerosols in four communities adjacent to metal recyclers in Houston, Texas, USA, Journal of the Air and Waste Management Association 70(5) (2020) 568-579.

[278] QuickFacts Galena Park City, Texas. https://www.census.gov/quickfacts/fact/table/galenaparkcitytexas/POP010210. (Accessed 10 April 2020).

[279] Galena Park Independent School District, TX. https://nces.ed.gov/Programs/Edge/ACSDashboard/4820250. (Accessed 10 April 2020).

[280] P.J. Landrigan, V.A. Rauh, and M.P. Galvez, Environmental Justice and the health of children, Mount Sinai Journal of Medicine 77(2) (2010) 178-187.

[281] T. Moreno, I. Rivas, L. Bouso, M. Viana, T. Jones, M. Alvarez-Pedrerol, A. Alastuey, J. Sunyer, and X. Querol, Variations in school playground and classroom atmospheric particulate chemistry, Atmospheric Environment 91 (2014) 162-171.

[282] S.M. Almeida, N. Canha, A. Silva, M.D. Freitas, P. Pegas, C. Alves, M. Evtyugina, and C.A. Pio, Children exposure to atmospheric particles in indoor of Lisbon primary schools, Atmospheric Environment 45(40) (2011) 7594-7599.

[283] B.J. Majestic, J.A. Turner, and A.R. Marcotte, Respirable antimony and other trace-elements inside and outside an elementary school in Flagstaff, AZ, USA, Science of The Total Environment 435-436 (2012) 253-61.

[284] W.J. Trompetter, M. Boulic, T. Ancelet, J.C. Garcia-Ramirez, P.K. Davy, Y. Wang, and R. Phipps, The effect of ventilation on air particulate matter in school classrooms, Journal of Building Engineering 18 (2018) 164-171.

[285] Q.Y. Meng, B.J. Turpin, J.H. Lee, A. Polidori, C.P. Weisel, M. Morandi, S. Colome, J.F. Zhang, T. Stock, and A. Winer, How does infiltration behavior modify the composition of ambient PM2.5 in indoor spaces? An analysis of RIOPA data, Environmental Science & Technology 41(21) (2007) 7315.

[286] L. Schibuola and C. Tambani, Indoor environmental quality classification of school environments by monitoring PM and CO2 concentration levels, Atmospheric Pollution Research 11(2) (2020) 332-342.

[287] F. Sanchez-Soberon, J. Rovira, J. Sierra, M. Mari, J.L. Domingo, and M. Schuhmacher, Seasonal characterization and dosimetry-assisted risk assessment of indoor particulate matter ($PM_{10-2.5}$, $PM_{2.5-0.25}$, and $PM_{0.25}$) collected in different schools, Environmental Research 175 (2019) 287-296.

[288] A. Pacitto, L. Stabile, M. Viana, M. Scungio, C. Reche, X. Querol, A. Alastuey, I. Rivas, M. Álvarez-Pedrerol, J. Sunyer, B.L. van Drooge, J.O. Grimalt, R. Sozzi, P. Vigo, and G. Buonanno, Particle-related exposure, dose and lung cancer risk of primary school children in two European countries, Science of The Total Environment 616-617 (2018) 720-729.

[289] V. Martins, T. Faria, E. Diapouli, M.I. Manousakas, K. Eleftheriadis, M. Viana, and S.M. Almeida, Relationship between indoor and outdoor size-fractionated particulate matter in urban microenvironments: Levels, chemical composition and sources, Environmental Research 183 (2020) 109203.

[290] A. Bozlaker, J. Peccia, and S. Chellam, Indoor/outdoor relationships and anthropogenic elemental signatures in airborne $PM_{2.5}$ at a high school: impacts of petroleum refining emissions on lanthanoid enrichment, Environmental Science & Technology 51(9) (2017) 4851-4859.

[291] B. Brunekreef and B. Forsberg, Epidemiological evidence of effects of coarse airborne particles on health, European Respiratory Journal 29 (2005) 309-318.

[292] ASHRAE, ANSI/ASHRAE Standard 52.2-2007: Method of Testing General Ventilation Air-Cleaning Devices for Removal Efficiency by Particle Size, American Society of Heating, Refrigerating and Air-Conditioning Engineers, Atlanta, GA, 2007.

[293] P. Azimi, D. Zhao, and B. Stephens, Estimates of HVAC filtration efficiency for fine and ultrafine particles of outdoor origin, Atmospheric Environment 98 (2014) 337-346.

[294] S.M. Almeida, J. Lage, B. Fernandez, S. Garcia, M.A. Reis, and P.C. Chaves, Chemical characterization of atmospheric particles and source apportionment in the vicinity of a steelmaking industry, Science of The Total Environment 521 (2015) 411-420.

[295] P. Blondeau, V. Iordache, O. Poupard, D. Genin, and F. Allard, Relationship between outdoor and indoor air quality in eight French schools, Indoor Air 15(1) (2005) 2-12.

[296] C. Chen and B. Zhao, Review of relationship between indoor and outdoor particles: I/O ratio, infiltration factor and penetration factor, Atmospheric Environment 45(2) (2011) 275-288.

[297] A.U. Raysoni, T.H. Stock, J.A. Sarnat, T.M. Sosa, S.E. Sarnat, F. Holguin, R. Greenwald, B. Johnson, and W.W. Li, Characterization of traffic-related air pollutant metrics at four schools in El Paso, Texas, USA: Implications for exposure assessment and siting schools in urban areas, Atmospheric Environment 80 (2013) 140-151.

[298] M. Viana, I. Rivas, X. Querol, A. Alastuey, J. Sunyer, M. Alvarez-Pedrerol, L. Bouso, and C. Sioutas, Indoor/Outdoor Relationships and Mass Closure of Quasi-Ultrafine, Accumulation and Coarse Particles in Barcelona Schools, Atmospheric Chemistry and Physics 14(9) (2014) 4459-4472.

[299] C.-S. Li, Relationships of indoor/outdoor inhalable and respirable particles in domestic environments, Science of The Total Environment 151(3) (1993) 205-211.

[300] E. Abt, H.H. Suh, C. Catalano, and P. Koutrakis, Relative contribution of outdoor and indoor particle sources to indoor concentrations, Environmental Science & Technology 34 (2000) 3579.

[301] M. Viana, I. Rivas, X. Querol, A. Alastuey, M. Alvarez-Pedrerol, L. Bouso, C. Sioutas, and J. Sunyer, Partitioning of trace elements and metals between quasi-ultrafine, accumulation and coarse aerosols in indoor and outdoor air in schools, Atmospheric Environment 106 (2014) 392-301.

[302] M. Mohammadyan, A. Alizadeh-Larimi, S. Etemadinejad, M.T. Latif, B. Heibati, K. Yetilmezsoy, S.A. Abdul-Wahab, and P. Dadvand, Particulate air pollution at schools: indoor-outdoor relationship and determinants of indoor concentrations, Aerosol and Air Quality Research 17(3) (2017) 857-864.

[303] H. Fromme, J. Diemer, S. Dietrich, J. Cyrys, J. Heinrich, W. Lang, M. Kiranoglu, and D. Twardella, Chemical and morphological properties of particulate matter (PM_{10}, $PM_{2.5}$) in school classrooms and outdoor air, Atmospheric Environment 42 (2008) 6597-6605.

[304] A.R. Ferro, R.J. Kopperud, and L.M. Hildemann, Elevated personal exposure to particulate matter from human activities in a residence, Journal of Exposure Analysis and Environmental Epidemiology 14 Suppl 1 (2004) S34-40.

[305] S. Hasheminassab, N. Daher, M.M. Shafer, J.J. Schauer, R.J. Delfino, and C. Sioutas, Chemical characterization and source apportionment of indoor and outdoor fine particulatematter (PM2.5) in retirement communities of the Los Angeles Basin, Science of The Total Environment 490 (2014) 528-537.

[306] H.A. Hochstetler, M. Yermakov, T. Reponen, P.H. Ryan, and S.A. Grinshpun, Aerosol particles generated by diesel-powered school buses at urban schools as a source of children's exposure, Atmospheric Environment 45(7) (2011) 1444-1453.

[307] C.C. Lin and C.K. Peng, Characterization of indoor PM_{10}, $PM_{2.5}$, and ultrafine particles in elementary school classrooms: A review, Environmental Engineering Science 27 (2010) 915-922.

[308] I. Rivas, M. Viana, T. Moreno, L. Bouso, M. Pandolfi, M. Alvarez-Pedrerol, J. Forns, A. Alastuey, J. Sunyer, and X. Querol, Outdoor infiltration and indoor contribution of UFP and BC, OC, secondary inorganic ions and metals in $PM_{2.5}$ in schools, Atmospheric Environment 106 (2015) 129-138.

[309] M. Stranger, S.S. Potgieter-Vermaak, and R. Van Grieken, Characterization of indoor air quality in primary schools in Antwerp, Belgium, Indoor Air 18 (2008) 454-463.

[310] B.J. Tunno, R. Dalton, L. Cambal, F. Holguin, P. Lioy, and J.E. Clougherty, Indoor source apportionment in urban communities near industrial sites, Atmospheric Environment 139 (2016) 30-36.

[311] J. Wichmann, T. Lind, M.A.M. Nilsson, and T. Bellander, $PM_{2.5}$, soot and NO_2 indoor-outdoor relationships at homes, pre-schools and schools in Stockholm, Sweden, Atmospheric Environment 44(36) (2010) 4536-4544.

[312] R.J. Kopperud, A.R. Ferro, and L.M. Hildemann, Outdoor versus indoor contributions to indoor particulate matter (PM) determined by mass balance methods, Journal of the Air and Waste Management Association 54 (2004) 1188-1196.

[313] J. Qian, D. Hospodsky, N. Yamamoto, W.W. Nazaroff, and J. Peccia, Size-resolved emission rates of airborne bacteria and fungi in an occupied classroom, Indoor Air 22(4) (2012) 339-351.

[314] J. Qian, J. Peccia, and A.R. Ferro, Walking-induced particle resuspension in indoor environments, Atmospheric Environment (2014).

[315] J.M. Logue, T.E. McKone, M.H. Sherman, and B.C. Singer, Hazard assessment of chemical air contaminants measured in residences, Indoor Air 21(2) (2011) 92-109.

[316] TCEQ, Air emission event report database, Texas Commission on Environmental Quality, 2014.

[317] Regulations; Standards - 29 CFR. https://www.osha.gov/laws-regs/regulations/standardnumber/1910. (Accessed 18 March 2020).

[318] IRIS Assessments. https://iris.epa.gov/AtoZ/?list_type=alpha. (Accessed 18 March 2020).

[319] OEHHA Acute, 8-hour and chronic reference exposure level (REL) summary. https://oehha.ca.gov/air/general-info/oehha-acute-8-hour-and-chronic-reference-exposure-level-rel-summary. (Accessed 18 March 2020).

[320] J.L. Edme, P. Shirali, M. Mereau, A. Sobaszek, C. Boulenguez, F. Diebold, and J.M. Haguenoer, Assessment of biological chromium among stainless steel and mild steel welders in relation to welding processes, International Archives of Occupational and Environmental Health 70(4) (1997) 237-242.

[321] X.L. Shi, Y. Mao, A.D. Knapton, M. Ding, Y. Rojanasakul, P.M. Gannett, N. Dalal, and K.J. Liu, Reaction of Cr(VI) with ascorbate and hydrogen-peroxide generates hydroxyl radicals and causes DNA-damage - role of a Cr(IV)-mediated fenton-like reaction, Carcinogenesis 15(11) (1994) 2475-2478.

[322] IARC, IARC Monographs on the Evaluation of Carcinogenic Risks to Humans: Arsenic, metals, fibres, and dusts, International Agency for Research on Cancer, 2012, pp. 147-167.

[323] B. Strasert, S.C. Teh, and D.S. Cohan, Air quality and health benefits from potential coal power plant closures in Texas, Journal of the Air and Waste Management Association 69 (2019) 333-350.

[324] S. Taner, B. Pekey, and H. Pekey, Fine particulate matter in the indoor air of barbeque restaurants: Elemental compositions, sources and health risks, Science of The Total Environment 454-455 (2013) 79-87.

[325] R. Sharma and R. Balasubramanian, Assessment and mitigation of indoor human exposure to fine particulate matter ($PM_{2.5}$) of outdoor origin in naturally ventilated residential apartments: A case study, Atmospheric Environment 212 (2019) 163-171.

[326] N. Jiang, Y. Guo, Q. Wang, P. Kang, R. Zhang, and X. Tang, Chemical composition characteristics of $PM_{2.5}$ in three cities in Henan, Central China, Aerosol and Air Quality Research 17(10) (2017) 2367-2380.

[327] C. Lovett, F. Shirmohammadi, M.H. Sowlat, and C. Sioutas, Commuting in Los Angeles: Cancer and non-cancer health risks of roadway, light-rail and subway transit routes, Aerosol and Air Quality Research 18(9) (2018) 2363-2374.

[328] N.A. Sulong, M.T. Latif, M.F. Khan, N. Amil, M.J. Ashfold, M.I.A. Wahab, K.M. Chan, and M. Sahani, Source apportionment and health risk assessment among specific age groups during haze and non-haze episodes in Kuala Lumpur, Malaysia, Science of The Total Environment 601-602 (2017) 556-570.

[329] R.L. Rudnick and S. Gao, Composition of the Continental Crust, Treatise on Geochemistry2014, pp. 1-51.

[330] M.E. Kitto, Trace-element patterns in fuel oils and gasolines for use in source apportionment, Journal of the Air & Waste Management Association 43(10) (1993) 1381-1388.

[331] I. Olmez and G.E. Gordon, Rare-earths - atmospheric signatures for oil-fired power-plants and refineries, Science 229(4717) (1985) 966-968.

[332] M.D. Hays, L. Beck, P. Barfield, R.J. Lavrich, Y.J. Dong, and R.L. Vander Wal, Physical and chemical characterization of residential oil boiler emissions, Environmental Science and Technology 42(7) (2008) 2496-2502.

[333] C.Y.W. Chao, Kelvin K., Residential indoor PM_{10} and $PM_{2.5}$ in Hong Kong and the elemental composition, Atmospheric Environment 36(2) (2002) 265-277.

[334] A. Polidori, K.L. Cheung, M. Arhami, R.J. Delfino, J.J. Schauer, and C. Sioutas, Relationships between size-fractionated indoor and outdoor trace elements at four retirement communities in southern California, Atmospheric Chemistry and Physics 9(14) (2009) 4521-4536.

[335] H.L. Smith and D.C. Hoffman, Ion-exchange separations of the lanthanides and actinides by elution with ammonium alpha-hydroxy-isobutyrate, Journal of Inorganic and Nuclear Chemistry 3(3) (1956) 243-247.

[336] A. Gross, D. Palchan, M.D. Krom, and A. Angert, Elemental and isotopic composition of surface soils from key Saharan dust sources, Chemical Geology 442 (2016) 54-61.

[337] T. Moreno, X. Querol, S. Castillo, A. Alastuey, E. Cuevas, L. Herrmann, M. Mounkaila, J. Elvira, and W. Gibbons, Geochemical variations in aeolian mineral particles from the Sahara-Sahel Dust Corridor, Chemosphere 65(2) (2006) 261-70.

[338] S. Castillo, Trace element variation in size-fractionated African desert dusts, Journal of arid environments 72(6) (2008) 1034-1045.

[339] TCEQ Hourly air pollution data. https://www.tceq.texas.gov/airquality/monops/hourly_data.html (Accessed April 22, 2018).

[340] B. Bocca, S. Caimi, P. Smichowski, D. Gómez, and S. Caroli, Monitoring Pt and Rh in Urban Aerosols from Buenos Aires, Argentina, Science of The Total Environment 358(1–3) (2006) 255.

[341] S. Pan, G. Zhang, Y. Sun, and P. Chakraborty, Accumulating characteristics of platinum group elements (PGE) in urban environments, China, Science of The Total Environment 407(14) (2009) 4248-4252.

[342] O. Morton-Bermea, O. Amador-Muñoz, L. Martínez-Trejo, E. Hernández-Álvarez, L. Beramendi-Orosco, and M.E. García-Arreola, Platinum in $PM_{2.5}$ of the Metropolitan Area of Mexico City, Environmental Geochemistry and Health 36(5) (2014) 987-94.

[343] S. Atilgan, S. Akman, A. Baysal, Y. Bakircioglu, T. Szigeti, M. Ovari, and G. Zaray, Monitoring of Pd in airborne particulates by solid sampling high-resolution continuum source electrothermal atomic absorption spectrometry, Spectrochimica Acta Part B-Atomic Spectroscopy 70 (2012) 33-38.

[344] F. Petrucci, B. Bocca, A. Alimonti, and S. Caroli, Determination of Pd, Pt and Rh in airborne particulate and road dust by high-resolution ICP-MS: a preliminary investigation of the emission from automotive catalysts in the urban area of Rome{, Journal of Analytical Atomic Spectrometry 15(5) (2000) 525-528.

[345] J.D. Whiteley and F. Murray, Anthropogenic platinum group element (Pt, Pd and Rh) concentrations in road dusts and roadside soils from Perth, Western Australia, Science of The Total Environment 317(1-3) (2003) 121-35.

[346] H.M. Prichard, J. Sampson, and M.J. Jackson, Platinum-group element distribution in Hathersage, a small town near Sheffield, UK : evidence for a single source from catalytic converters, in: S. Rauch, G.M. Morrison, A. Monzón (Eds.), Highway and Urban Environment: Proceedings of the 9th Highway and Urban Environment symposium, Springer Netherlands, Dordrecht, 2010, pp. 151-160.

[347] J. Schäfer, J.-D. Eckhardt, Z.A. Berner, and D. Stüben, Time-dependent increase of traffic-emitted platinum-group elements (PGE) in different environmental compartments, Environmental Science & Technology 33(18) (1999) 3166-3170.

[348] M. Niemela, S. Pitkaaho, S. Ojala, R.L. Keiski, and P. Peramaki, Microwave-assisted aqua regia digestion for determining platinum, palladium, rhodium and lead in catalyst materials, Microchemical Journal 101(Supplement C) (2012) 75-79.

[349] B.A. Lesniewska, B. Godlewska-Zylkiewicz, A. Ruszczynska, E. Bulska, and A. Hulanicki, Elimination of interferences in determination of platinum and palladium in environmental samples by inductively coupled plasma mass spectrometry, Analytica Chimica Acta 564(2) (2006) 236-242.

[350] B. Leśniewska, S. Sawicka, and B. Godlewska-Żyłkiewicz, On the underestimated factors influencing the accuracy of determination of Pt and Pd by electrothermal atomic absorption spectrometry in road dust samples, in: F. Zereini, C.L.S. Wiseman (Eds.), Platinum Metals in the Environment, Springer Berlin Heidelberg, Berlin, Heidelberg, 2015, pp. 53-65.

[351] P. Kulkarni, S. Chellam, and D.W. Mittlefehldt, Microwave-assisted extraction of rare earth elements from petroleum refining catalysts and ambient fine aerosols prior to inductively coupled plasma-mass spectrometry, Analytica Chimica Acta 581(2) (2007) 247-259.

[352] S.D. Tanner and V.I. Baranov, A dynamic reaction cell for inductively coupled plasma mass spectrometry (ICP-DRC-MS). II. Reduction of interferences produced within the cell, Journal of the American Society for Mass Spectrometry 10(11) (1999) 1083-1094.

[353] U.S. Environmental Protection Agency, SPECIATE Version 4.5 (Profile IDs: 135052.5 and 1350510); Research Triangle Park, NC, Washington, DC, 2016. https://www.epa.gov/air-emissions-modeling/speciate-version-45-through-32. (Accessed 01 July 2019).

[354] D.S. Hjortenkrans, B.G. Bergback, and A.V. Haggerud, Metal emissions from brake linings and tires: case studies of Stockholm, Sweden 1995/1998 and 2005, Environmental Science & Technology 41(15) (2007) 5224-5230.

[355] I. Olmez and G.E. Gordon, Rare Earths: Atmospheric Signatures for Oil-Fired Power Plants and Refineries, Science 229(4717) (1985) 966-8.

[356] S.A. Stout, E. Litman, and D. Blue, Metal concentrations in used engine oils: Relevance to site assessments of soils, Environmental Forensics 19(3) (2018) 191-205.

[357] A.L. Miller, C.B. Stipe, M.C. Habjan, and G.G. Ahlstrand, Role of lubrication oil in particulate emissions from a hydrogen-powered internal combustion engine, Environmental Science & Technology 41(19) (2007) 6828-6835.

[358] G. Pirovano, C. Colombi, A. Balzarini, G.M. Riva, V. Gianelle, and G. Lonati, $PM_{2.5}$ source apportionment in Lombardy (Italy): Comparison of receptor and chemistry-transport modelling results, Atmospheric Environment 106 (2015) 56-70.

[359] S. Lawrence, R. Sokhi, K. Ravindra, H. Mao, H.D. Prain, and I.D. Bull, Source apportionment of traffic emissions of particulate matter using tunnel measurements, Atmospheric Environment 77 (2013) 548-557.

[360] Y.G. Wang, P.K. Hopke, X.Y. Xia, O.V. Rattigan, D.C. Chalupa, and M.J. Utell, Source apportionment of airborne particulate matter using inorganic and organic species as tracers, Atmospheric Environment 55 (2012) 525-532.

[361] A.L. Clements, M.P. Fraser, P. Herckes, and P.A. Solomon, Chemical mass balance source apportionment of fine and PM_{10} in the Desert Southwest, USA, AIMS Environmental Science 3(1) (2016) 115-132.

[362] G. Rolph, A. Stein, and B. Stunder, Real-time Environmental Applications and Display sYstem: READY, Environmental Modelling & Software 95(Supplement C) (2017) 210-228.

[363] https://neo.sci.gsfc.nasa.gov. (Accessed 06 Feb 2022).

APPENDIX A

SUPPORTING INFROMATION FOR CHAPTER II

Table A1. Instrumental settings and operating parameters for q-ICP-MS. Thermo Scientific™ iCAP™ RQ ICP-MS was used to monitor elution of analytes of interest (Rb, Sr, Ti, Hf, Lu, Yb, Nd, Sm) for isotopic analysis during column optimization. All other elemental analysis and monitoring were performed with PerkinElmer® NexION® 300 (DRC-q-ICP-MS). The standard mode refers to the absence of a collision cell gas and DRC mode refers to the use of ammonia as the collision cell gas.

Instrument	PerkinElmer® NexION® 300	Thermo Scientific™ iCAP™ RQ ICP-MS
Nebulizer	Concentric (Meinhard) [Type A0.5]	
Spray chamber	Baffled quartz cyclonic	
Torch injector	Quartz	
Auto lens	On	On
RF power	1600 W	1550W
Gas flow rates		
Sample	18 L min^{-1}	15 L min^{-1}
Nebulizer	0.96-1.18 L min^{-1}	0.67 L min^{-1}
Auxiliary	1-1.2 L min^{-1}	0.8 L min^{-1}
Interface	Platinum cones	Standard Nickel cones with high sensitivity inserts
Sampler cone	1.1 mm orifice diameter	iCAP™ Q/Qnova Series sample cones
Skimmer cone	0.9 mm orifice diameter	iCAP™ Q/Qnova Series skimmer cones
Measurement parameters		
Scanning mode	Peak hopping	
Sweeps/reading	20	20
Readings/replicate	1	1

Replicates	3	3
Dwell time	50 ms (standard mode); 100 ms (DRC mode)	
Sampling parameters	AS-93 plus auto-sampler	Manual
Sample flush time	45 s	60 s
Sample flush pump speed	20 rpm	40 rpm
Read delay	65 s	12 s
Read delay pump speed	24 rpm	40rpm
Wash time	60 s	60 s
Wash pump speed	24 rpm	60 rpm
		NA
Cell gas	NH_3 (0.2-1.0 mL min^{-1})	NA
RPq	0.25-0.75	NA
RPa	0	NA

A.1. QA/QC

Recovery of elements with the microwave digestion method was validated with DRC-q-ICP-MS analysis. The measured recovery range was 84-113% for all certified elements (comparing with respective certificates from National Institute of Standards and Technology (NIST), The United States Geological Survey (USGS) or European Union – Joint Research Centre) validating the accuracy and precision of our laboratory methods for elemental analysis.

Table A2. Quantitative recoveries of elements from four different reference materials (NIST 1648a, BCR723, BCR2, and NIST 1633b) after microwave digestion and measurement with DRC-q-ICP-MS by comparing with certified values validating the methods and measurements in this study. N.D. represents the normalized deviation of measured mean from certified mean and is given by N.D. = Difference of means / expanded uncertainty. Expanded uncertainty = 2×(sum of squares of uncertainties associated with measured mean and certified mean values)^0.5 as per ERM Application Notes 1 [113]. N.D. less than 1 shows statistically insignificant difference between means.

Table A2 (a) Recoveries for NIST SRM 1648a

Element	Certified values		Measured values					Certified values		Measured values			
	Mean µg g^{-1}	Unc	Mean µg g^{-1}	Unc	Recovery %	N.D.		Mean µg g^{-1}	Unc	Mean µg g^{-1}	Unc	Recovery %	N.D.
Li							Cd	73.7	2.3	72	8	98	0.12
Be							Sn			0	0		
Na	4240	60	3900	590	92	0.28	Sb	45.4	1.4	45	5	98	0.07
Mg	8130	120	6980	570	86	0.99	Cs	3.4	0.2	3.7	0.4	109	0.33

Al	34300	1300	32200	3000	94	0.33	Ba						
Si	128000	4000	113700	17500	89	0.4	La	39	3	34	3	88	0.53
K	10560	490	9800	1400	93	0.25	Ce	54.6	2.2	49	4	90	0.57
Ca	58400	1900	52900	8100	91	0.33	Pr						
Sc							Nd						
Ti	4021	86	3462	530	86	0.52	Sm	4.3	0.3	3.6	0.3	84	0.7
V	127	11	118	18	93	0.22	Eu						
Cr	402	13	440	70	108	0.24	Gd						
Mn	790	44	740	110	94	0.19	Tb						
Fe	39200	2100	39400	6100	100	0.01	Dy						
Co	17.93	0.68	17.9	2.8	100	0.01	Ho						
Ni	81.1	6.8	79	13	97	0.08	Er						
Cu	610	70	529	82	87	0.37	Tm						
Zn	4800	270	4350	670	91	0.31	Yb						
Ga							Lu						
Ge							Hf	5.2	0	5.1	0.3	98	0.13
As	115.5	3.9	104	16	90	0.36	Ta	1.8	0	1.6	0.3	92	0.21
Se	28.4	1.1	26.5	2.8	93	0.31	W	4.6	0.3	5.1	0.9	111	0.24
Rb	51	1.5	50.2	6.5	98	0.06	Pb	6550	330	6100	500	93	0.37
Sr	215	17	216	20	101	0.02	Te						
Mo													

Table A2 (b) Recoveries for BCR-2

Elements	Certified values		Measured values					Certified values		Measured values			
	Mean µg g^{-1}	Unc	Mean µg g^{-1}	Unc	Recovery %	N.D.		Mean µg g^{-1}	Unc	Mean µg g^{-1}	Unc	Recovery %	N.D.
Li	9	2	9	1	98	0.06	Cd						
Be							Sn						
Na	23400	800	21800	3300	93	0.24	Sb						
Mg	21600	300	18500	1500	86	0.99	Cs	1.1	0.1	1.0	0.1	91	0.2
Al	71400	1000	78500	7200	110	0.49	Ba	683	28	710	70	104	0.17
Si	253000	4000	220000	34000	87	0.49	La	25	1	27	3	107	0.31
K	14900	400	16200	2300	109	0.29	Ce	53	2	48.6	4.0	92	0.49
Ca	50900	800	46600	7200	92	0.3	Pr	6.8	0.3	7.3	0.6	107	0.35
Sc	33	2	28	4	85	0.48	Nd	28	2	26	2	92	0.44
Ti	13500	300	14200	2200	105	0.17	Sm	6.7	0.3	6.9	0.6	103	0.14
V	416	14	400	61	96	0.13	Eu	2.0	0.1	2.0	0.3	100	0.04
Cr	18	2	17	3	94	0.18	Gd	6.8	0.3	7.4	0.7	109	0.38
Mn	1520	60	1580	240	104	0.12	Tb	1.07	0.04	1.1	0.2	103	0.09
Fe	96500	1500	97000	15000	101	0.02	Dy						
Co	37	3	35	5	95	0.2	Ho	1.33	0.06	1.34	0.2	105	0.14
Ni							Er						
Cu	19	2	18	3	95	0.1	Tm	0.54	0	0.53	0.08	98	0.06

Zn	127	9	140	20	107	0.21	Yb	3.5	0.2	3.2	0.3	90	0.47
Ga	23	2	20	3	87	0.39	Lu	0.51	0.02	0.53	0.07	104	0.14
Ge							Hf	4.8	0.2	4.3	0.3	89	0.8
As							Ta						
Se							W						
Rb	48	2	45	6	94	0.28	Pb	11	2	12.4	1	113	0.25
Sr	346	14	299	28	86	0.76	Te						
Y	37	2	36	6	97	0.06	Th	6.2	0.7	6.0	0.7	97	0.08
Zr	188	16	188	23	100	0.01	U	1.7	0.2	1.6	0.2	95	0.14
Mo	248	17	243	20	98	0.1							

Table A2 (c) Recoveries for BCR-723

Elements	Certified values		Measured values					Certified values		Measured values			
	Mean µg g^{-1}	Unc	Mean µg g^{-1}	Unc	Recovery %	N.D.		Mean µg g^{-1}	Unc	Mean µg g^{-1}	Unc	Recovery %	N.D.
Li							Cd	2.5	0.4	2.4	0.3	96	0.12
Be							Sn						
Na							Sb	28.2	2.3	28	3	99	0.03
Mg							Cs						
Al	37500	2200	36100	3300	96	0.18	Ba	460	40	490	50	106	0.22
Si							La						
K							Ce						
Ca							Pr						
Sc							Nd						
Ti	2580	130	2780	430	108	0.22	Sm						
V	74.9	1.9	69	11	92	0.26	Eu						
Cr	440	18	390	60	89	0.37	Gd						
Mn	1280	40	1160	180	90	0.34	Tb						
Fe	32900	2000	34800	5400	106	0.16	Dy						
Co	29.8	1.6	31	5	104	0.12	Ho						
Ni	171	3	180	30	106	0.16	Er						
Cu							Tm						

Zn	1660	100	1470	230	88	0.39	Yb						
Ga							Lu						
Ge							Hf	2.2	0.7	2.0	0.1	91	0.11
As							Ta						
Se							W						
Rb	75	5	78	10	105	0.15	Pb	866	16	830	70	95	0.28
Sr	254	19	269	25	106	0.24	Te						
Y	12.5	1.8	13.4	2.1	107	0.16	Th	4.8	0.5	4.3	0.5	90	0.33
Zr			0	0			U						
Mo	40	0.6	43	4	107	0.38							

Table A2 (d) Recoveries for NIST SRM 1633b

Elements	Certified values		Measured values					Certified values		Measured values			
	Mean µg g^{-1}	Unc	Mean µg g^{-1}	Unc	Recovery %	N.D.		Mean µg g^{-1}	Unc	Mean µg g^{-1}	Unc	Recovery %	N.D.
Li							Cd	0.784	0.006	0.78	0.08	99	0.02
Be							Sn						
Na	2010	30	1810	280	90	0.36	Sb	6		5.3	0.6	88	0.66
Mg	4820		5160	420	107	0.4	Cs	11		10.4	1.2	94	0.28
Al	150000	2700	163000	15000	109	0.44	Ba	709	27	770	80	109	0.37
Si	230000	800	197600	30400	86	0.53	La	94		92	9	98	0.13
K	19500	300	20700	290	106	0.21	Ce	190		180	14	95	0.53
Ca	15100	600	16000	2500	106	0.18	Pr						
Sc	41		40	6	98	0.11	Nd	85		78	5	92	0.61
Ti	7910	140	7870	1200	99	0.02	Sm	20		20	2	100	0.01
V	295.7	3.6	269	41	91	0.32	Eu	4.1		3.9	0.5	94	0.26
Cr	198.2	0	208	33	105	0.14	Gd	13		13.1	1.2	101	0.04
Mn	131.8	1.7	115	18	87	0.49	Tb	2.6		2.7	0.4	102	0.07
Fe	77800		74300	11400	96	0.15	Dy	17		15.3	1.0	90	0.83
Co	50		51	8	102	0.07	Ho	3.5		3.7	0.6	105	0.17
Ni	120.6	1.8	104	17	87	0.47	Er						
Cu	112.8	2.6	123	19	109	0.26	Tm	2.1		1.8	0.3	85	0.58

Zn	210		223	34	106	0.19	Yb	7.6		6.6	0.7	86	0.8
Ga							Lu	1.2		1.2	0.2	100	0.2
Ge							Hf	6.8		6.1	0.4	90	0.86
As	136.2	2.6	119	18	87	0.46	Ta	1.8		1.8	0.4	102	0.05
Se	10.26	0.17	10	1	97	0.12	W	5.6		6.1	1.0	109	0.24
Rb	140		145.5	19	104	0.14	Pb	68.2	1.1	69	6	101	0.06
Sr	1041	14	1139	106	109	0.46	Te						
Y							Th	25.7	1.3	27.5	3.3	107	0.25
Zr							U	8.79	0.36	8.6	1.3	98	0.06
Mo													

Table A3. Parameters set for ESI Apex Ω.

Instrument	ESI Apex Omega Ω		
Temperature profile	Sr	Nd	Hf
Spray chamber (°C)	105°C	105°C	105°C
Peltier cooler (°C)	2°C	2°C	2°C
Dissolvator (°C)	145°C	145°C	145°C
Ar sweep gas flow (L min^{-1})	2.9	2.7	2.8
N_2 gas flow (mL min^{-1})	0	1.5	0
Reference isotope	^{88}Sr	^{142}Nd	^{178}Hf
Sensitivity (V (mg $L^{-1})^{-1}$)	400	150	120

Table A4. Instrumental setup for Neptune Plus MC-ICP-MS

Isotope Ratio	$^{87}Sr/^{86}Sr$	$^{143}Nd/^{144}Nd$	$^{176}Hf/^{177}Hf$
Instrumental setup			
RF Power (W)	1200	1200	1200
Skimmer cone	Nickel, X-Version	Nickel, X-Version	Nickel, X-Version
Skimmer cone orifice dia (mm)	0.4	0.4	0.4
Sampler cone	Nickel	Nickel	Nickel
Sampler cone orifice dia (mm)	1.2	1.2	1.2
Amplifier resistance (Ω)	10^{11}	10^{11}	10^{11}
Method setup			
Center cup	^{86}Sr	^{145}Nd	^{177}Hf
Isotopes measured	^{83}Kr, ^{84}Sr, ^{85}Rb, ^{86}Sr, ^{87}Sr, ^{88}Sr, ^{89}Sr, ^{90}Zr	^{140}Ce, ^{142}Nd, ^{143}Nd, ^{144}Nd, ^{145}Nd, ^{146}Nd, ^{147}Sm, ^{148}Nd, ^{150}Nd	^{172}Yb, ^{174}Hf, ^{175}Lu, ^{176}Hf, ^{177}Hf, ^{178}Hf, ^{179}Hf, ^{180}Hf
Correction method	Russell's law	Russell's law	Russell's law
Isotopes monitored for interference	^{83}Kr, ^{85}Rb	^{140}Ce, ^{147}Sm	^{172}Yb, ^{175}Lu
Ratios for interference correction	$^{83}Kr/^{86}Kr$ = 0.664740; $^{85}Rb/^{87}Rb$ = 2.592310	$^{147}Sm/^{144}Sm$ = 4.838710	$^{172}Yb/^{176}Yb$ = 1.710815; $^{175}Lu/^{176}Lu$ = 37.61
Normalizing ratio	$^{88}Sr/^{86}Sr$ = 8.375209	$^{146}Nd/^{144}Nd$ = 0.7219	$^{176}Hf/^{177}Hf$
Baseline readings (1.04s for each reading)	100 (at start of each reading)	100 (at start of each reading)	100 (at start of each reading)
Cup rotation	ON	ON	ON
Number of blocks	100	50	50

Integration time (s)	1.04	2.08	2.08
Total time of analysis (min)	35 min	35 min	40 min
Number of readings per block	100	50	50
Wash time (min)	5	5	7
Lens tuning	Manual	Manual	Manual
Cool gas (argon) (L min^{-1})	15	15	15
Aux gas (argon) (L min^{-1})	0.7	0.7	0.7
Sample Gas (argon) (L min^{-1})	0.925	0.925	0.925

Table A5. Description and their representative names for each source sample analysed. Bulk samples were sieved with a plastic 40 µm polyethylene mesh screen. The asterix (*) denote data for vehicle samples reported after subtracting background samples from respective tunnel samples.

Sample	ID	Description	Sample collection	Mass dissolved for analysis (mg)
CRM	SRM 1648a	Urban Particulate Matter standard	Samples were purchased in ground form and not sieved	25
CRM	BCR-2	Basalt rock standard		25
CRM	BCR-723	Road Dust standard		25
CRM	SRM 1633b	Coal Fly Ash standard		25
Soil	1	First sample of soil collected near Clinton Drive	Sampled with spatula and brush; dried, sieved to 40 µm, and weighed before digestion	25
Soil	2	Second sample of soil collected near Clinton Drive		25
Soil	3	Third sample of soil collected near Clinton Drive		25
Soil	4	Fourth sample of soil collected near Clinton Drive		25
Construction	1	First sample of concrete dust	Sieved to 40 µm and weighed before digestion	25
Construction	2	Second sample of concrete dust		25
Tunnel	1	Aerosols collected inside Washburn Tunnel 03Jan-02Feb 2013	$PM_{2.5}$ air sampler; sample collected on PTFE filters	26.2
Tunnel	2	Aerosols collected inside Washburn Tunnel 02Feb-14Feb 2013		13.9
Background	1	Aerosols collected at Tunnel exhaust room 03Jan-02Feb 2013 (Background for Tunnel 1)		7.5
Background	2	Aerosols collected at Tunnel exhaust room 02Feb-14Feb 2013 (Background for Tunnel 1)		3.6
Vehicle*	1	Aerosol characterized after background subtraction inside Tunnel during 03 January -02 February 2013		18.7

Vehicle*	2	Aerosol characterized after background subtraction inside Tunnel during 02 February -14 February 2013		10.3
FCC	1	Fresh catalyst from manufacturer	Sieved to 40 µm and weighed before digestion	25
FCC	2	Fresh catalyst from manufacturer		25
FCC	3	Fresh catalyst from manufacturer		25
FCC	Spent	Spent (or equilibrium) catalyst from refinery		25

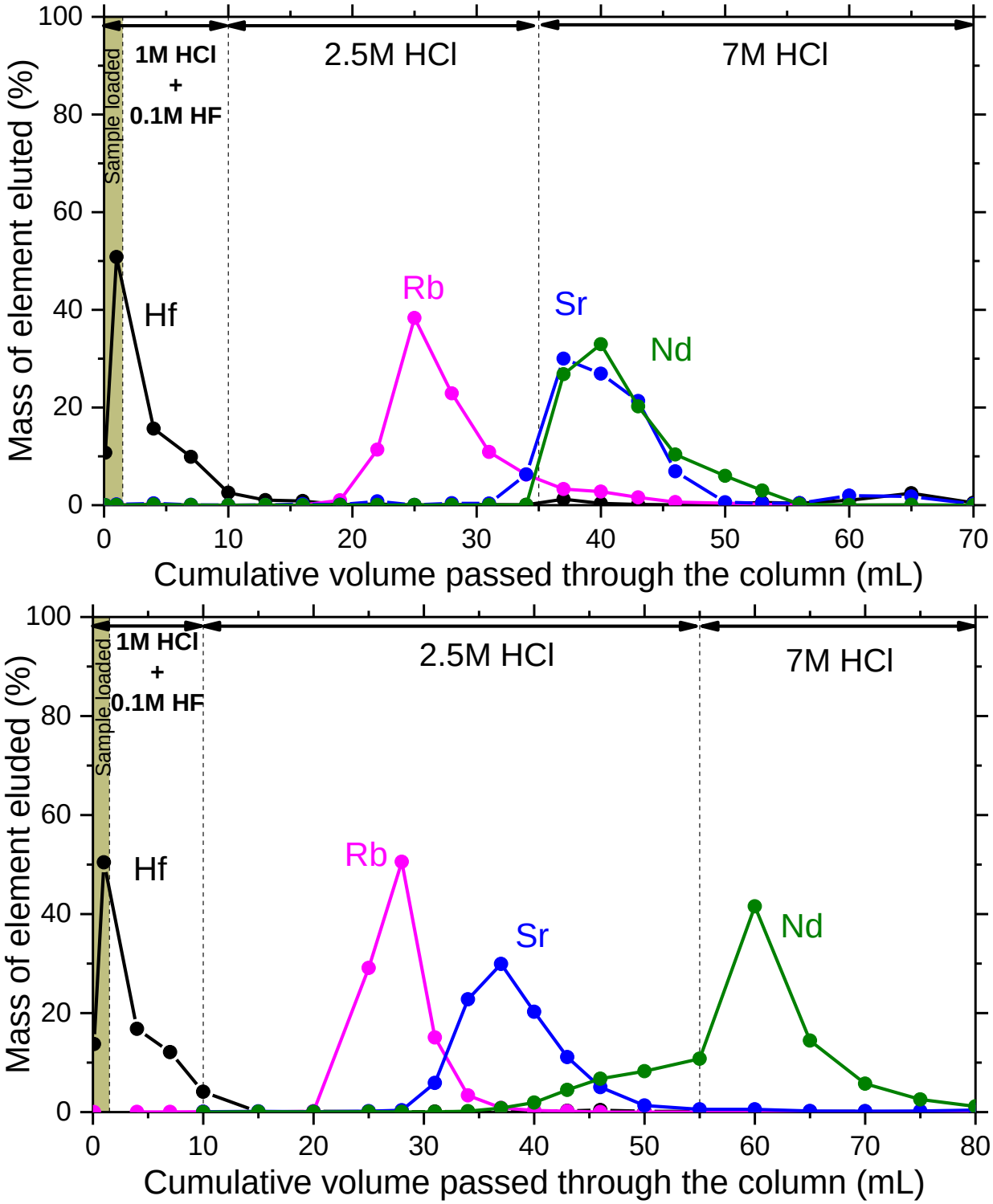

Figure A1. Attempts at separating Sr and Nd with cation exchange resin (50WX8) in column 1 did not yield full recovery. The top graph shows Sr and Nd co-eluting when only 25 mL of 2.5 M HCl passed after 10 mL of 1 M HCl + 0.1 M HF whereas an additional 25 mL (bottom) did separate Sr partially from Nd.

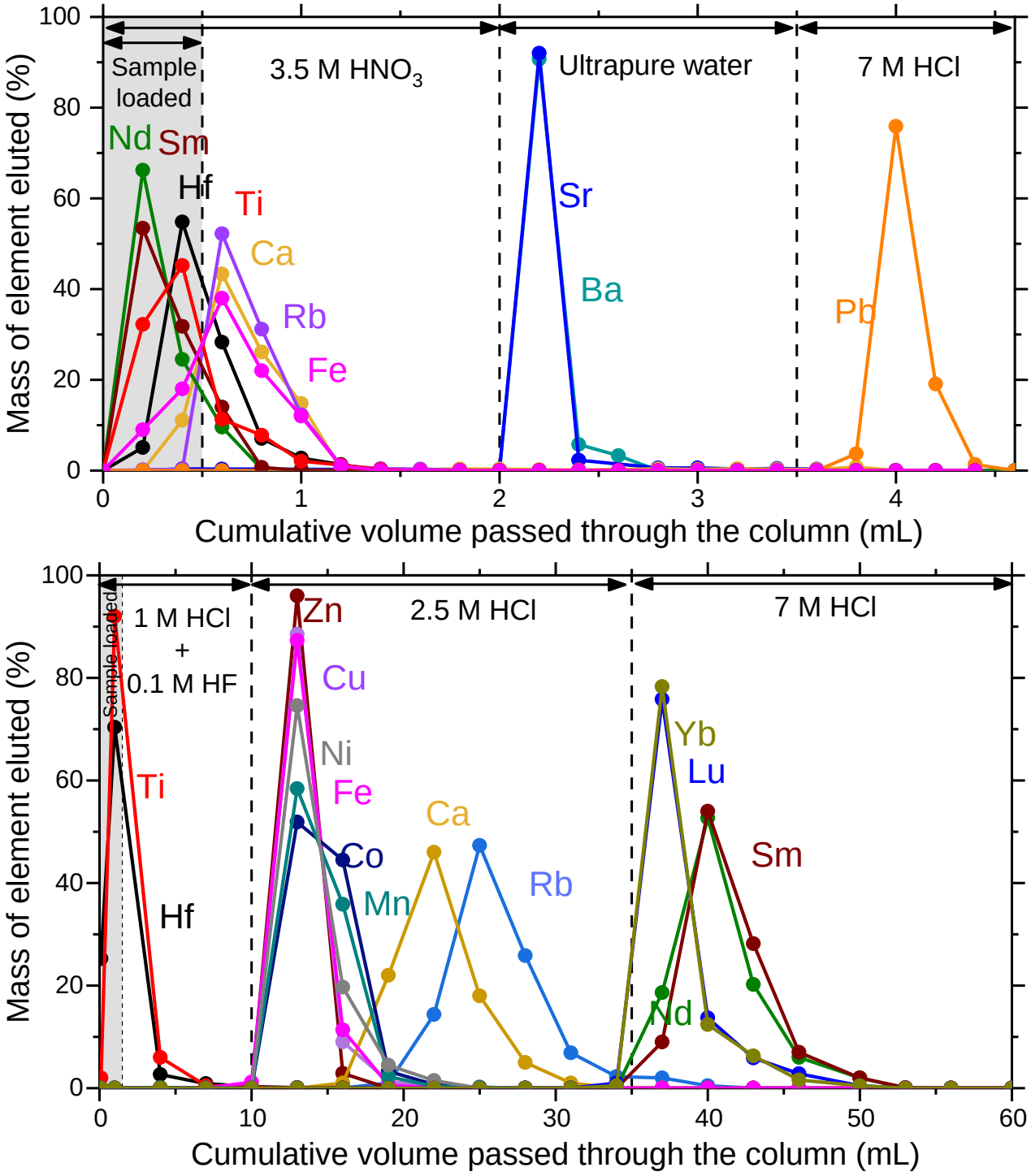

Figure A2. Elution curve for elements in step 1/column 2 (top) and step 2/column 1 (bottom) with 25 mg of SRM 1648a.

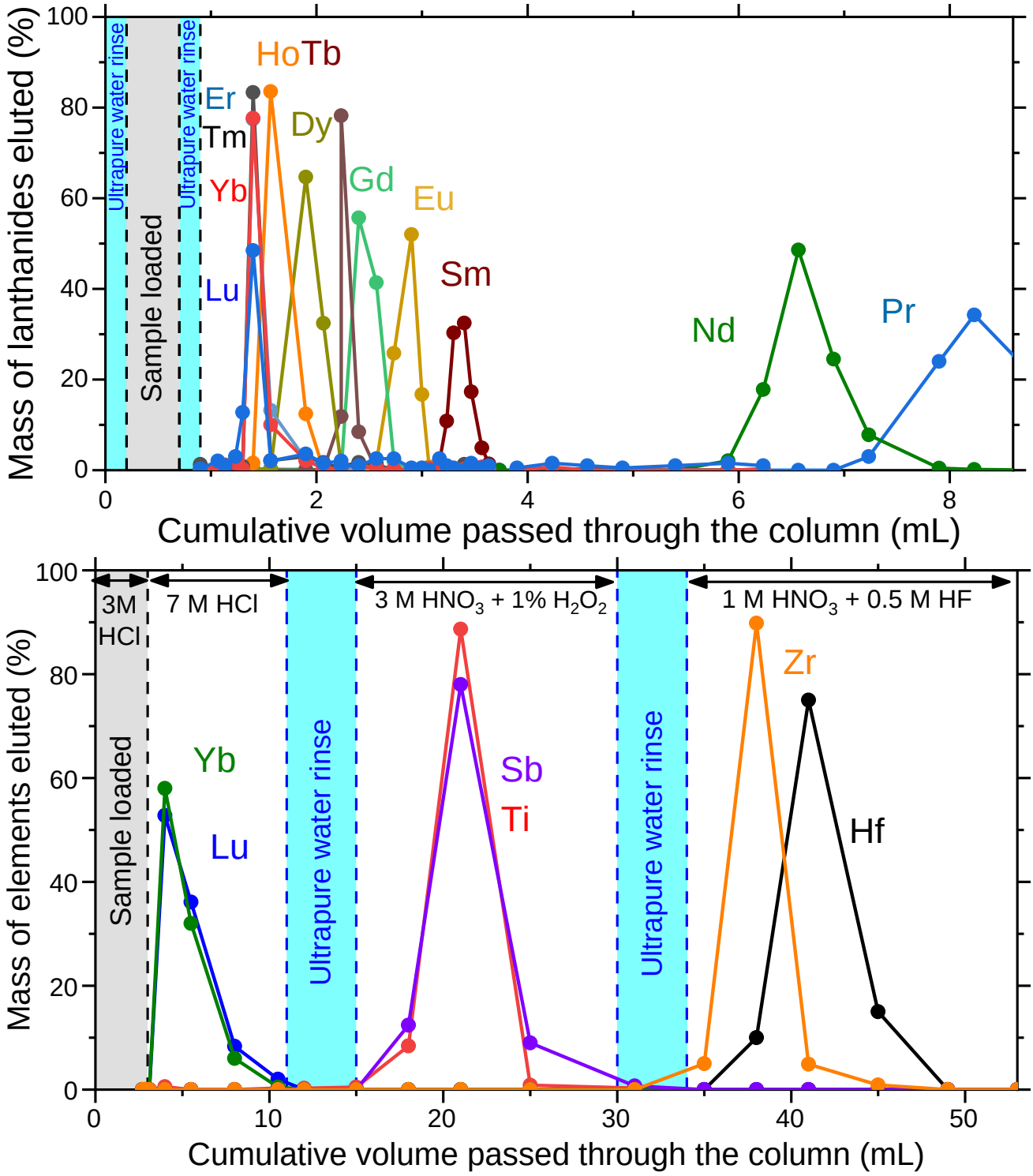

Figure A3. Elution curve for elements in step 3/column 3 (top) and step 4/column 4 (bottom) with 25 mg of SRM 1648a.

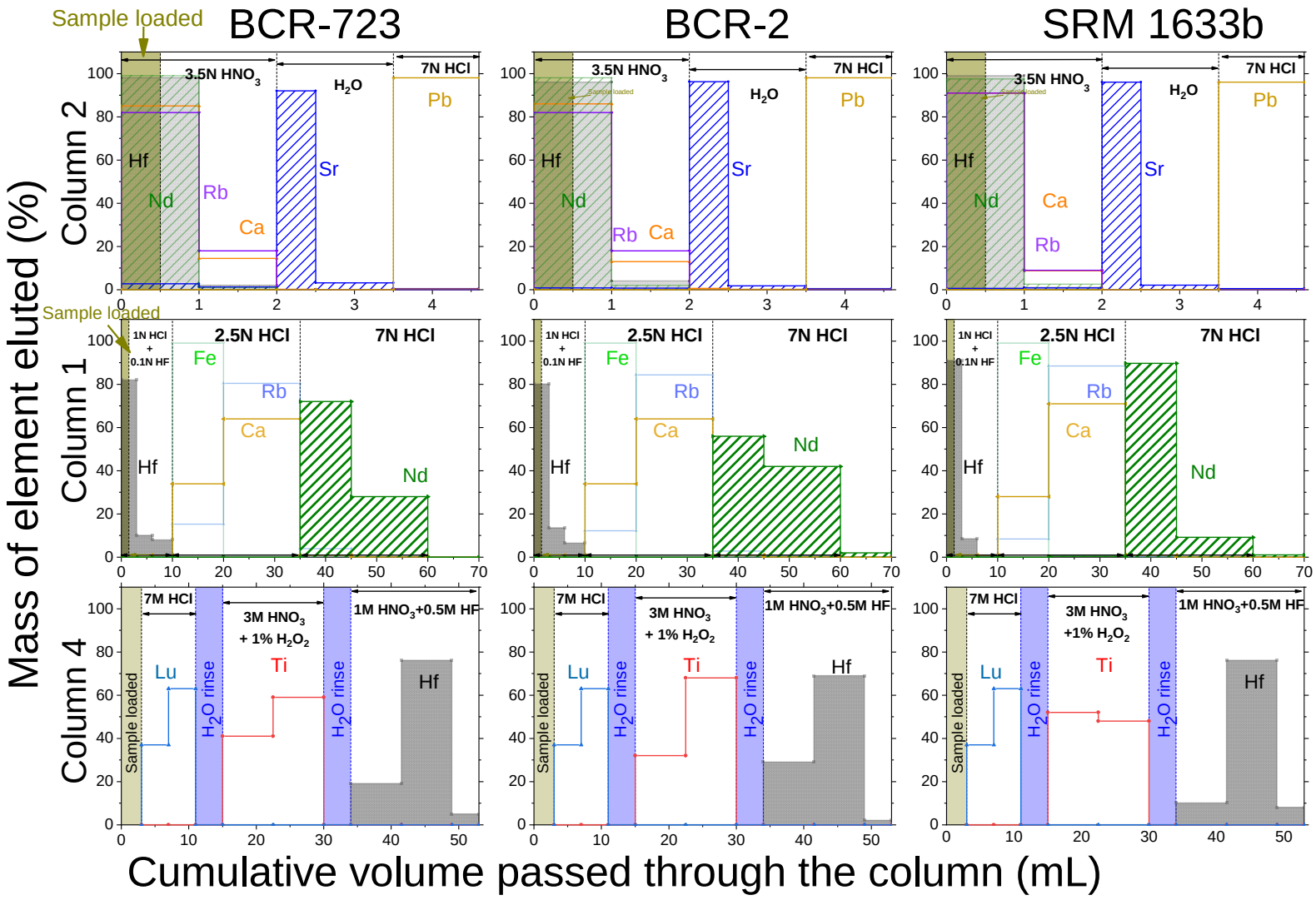

Figure A4. Elution curves for elements from step 1/column 2 (top), step 2/column 1 (middle), and step 4/column 4 (bottom) with the low mass equivalent samples (0.3 mg) of BCR-723 (left), BCR-2 (centre), and SRM 1633b (right).

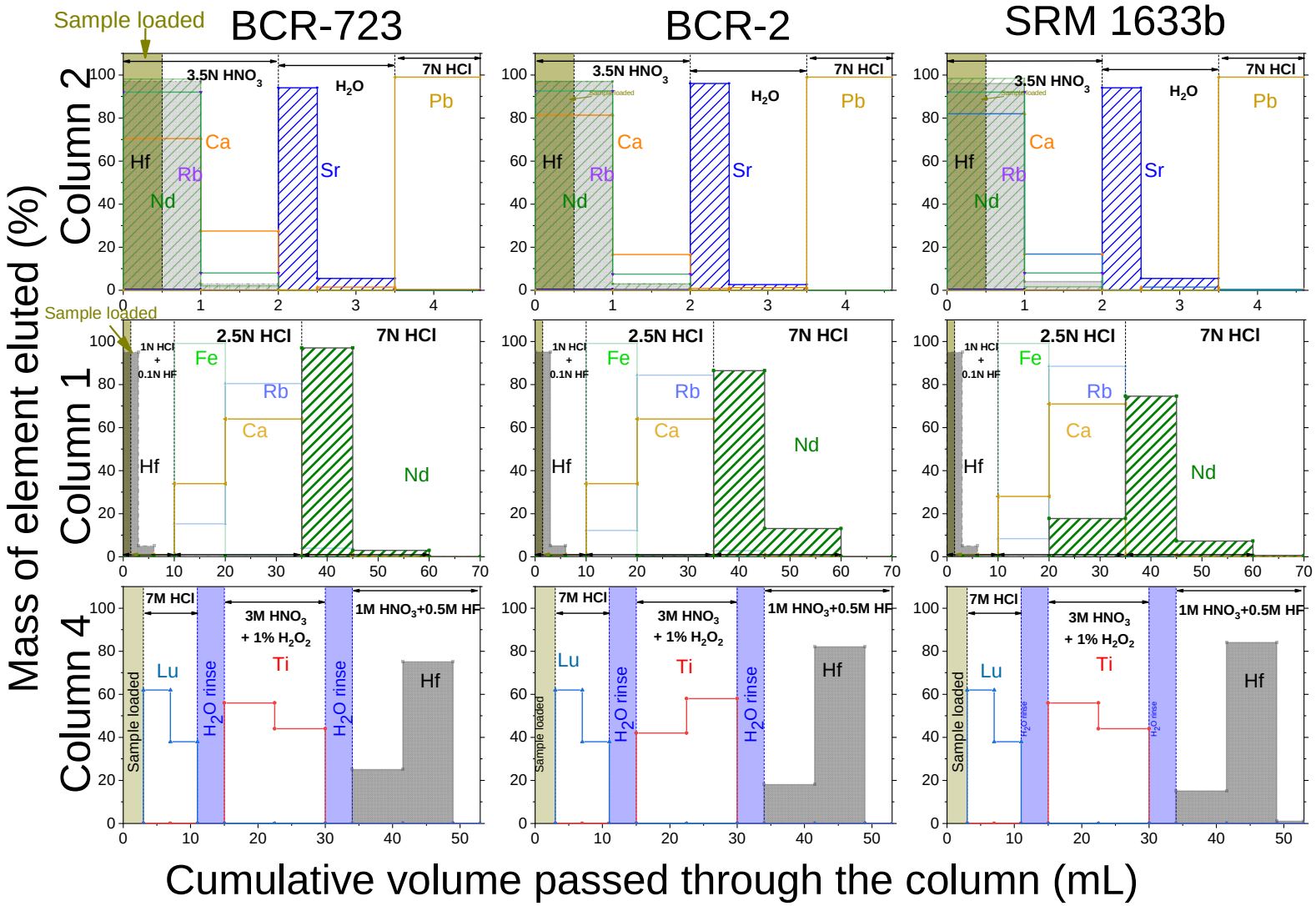

Figure A5. Elution curves of elements from step 1/column 2 (top), step 2/column 1 (middle), and step 4/column 4 (bottom) with 25 mg of BCR-723 (left), BCR-2 (centre), and 1633b (right).

Table A6. Final scheme of chromatography for preparing samples before MC-ICP-MS analysis. The total procedural time was less than 9 hours when Steps 3 and 4 are performed in parallel.

Description	Reagent	Volume	Elements eluted	Comments
Step 1: Sr separation (Sr spec resin) (runtime < 2 hr)				
Loading	3.5M HNO_3	0.5 mL	Ca, Rb, REEs, Matrix elements	The collected cut was dried for Step 2
Rinse	3.5M HNO_3	1.5 mL (0.5x3)		
Collect	H_2O	1.5 mL (0.5x3)	Sr, Ba	Collected cut brought to 2% HNO_3 matrix before analysis
Collect	7M HCl	2 mL (1x2)	Pb	
Step 2: Hf-REE separation (50W-X8 resin) (runtime <2hr)				
Loading	1M HCl + 0.1M HF	1.5 mL	Hf, Ti, Sb, Na, Zr	The collected cut was dried for step 4
Collect	1M HCl + 0.1M HF	8.5 mL (3.5+5)		
Rinse	2.5M HCl	10 mL (5x2)	Fe, Zn, Cu, Mn, Co	
Rinse	2.5M HCl	10 mL (5x2)	Ca, Rb	
Collect	7M HCl	25 mL (5x4)	REEs	The collected cut was dried for step 3
Step 3: Nd-Sm separation (AG 50W-X4 resin) (runtime <5hr)				
Wash	H_2O	0.2 mL		
Load	0.1M HCl	0.5 mL		
Wash	H_2O	0.2 mL		
Collect	0.225M HIBA	3 mL	Lu, Sm	
Collect	0.225M HIBA	5 mL	Nd, Pr	The collected Nd cut was mixed with *Aqua Regia* and heated overnight to 105 °C to eliminate α-HIBA. Finally redissolved in 2% HNO_3 before analysis

Step 4: Ti-Hf separation (Ln-spec resin) (runtime <3hr)				
Load	3M HCl	3 mL	Na and other matrices	
Load	7M HCl	7 mL		
Wash	H_2O	2 mL		
Rinse	3M HNO_3 + 1% H_2O_2	15 mL	Ti, Sb	
Wash	H_2O	2 mL		
Collect	1M HNO_3 + 0.5M HF	5 mL	Hf, Zr	The collected cut was dried redissolved in 2% HNO_3 + trace HF before analysis

A.2. Column calibration procedure

All aliquots collected from chromatography columns were dried in 7 mL and 15 mL PFA vials (Manufacturer: Savillex). Vials were dried overnight at 80 °C on a hot plate that was partially covered to avoid dry samples escaping due to the motion of air inside the evaporation box. Dried samples were dissolved in 2 mL – 5 mL (based on the analyte expected to elute) of 2 % nitric acid before analyzing with an ICP-MS.

Sample prep and loading step

Column I (Sr-Spec mesh 50-100 µm)

Digested samples (of CRMs) were dried in 7 mL PFA vials at 80 °C over a hot plate overnight with a loosely closed cap. Samples were re-dissolved in 0.5 mL of 14 M HNO_3 + 1 M HF and dried again before re-dissolving in 0.5 mL of 3.5 M HNO_3. Samples were centrifuged for 10 min at 8000 rpm. The supernatant was loaded onto the column and each elution aliquot of 0.5 mL were collected in 7 mL PFA vials. Columns with resins were rinsed with 4 mL of 7M HCl, ultrapure H_2O and 3.5M HNO_3 each.

Column II (50W-X8, mesh 200-400 µm, hydrogen form)

Digested samples (of CRMs) were dried in 7 mL PFA vials at 80 °C over a hot plate overnight with loosely closed cap. Samples were redissolved in 0.5 mL of 7 M HCl + 1 M HF and dried again before re-dissolving in 1.5 mL of 1 M HCl + 0.1 M HF. These solutions were centrifuged for 10 min at 8000 rpm. The supernatant was loaded onto the column and elution aliquots were collected in 7 mL PFA vials. Due to high concentration of matrix elements (e.g., Al, Ca, Fe), 0.5 mL of eluants was collected at every 3 mL when passing 2.5 M HNO_3.

Column III (AG 50W-X4, mesh 100-200µm, hydrogen form; 0.225M α-HIBA acid; pH = 4.7)

The aliquots eluted with 7 M HCl from Column I were dried in two 15 mL PFA vials at 80 °C over a hot plate overnight with loosely closed cap. Sample were re-dissolved in 5 mL of 14 M HNO_3 and transferred into vials before drying again and re-dissolving in 0.5 mL of 0.1 M HCl. Samples were centrifuged for 10 min at 8000 rpm. The supernatant was loaded onto the column and each elution aliquot of 0.5 mL was collected in a 7 mL PFA vial. PFA vials were heated overnight at 105 °C after y adding 2 mL of *Aqua Regia* and loosely capping them to destroy the α-HIBA acids and then re-dried before dissolving for ICP-MS analysis. pH of the reagents was measured with an Oakton pH 1100 Benchtop Meter.

Column IV (Ln-Spec mesh 50-100 µm)

The aliquots eluted with 1 M HCl + 0.1 M HF from Column II were dried in 15 mL PFA vials at 80 °C, over a hot plate overnight with loosely closed cap. Samples were re-dissolved in 5 mL of 7 M HCl and dried again before re-dissolving in 3 mL of 3 M HCl. Samples were centrifuged for 10 min at 8000 rpm. The supernatant was loaded onto the column and each elution aliquot of 5 mL was collected in a 7 mL PFA vial.

Steps for reducing contamination

All chemical preparations were conducted on special class 100 work benches inside a class 1000 clean laboratory. All labware (all non-glass columns, vials, frits for columns and pipette tips) were rinsed with ultrapure water before submerging it in acid bath (30% HNO_3 + 0.5M HF) and kept overnight on a hot plate set at 80 °C. Resins were used fresh for all columns except 50WX8 and Ln-Spec resins which were washed with 25 mL of 7M HCl and 5 mL 2M HF. For Ln-Spec

resins HF wash preceded the HCl wash to remove any traces HF in resins before next use, which could have otherwise resulted in leaching of Hf during the loading step. Post acid bath, all apparatus was rinsed thrice with ultrapure water and dried inside a Class 100 laminar flow chemical fume hood. The glass columns, which were used for Sm-Nd separation, were rinsed with 7M HNO_3 followed by ultrapure water before each analysis. The mesh screen used for filtering bulk samples was wiped with alcohol wipes followed by rinsing with 0.05 M HNO_3 solution and ultrapure water after each use.

Purification of reagents

HNO_3, HCl, HF – ACS grade (manufacturer – Fisher chemicals) acids were triple distilled – first by using Savlliex DST-1000 purification system followed by twice through traditional elbow style distillation system. The α-HIBA used in this study was prepared from 2-Hydroxyisobutyric acid in crystalline form obtained from Sigma Aldrich (CAS 594-61-6) following the methods described in Smith and Hoffman, 1956 [335]. Acid crystals were purified by sublimation from a pre-cleaned heated Teflon watch glass on a hot plate in clean-air flow box. Purified crystals condensed in an inverted pre-cleaned Teflon beaker covering the watch glass and were periodically harvested from the walls of the beaker over a two-week period. Purified crystals were then dissolved in an amount of Milli-Q purified H_2O to obtain an approximate 1M solution. This solution was titrated and buffered with ultra-pure ammonium hydroxide, diluted with Milli-Q water, and adjusted to a pH of 4.7 to obtain the 0.225M solution used in this study.

Table A7. Details of all the reagents used in this study. In-house reagents were purified in lab and brought down to metal impurities below 1 ng L^{-1} for Sr, Nd, and Hf (rest other elements were below detection limit with q-ICP-MS). Total contamination from acid blanks have been reported in Table II-1 of the main manuscript.

Reagents used	Steps involving the reagent	Manufacturer	Purity Grade
70% HNO_3	Dissolution	Fisher Chemical™	Optima™
49% HF	Dissolution	Fisher Chemical™	Optima™
99.9995% H_3BO_3	Dissolution	Thermo Scientific™	Puratronic®
7M HCl	Column Chromatography	In house	<1 ng L^{-1} (Sr, Nd, Hf)
20M HF	Column Chromatography	In house	<1 ng L^{-1} (Sr, Nd, Hf)
14M HNO_3	Column Chromatography	In house	<1 ng L^{-1} (Sr, Nd, Hf)
31% H_2O_2	Column Chromatography	Fisher Chemical™	Optima™
2.5M α-HIBA	Column Chromatography		
14.8M NH_4OH	pH correction for α-HIBA	Fisher Chemical™	Optima™

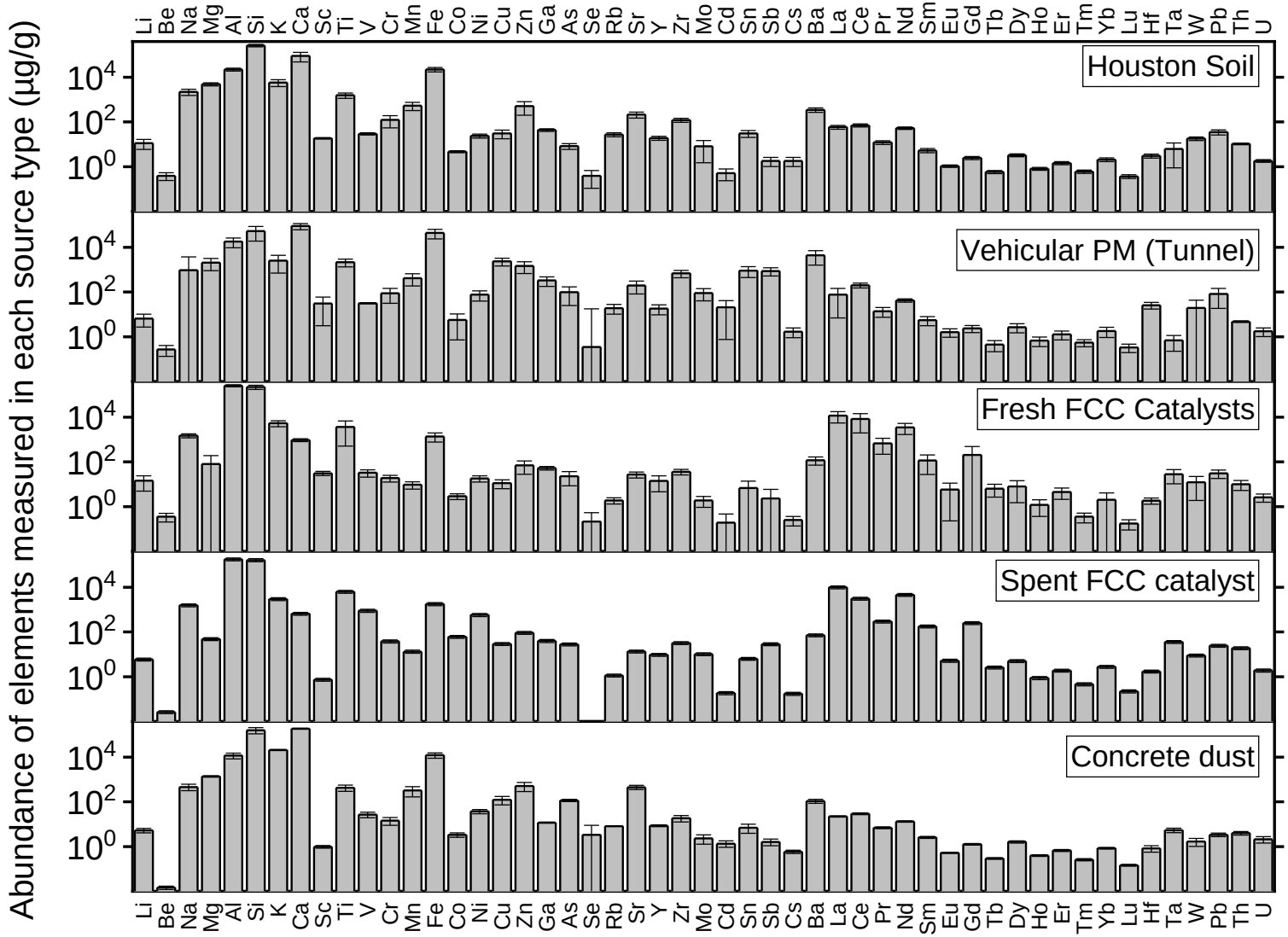

Figure A6. Abundance of elements measured in this study[120] for various PM source samples with DRC-q-ICP-MS expressed as µg element/g sample. Enrichment factor calculated from the abundance has been reported in figure 6 of the main manuscript.

Table A8. Elemental ratios measured in source samples and comparison with long-range transported North African dust composition from our earlier publications [29, 74]. Importantly, elemental ratios in North African dust and soil were either overlapping or were obscured by these ratios measured in anthropogenic sources, which makes North African dust indistinguishable from Houston soil simply by elemental characterization. The highest elemental ratios are written in bold and the corresponding cells are highlighted in blue to aid in reading.

Ratio	N. African dust in Barbados (Bozlaker et al 2018, 2013)		Local Houston soil		Vehicular PM		Concrete dust		FCC catalysts	
	Avg ± Std dev	Range	Avg ± Std dev	Range	Avg ± Std dev		Avg ± Std dev	Range	Avg ± Std dev	Range
Mineral dust marker elements (N. African dust, Soil, Concrete)										
Si/Al	1.4 ± 0.5	0.8 - 2.5	12 ± 3	9 - 14	2.8 ± 0.6	2.4 - 3.2	15 ± 9	9 – 21	0.9 ± 0.1	0.8 - 1.0
Ti/Al	0.05 ± 0.01	0.05 - 0.06	0.07 ± 0.02	0.054 - 0.10	0.12 ± 0.01	0.12 - 0.13	0.036 ± 0.001	0.036 - 0.037	0.02 ± 0.01	0.01 - 0.04
K/Al	0.27 ± 0.05	0.2 - 0.35	0.3 ± 0.1	0.2 - 0.4	0.13 ± 0.04	0.1 - 0.16	1.85 ± 0.5	1.53 - 2.18	0.021 ± 0.006	0.015 - 0.027
Ca/Al	0.6 ± 0.2	0.4 - 0.9	4 ± 2	2 - 7	5.2 ± 0.9	4.6 - 5.8	17 ± 4	14 - 19	0.004 ± 0.001	0.003 - 0.004
Fe/Al	0.51 ± 0.02	0.47 - 0.52	1.0 ± 0.3	0.8 - 1.4	2.46 ± 0.02	2.45 - 2.47	1.04 ± 0.03	1.02 - 1.06	0.007 ± 0.002	0.005 - 0.010
Si/Fe	2.8 ± 1	1.6 - 4.9	12 ± 4	10 - 18	1.2 ± 0.2	1.0 - 1.3	14 ± 8	9 - 20	150 ± 4	93 - 190
Ti/Fe	0.11 ± 0.01	0.1 - 0.12	0.08 ± 0.04	0.05 - 0.13	0.05 ± 0.01	0.04 - 0.05	0.035 ± 0.002	0.034 - 0.036	2.4 ± 0.8	1.8 - 3.6
K/Fe	0.54 ± 0.09	0.42 - 0.69	0.3 ± 0.2	0.2 - 0.5	0.05 ± 0.02	0.04 - 0.07	1.8 ± 0.4	1.5 - 2.1	3.4 ± 1.5	1.7 - 5.0
Ca/Fe	1.1 ± 0.3	0.9 - 1.9	4 ± 1	2 - 5	2.1 ± 0.4	1.9 - 2.4	15.8 ± 3.4	13.4 - 18.2	0.6 ± 0.1	0.4 - 0.7
FCC marker elements										
La/Ce	0.48 ± 0.01	0.46 - 0.48	0.9 ± 0.2	0.6 - 1.1	0.4 ± 0.3	0.2 - 0.5	0.75 ± 0.02	0.74 - 0.76	2.6 ± 1.2	1.3 – 4.0
La/Pr	4.2 ± 0.1	4.1 - 4.2	23 ± 7	14 - 32	22 ± 12	13 - 31	14.3 ± 0.5	14 - 14.7	24 ± 9	14 - 34
La/Nd	1.10 ± 0.01	1.09 - 1.10	1.1 ± 0.1	0.9 - 1.2	1.7 ± 1.3	0.7 - 2.6	1.70 ± 0.01	1.66 - 1.67	3.1 ± 1.5	1.6 - 4.9
La/Sm	5.9 ± 0.1	5.8 - 6.1	12 ± 4	7 - 16	12 ± 7	7 - 17	8.6 ± 0.4	8.4 - 8.9	76 ± 16	56 - 93
Vehicular marker elements										
Cu/Ti×100	1.9 ± 1.0	0.8 - 4.3	0.13 ± 0.07	0.03 - 0.19	39.7 ± 0.6	39.3 - 40.2	0.38 ± 0.01	0.37 - 0.38	0.1 ± 0.2	0.02 - 0.5
Cd/Ti×100	0.03 ± 0.01	0.01 - 0.04	2 ± 1	0.6 - 3	110 ± 0.3	110 - 110	29 ± 3	26 - 31	0.34 ± 0.08	0.29 - 0.46
Pb/Ti×100	0.7 ± 0.1	0.6 - 1	0.04 ± 0.02	0.01 - 0.06	0.85 ± 0.6	0.42 - 1.27	0.314 ± 0.003	0.311 - 0.317	0.002 ± 0.001	0.002 - 0.003
Mo/Ti×100	0.04 ± 0.01	0.03 - 0.06	0.3 ± 0.1	0.1 - 0.4	4.0 ± 0.8	3.5 - 4.6	0.5 ± 0.1	0.5 - 0.6	0.04 ± 0.01	0.04 - 0.05
Sb/Zn×100	0.6 ± 0.2	0.4 – 1.0	2 ± 1	1 - 3	3 ± 2	2 - 5	0.8 ± 0.1	0.7 - 0.9	0.7 ± 0.2	0.4 - 0.8
Cu/Zn×100	40 ± 20	9 - 60	0.4 ± 0.1	0.3 - 0.5	61 ± 10	55 - 68	0.32 ± 0.04	0.29 - 0.35	9 ± 15	1.3 - 31
Cd/Zn×100	0.5 ± 0.2	0.2 - 0.7	7 ± 2	4 - 10	170 ± 30	150 - 190	24.3 ± 0.5	23.8 - 24.7	22 ± 8	14 - 32
Mo/Zn×100	0.9 ± 0.5	0.1 - 1.4	0.8 ± 0.2	0.5 - 1.1	6.2 ± 0.1	6.1 - 6.2	0.4 ± 0	0.4 - 0.4	5 ± 4	2 - 11

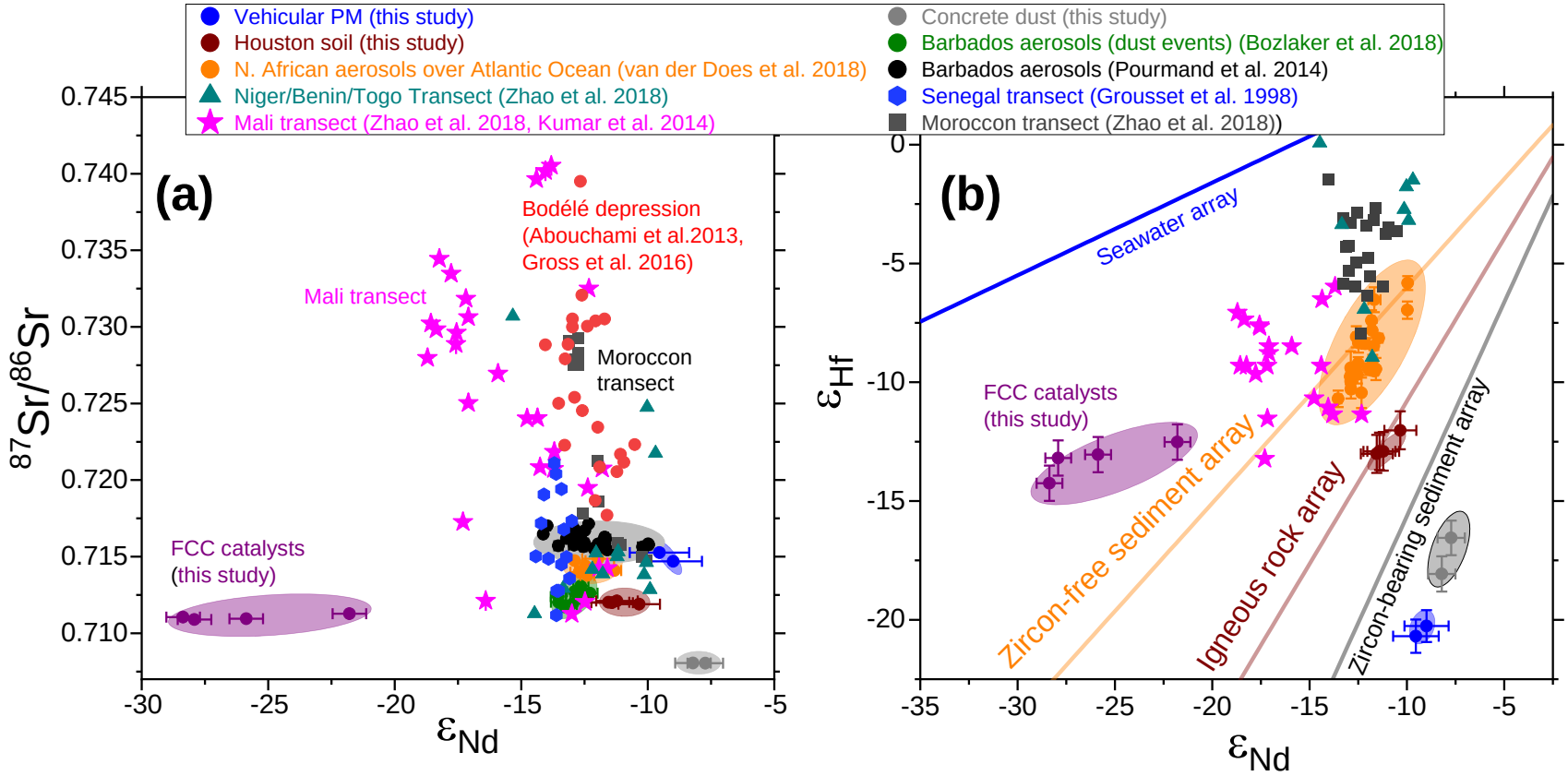

Figure A7. Comparison of Houston urban sources with potential source areas (PSAs) for North African dust [72, 74] show clear contrast in both (a) Sr-Nd isotopic ratio graph and (b) Hf-Nd isotopic ratio graph. PSAs shown in the figures are compiled from literature studies of North African regions – Niger/Benin/Togo [72], Mali [46, 72], Senegal [144], Morocco [72], and Chad [71, 336].

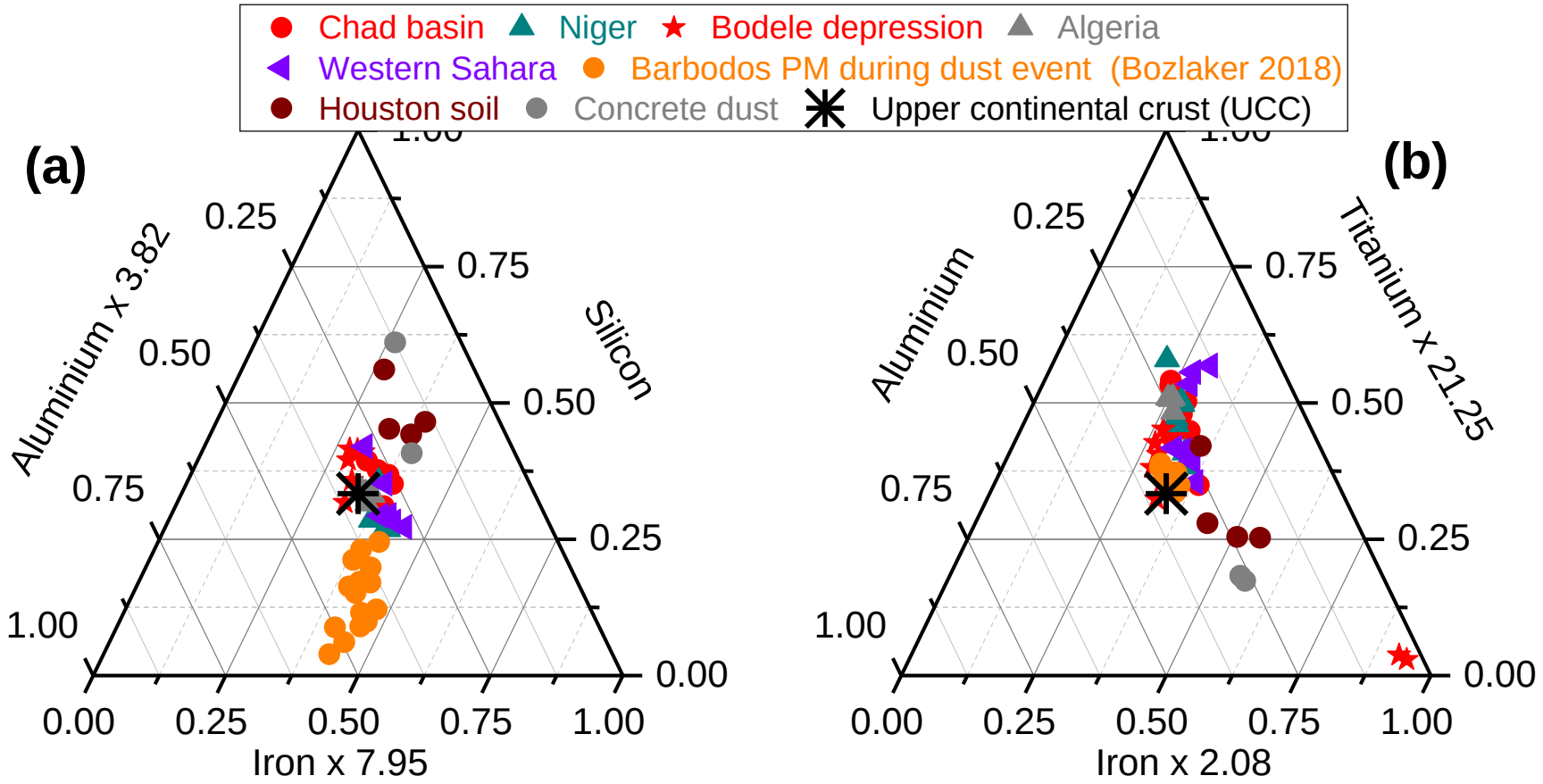

Figure A8. Contrary to isotopic ratios (Appendix Figure A7) key major elemental compositions (left panel Figure (a) Fe-Si-Al and right panel Figure (b) Fe-Ti-Al) did not show very distinct characteristics between mineral sources (this study), North African dust PM collected at Barbados [74] and various potential source regions in North Africa [71, 337, 338]. Mineral sources clustering near the centre shows these elements as weak tracers. Ternary graphs have been normalized to make upper continental crust (UCC) [120] lie at the centre.

Table A9. Method detection limits (MDLs) and average PTFE filter blank concentrations measured by DRC-q-ICP-MS. PTFE blanks represent blanks for $PM_{2.5}$ aerosols collected by an air sampler (Thermo Fisher Partisol™ 2025i Sequential Air Sampler) and used as a negative control in this study (for aerosols collected at Washburn Tunnel). BDL = Below detection limit. STD – analytes measured in standard mode (i.e., using no collision cell gas). DRC – analytes measures with dynamic reaction cell method with ammonia as cell gas.

Element	m/z	MDL (µg L-1)	Mode	Average PTFE filter blank (ng)	Element	m/z	MDLs (µg L-1)	Mode	Average PTFE filter blank (ng)
Li	7	0.03	STD	<2.25	La	139	0.014	STD	<1.05
Be	9	0.03	STD	<2.25	Ce	140	0.015	STD	<1.13
Mg	25	0.4	STD	44 ± 14	Pr	141	0.007	STD	<0.53
Al	27	0.61	DRC	195±48	Nd	146	0.008	STD	0.020
Si	29	35	STD	<2625	Sm	152	0.002	STD	<0.15
K	39	1.2	STD	<90	Eu	153	0.002	STD	<0.15
Ca	44	11.5	STD	3000 ± 1590	Gd	158	0.002	STD	<0.15
Ti	47	0.22	STD	<16.5	Tb	159	0.002	STD	<0.15
V	51	0.79	DRC	<59.3	Dy	164	0.003	STD	<0.225
Cr	52	0.1	DRC	<7.5	Ho	165	0.003	STD	<0.225
Mn	55	0.03	STD	<2.25	Er	166	0.003	STD	<0.225
Fe	57	1.7	DRC	<128	Yb	174	0.002	STD	<0.15
Ni	58	0.03	DRC	<2.25	Lu	175	0.002	STD	<0.15
Co	59	0.05	STD	<3.75	Hf	178	0.001	STD	0.040
Cu	65	0.004	DRC	<0.3	W	184	0.04	STD	<3
Zn	66	0.01	DRC	<0.75	Pb	208	0.05	STD	<3.75
Ga	69	0.05	STD	<3.75	Th	232	0.012	STD	<0.9
As	75	0.04	DRC	<3	U	238	0.009	STD	<0.68
Se	82	0.11	DRC	<8.25					
Rb	85	0.04	STD	<3					
Sr	88	0.04	STD	0.12					
Y	89	0.03	STD	<2.25					
Zr	90	0.04	STD	<3					

Mo	96	0.04	STD	<3					
Cd	113	0.04	STD	<3					
Sn	118	0.04	STD	<3					
Sb	121	0.04	STD	<3					
Cs	133	0.03	STD	<2.25					
Ba	138	0.22	STD	<16.5					

Table A10. Ratio of signal isobaric interference to total measured signal in the isotope of interest show degree of cleaning by our column procedure. The signals measured in each Faraday cup is reported (all signal values in Volts). $^{n}\Sigma$ represents cumulative sum of all isotopes at mass '*n*'. Less than 0.2% of total signal were from ^{86}Kr, ^{87}Rb, and ^{144}Sm interference on ^{86}Sr, ^{87}Sr and ^{144}Nd respectively. ^{176}Lu and ^{176}Yb had less than 0.01% of interference on ^{176}Hf.

Samples	Signal measured by Faraday cups (Volts)									Proportion of Interfering Signal	
Faraday cups	L4	L3	L2	L1	C (Center)	H1	H2	H3	H4		
Isotope Ratio	$^{87}Sr/^{86}Sr$									$^{86}Kr/^{86}\Sigma$	$^{87}Rb/^{87}\Sigma$
Mass measured	82	83	84	85	86	87	88	90			
Blank	5.42E-04	3.35E-04	1.69E-03	2.43E-04	1.55E-03	1.25E-03	3.58E-03	4.80E-07		3.26E-01	6.07E-02
0.3 mg SRM 1648a	6.26E-04	3.61E-04	4.51E-02	7.82E-04	3.96E-01	2.87E-01	3.43E+00	1.30E-06		1.37E-03	7.62E-04
25 mg SRM 1648a	6.43E-04	5.80E-04	9.27E-02	1.10E-03	1.64E+00	1.19E+00	1.42E+01	3.13E-06		5.32E-04	2.59E-04
Isotope Ratio	$^{143}Nd/^{144}Nd$									$^{144}Sm/^{144}\Sigma$	
Mass measured	140	142	143	144	145	146	147	148	150		
Blank	5.67E-02	1.70E-02	4.39E-03	8.69E-03	3.03E-03	6.37E-03	1.07E-04	2.26E-03	2.22E-03	2.54E-03	
0.3 mg SRM 1648a	2.82E-02	9.20E-01	2.71E-01	5.35E-01	1.88E-01	3.93E-01	5.34E-03	1.37E-01	1.36E-01	2.06E-03	
25 mg SRM 1648a	1.47E-02	3.90E+01	1.76E+01	3.48E+01	1.22E+01	2.56E+01	4.39E-02	8.73E+00	8.69E+00	2.61E-04	
Isotope Ratio	$^{176}Hf/^{177}Hf$									$^{176}Yb/^{176}\Sigma$	$^{176}Lu/^{176}\Sigma$
Mass measured	172	174	175	176	177	178	179	180			
Blank	4.19E-06	5.38E-06	1.93E-06	1.21E-04	4.24E-04	6.26E-04	3.17E-04	8.22E-04		5.77E-03	8.21E-05
0.3 mg SRM 1648a	4.41E-06	3.82E-04	5.31E-06	1.26E-02	4.50E-02	6.65E-02	3.34E-02	8.66E-02		5.73E-05	2.13E-06
25 mg SRM 1648a	9.53E-06	1.03E-02	5.49E-06	3.42E-01	1.22E+00	1.80E+00	9.08E-01	2.36E+00		4.57E-06	8.10E-08

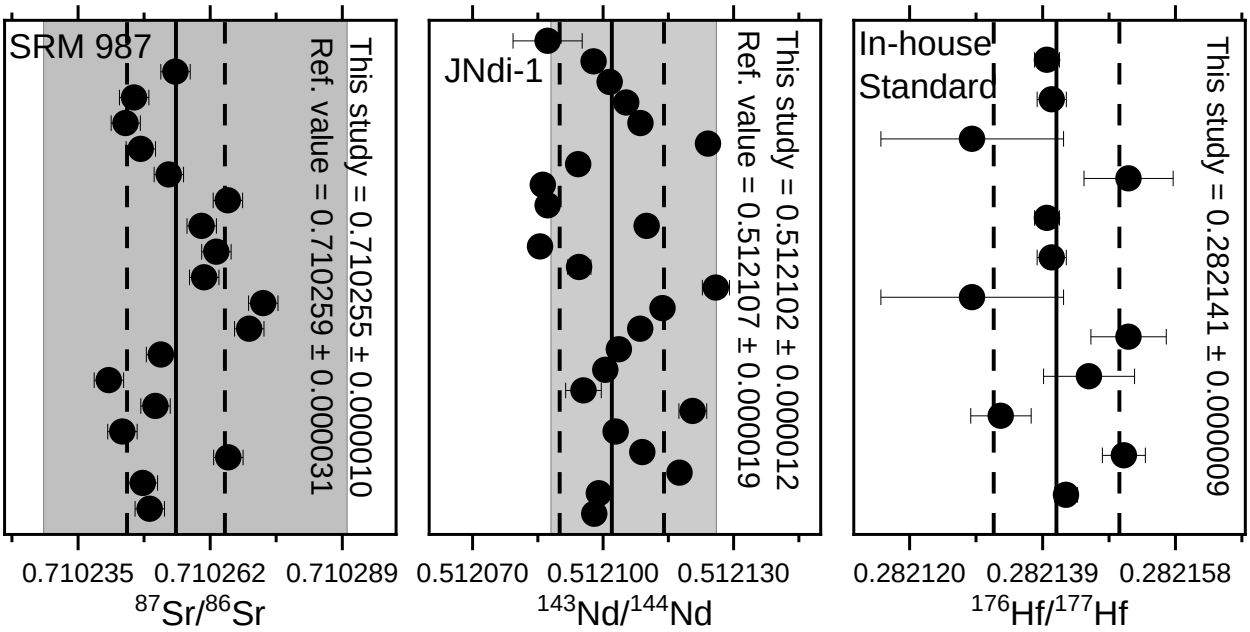

Figure A9. SRM 987, JNdi-1, and an in-house prepared standard were measured over 2-years to establish the intermediate precision and calculate the predicted external error/uncertainty propagation. The gray bands represent the ± standard deviation of range of values reported since the year 2015 for the reference standards [112]. The data reported here represented the mean value ± standard deviation measured in this study.

Table A11. The error propagated due to external factors calculated as 2×standard deviations (95% prediction interval) from repetitive measurements of solution-based standards (shown in Figure A.6)

Isotope ratio	Uncertainty propagated due to long-term instrumental variation (10^{-6})
$^{87}Sr/^{86}Sr$	20
$^{143}Nd/^{144}Nd$	24
$^{176}Hf/^{177}Hf$	19

Table A12. Isotopic measurements of source samples analyzed in this study.

Sample type	Sample ID	$^{87}Sr/^{86}Sr$	95% C.I.	$^{143}Nd/^{144}Nd$	95% C.I.	$^{176}Hf/^{177}Hf$	95% C.I.
Soil	Soil1	0.711990	0.000009	0.512053	0.000007	0.28241	0.00001
	Soil2	0.712020	0.000009	0.512046	0.000007	0.28240	0.00002
	Soil3	0.711900	0.000009	0.512108	0.000007	0.28243	0.00001
	Soil4	0.712110	0.000009	0.512063	0.000007	0.28241	0.00002
Average		0.71201	0.00008	0.51207	0.00003	0.28241	0.00002
FCC catalyst	FCC1	0.710900	0.000004	0.511207	0.000003	0.282399	0.000002
	FCC2	0.710943	0.000004	0.511312	0.000003	0.282403	0.000002
	FCC3	0.711052	0.000005	0.510984	0.000003	0.282369	0.000002
	FCC Spent	0.711276	0.000004	0.511521	0.000003	0.282418	0.000002
Average		0.7110	0.0002	0.5113	0.0002	0.28240	0.00002
Concrete dust/ Construction activity	Construction1	0.708060	0.000009	0.512217	0.000004	0.282261	0.000010
	Construction2	0.708040	0.000009	0.512242	0.000004	0.282304	0.000009
Average		0.70805	0.00002	0.51223	0.00002	0.28228	0.00003
Vehicular PM	Tunnel1	0.714691	0.000006	0.512152	0.000009	0.28220	0.00002
	replicate	0.714656	0.000006		0.000009		
	Tunnel2	0.715281	0.000007	0.512092	0.000009	0.282189	0.000005
	replicate	0.715256	0.000007		0.000009		
	Background1	0.711210	0.000007	0.51193	0.00001	0.282161	0.000005
	Background2	0.715536	0.000007	0.51158	0.00001	0.282213	0.000005
	Vehicle1	0.714691	0.000009	0.51218	0.00002	0.282199	0.000005
	Vehicle2	0.715266	0.000010	0.51215	0.00002	0.282187	0.000007
Average		0.7150	0.0004	0.51216	0.00004	0.28219	0.00002

Table A13. Isotope ratios measured for four reference materials (BCR-2, SRM 1648a, BCR-723, and SRM 1633b) with replicate measurements.

Reference material	$^{87}Sr/^{86}Sr$	95% C.I.	$^{143}Nd/^{144}Nd$	95% C.I.	$^{176}Hf/^{177}Hf$	95% C.I.
	0.705017	0.000006	0.512685	0.000007	0.282841	0.000003
	0.705024	0.000006	0.512646	0.000007	0.282842	0.000003
BCR2	0.705021	0.000006	0.512624	0.000007	0.282849	0.000003
	0.705012	0.000006	0.512598	0.000008	0.282855	0.000003
	0.704996	0.000006	0.512611	0.000007	0.282861	0.000002
Average	0.705014	0.000012	0.512633	0.000031	0.282850	0.000008
	0.712575	0.000004	0.511758	0.000008	0.282399	0.000002
	0.712595	0.000004	0.511734	0.000008	0.282403	0.000002
1648a	0.712569	0.000005	0.511710	0.000008	0.282369	0.000002
	0.712575	0.000004	0.511734	0.000008	0.282418	0.000002
	0.712575	0.000005	0.511764	0.000008	0.282386	0.000002
Average	0.712578	0.000010	0.511740	0.000021	0.282395	0.000017
	0.709961	0.000009	0.512206	0.000005	0.282261	0.000010
	0.710021	0.000009	0.512223	0.000006	0.282304	0.000009
BCR723	0.709971	0.000009	0.512216	0.000005	0.282247	0.000009
	0.710017	0.000009	0.512246	0.000005	0.282289	0.000009
	0.709998	0.000010	0.512223	0.000005	0.282243	0.000009
Average	0.709994	0.000026	0.512223	0.000014	0.282269	0.000026
	0.703040	0.000006	0.512623	0.000005	0.282461	0.000005
	0.703049	0.000007	0.512597	0.000004	0.282439	0.000005
1633b	0.703032	0.000007	0.512571	0.000004	0.282465	0.000005
	0.703046	0.000007	0.512598	0.000004	0.282437	0.000005
	0.703058	0.000007	0.512568	0.000004	0.282470	0.000005
Average	0.703045	0.000011	0.512591	0.000021	0.282454	0.000015

A.3. Uncertainty calculation

The measured isotope ratio of a sample can be represented as the actual ratio plus the bias due to three major sources [100]; (i) electronic noise and fractionation (*f(r)*), (ii) blank *(P_{bk})*, and (iii) long term (external) bias (P_{ex}). To obtain total uncertainty in the measured ratio (*R*), biases due to instrumental noise, mass fractionation, interference, blank contamination, and external factors can be expressed as:

$$r = g(R, f(r), P_{bk}, P_{ex}) \tag{A1}$$

In Equation (A1) $g()$ is the function that calculates the actual ratio (*r*) based on several bias corrections as mentioned above. The actual ratio (*r*) is a fixed value that is unknown, theoretically does not have uncertainty. The uncertainty in the measured ratio (*R*) needs to be calculated which is accumulated from the above discussed biases. The net uncertainty based on independent correction from instrumental noise, and fractionation correction ($f(r)$), blank correction (P_{bk}) and long-term instrumental bias correction (P_{ex}). The uncertainty model for the equation above (A1) can be written as

$$u(R) = h\left(u\big(f(r)\big), u(P_{bk}), u(P_{ex})\right) \tag{A2}$$

Where $h()$ is the uncertainty function based on the correction function $g()$. The first expression refers to internal standard error measured from a single measurement after fractionation correction and instrumental noise subtraction. This was empirically determined as a function of signal (*N*) for the reference isotope of each element (see Figure 3 in the main manuscript). The modeled uncertainty function was based on error propagation from different variables [100], and can be represented as:

$$u(f(r)) = \sqrt{\left(\frac{k_1}{\sqrt{N}}\right)^2 + \left(\frac{k_2}{N}\right)^2} \quad \text{(A3)}$$

Where k_1 and k_2 are constants that were empirically calculated for each element. First-term is based on uncertainties of primary isotopes whereas the second term may have been from fractionation corrections which becomes prominent in low concentration samples [99, 100].

The effect of blanks on the current measurements can be corrected by an end-member mixing model where the first end member is blank and the other being the actual sample ratio [101, 102]. Blank corrections can be represented as:

$$R_{spl} = \frac{N_{ms}R_{ms} - N_{bk}R_{bk}}{N_{ms} - N_{bk}} \quad \text{(A4)}$$

Where R_{spl} is the actual ratio of the sample, R_{ms} is the measured ratio of the sample, R_{bk} is the ratio measured for blanks. $N_{ms}\ and\ N_{bk}$ are the signal measured for a sample and blank, respectively. Since blank signals are at least 100 times lower (see Figure 3 in the main manuscript) than any sample we can rewrite blank correction as:

$$R_{spl} = R_{ms} - \left(\frac{N_{bk}}{N_{ms}}\right)(R_{bk} - R_{ms}) \quad \text{(A5)}$$

Where $R_{spl} - actual\ ratio\ of\ the\ sample\ ;\ R_{ms} - measured\ ratio; N - singal\ measured$. Hence,

$$P_{bk} = \left(\frac{N_{bk}}{N_{ms}}\right)(R_{bk} - R_{ms}) \quad \text{(A6)}$$

$$u(P_{bk}) = \left(\frac{N_{bk}}{N_{ms}}\right).\sqrt{\left(u(R_{bk})\right)^2 + \left(u(R_{ms})\right)^2} \quad \text{(A7)}$$

Since uncertainty is observed to have inverse proportionality to signal $u(R_{bk}) \gg u(R_{ms})$. Therefore,

$$u(P_{bk}) = \left(\frac{N_{bk}}{N_{ms}}\right).u(R_{bk}) \quad \text{(A8)}$$

Quantifying blank and its effect was difficult as some signals lie below or near baseline resulting in large noise on both primary isotope ratio as well as reference isotope ratio used for fractionation correction. Hence, an improvised method was adopted based on the standard-sample bracketing (SSB) method [7] by making calibration curves with standards at different concentrations for each batch run. This method also minimized the long-term repeatability bias that may occur due to small day-to-day changes in instrument behavior. Calibration curves with three or four data points were used to calculate R_{bk} as well as R_{std}. The value of the latter was used to normalize any deviation caused by instrumental drift due to changes in instrumental settings and user.

Hence,

$$R = (f(r) + P_{bk}).P_{ex} \quad \text{(A9)}$$

$$u(R) = u(P_{ex}) + \sqrt{\left(u\left(f(r)\right)\right)^2 + \left(u(P_{bk})\right)^2} \quad \text{(A10)}$$

P_{ex} was calculated as twice the standard deviation obtained from measuring external standards at very high concentrations (nullifying the effect of uncertainty due to instrumental noise, interference correction, and blank corrections) on different days over a 2-year time span. Measured values are presented in Table A12. Since P_{ex} was a constant, *u(R)* was a function of signal (*N*)

The above equation (A10) was valid only if the time of analysis was fixed (~34 min in this study). The uncertainty (the 95% confidence band) decreases as the time of analysis is increased. The standard deviation stabilized after ~3 min (see Figure A.7). The uncertainty after stabilization point was inversely proportional to $\sqrt{t}$ as the number of measurements increased without change in standard deviation.

$$u(R,t) = u(R,t_0)\sqrt{\frac{t_0}{t}} \tag{A11}$$

Where $u(R,t_0)$ is the uncertainty in measurement when a sample is analyzed with reference time t_0 (equation A10), which was set at 34 min in this study and t = time of analysis.

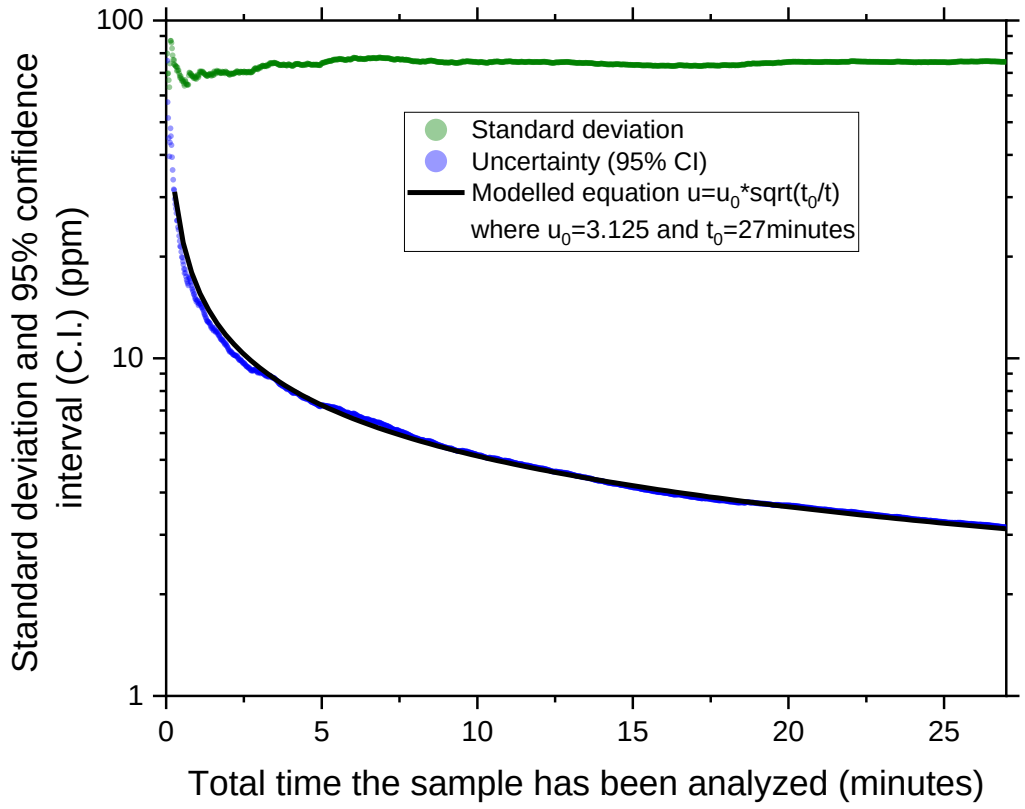

Figure A10. Decrease in standard error and thus the 95% confidence interval (CI) is an inverse square root function of time (u= u_0 √(t_0/t)) with u_0 = 3.125 and t_0 = 27 minutes.

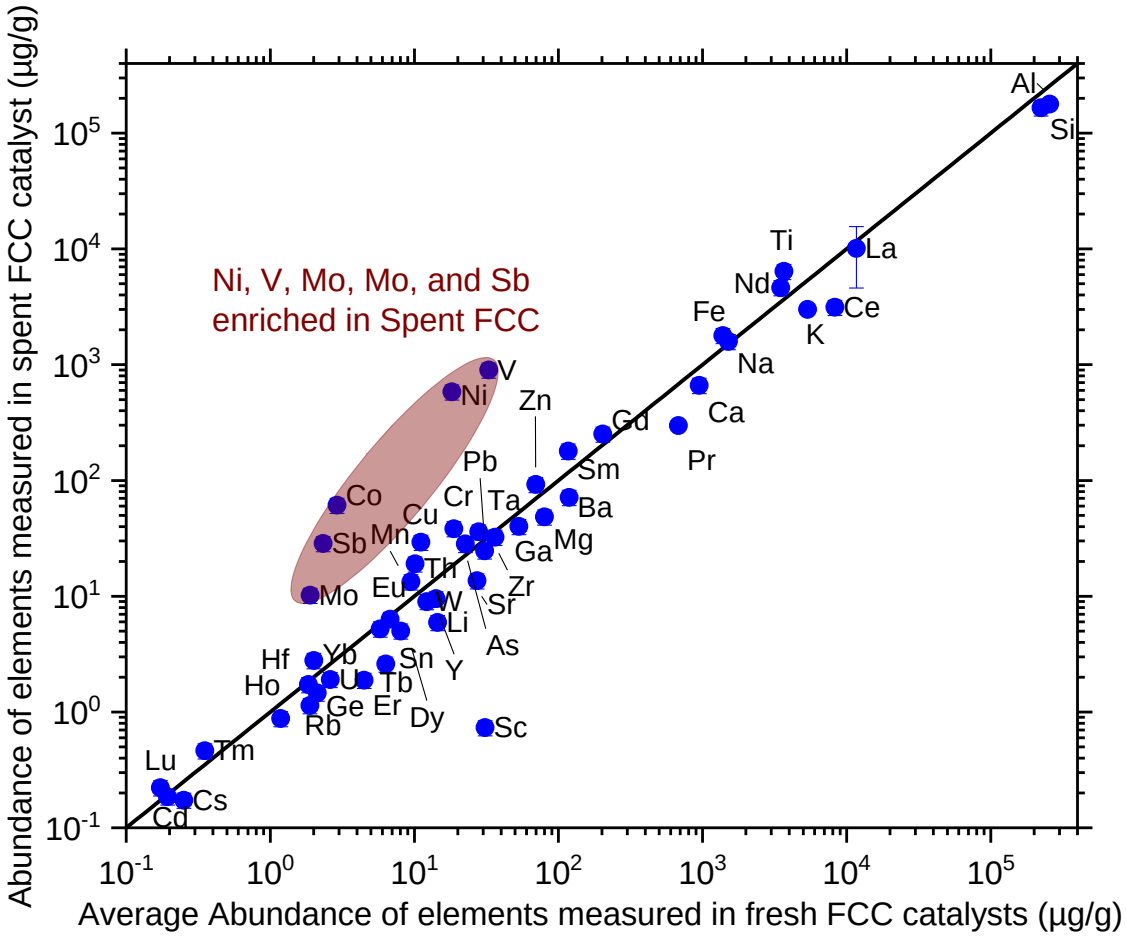

Figure A11. Comparison between metal composition in spent FCC and fresh FCC catalysts show significant enrichment of trace metals (V, Co, Ni, Co, Mo, and Sb) attributed to metal poisoning of catalysts after prolonged use in the fluid catalyst cracking unit.

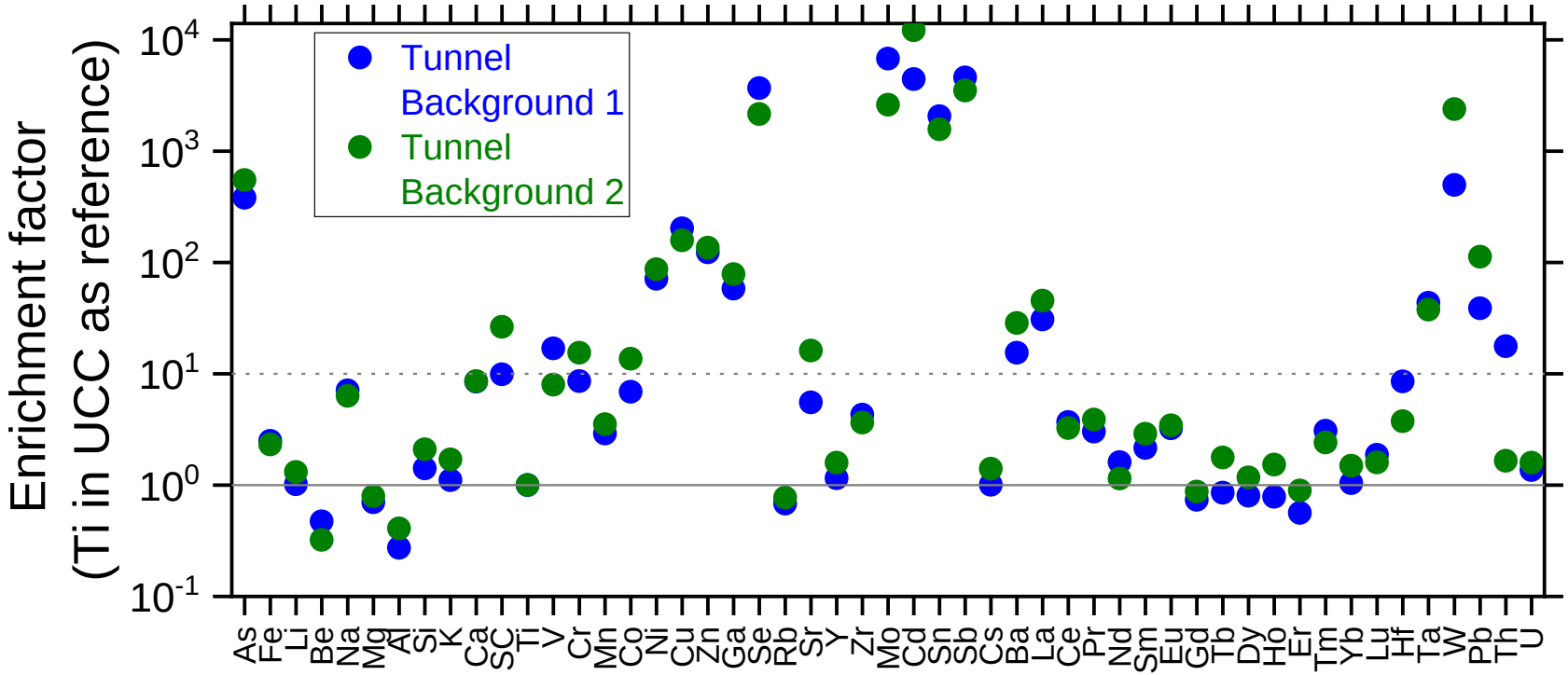

Figure A12. Enrichment factors in Washburn Tunnel background (ventilation room samples) were >100 for multiple transition and post-transition metals attributed to one or more unknown anthropogenic influences such as petroleum refineries, and shipping activities [21, 23].

APPENDIX B

SUPPORTING INFROMATION FOR CHAPTER III

Table B1. Abbreviation and description of all samples collected and analyzed in this study. PM concentration calculated based on particulates weighed on filters.

Sample number	Sample ID	Description	Sample start date	Sample end date	Location	PM concentration (in μg m^{-3})
B1	BAD1	TSP sample collected in Barbados during active dust event	25-Jun-17	28-Jun-17	13.165N, 59.432W	85.8
B2	BAD2	TSP sampled collected in Barbados a day after the dust event	28-Jun-17	29-Jun-17	13.165N, 59.432W	9.2
B3	BAD3	TSP sample collected in Barbados during active dust event	21-Jul-17	22-Jul-17	13.165N, 59.432W	36.6
B4	BAD4	TSP sampled collected in Barbados a day after the dust event	22-Jul-17	23-Jul-17	13.165N, 59.432W	56.9
1	CL1	$PM_{2.5}$ collected at Clinton Dr., Houston	28-Jun-17	29-Jun-17	29.734N, 95.258W	9.3
2	CL2	$PM_{2.5}$ collected at Clinton Dr., Houston	29-Jun-17	30-Jun-17	29.734N, 95.258W	16.3
3	CL3	$PM_{2.5}$ collected at Clinton Dr., Houston	30-Jun-17	1-Jul-17	29.734N, 95.258W	31.7
4	CL4	$PM_{2.5}$ collected at Clinton Dr., Houston	1-Jul-17	2-Jul-17	29.734N, 95.258W	29.0
5	CL5	$PM_{2.5}$ collected at Clinton Dr., Houston	2-Jul-17	3-Jul-17	29.734N, 95.258W	12.9

6	CL6	$PM_{2.5}$ collected at Clinton Dr., Houston	3-Jul-17	4-Jul-17	29.734N, 95.258W	11.7
7	CL7	$PM_{2.5}$ collected at Clinton Dr., Houston	25-Jul-17	26-Jul-17	29.734N, 95.258W	10.2
8	CL8	$PM_{2.5}$ collected at Clinton Dr., Houston	26-Jul-17	27-Jul-17	29.734N, 95.258W	25.2
9	CL9	$PM_{2.5}$ collected at Clinton Dr., Houston	27-Jul-17	28-Jul-17	29.734N, 95.258W	32.3
10	CL10	$PM_{2.5}$ collected at Clinton Dr., Houston	28-Jul-17	29-Jul-17	29.734N, 95.258W	17.9
11	CL11	$PM_{2.5}$ collected at Clinton Dr., Houston	29-Jul-17	30-Jul-17	29.734N, 95.258W	10.3
12	CL12	$PM_{2.5}$ collected at Clinton Dr., Houston	30-Jul-17	31-Jul-17	29.734N, 95.258W	13.4

TSP stands for Total Suspended Particulate matter

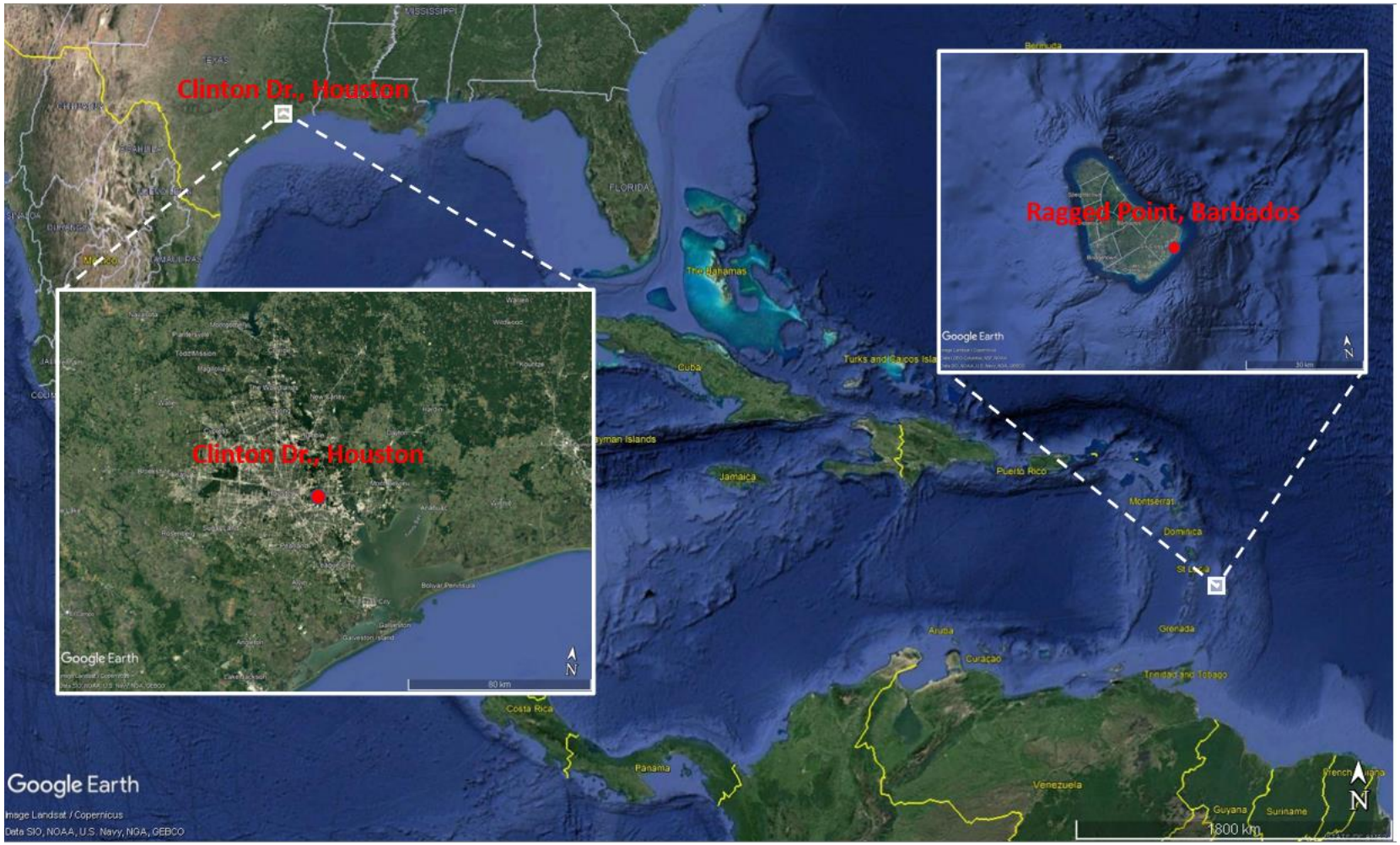

Figure B1. Map of the sampling location in Clinton Drive, Houston (latitude: 29.734, longitude: -95.258) for urban $PM_{2.5}$ and Ragged Point, Barbados (latitude:13.165, longitude: -59.432) for incoming North African dust characterization. The above graphic was created using a Google product. Map data: Google Earth

B.1. QUALITATIVE EVIDENCE OF AFRICAN DUST

HYSPLIT Trajectories

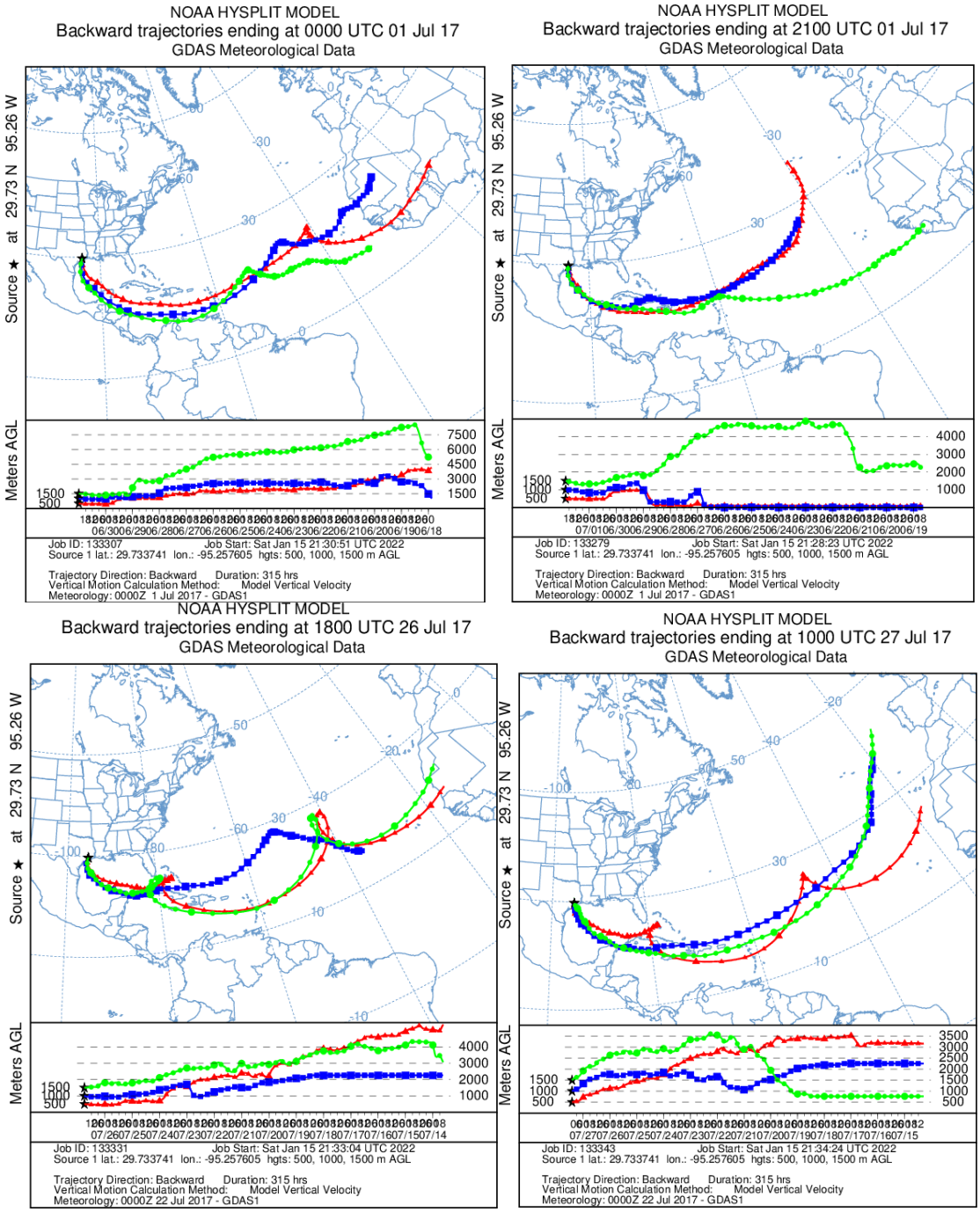

Figure B2. HYPLIT back trajectory models show wind originating from North-west African regions possibly bringing in the dust.

AOD MEASUREMENTS BY AERONET

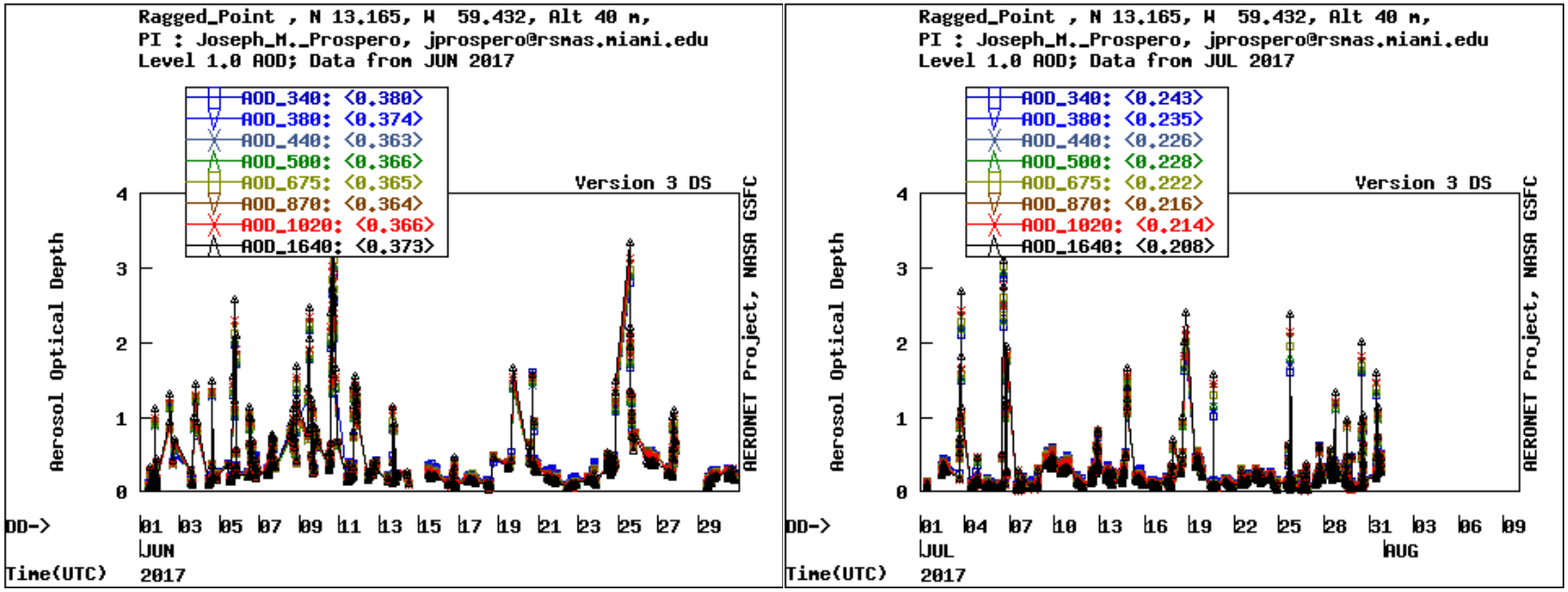

Figure B3. Aerosol optical depth measured at Ragged Point in June and July of 2017 confirms the presence of North African dust in a substantial amount, during the sampling period.

NAAPS AEROSOL MODEL

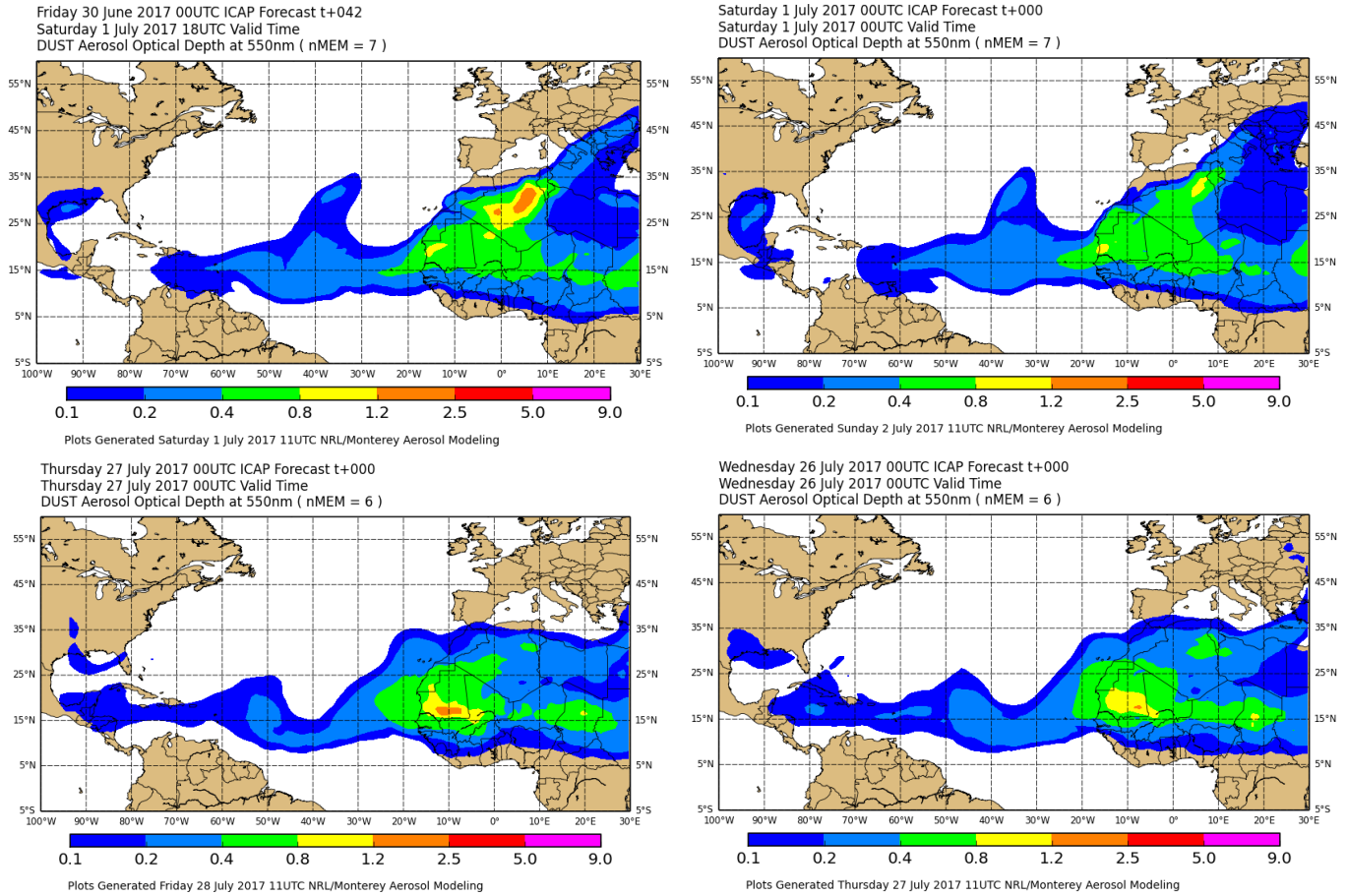

Figure B4. NAAPS model confirms the presence of North African dust in substantial amounts during the high dust days. A trail of dust over the North Atlantic Ocean additionally confirms the transport of dust to the North American continent.

Quality assurance and quality control

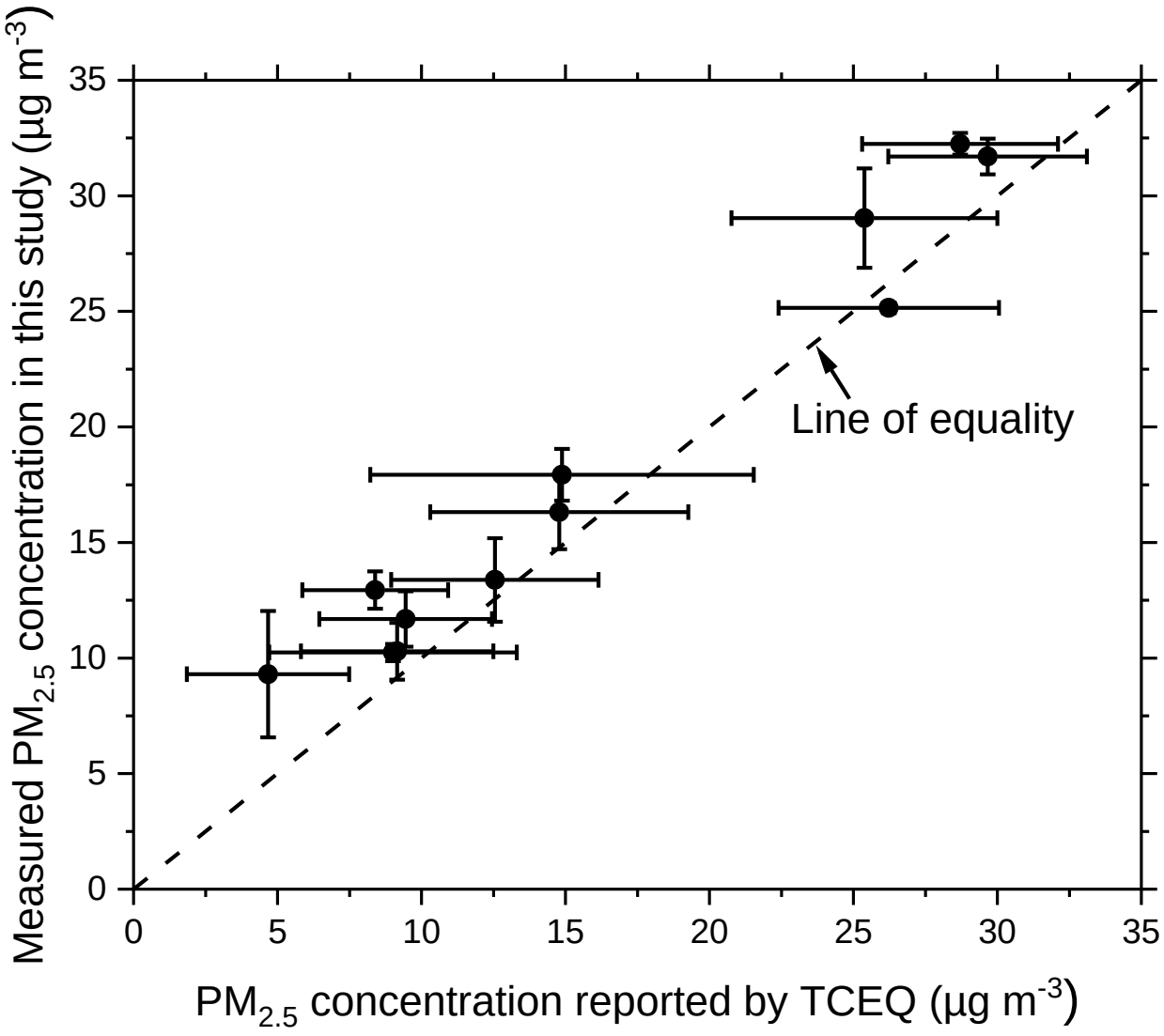

Figure B5. $PM_{2.5}$ concentration measured in this study agreed with TCEQ reported concentration [339].

Elemental Recoveries measured by DRC-ICP-MS confirm the total dissolution of all elements of interest. Recoveries of certified reference materials are shown below in Table S2 to Table S5

Table B2. Elemental recoveries for NIST SRM 1648a

Element	Certified values		Measured values		
	Mean µg g^{-1}	Uncertainty µg g^{-1}	Mean µg g^{-1}	Uncertainty µg g^{-1}	Recovery %
Na	4240	60	3900	590	92
Mg	8130	120	6980	570	86
Al	34300	1300	32200	3000	94
Si	128000	4000	113700	17500	89
K	10560	490	9800	1400	93
Ca	58400	1900	52900	8100	91
Ti	4021	86	3462	530	86
V	127	11	118	18	93
Cr	402	13	440	70	108
Mn	790	44	740	110	94
Fe	39200	2100	39400	6100	100
Co	17.93	0.68	17.9	2.8	100
Ni	81.1	6.8	79	13	97
Cu	610	70	529	82	87
Zn	4800	270	4350	670	91
As	115.5	3.9	104	16	90
Se	28.4	1.1	26.5	2.8	93
Rb	51	1.5	50.2	6.5	98
Sr	215	17	216	20	101
Cd	73.7	2.3	72	8	98
Sb	45.4	1.4	45	5	98
Cs	3.4	0.2	3.7	0.4	109

La	39	3	34	3	88
Ce	54.6	2.2	49	4	90
Sm	4.3	0.3	3.6	0.3	84
Hf	5.2	0	5.1	0.3	98
Ta	1.8	0	1.6	0.3	92
W	4.6	0.3	5.1	0.9	111
Pb	6550	330	6100	500	93

Table B3. Elemental recoveries for BCR-2

Elements	Certified values		Measured values		
	Mean	Uncertainty	Mean	Uncertainty	Recovery
	µg g^{-1}	µg g^{-1}	µg g^{-1}	µg g^{-1}	%
Li	9	2	9	1	98
Na	23400	800	21800	3300	93
Mg	21600	300	18500	1500	86
Al	71400	1000	78500	7200	110
Si	253000	4000	220000	34000	87
K	14900	400	16200	2300	109
Ca	50900	800	46600	7200	92
Sc	33	2	28	4	85
Ti	13500	300	14200	2200	105
V	416	14	400	61	96
Cr	18	2	17	3	94
Mn	1520	60	1580	240	104
Fe	96500	1500	97000	15000	101
Co	37	3	35	5	95
Cu	19	2	18	3	95
Zn	127	9	140	20	107
Ga	23	2	20	3	87
Rb	48	2	45	6	94
Sr	346	14	299	28	86

Y	37	2	36	6	97
Zr	188	16	188	23	100
Mo	248	17	243	20	98
Cs	1.1	0.1	1	0.1	91
Ba	683	28	710	70	104
La	25	1	27	3	107
Ce	53	2	48.6	4	92
Pr	6.8	0.3	7.3	0.6	107
Nd	28	2	26	2	92
Sm	6.7	0.3	6.9	0.6	103
Eu	2	0.1	2	0.3	100
Gd	6.8	0.3	7.4	0.7	109
Tb	1.07	0.04	1.1	0.2	103
Ho	1.33	0.06	1.34	0.2	105
Tm	0.54	0	0.53	0.08	98
Yb	3.5	0.2	3.2	0.3	90
Lu	0.51	0.02	0.53	0.07	104
Hf	4.8	0.2	4.3	0.3	89
Pb	11	2	12.4	1	113
Th	6.2	0.7	6	0.7	97
U	1.7	0.2	1.6	0.2	95

Table B4. Elemental recoveries for BCR-723

Elements	Certified values		Measured values		
	Mean	Uncertainty	Mean	Uncertainty	Recovery
	µg g^{-1}	µg g^{-1}	µg g^{-1}	µg g^{-1}	%
Al	37500	2200	36100	3300	96
Ti	2580	130	2780	430	108
V	74.9	1.9	69	11	92
Cr	440	18	390	60	89
Mn	1280	40	1160	180	90

Fe	32900	2000	34800	5400	106
Co	29.8	1.6	31	5	104
Ni	171	3	180	30	106
Zn	1660	100	1470	230	88
Rb	75	5	78	10	105
Sr	254	19	269	25	106
Y	12.5	1.8	13.4	2.1	107
Mo	40	0.6	43	4	107
Cd	2.5	0.4	2.4	0.3	96
Sb	28.2	2.3	28	3	99
Ba	460	40	490	50	106
Hf	2.2	0.7	2	0.1	91
Pb	866	16	830	70	95
Th	4.8	0.5	4.3	0.5	90

Table B5. Elemental recoveries for NIST SRM 1633b

Elements	Certified values		Measured values		
	Mean	Uncertainty	Mean	Uncertainty	Recovery
	µg g^{-1}	µg g^{-1}	µg g^{-1}	µg g^{-1}	%
Na	2010	30	1810	280	90
Mg	4820		5160	420	107
Al	150000	2700	163000	15000	109
Si	230000	800	197600	30400	86
K	19500	300	20700	290	106
Ca	15100	600	16000	2500	106
Sc	41		40	6	98
Ti	7910	140	7870	1200	99
V	295.7	3.6	269	41	91
Cr	198.2	0	208	33	105
Mn	131.8	1.7	115	18	87
Fe	77800		74300	11400	96

Co	50		51	8	102
Ni	120.6	1.8	104	17	87
Cu	112.8	2.6	123	19	109
Zn	210		223	34	106
As	136.2	2.6	119	18	87
Se	10.26	0.17	10	1	97
Rb	140		145.5	19	104
Sr	1041	14	1139	106	109
Cd	0.784	0.006	0.78	0.08	99
Sb	6		5.3	0.6	88
Cs	11		10.4	1.2	94
Ba	709	27	770	80	109
La	94		92	9	98
Ce	190		180	14	95
Nd	85		78	5	92
Sm	20		20	2	100
Eu	4.1		3.9	0.5	94
Gd	13		13.1	1.2	101
Tb	2.6		2.7	0.4	102
Dy	17		15.3	1	90
Ho	3.5		3.7	0.6	105
Tm	2.1		1.8	0.3	85
Yb	7.6		6.6	0.7	86
Lu	1.2		1.2	0.2	100
Hf	6.8		6.1	0.4	90
Ta	1.8		1.8	0.4	102
W	5.6		6.1	1	109
Pb	68.2	1.1	69	6	101
Th	25.7	1.3	27.5	3.3	107
U	8.79	0.36	8.6	1.3	98

DETECTION LIMITS AND BLANK FILTER CHARACTERIZATION

Table B6. Method detection limits (MDLs) and average PTFE filter blank concentrations measured by DRC-q-ICP-MS and MC-ICP-MS (for Sr, Nd, and Hf). PTFE blanks represent blanks for $PM_{2.5}$ aerosols collected by an air sampler (Thermo Fisher Partisol™ 2025i Sequential Air Sampler) and used as a negative control in this study. BDL = Below detection limit. STD – analytes measured in standard mode (i.e., using no collision cell gas). DRC – analytes measures with dynamic reaction cell method with ammonia as cell gas. Isotope ratios of blank are provided in Table S9.

Element	m/z	MDL (µg L^{-1})	Mode	Average PTFE filter blank (ng)	Element	m/z	MDL (µg L^{-1})	Mode	Average PTFE filter blank (ng)
Li	7	0.03	STD	<2.25	La	139	0.014	STD	<1.05
Be	9	0.03	STD	<2.25	Ce	140	0.015	STD	<1.13
Mg	25	0.4	STD	44 ± 14	Pr	141	0.007	STD	<0.53
Al	27	0.61	DRC	195±48	Nd	146	0.008	STD	0.020
Si	29	35	STD	<2625	Sm	152	0.002	STD	<0.15
K	39	1.2	STD	<90	Eu	153	0.002	STD	<0.15
Ca	44	11.5	STD	3000 ± 1590	Gd	158	0.002	STD	<0.15
Ti	47	0.22	STD	<16.5	Tb	159	0.002	STD	<0.15
V	51	0.79	DRC	<59.3	Dy	164	0.003	STD	<0.225
Cr	52	0.1	DRC	<7.5	Ho	165	0.003	STD	<0.225
Mn	55	0.03	STD	<2.25	Er	166	0.003	STD	<0.225
Fe	57	1.7	DRC	<128	Yb	174	0.002	STD	<0.15
Ni	58	0.03	DRC	<2.25	Lu	175	0.002	STD	<0.15
Co	59	0.05	STD	<3.75	Hf	178	0.001	STD	0.040
Cu	65	0.004	DRC	<0.3	W	184	0.04	STD	<3
Zn	66	0.01	DRC	<0.75	Pb	208	0.05	STD	<3.75
Ga	69	0.05	STD	<3.75	Th	232	0.012	STD	<0.9
As	75	0.04	DRC	<3	U	238	0.009	STD	<0.68
Se	82	0.11	DRC	<8.25					
Rb	85	0.04	STD	<3					

Sr	88	0.04	STD	0.12					
Y	89	0.03	STD	<2.25					
Zr	90	0.04	STD	<3					
Mo	96	0.04	STD	<3					
Cd	113	0.04	STD	<3					
Sn	118	0.04	STD	<3					
Sb	121	0.04	STD	<3					
Cs	133	0.03	STD	<2.25					
Ba	138	0.22	STD	<16.5					

INSTRUMENTAL SETTING

Table B7. Instrumental settings and operating parameters for DRC-ICP-MS (PerkinElmer® NexION® 300).

Instrument	PerkinElmer® NexION® 300
Nebulizer	Concentric (Meinhard) [Type A0.5]
Spray chamber	Baffled quartz cyclonic
Torch injector	Quartz
Auto lens	On
RF power	1600 W
Sample	18 L min^{-1}
Nebulizer	0.96-1.18 L min^{-1}
Auxiliary	1-1.2 L min^{-1}
Interface	Platinum cones
Sampler cone	1.1 mm orifice diameter
Skimmer cone	0.9 mm orifice diameter
Scanning mode	Peak hopping
Sweeps/reading	20
Readings/replicate	1
Replicates	3
Dwell time	50 ms (standard mode); 100 ms (DRC mode)
Sampling parameters	AS-93 plus auto-sampler
Sample flush time	45 s
Sample flush pump speed	20 rpm
Read delay	65 s
Read delay pump speed	24 rpm
Wash time	60 s
Wash pump speed	24 rpm
Cell gas	NH_3 (0.2-1.0 mL min^{-1})
RPq	0.25-0.75
RPa	0

Table B8. Parameter set for ESI Apex Ω, used for signal enhancement in MC-ICPMS analysis

Instrument	ESI Apex Omega Ω		
Temperature profile	Sr	Nd	Hf
Spray chamber (°C)	105°C	105°C	105°C
Peltier cooler (°C)	2°C	2°C	2°C
Dissolvator (°C)	145°C	145°C	145°C
Ar sweep gas flow (L min^{-1})	2.9	2.7	2.8
N_2 gas flow (mL min^{-1})	0	1.5	0
Reference isotope	^{88}Sr	^{142}Nd	^{178}Hf
Sensitivity (V (mg $L^{-1})^{-1}$)	400	150	120

Table B9. Instrumental setup for Neptune Plus MC-ICP-MS

Isotope Ratio	$^{87}Sr/^{86}Sr$	$^{143}Nd/^{144}Nd$	$^{176}Hf/^{177}Hf$
Instrumental setup			
RF Power (W)	1200	1200	1200
Skimmer cone	Nickel, X-Version	Nickel, X-Version	Nickel, X-Version
Skimmer cone orifice dia (mm)	0.4	0.4	0.4
Sampler cone	Nickel	Nickel	Nickel
Sampler cone orifice dia (mm)	1.2	1.2	1.2
Amplifier resistance (Ω)	10^{11}	10^{11}	10^{11}
Method setup			
Center cup	^{86}Sr	^{145}Nd	^{177}Hf
Isotopes measured	^{83}Kr, ^{84}Sr, ^{85}Rb, ^{86}Sr, ^{87}Sr, ^{88}Sr, ^{89}Sr, ^{90}Zr	^{140}Ce, ^{142}Nd, ^{143}Nd, ^{144}Nd, ^{145}Nd, ^{146}Nd, ^{147}Sm, ^{148}Nd, ^{150}Nd	^{172}Yb, ^{174}Hf, ^{175}Lu, ^{176}Hf, ^{177}Hf, ^{178}Hf, ^{179}Hf, ^{180}Hf
Isotopes monitored for interference	^{83}Kr, ^{85}Rb	^{140}Ce, ^{147}Sm	^{172}Yb, ^{175}Lu
Ratios for interference correction	$^{83}Kr/^{86}Kr$ = 0.664740; $^{85}Rb/^{87}Rb$ = 2.592310	$^{147}Sm/^{144}Sm$ = 4.838710	$^{172}Yb/^{176}Yb$ = 1.710815; $^{175}Lu/^{176}Lu$ = 37.61
Normalizing ratio	$^{88}Sr/^{86}Sr$ = 8.375209	$^{146}Nd/^{144}Nd$ = 0.7219	$^{176}Hf/^{177}Hf$
Baseline readings (1.04s for each reading)	100 (at start of each reading)	100 (at start of each reading)	100 (at start of each reading)
Cup rotation	ON	ON	ON
Number of blocks	100	50	50
Integration time (s)	1.04	2.08	2.08
Number of readings per block	100	50	50
Wash time (min)	5	5	7
Lens tuning	Manual	Manual	Manual
Cool gas (argon) (L min^{-1})	15	15	15
Aux gas (argon) (L min^{-1})	0.7	0.7	0.7
Sample Gas (argon) (L min^{-1})	0.925	0.925	0.925

B.2. NORTH AFRICAN DUST CHARACTERIZATION

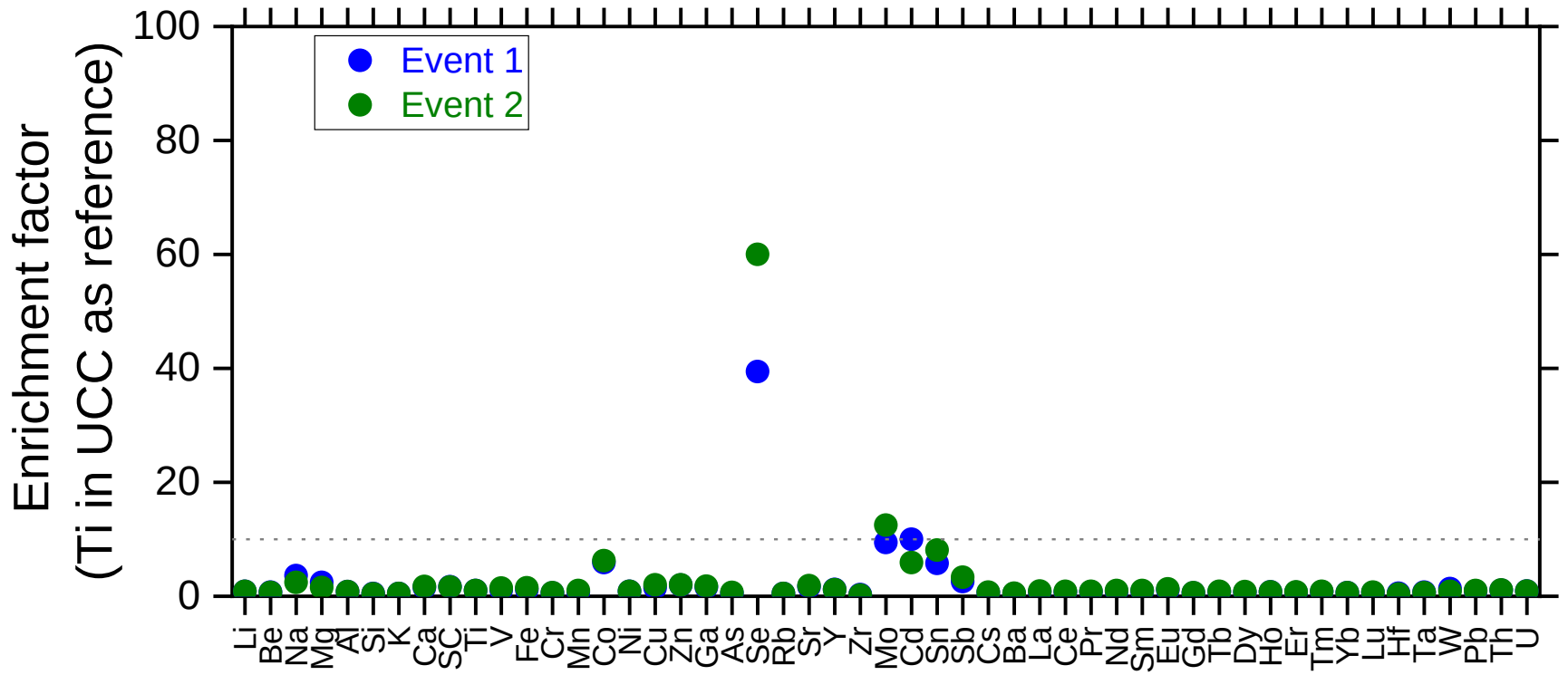

Figure B6. The enrichment factor of all elements measured in this study for the North African dust profile observed in Barbados. Event 1 refers to the dust outbreak during June 28 – July 3, 2017, and event 2 refers to the dust outbreak from July 22 – July 27, 2017.

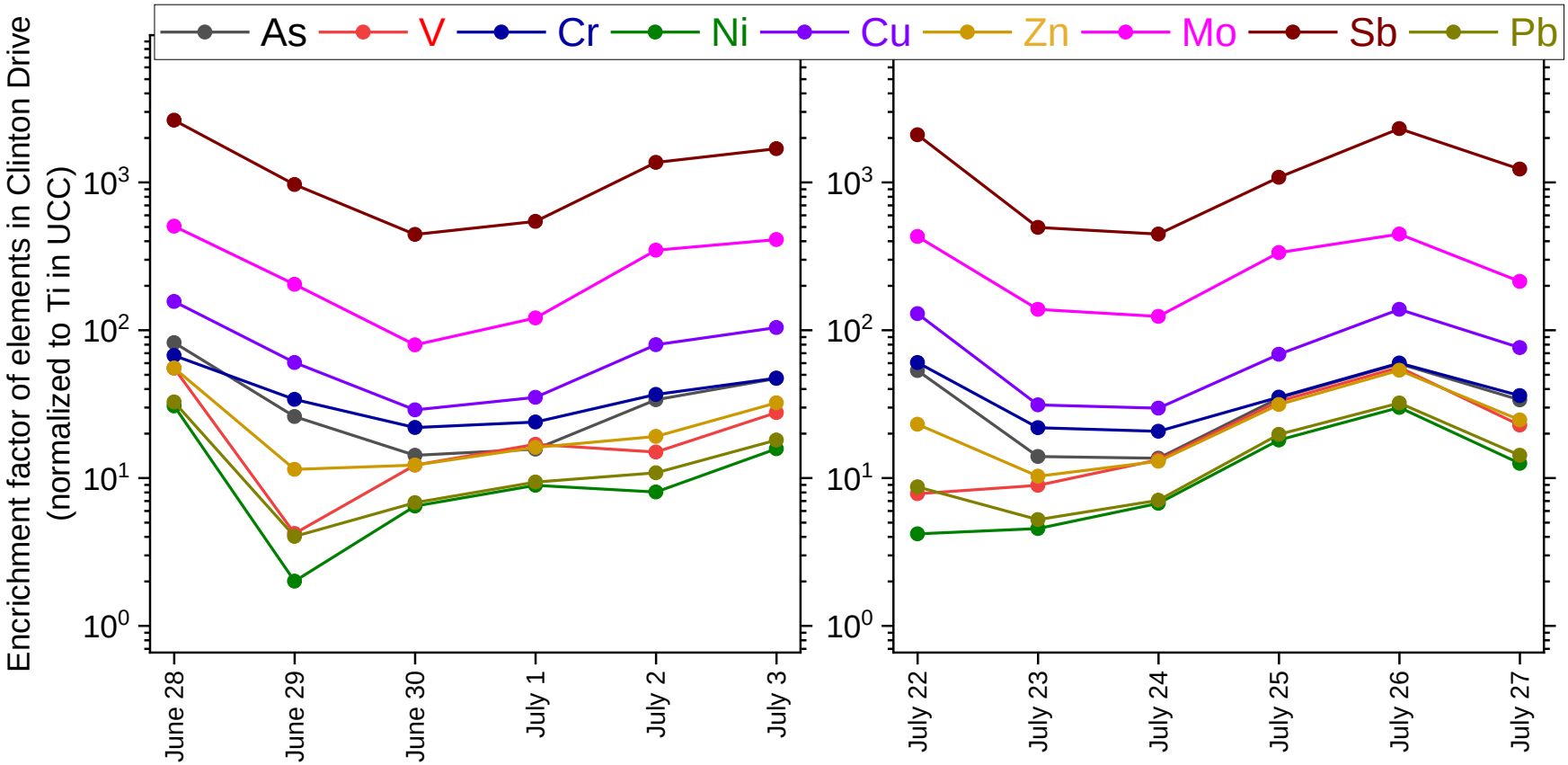

Figure B7. Enrichment factor (EF) of anthropogenic elements measured in Clinton Drive samples. Dips in EF indicate the presence of mineral sources. All values are normalized to Ti and upper continental crust (UCC)[120] as reference.

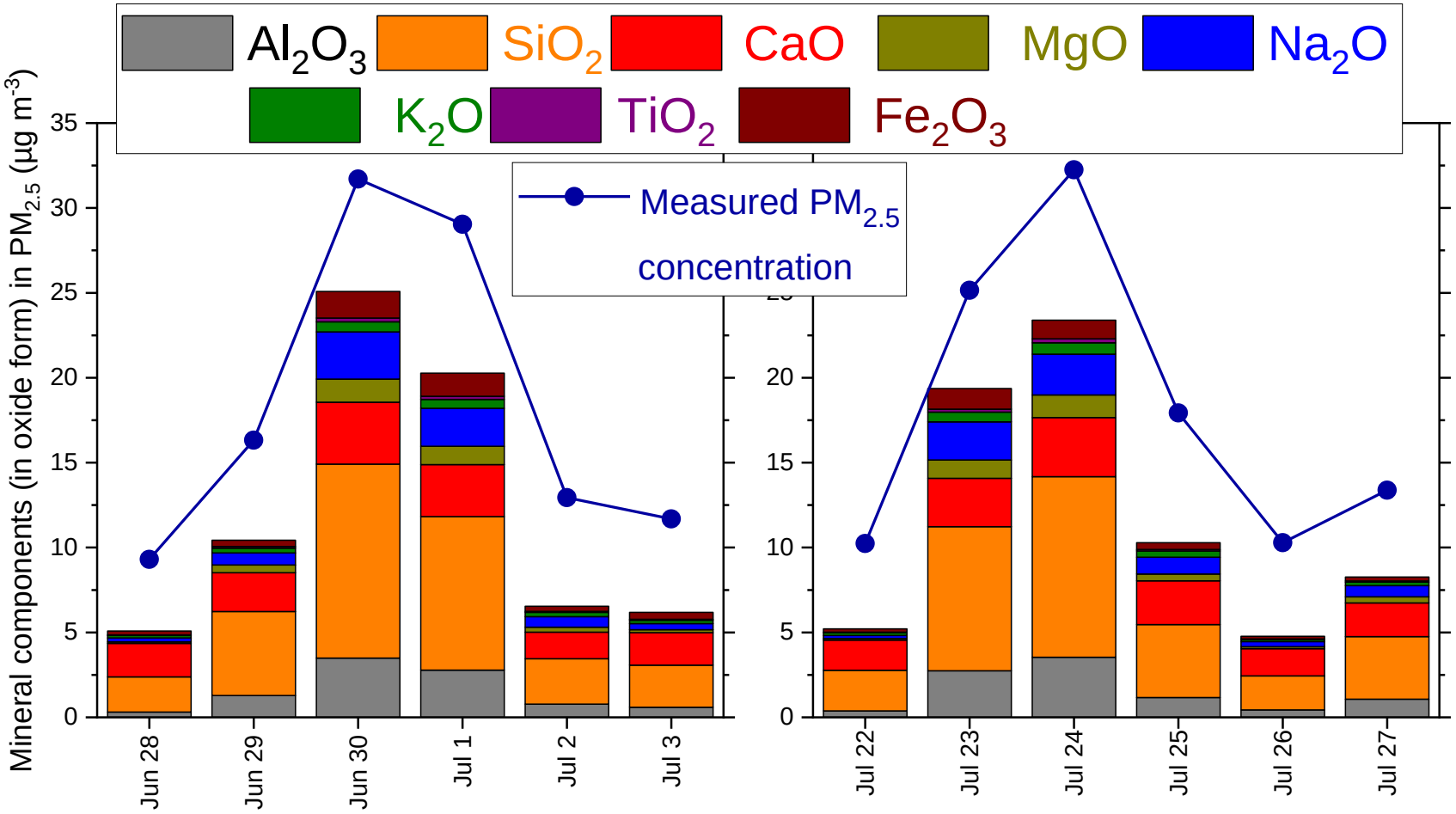

Figure B8. Variation in measured mineral components (as oxides of Al, Si, Ca, Mg, Na, Ti, Fe, and K) was coherent with $PM_{2.5}$ variation indicating an outbreak of mineral dust may have caused a spike in $PM_{2.5}$ concentrations at Clinton Drive.

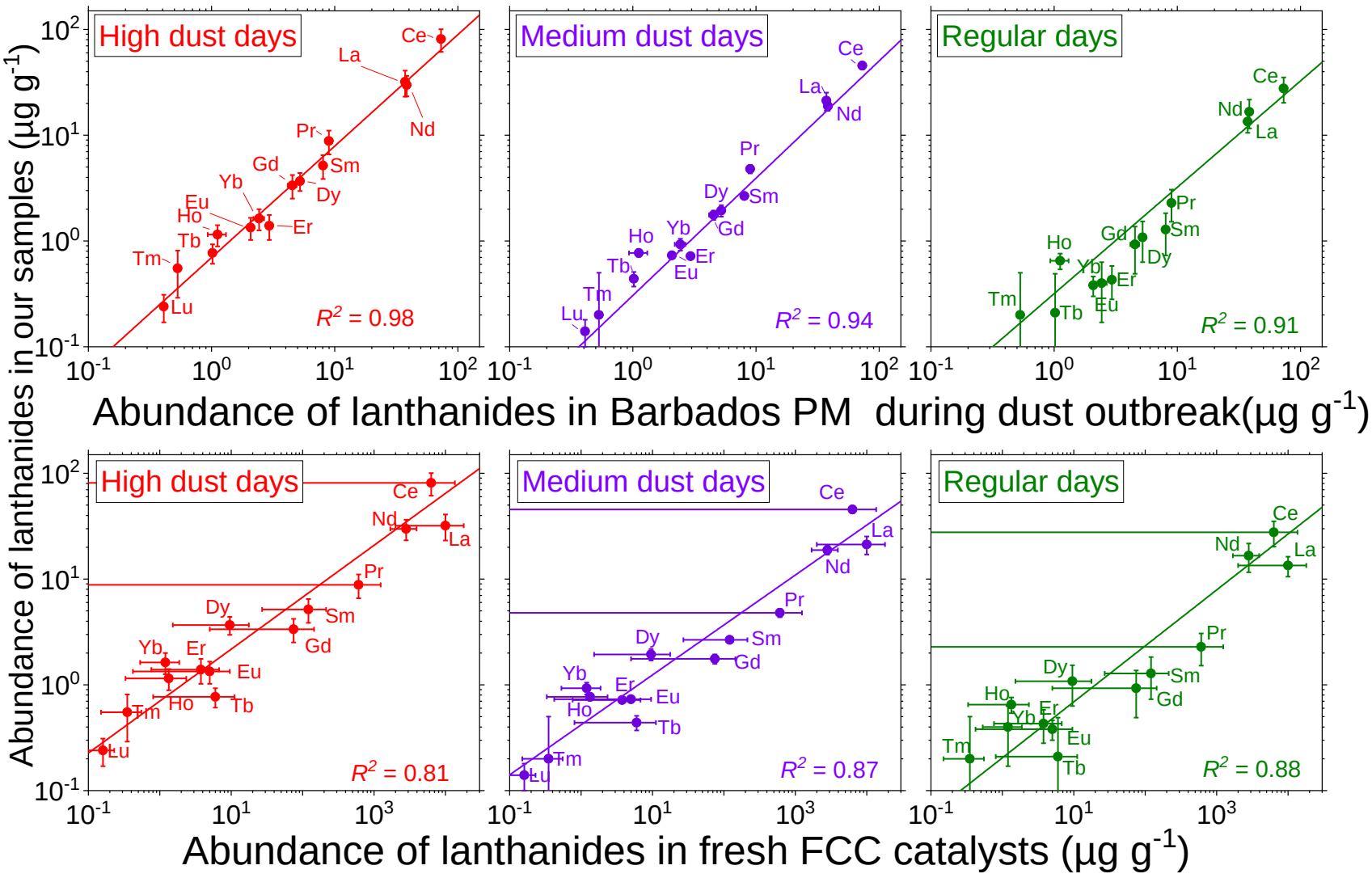

Figure B9. Lanthanide abundances in all our samples (left: high dust, middle: medium dust, and right: regular days) correlate better with North African dust captured in Barbados (This study) than FCC catalyst reported in literature[51].

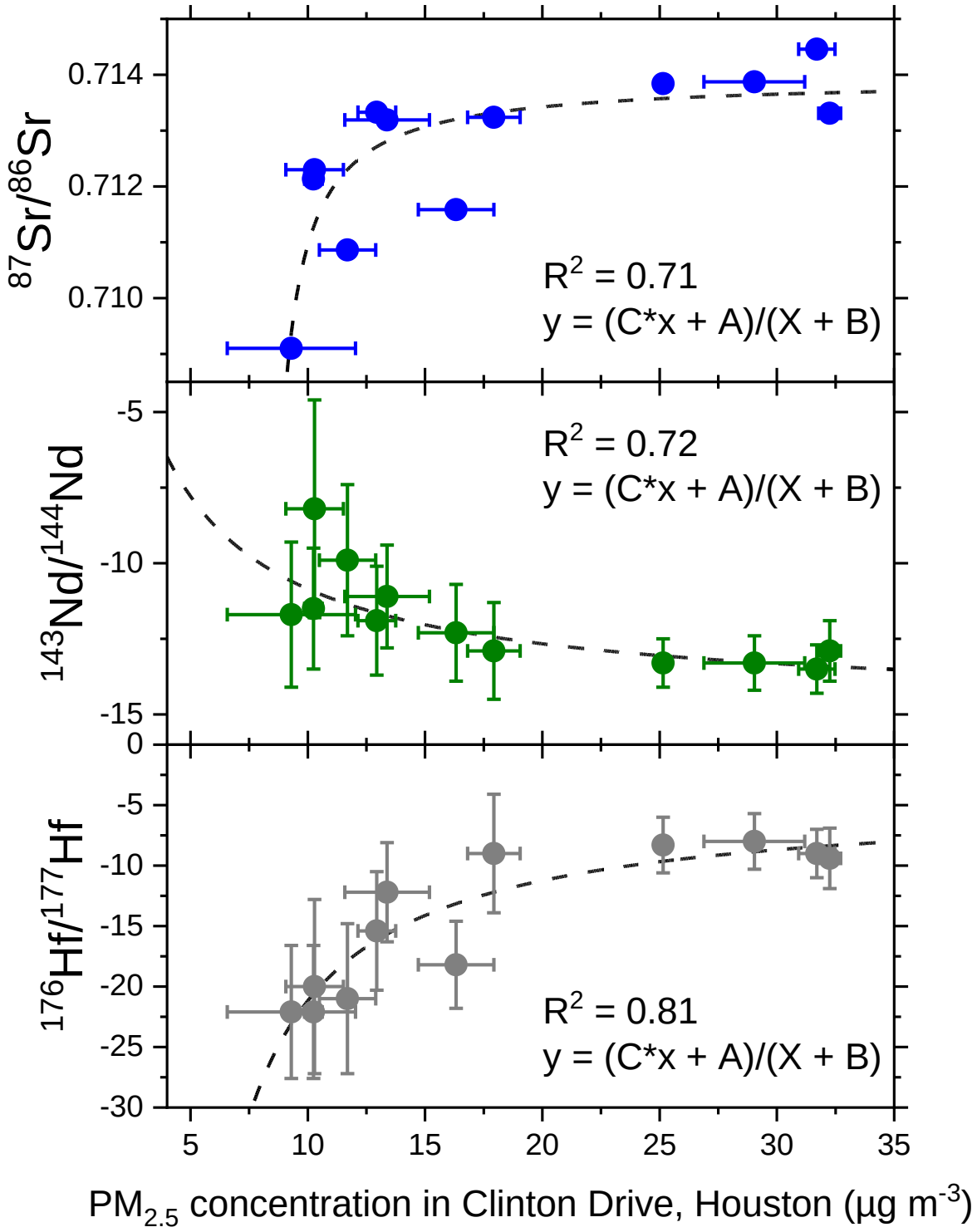

Figure B10. Sr (top), Nd(middle), and Hf(bottom) isotope ratios were non-linearly correlated with the increase in PM mass indicating isotope mixing of urban Pm with North African dust.

Table B10. A Summary of all isotopic ratios and key elemental ratios significant to sources in Houston. Si/Al and Ca/Al are used for mineral dust tracing, La/Ce is significant to FCC, and Sb/Cu is important for motor vehicle tracing. Urban sources from literature[51] are added for comparison

Sample name	$^{87}Sr/^{86}Sr$		$^{143}Nd/^{144}Nd$		$^{176}Hf/^{177}Hf$		Si/Al	Ca/Al	La/Ce	Sb/Cu
	Mean	Unc	Mean	Unc	Mean	Unc				
BAD1	0.71392	2.03E-05	0.51189	3.75E-05	0.28267	3.10E-05	0.75	0.17	4.35	0.385
BAD2	0.71065	2.03E-05	0.51207	8.09E-05	0.28218	1.04E-04	0.78	0.1	20.65	0.177
BAD3	0.71174	2.03E-05	0.51242	2.92E-05	0.28228	5.44E-05	0.73	0.13	4.16	0.331
BAD4	0.71297	2.03E-05	0.5121	2.00E-05	0.28259	3.76E-05	0.73	0.13	6	0.354
CL1	0.709099	2.68E-05	0.512028	1.22E-04	0.282039	1.55E-04	5.81	8.49	0.64	0.35
CL2	0.711585	2.66E-05	0.512003	8.43E-05	0.282271	1.01E-04	3.42	2.41	0.56	0.33
CL3	0.71446	2.31E-05	0.511939	4.24E-05	0.282514	5.79E-05	2.89	1.41	0.59	0.32
CL4	0.713875	2.33E-05	0.511951	4.52E-05	0.282562	6.47E-05	2.87	1.49	0.61	0.32
CL5	0.713328	2.78E-05	0.512021	9.43E-05	0.282348	1.39E-04	3.04	2.71	0.58	0.36
CL6	0.710862	2.60E-05	0.512117	1.29E-04	0.282166	1.76E-04	3.66	4.34	0.79	0.34
CL7	0.712134	3.06E-05	0.512043	1.04E-04	0.282117	1.55E-04	5.59	6.37	0.57	0.34
CL8	0.713841	2.34E-05	0.511952	4.33E-05	0.282553	6.47E-05	2.73	1.4	0.68	0.33
CL9	0.71331	2.37E-05	0.511966	5.02E-05	0.282524	7.16E-05	2.66	1.33	0.68	0.31
CL10	0.713238	2.64E-05	0.511971	8.43E-05	0.28222	1.39E-04	3.27	2.99	0.79	0.33
CL11	0.7123	3.25E-05	0.512207	1.87E-04	0.282532	2.04E-04	4.02	4.9	0.97	0.35
CL12	0.713193	2.71E-05	0.51206	8.82E-05	0.282438	1.16E-04	3.04	2.5	0.86	0.34
Clinton Dr. Soil	0.712005	7.79E-05	0.512067	2.59E-05	0.282412	1.93E-05	12 ± 3	4 ± 2	0.48 ± 0.01	0.06 ± 0.01
Concrete dust	0.70805	1.55E-05	0.51223	1.61E-05	0.282282	2.85E-05	15 ± 9	17 ± 4	0.4 ± 0.3	0.013 ± 0.001
Vehicular PM	0.714978	0.000364	0.512163	3.60E-05	0.282193	1.62E-05	2.8 ± 0.6	5.2 ± 0.9	0.9 ± 0.2	0.36 ± 0.01
FCC/Refinery emission	0.711043	0.00015	0.511256	0.0002	0.282397	1.85E-05	0.9 ± 0.1	0.004 ± 0.001	0.75 ± 0.02	0.07 ± 0.03
Blank filter	0.705	0.001	0.513	0.001	0.280	0.001	-	-	-	-

B.3. SOURCE APPORTIONMENT MODELLING

Transformation of linear equations for isotope mass balance: The equations for isotopic mass balance were transformed to make the calculation algorithm simple and quicker to process. The derivation of the transformed equation is shown below:

$$C_i \bullet \hat{R}_i = \sum_{j=1}^{J} F_{ij} \bullet S_j \bullet R_{ij}$$

$$0 = \sum_{j=1}^{J} F_{ij} \bullet S_j \bullet R_{ij} - C_i \bullet \hat{R}_i$$

$$0 = \sum_{j=1}^{J} F_{ij} \bullet S_j \bullet R_{ij} - \sum_{j=1}^{J} F_{ij} \bullet S_j \bullet \hat{R}_i$$

$$\sum_{j=1}^{J} F_{ij} \bullet S_j \bullet (R_{ij} - \hat{R}_i) = 0$$

Where C_i is the weighted ambient concentration if the i^{th} element, F_{ij} is the abundance of i^{th} element in j^{th} source, S_j is the source contribution j^{th} source to ambient $PM_{2.5}$, R_{ij} is the isotope ratio of the j^{th} source corresponding to isotopic element i (Sr, Nd, and Hf in our case). $\hat{R}_i$ is the isotope ratio corresponding to isotopic element i.

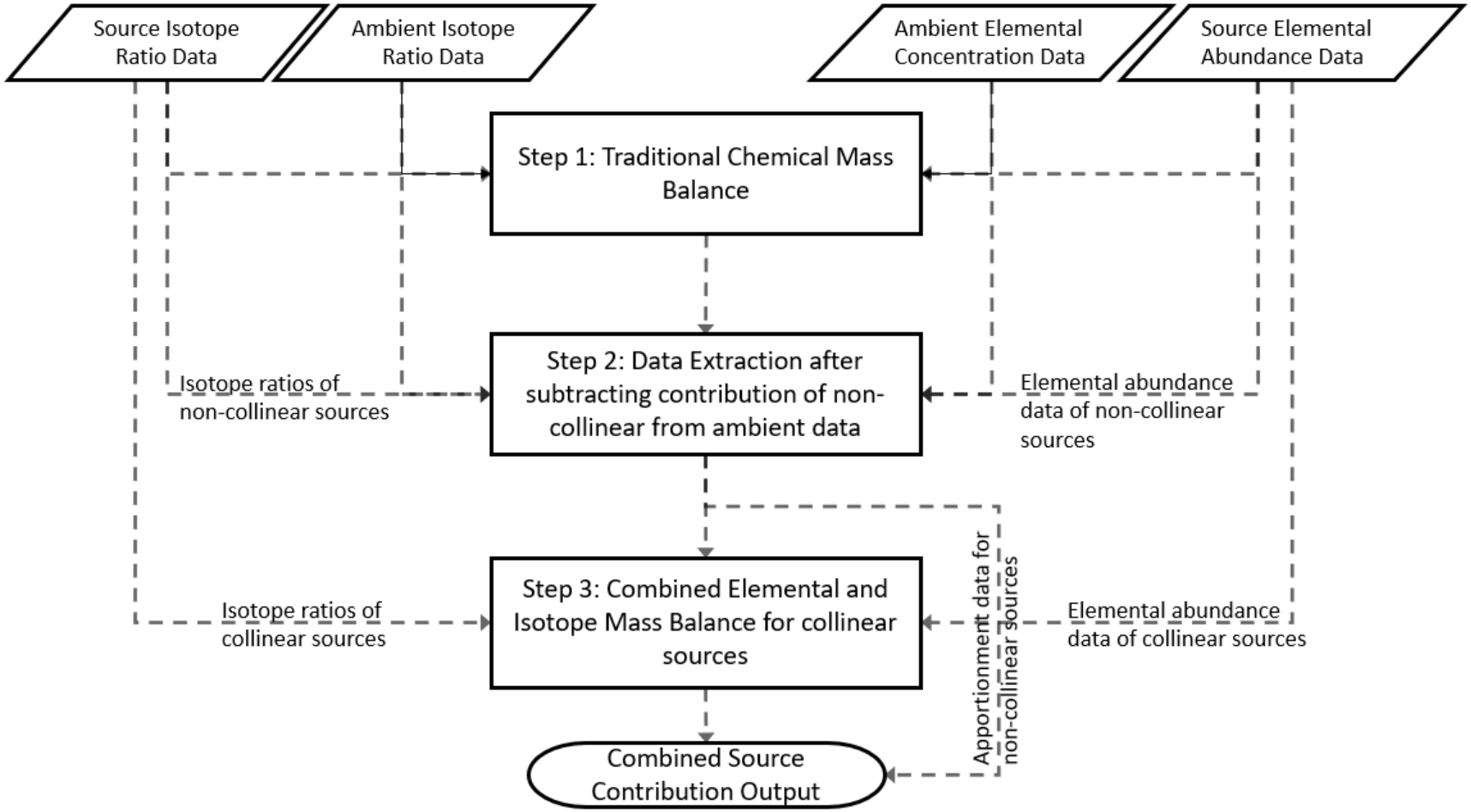

Figure B11. A flow chart describing the whole method of source apportionment calculations adopted in this study

Table B11. Source Profiles used in creating synthetic dataset

Source Category/Species	Local Soil	North African dust	Vehicular PM	Oil combustion	Concrete dust	Coal combustion	Biomass burning	FCC
Li	9.84E-06	3.52E-05	5.94E-06		5.31E-06			1.88E-05
Be	3.41E-07	2.07E-06	2.52E-07		1.46E-08			3.11E-07
Na	2.19E-03	4.72E-02	1.80E-03	2.98E-02	4.63E-04	1.29E-03	3.77E-03	1.73E-03
Mg	4.73E-03	3.14E-02	1.91E-03	4.00E-05	1.38E-03	4.58E-03	3.05E-04	3.28E-05
Al	2.31E-02	8.17E-02	1.68E-02	3.13E-03	1.18E-02	4.16E-02	5.71E-04	2.61E-01
Si	2.65E-01	1.91E-01	4.83E-02	4.46E-03	1.62E-01	7.98E-02	1.32E-03	2.56E-01
K	5.10E-03	1.81E-02	2.29E-03	1.54E-03	2.11E-02	4.19E-03	5.35E-02	6.84E-03
Ca	9.48E-02	2.09E-02	8.57E-02	1.21E-02	1.87E-01	3.47E-02	9.85E-04	9.32E-04
Sc	1.89E-05	2.57E-05	2.71E-05		9.80E-07			3.49E-05
Ti	1.41E-03	5.42E-03	2.06E-03	2.35E-04	4.30E-04	1.96E-03	2.20E-05	3.09E-03
V	2.90E-05	1.18E-04	3.19E-05	1.58E-02	2.71E-05	1.04E-04	2.00E-06	3.55E-05
Cr	1.28E-04	8.79E-05	8.04E-05	1.67E-04	1.44E-05	6.90E-05	1.00E-05	1.83E-05
Fe	2.25E-02	5.77E-04	4.13E-02	8.56E-03	1.22E-02	1.90E-02	2.21E-04	1.36E-03
Mn	5.56E-04	4.05E-02	3.88E-04	1.20E-04	3.24E-04	1.57E-04	8.50E-06	1.06E-05
Co	4.64E-06	9.19E-05	4.97E-06	5.00E-05	3.32E-06	5.00E-06		2.41E-06
Ni	2.52E-05	2.95E-05	7.18E-05	4.85E-03	3.74E-05	3.30E-05	1.10E-05	1.46E-05
Cu	3.34E-05	4.46E-05	2.26E-03	1.50E-04	1.25E-04	1.15E-04	1.40E-05	9.03E-06
Zn	5.19E-04	1.87E-04	1.36E-03	3.96E-03	5.17E-04	3.39E-04	2.82E-04	4.49E-05

Ga	4.49E-05	3.93E-05	3.09E-04	5.00E-06	1.18E-05			4.85E-05
As	8.78E-06	1.81E-06	8.82E-05	2.65E-05	1.17E-04		6.00E-06	8.86E-06
Se	3.91E-07	5.66E-06	1.23E-05	6.30E-05	6.68E-06	3.30E-03	5.50E-06	1.79E-07
Rb	2.63E-05	6.67E-05	1.78E-05		8.24E-06	3.00E-05	3.60E-05	2.04E-06
Sr	2.20E-04	2.06E-04	1.81E-04	9.50E-05	4.52E-04	1.13E-03	1.20E-05	2.77E-05
Y	1.76E-05	4.97E-05	1.69E-05		8.56E-06			1.15E-05
Zr	1.19E-04	6.99E-05	6.53E-04		1.85E-05	7.40E-05	5.00E-06	3.75E-05
Mo	3.68E-06	4.18E-06	8.37E-05	4.00E-05	2.31E-06	1.49E-01		1.25E-06
Cd	3.70E-07	1.16E-06	2.07E-05	1.00E-05	1.35E-06	2.70E-05	5.50E-06	7.11E-08
Sn	1.75E-05	2.11E-05	8.37E-04	1.00E-04	6.95E-06	1.50E-04	9.00E-06	2.79E-06
Sb	2.00E-06	1.58E-06	8.18E-04	2.00E-04	1.62E-06		5.50E-06	5.62E-07
Cs	1.67E-06	3.66E-06	1.57E-06		5.87E-07			2.38E-07
Ba	3.43E-04	4.49E-04	4.02E-03	6.00E-05	1.08E-04	2.24E-03	2.05E-05	1.51E-04
La	3.29E-05	3.73E-05	6.69E-05	3.50E-05	2.21E-05	2.00E-05		6.12E-03
Ce	5.29E-05	7.29E-05	1.95E-04	5.00E-06	2.94E-05			3.22E-03
Pr	7.74E-06	8.97E-06	1.30E-05		6.96E-06			3.27E-04
Nd	2.92E-05	3.84E-05	4.16E-05	5.00E-06	1.33E-05			2.91E-03
Sm	4.75E-06	8.04E-06	5.22E-06	1.85E-06	2.57E-06			8.52E-05
Eu	1.01E-06	2.08E-06	1.51E-06		5.23E-07			2.72E-06
Gd	2.29E-06	4.53E-06	2.26E-06		1.27E-06			4.15E-05
Tb	5.48E-07	1.02E-06	4.15E-07		2.95E-07			3.54E-06
Dy	3.17E-06	5.22E-06	2.51E-06		1.63E-06			5.91E-06

Ho	7.86E-07	1.12E-06	6.26E-07		3.94E-07			8.82E-07
Er	1.42E-06	2.95E-06	1.19E-06		6.68E-07			2.22E-06
Tm	3.04E-07	5.30E-07	5.17E-07		2.60E-07			3.01E-07
Yb	2.07E-06	2.43E-06	1.67E-06		8.42E-07			1.00E-06
Lu	3.68E-07	4.14E-07	3.12E-07		1.46E-07			1.47E-07
Hf	2.93E-06	3.93E-06	2.46E-05		8.30E-07			1.90E-06
Ta	3.10E-07	8.31E-07	6.23E-08		5.43E-07			2.68E-06
W	5.11E-06	1.58E-06	1.59E-05		1.66E-06			6.40E-06
Pb	3.54E-05	1.94E-05	7.30E-05	1.52E-03	3.37E-06	4.00E-05	1.55E-05	2.32E-05
Th	1.07E-05	1.56E-05	4.80E-06		3.98E-06			1.17E-05
Sr	0.712005	0.714509	0.714978		0.708050			0.711043
Nd	0.512067	0.511880	0.512163		0.512230			0.511256
Hf	0.282412	0.282676	0.282193		0.282282			0.282397

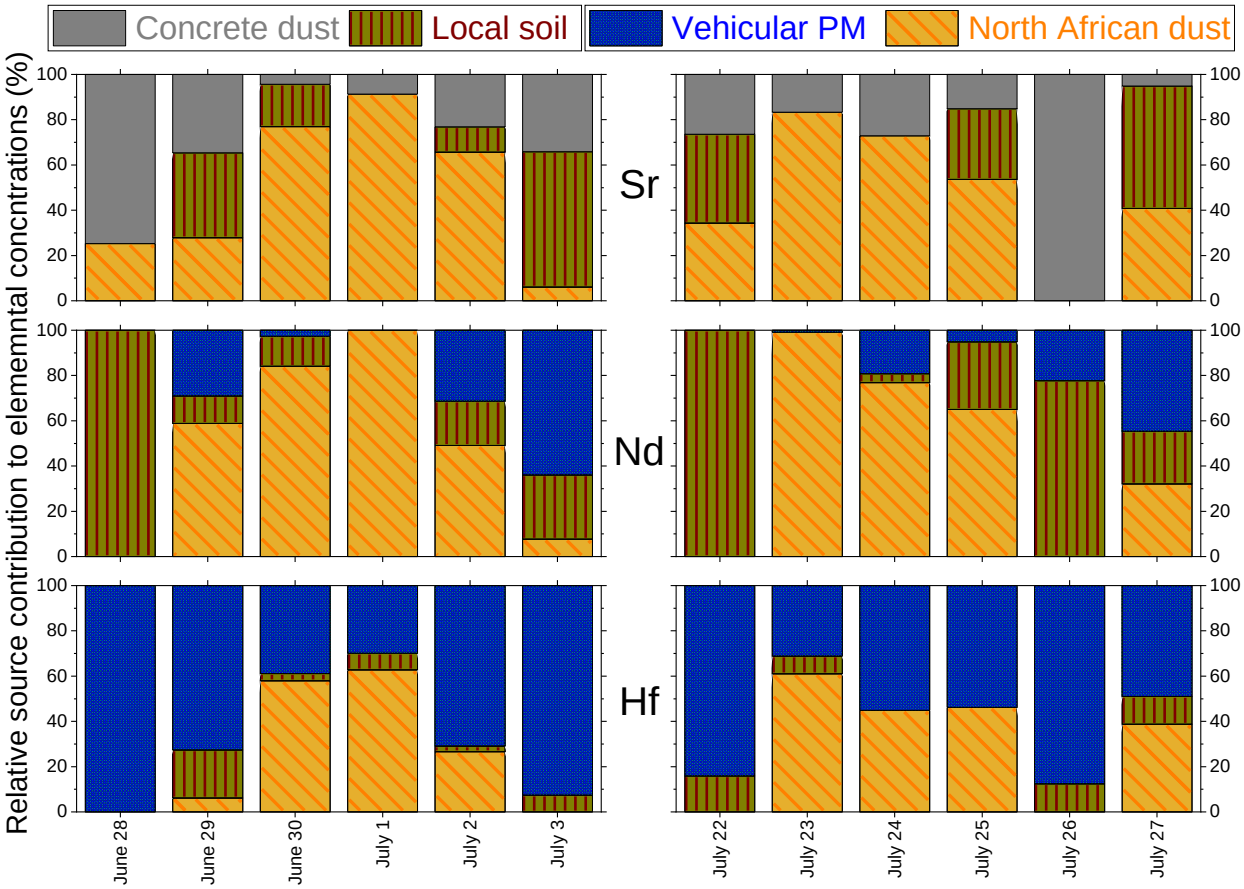

Figure B12. Source Apportionment of Sr (top), Nd (middle), and Hf (bottom) estimated from isotopic end member mixing analysis.

Table B12. Summary of elemental concentration in the synthetic dataset and $PM_{2.5}$ sampled in this study

Elements	Synthetic dataset ng m^{-3}	Houston $PM_{2.5}$ ng m^{-3}	Elements	Synthetic dataset ng m^{-3}	Houston $PM_{2.5}$ ng m^{-3}
Li	0.13 - 64.2	0.43 - 5.45	Sn	3.8 - 5.1	3.8 - 4.9
Be	0.02 - 50.27	0 - 0.32	Sb	3.5 - 4.1	3.4 - 4.4
Na	133 - 982	74 - 1149	Cs	0.014 - 0.065	0.008 - 0.059
Mg	57 - 719	36 - 571	Ba	19.7 - 30.4	20.2 - 39.8
Al	321 - 1389	116 - 1310	La	3.22 - 6.73	0.53 - 1.57
Si	1091 - 4641	655 - 3737	Ce	2.53 - 6.06	0.85 - 2.29
K	104 - 345	70 - 390	Pr	0.24 - 0.59	0.07 - 0.22
Ca	799 - 1802	781 - 1825	Nd	1.54 - 2.44	0.21 - 0.85
Sc	0.23 - 0.82	0.16 - 0.6	Sm	0.085 - 0.223	0.032 - 0.154
Ti	19 - 90	13 - 98	Eu	0.013 - 0.043	0.007 - 0.038
V	3.9 - 7.8	2.5 - 22.9	Gd	0.041 - 0.124	0.013 - 0.08
Cr	1.2 - 76.7	11.2 - 25.9	Tb	0.007 - 0.022	0.003 - 0.017
Mn	3.8 - 13.2	3.4 - 12.5	Dy	0.027 - 0.099	0.016 - 0.089
Fe	285 - 872	224 - 770	Ho	0.006 - 0.024	0.004 - 0.021
Co	0.2 - 1.3	0.2 - 2.8	Er	0.012 - 0.052	0.007 - 0.049
Ni	1.5 - 3.2	0.5 - 4.3	Tm	0.004 - 0.012	0.003 - 0.011
Cu	10.1 - 12.3	9.6 - 13.9	Yb	0.014 - 0.052	0.01 - 0.048
Zn	9.9 - 17.5	7.3 - 22	Lu	0.003 - 0.009	0.002 - 0.008
Ga	1.5 - 2.3	1.3 - 2.4	Hf	0.113 - 0.18	0.092 - 0.195
As	0.7 - 1.16	0.5 - 0.79	Ta	0.004 - 0.018	0.001 - 0.014
Se	0.33 - 1.01	0.32 - 1.13	W	0.1 - 0.21	0.14 - 0.29
Rb	0.22 - 1.16	0.15 - 1.2	Pb	0.86 - 2.5	0.6 - 2.72
Sr	2.3 - 5.7	2.3 - 9.3	Th	0.07 - 0.3	0.05 - 0.4
Y	0.4 - 4.7	0.3 - 4.7	U	0.02 - 0.069	0.017 - 0.095
Zr	3 - 4.1	2.8 - 4.2			
Mo	0.7 - 12.49	0.48 - 0.87			
Cd	0.13 - 0.21	0.12 - 0.15			

Table B13. A comparison of standardized root means squared error (SRMSE), obtained by performing source apportionment calculation with traditional CMB and IRCMB, shows the superiority of combining isotope and elemental tracers as compared to elemental tracers alone.

	Traditional CMB	IRCMB	Reduction in error (%)
Local soil and road dust	0.57	0.27	53
North African dust	0.21	0.17	19
Concrete dust	0.82	0.17	79
Vehicular PM	0.16	0.16	0
Oil combustion	0.6	0.6	0
Coal combustion	0.9	0.9	0
Biomass burning	0.63	0.48	24
FCC	1.5	1.4	7
Sea salt	1.9	2.1	(10)

Table B14. A summary of source apportionment results of $PM_{2.5}$ in Clinton Dr., Houston estimated by IRCMB in this study. Results are categorized by mass concentration (high dust, low dust, and regular) as described in the methods section of the main manuscript.

Sample Category	High dust days				Low dust days				Regular			
	Mean	Std	Min	Max	Mean	Std	Min	Max	Mean	Std	Min	Max
$PM_{2.5}$ concentration	29.5	3.2	25.2	32.3	15.1	2.4	12.9	17.9	11.2	1.8	9.3	13.4
North African Dust	13.77	2.36	11.65	15.96	3.41	0.66	2.55	4.14	0.57	0.45	0	1.02
Local soil and road dust	1.51	0.54	0.79	2.09	1.21	0.67	0.55	2.06	0.77	0.35	0.27	1.05
Vehicular PM	5.1	0.4	4.6	5.58	4.63	0.5	3.92	5.04	3.96	1.13	2.27	4.7
Oil combustion	1.02	0.3	0.59	1.23	0.6	0.48	0.1	1.21	0.61	0.36	0.11	0.91
Concrete dust	1.07	0.61	0.65	1.95	1.22	0.69	0.73	2.24	1.95	0.74	1.29	2.87
Coal combustion	0.1	0.11	0	0.21	0.15	0.12	0.04	0.25	0.16	0.12	0.05	0.27
Biomass burning	0.88	0.26	0.68	1.22	0.69	0.65	0.1	1.35	0.17	0.16	0	0.38
FCC	0.01	0	0.01	0.02	0.02	0.02	0	0.03	0.02	0.02	0	0.04
Sea salt	1.78	0.25	1.48	2.09	0.58	0.22	0.39	0.89	0.24	0.06	0.17	0.32
Unapportioned mass	4.3	0.96	2.97	5.21	2.65	0.61	1.73	3.0	1.93	0.29	1.65	2.2

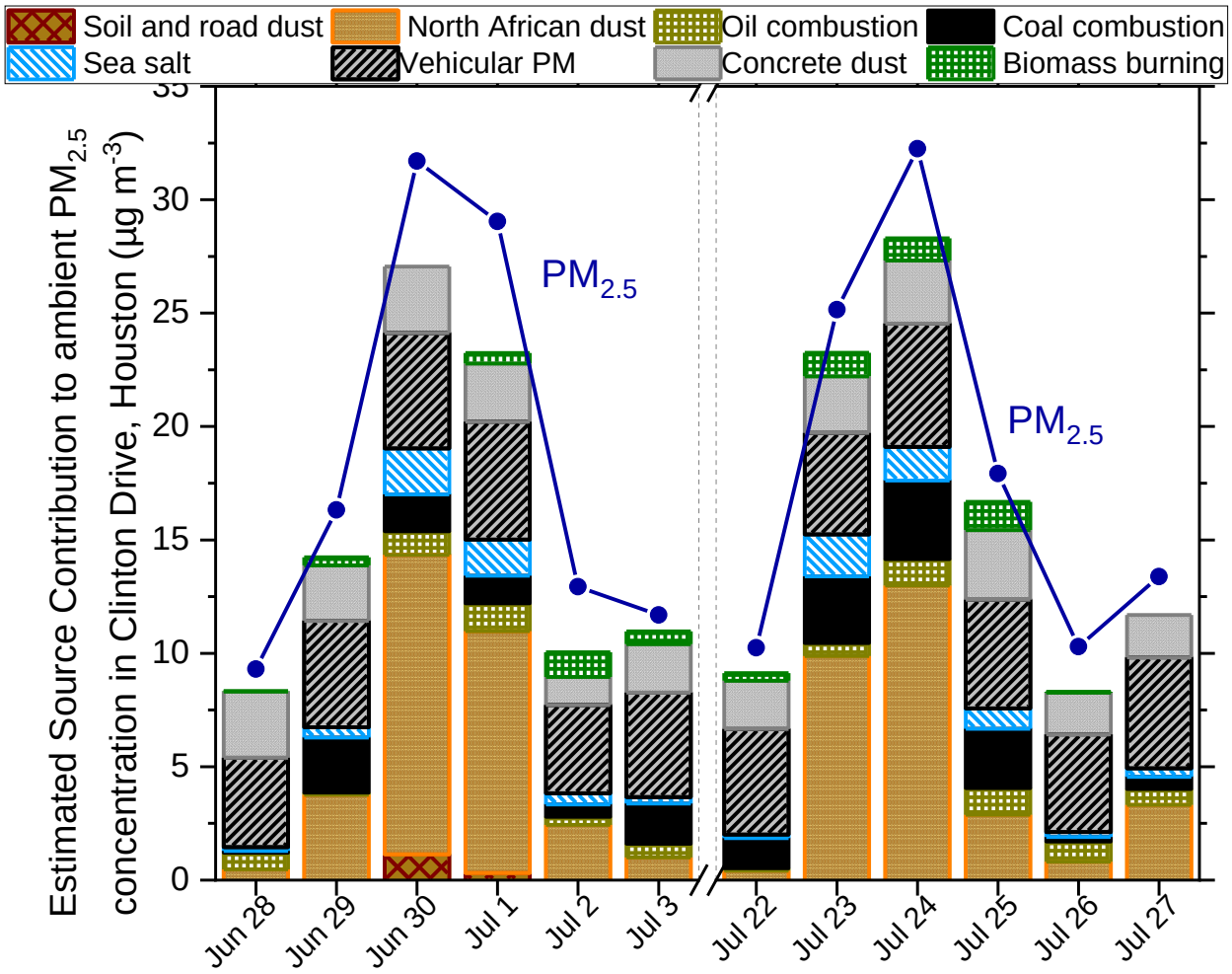

Figure B13. Source apportionment results with traditional CMB. Local soil did not separate from North African dust in 10 out of 12 samples.

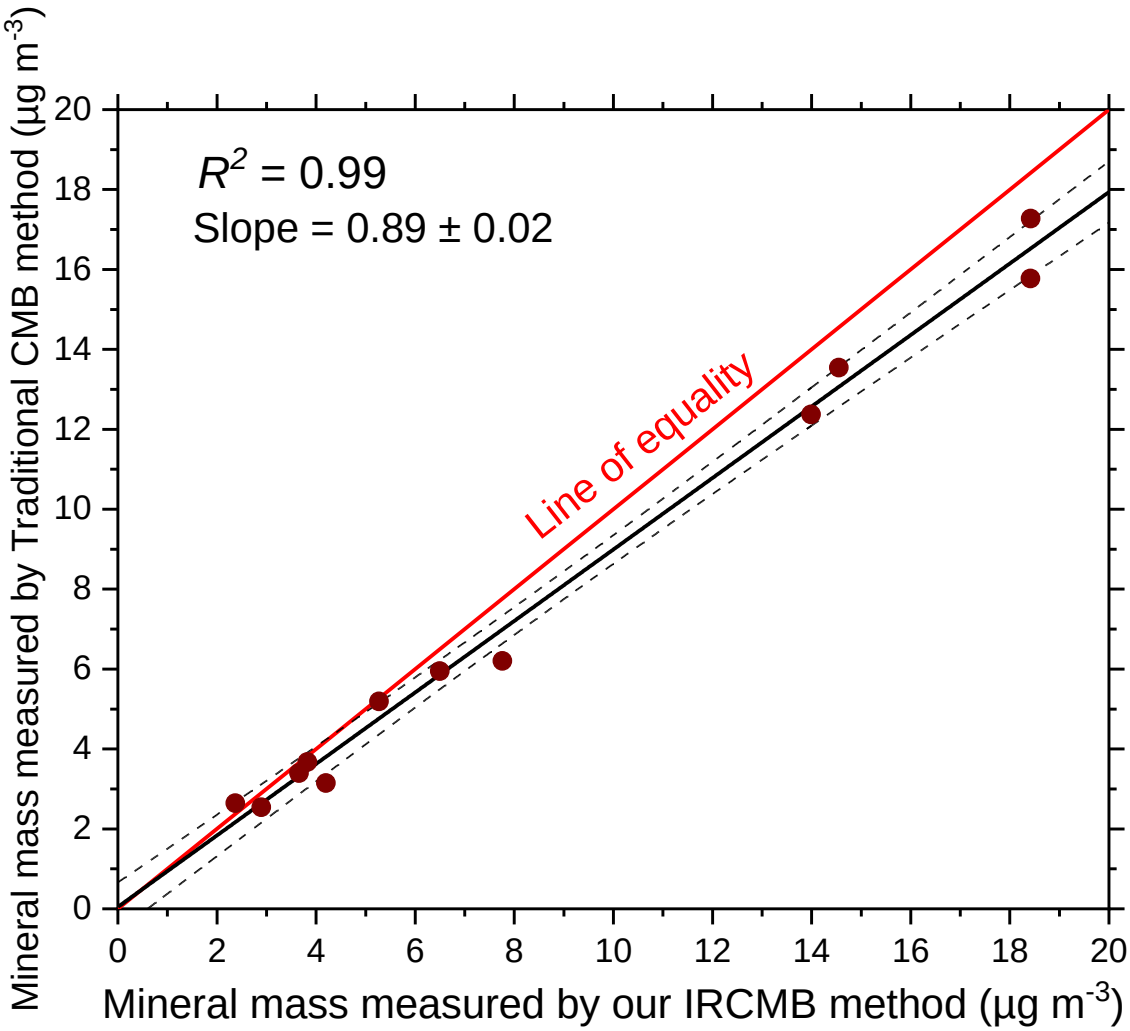

Figure B14. Total mineral mass (North African dust + local soil +concrete dust) calculated by traditional CMB and IRCMB show good correlation, however, a slop of 0.89 implies CMB underestimated total mineral mass by ~11% consistently in our dataset.

Table B15. Elemental source profile of North African dust measured in Barbados.

Element	Abundance (%)	Uncertainty (%)
Li	3.52×10^{-3}	1.84×10^{-3}
Be	2.07×10^{-4}	6.75×10^{-5}
Na	4.72×10^{0}	2.76×10^{0}
Mg	3.14×10^{0}	2.11×10^{0}
Al	8.17×10^{0}	1.44×10^{0}
Si	1.91×10^{1}	4.99×10^{0}

K	1.81×10^{0}	3.25×10^{-1}
Ca	2.09×10^{0}	1.51×10^{-1}
Sc	2.57×10^{-3}	2.1×10^{-3}
Ti	5.42×10^{-1}	1.05×10^{-1}
V	1.18×10^{-2}	9.69×10^{-3}
Cr	8.79×10^{-3}	6.58×10^{-3}
Mn	5.77×10^{-2}	6.42×10^{-3}
Fe	4.05×10^{0}	1.01×10^{0}
Co	9.19×10^{-3}	1.38×10^{-3}
Ni	2.95×10^{-3}	1.45×10^{-3}
Cu	4.46×10^{-3}	3.22×10^{-3}
Zn	1.87×10^{-2}	3.25×10^{-3}
Ga	3.93×10^{-3}	3.67×10^{-4}
As	1.81×10^{-4}	6.2×10^{-5}
Se	5.66×10^{-4}	1.42×10^{-5}
Rb	6.67×10^{-3}	1.28×10^{-3}
Sr	2.06×10^{-2}	2.69×10^{-3}
Y	4.97×10^{-3}	8.89×10^{-3}
Zr	6.99×10^{-3}	4.39×10^{-3}
Mo	4.18×10^{-4}	1.7×10^{-4}
Cd	1.16×10^{-4}	8.18×10^{-5}
Sn	2.11×10^{-3}	1.71×10^{-3}
Sb	1.58×10^{-4}	2.24×10^{-5}
Cs	3.66×10^{-4}	2.76×10^{-5}
Ba	4.49×10^{-2}	4.79×10^{-3}
La	3.73×10^{-3}	2.56×10^{-4}
Ce	7.29×10^{-3}	5.18×10^{-4}
Pr	8.97×10^{-4}	1.06×10^{-4}
Nd	3.84×10^{-3}	2.77×10^{-4}
Sm	8.04×10^{-4}	8.71×10^{-5}

Eu	2.08×10^{-4}	3.08×10^{-5}
Gd	4.53×10^{-4}	6.99×10^{-5}
Tb	1.02×10^{-4}	1.83×10^{-5}
Dy	5.22×10^{-4}	4.26×10^{-5}
Ho	1.12×10^{-4}	3.32×10^{-5}
Er	2.95×10^{-4}	2.88×10^{-5}
Tm	5.3×10^{-5}	1.17×10^{-5}
Yb	2.43×10^{-4}	3.98×10^{-5}
Lu	4.14×10^{-5}	8.79×10^{-6}
Hf	3.93×10^{-4}	1.89×10^{-4}
Ta	8.31×10^{-5}	3.55×10^{-5}
W	1.58×10^{-4}	9.62×10^{-5}
Pb	1.94×10^{-3}	2.18×10^{-4}
Th	1.56×10^{-3}	3.59×10^{-4}
U	3.13×10^{-4}	9.08×10^{-5}

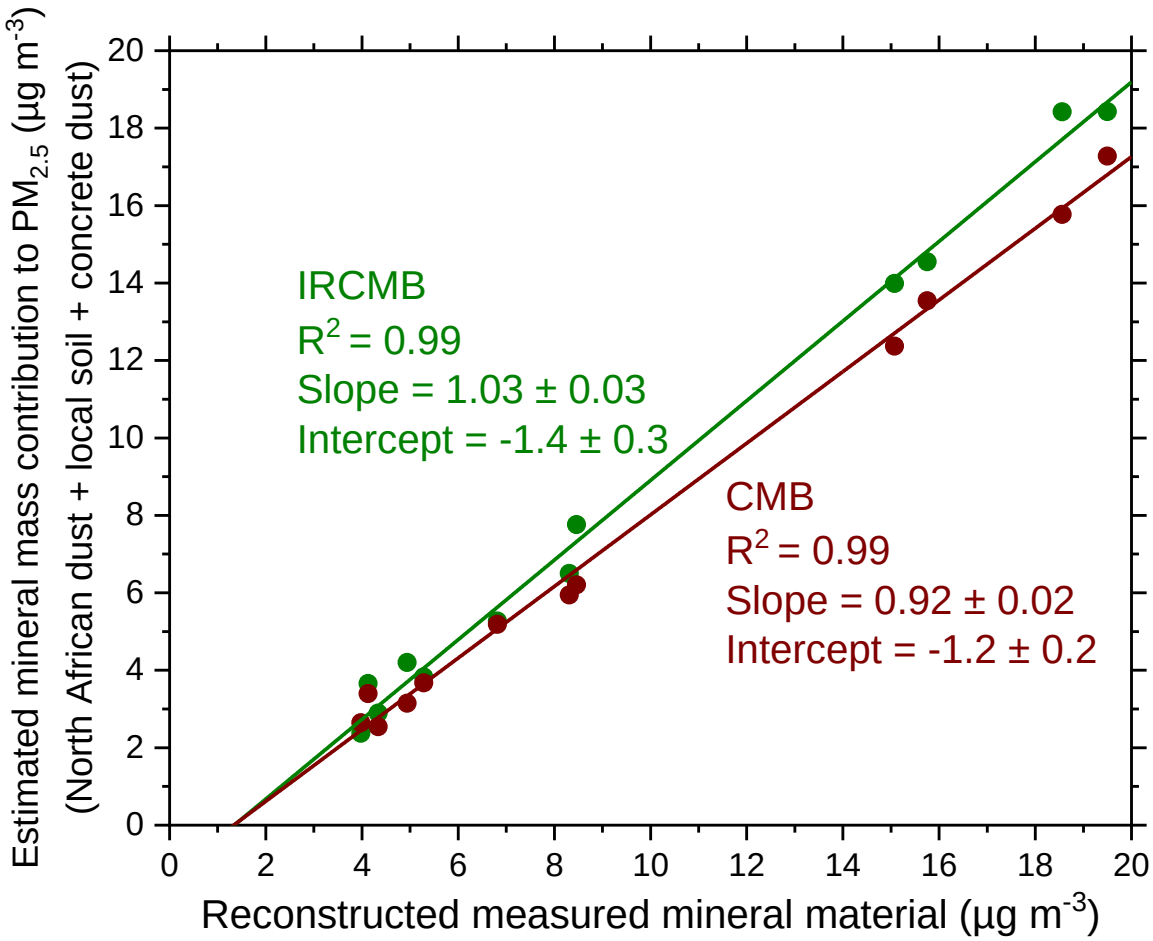

Figure B15. Reconstructed measured mineral material (RMMM) correlated with both IRCMB (in green) and CMB (in brown) but IRCMB had a slope ~1 whereas CMB had slope <1 that suggests that traditional CMB underestimates the mineral mass.

Reconstructed measured mineral material (RMMM) was calculated as the sum of oxides of mineral elements[23, 29] (Al, Si, Ca, Ti, Mg, Na and Fe) and is representative of the net mineral mass in our samples.

$$RMMM = 1.89 \times Al + 2.14 \times Si + 1.40 \times Ca + 1.67 \times Ti + 1.67 \times Mg + 1.43 \times Fe + 1.34 \times \mathrm{Na}$$

APPENDIX C

SUPPORTING INFROMATION FOR CHAPTER III

C.1. Sampling and Site Photographs

Entrance and front of school.

View of frontage road and Interstate 10 from school. For reference, the truck labelled “Con-way” is traveling eastbound on I 10 highway.

Sampling equipment at the rear end of the school showing PM samplers and TCEQ’s trailer.

Figure C1. Pictures of Interstate 10, the frontage road, and samplers at R.P. Harris Elementary school. Photograph of the school (top), the I-10 highway with frontage road (middle), and our samplers (bottom).

C.2. Summary of literature PGE concentration data for in ambient PM from various locations across the world

Table C1. Compilation of PGE studies shows average concentration (in pg m^{-3}) of Pt, Pd and Rh measured in different cities around the world. A significant difference in characteristics of ambient PGEs in European to that of American studies can be observed. An increase in Pd concentration with respect to Pt is also observed from previous decades to the modern era as described by Zereini.*[22, 179, 208]* (n.d. = not detected or below detection limit)

Reference	PGEs analyzed	Sampling Period	Location	Size	Rh (pg m^{-3})		Pd (pg m^{-3})		Pt (pg m^{-3})	
					Avg	Stdev	Avg	Stdev	Avg	Stdev
Rauch et al., 2001 [163]	Pt, Pd, Rh	May- November 1999	Göteborg, Sweden	PM_{10}	2.9	1	4.9	3.1	14.1	3.7
				$PM_{2.5}$	1.6	0.6	1.5	0.5	5.4	1
				PM_{10}	0.6	0.3	1.8	1.6	2.1	0.8
				$PM_{2.5}$	0.5	0.1	1.4	0.8	2.7	1.7
Kanitsar et al., 2003 [166]	Pt, Pd, Rh	Summer 2002	Vienna, Austria	TSP	6.6	2.4	14.4	3.1	38.1	6.3
				PM_{10}	0.4	0.1	2.6	0.6	4.3	1.7
Zereini et al., 2004 [169]	Pt, Pd, Rh	Aug 2001 to July 2002	Frankfurt am Main, Germany	PM_{10}	2.9		25.1		15.7	
					0.7		8.9		6.2	
					0.8		7.8		5.2	
Rauch et al., 2005a [158]	Pt, Pd, Rh	N/A	Göteborg, Sweden	PM_7	2.9	1.1	4.9	3.1	14.1	3.7
			Boston	PM_{10}	1.1	0.9	7.5	5.0	6.7	4.8
			Tokyo	PM_7	0.47		0.79		2.1	
Rauch et al., 2005b [154]	Pt, Pd, Rh	Nov 2002 to Mar 2003	Boston, Massachusetts, USA	PM_{10}	1.3	0.5	7.1	1.9	6.2	2.2
					2.2	1.7	11	5	9.4	3.3
Rauch et al., 2006 [203]	Pt, Pd, Rh	2003	Mexico city, Mexico	PM_{10}	3.2	2.2	11	4	9.3	1.9
Bocca et al., 2006 [340]	Pt, Rh	summer of 2000 and winter of 2001	Buenos Aires, Argentina	PM_{10}	4.3				13.9	
Wichmann et al., 2007 [165]	Pt, Pd, Rh	2005	Braunschweig, Northern Germany	<63µm	10		37.8		159	
		1999			1.2		33.9		6	
Zhang et al., 2008 [162]	Pt, Pd, Rh	Jan-Dec, 2003	Denver, CO, USA	Water soulubl e$PM_{2.5}$	0.5	0.9	4.4	5.1	1.2	1.2
Limbeck et al., 2007 [164]	Pt, Pd	April 21 and May 18, 2005	Vienna	TSP			18	5.9	79	23
				PM_{10}			8.8	3	30	9.2
				$PM_{2.5}$			4.9	1.7	12	4.3

Pan et al. 2009 [341]	Pt, Rh	2007	Beijing, China	TSP	7.44				21.8	
			Guangzhou, China		4.68				10.9	
Zereini et al., 2012 [168]	Pt, Pd, Rh	Jul 2008–Aug 2009	Frankfurt am main, Germany	PM_{10}	3.2		43.9		12.4	
		Jan2008–Jun2009	Deuselbach, Germany		1.2		2.1		2	
		Feb 2008 -Jul 2009	Neuglobsow, Germany		0.3		2.6		1.9	
			Frankfurt, Germany	$PM_{2.5}$	1.8		16.1		9.4	
			Frankfurt, Germany	PM_{1}	0.6		8.4		3.2	
Hays et al., 2011 [219]	Pt, Pd, Rh	Summer,2006	Raleigh, NC, USA	Course ($PM_{10-2.5}$)	0.4	1	1	2	3	4
				Fine ($PM_{2.5}$)	1	2	10	10	10	20
Pakbin et al., 2011 [161]	Rh, Pd, Pt	April 2008 to March 2009	Los Angeles, US	Course ($PM_{10-2.5}$)	1.13	0.31	n.d.	n.d.	2.27	0.74
Puls et al., 2012 [171]	Pd, Pt	2009-11-09 to 2011-12-03	Vienna, Austria	TSP			13.9	6.9	15.6	5.8
				PM_{10}			10.6	4.5	9.9	4.1
				$PM_{2.5}$			4.9	2.3	2.3	1
Morton-Bermea et al., 2014 [342]	Pt	2011	Mexico city	$PM_{2.5}$					45.8	
Rinkovec et al., 2018 [170]	Pt, Pd, Rh	27 Apr 2015 - 6 Mar 2017	Zagreb (North), Croatia	PM_{10}	0.44		3.86		0.49	
				$PM_{2.5}$	0.28		1.46		0.31	
			Zagreb (Centre), Croatia	PM_{10}	0.64		5.4		0.93	
			Zagreb (South), Croatia		0.75		5.6		1.05	
Zhang et al., 2019 [206]	Pt, Pd, Rh	15 Oct, 2014 - 30 Nov, 2014	Beijing, China	$PM_{2.5}$	1.31	2.78	76.9	50.1	9.35	4.69
Liu et al., 2018 [207]	Pt, Pd, Rh	Jan - Dec 2015	Changji, China	PM_{1}	60 (n.d.–210)		1990 (n.d.–10770)		50 (n.d.–190)	
Gomez et al., 2003 [167]	Pt, Pd, Rh	1994-1998	Madrid, Spain	PM_{10}	27	1	5.1	0.9	15	2
					9.1	0.2	32	1	19	1
Diong et al., 2016 [205]	Pt, Pd, Rh	2013-2014	Kolkata, India	PM_{10}	516	201	17462	12593	3490	2070
Atilgan et al., 2012 [343]	Pd	Jun 2010- May 2011	Budapest, Hungary	$PM_{2.5}$			0.45	0.11		
			Istanbul, Turkey				0.48	0.19		

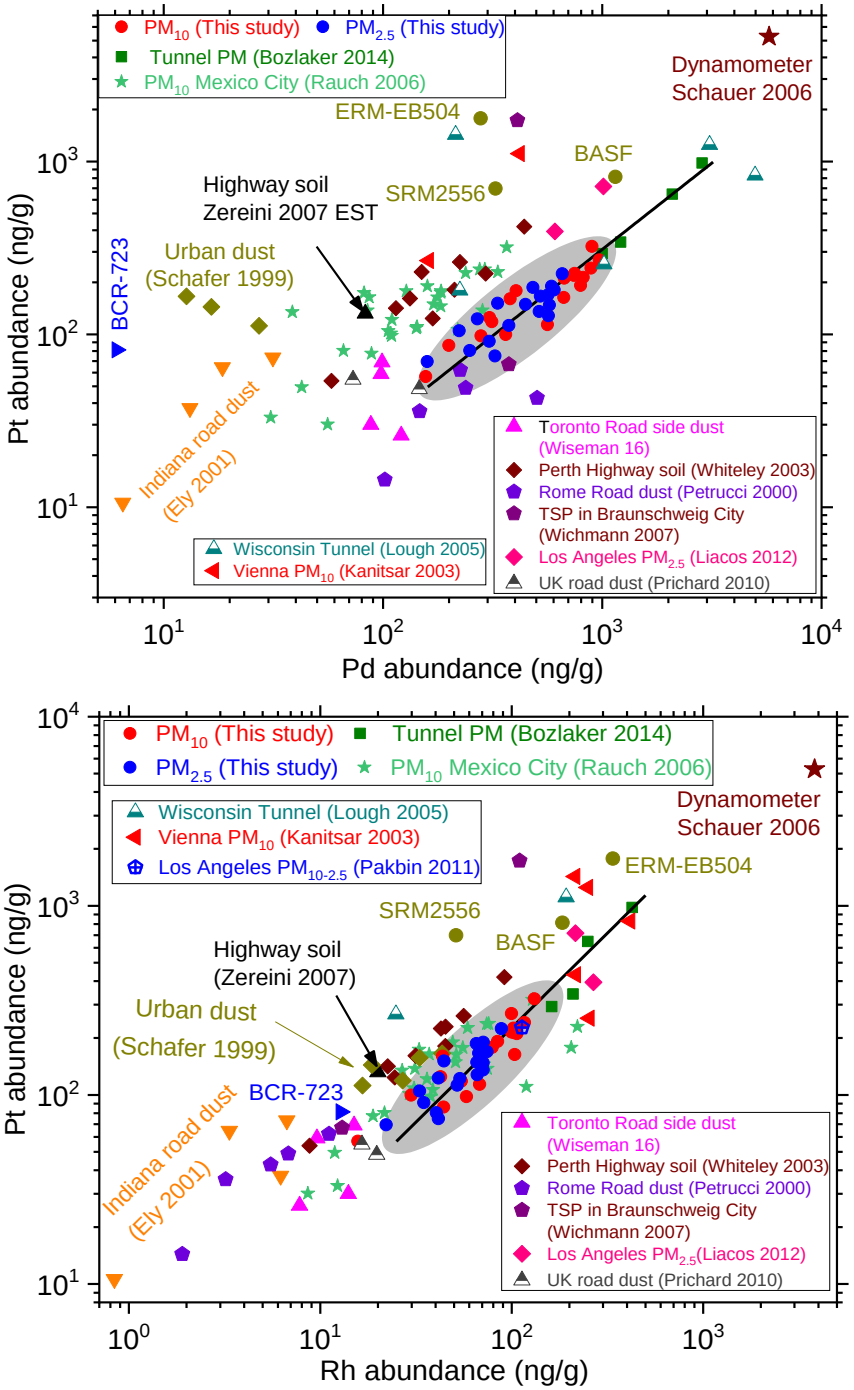

Figure C2. A compilation of Pt, Pd and Rh abundances found in our PM samples compared to other environmental matrices, which include airborne PM [160, 161, 165, 166, 203, 224], roadside soil [178-180, 344-347], and dynamometer room PM.[217] Tunnel PM in green square symbols are from our previous study in Houston [21]. For reference, we show abundance values of mixed-lot used catalyst (BASF) [21], reference materials NIST SRM 2556 (recycled autocatalyst), BCR-723 (European road dust) and ERM-EB504 (used automobile catalyst from Europe).

C.3. Sample Preparation and Laboratory Analysis

All plasticware and Teflonware was first cleaned by soaking overnight in 10% HCl and then in 20% HNO_3. Filters were first placed in 8mL concentrated aqua regia (6 mL 32-35% w/w Optima grade HCl: 2mL 65% w/w Suprapur grade HNO_3) and digested (CEM Mars 5) three times, each at 200 °C and 200 psig with 20 minute dwell time.[18] The digestate was separated into two equal parts (4 mL each) – one for PGE analysis and another for all other elements. Samples for PGE analyses were prepared by heating (80 °C) one part of the aliquot to dryness in a loosely capped vessel, a process that was repeated three times while re-dissolving with concentrated HCl two times and finally using 0.5 M HCl to eliminate HNO_3 matrix along with stable nitrosyl and hydroxynitrate compounds leaving only stable chlorocomplexes [348-350]. The resulting acid solution was passed through cation exchange resins (Dowex 50WX8) to remove polyatomic interferences (resulting from isotopes ^{63}Cu, ^{65}Cu, ^{66}Zn, ^{87}Rb, ^{87}Sr, ^{89}Y, ^{90}Zr and ^{179}Hf) and diluted with 0.5M HCl before analyzing with magnetic sector field ICP-MS (Thermo Scientific ELEMENT). Indium and Bismuth were used as internal standards.

Concentrated (48%, 0.5mL) HF was added to the second aliquot and digested (200 °C, 200 psig, 20 minute) three more times to dissolve the siliceous matrix. Next, 4 mL H_3BO_3 (5% w/v) was added to mask free fluoride ions and re-dissolve fluoride precipitates of La, Ce, Th, and Mg and digesting three more times.[18, 351] This was diluted to 2% HNO_3 using ultrapure water and then analyzed for 18 representative elements (Li, Be, Na, Mg, Al, Si, K, Ca, Ga, As, Se, Rb, Sr, Sn, Sb, Cs, Ba, Pb), 15 transition metals (Sc, Ti, V, Cr, Mn, Fe, Co, Ni, Cu, Zn, Y, Zr, Mo, Cd, W), 14 lanthanides (La, Ce, Pr, Nd, Sm, Eu, Gd, Tb, Dy, Ho, Er, Tm, Yb, Lu) and 2 actinides (Th, U) using dynamic reaction cell-quadrupole-inductively coupled plasma-mass spectrometry (DRC-

q-ICP-MS). V, Fe, Ni, Cd were analyzed using NH_3 as a cell gas[352] to minimize polyatomic interferences under dynamic mass bandpass.[87] Instrumental settings for ICP-MS are listed in

Table C2. Instrumental settings and operating parameters for DRC-q-ICP-MS.

Instrument	Perkin Elmer NexION 300
Nebulizer	Concentric (Meinhard) [Type A0.5]
Spray chamber	Baffled quartz cyclonic
Torch injector	Quartz
Auto lens	On
RF power	1600 W
Gas flow rates	
Plasma	18 L min^{-1}
Nebulizer	0.96-1.18 L min^{-1}
Auxiliary	1-1.2 L min^{-1}
Interface	Platinum cones
Sampler	1.1 mm in diameter
Skimmer	0.9 mm in diameter
Measurement parameters	
Scanning mode	Peak hopping
Sweeps/reading	20
Readings/replicate	1
Replicates	3
Dwell time	50 ms (standard mode); 100 ms (DRC mode)
Sampling parameters	AS-93 plus auto-sampler
Sample flush time	45 s
Sample flush pump speed	20 rpm
Read delay	65 s
Read delay pump speed	24 rpm
Wash time	60 s
Wash pump speed	24 rpm
DRC parameters	
Cell gas	NH_3 (0.2-1.0 mL min^{-1})
RPq	0.25-0.75
RPa	0

C.4. Quality Assurance and Control

Three reference materials, viz. BCR 723 (European Commission road dust), SRM 2556 (National Institute of Standards and Technology, NIST used auto catalyst) and SRM 1648a (NIST urban particulate matter) were used for quality assurance and control. PGE recoveries from BCR 723 and SRM 2556 were in the range 88-115% and all other elements from the three reference materials were recovered between 85% and 118% (see Figure C4). Additionally, the mid-point concentration level spike, introduced every 10^{th} sample, was quantitated within 90-110% of the expected value. Quantitative recoveries of all certified and uncertified elements in reference materials and spiked-concentrations demonstrated the accuracy and precision of our sample preparation and ICP protocols and that the instrument performed consistently with minimal drift over the duration of our laboratory work. Method detection limits were calculated by analyzing seven blank matrix solution and multiplying the resultant standard deviation by three times. Average elemental concentrations analyzed in our field blanks, along with their respective detection limits are presented in Table C3.

The PGE content of PM was quantitatively compared with a mixed spent catalyst sample donated by BASF (Engelhard), who developed the first production catalytic converter. They are also a leading refiner of PGEs from scrap automotive catalytic converters and provided a sample ground to 60-mesh and recycled from a random lot of different manufacturers and models. This batch, which expected to be representative of the U.S. fleet, contained 184, 1148, and 814 $\mu g\ g^{-1}$, respectively of Rh, Pd, and Pt [21].

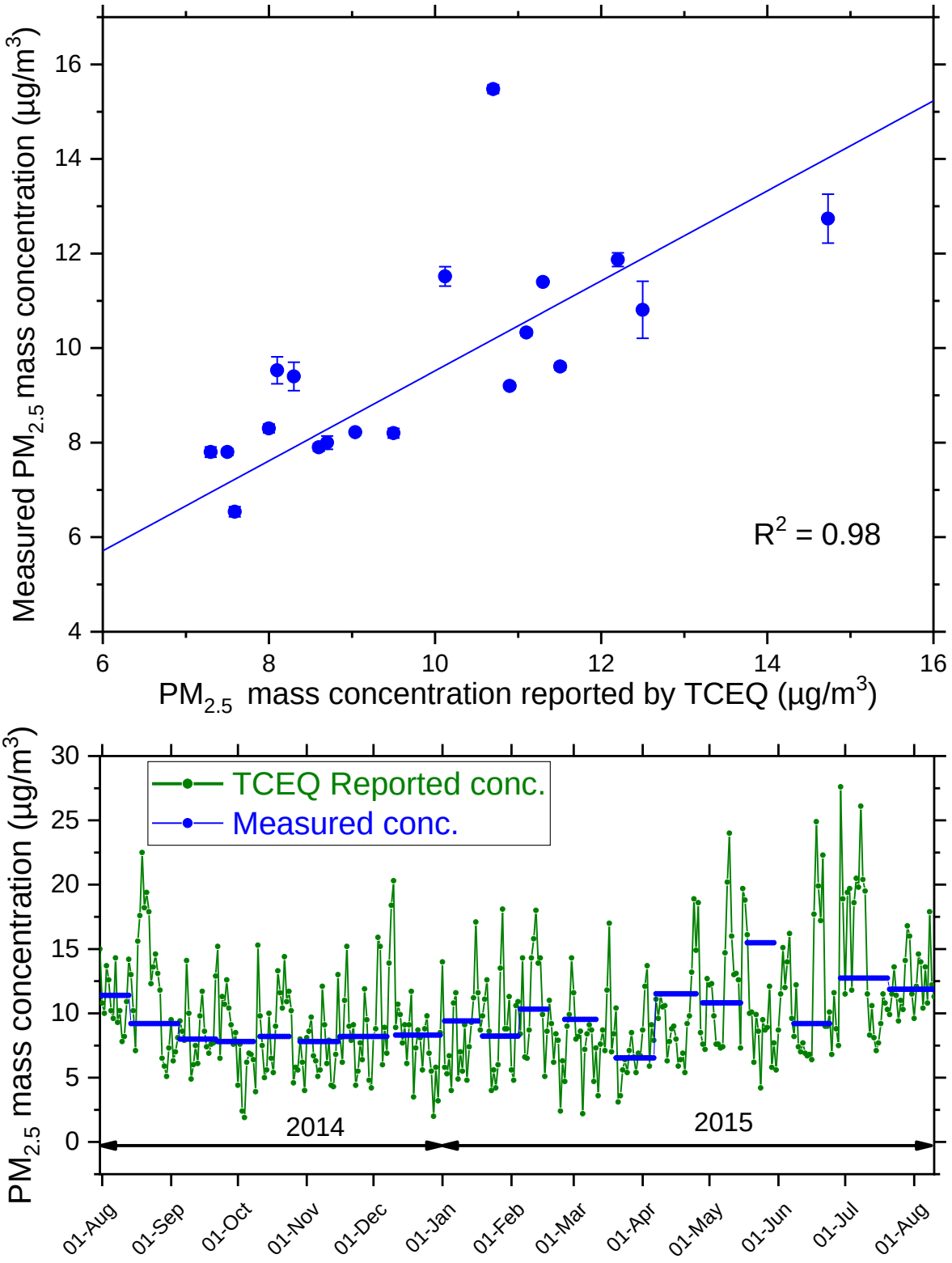

Figure C3. $PM_{2.5}$ mass concentration measured correlated with TCEQ measurements (top). Bottom figure shows the daily variation of $PM_{2.5}$ concentration reported by TCEQ. All TCEQ data obtained from TCEQ online database *[339]*.

Table C3. Method detection limits (MDL) and average blank concentrations. BDL = Below detection limit

Element	m/z	MDLs (µg/L)	RSD (%)	Average Blank (µg/L)	Element	m/z	MDLs (µg/L)	Average Blank (µg/L)	RSD (%)
Li	7	0.03	11.7	BDL	Ba	138	0.22	10	9.01
Be	9	0.03	12.6	BDL	La	139	0.02	BDL	9.4
Mg	25	0.4	8.2	0.59±0.19	Ce	140	0.02	BDL	8.3
Al	27	0.61	9.2	2.6±0.64	Pr	141	0.02	BDL	7.9
Si	29	35	15.4	BDL	Nd	146	0.02	BDL	6.8
K	39	1.2	14	BDL	Sm	152	0.02	BDL	9.2
Ca	44	11.5	15.4	102±41.2	Eu	153	0.02	BDL	12.5
Ti	47	0.22	15.3	BDL	Gd	158	0.02	BDL	9.4
V	51	0.79	15.3	BDL	Tb	159	0.02	BDL	15.1
Cr	52	0.1	15.9	BDL	Dy	164	0.03	BDL	6.8
Mn	55	0.03	15.4	BDL	Ho	165	0.03	BDL	15.1
Fe	57	1.7	15.4	BDL	Er	166	0.03	BDL	10
Ni	58	0.03	16.2	BDL	Yb	174	0.02	BDL	10
Co	59	0.05	15.5	BDL	Lu	175	0.02	BDL	12.9
Cu	65	0.08	15.4	BDL	W	184	0.04	BDL	16.8
Zn	66	0.22	15.4	BDL	Pt	195	0.02	BDL	15
Ga	69	0.05	15.3	BDL	Pb	208	0.05	BDL	8.3
As	75	0.04	15.4	BDL	Th	232	1.2	BDL	12
Se	82	0.11	10.7	BDL	U	238	0.02	BDL	15.6
Rb	85	0.04	13	BDL					
Sr	88	0.04	9.3	BDL					
Y	89	0.03	15.4	BDL					
Zr	90	0.04	12.5	BDL					
Mo	96	0.04	8.2	BDL					
Rh	103	0.02	15	BDL					
Pd	105	0.06	15	BDL					
Cd	113	0.04	10.5	BDL					
Sn	118	0.04	12.6	BDL					
Sb	121	0.04	10.7	BDL					
Cs	133	0.03	10.8	BDL					

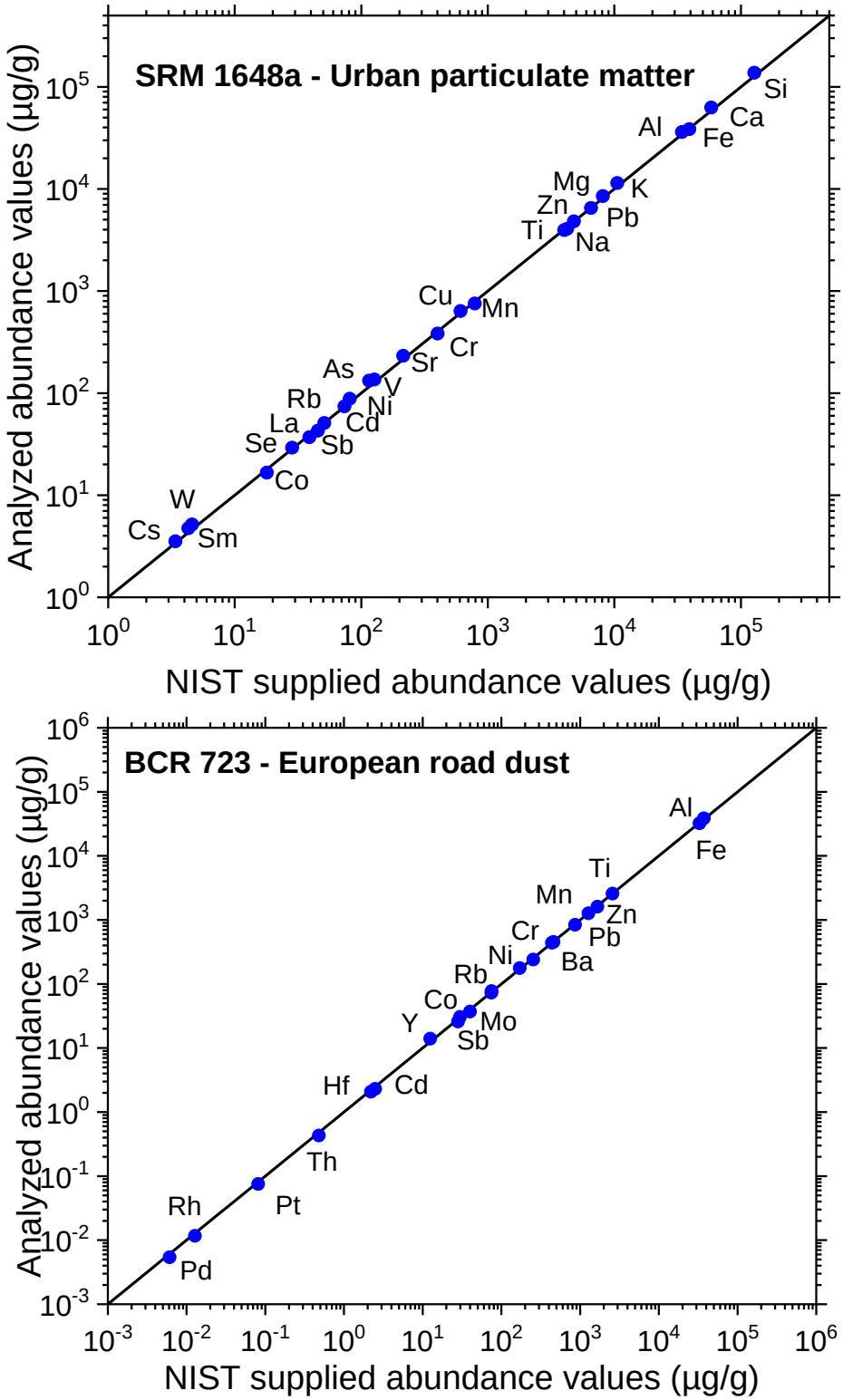

Figure C4. Recoveries in SRM 1648a – Urban particulate matter (top) and BCR 723 – Road dust (bottom), obtained through our digestion procedure and ICP-MS analysis over the course of this study

C.5. PM and NO_x Data at this Site

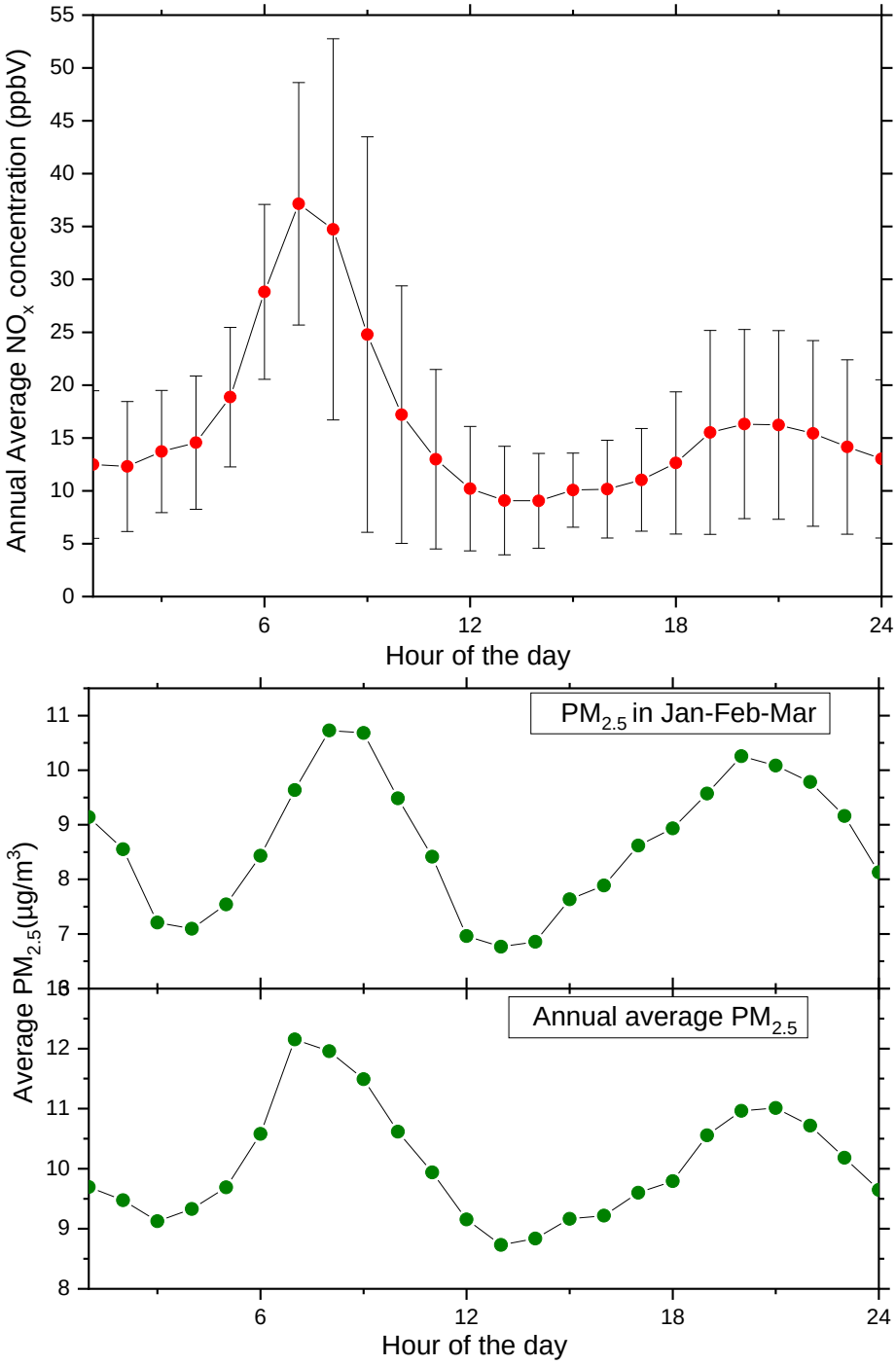

Figure C5. Plots of annual-averaged hourly NO_x data (top), winter-averaged hourly $PM_{2.5}$ (middle), and annual-average hourly $PM_{2.5}$ (bottom) for the Texas Commission on Environmental Quality (TCEQ) site CAMS 0001 (our site) which shows early morning and evening peaks. Both NO_x and $PM_{2.5}$ data are adopted from the TCEQ online database [339].

Morning peaks and evening peaks (see Figure C5***Error! Reference source not found.***) are t ypical because of the strong influence of traffic sources at the site. Peaks at similar times were observed in previous studies in Houston [189] on vehicular emissions. This demonstrates that our current site was also heavily influenced by vehicular emissions even though our sampler was placed only at the rear of the school.

C.6. Source Apportionment

PM masses were apportioned by the Chemical Mass Balance model (EPA CMB8.2) using elemental source profiles for vehicular emissions [21], soil and road dust [18] North African dust [29], petroleum refinery fluid catalytic cracking activities [86], coal combustion [138] oil combustion, and shipping activities,[193, 194, 353] biomass burning and municipal incineration [138, 194] and cement manufacturing [193, 195]. Based on source signatures and high signal-to-noise ratio (>2), Na, Mg, Al, Si, K, Ca, Ti, V, Cr, Mn, Fe, Co, Cu, As, Se, Zn, Sr, Zr, Mo, Rh, Pd, Cd, Sn, Sb, Ba, La, Ce, Pr, Nd, Sm, W, Pt, and Pb were chosen as fitting species. Pt, Pd, and Rh are strong markers for light-duty vehicle tailpipe emissions. Fe, Zn, Cu, Zr, Mo, Sb, and Ba are marker species for brake lining and tire wear [218, 224, 354]. Light lanthanoids, La, Ce, Pr, Nd, and Sm are excellent markers of both fluid catalytic cracking [86] and oil combustion [355] whereas V separates oil burning from catalytic cracking.

C.7. PM Gravimetric Mass and Elemental Concentrations

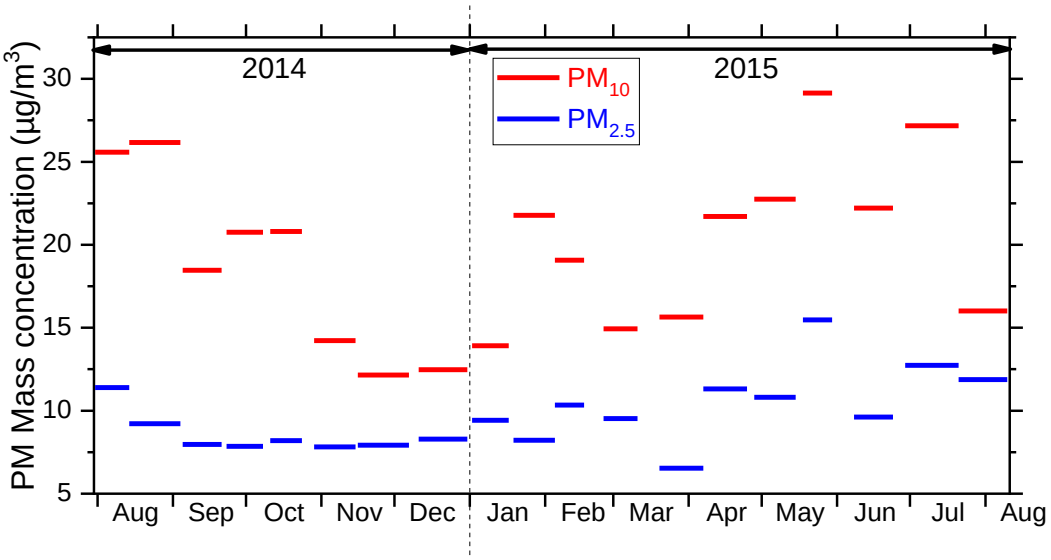

Figure C6. $PM_{2.5}$ and PM_{10} mass concentrations measured gravimetrically over the entire sampling period.

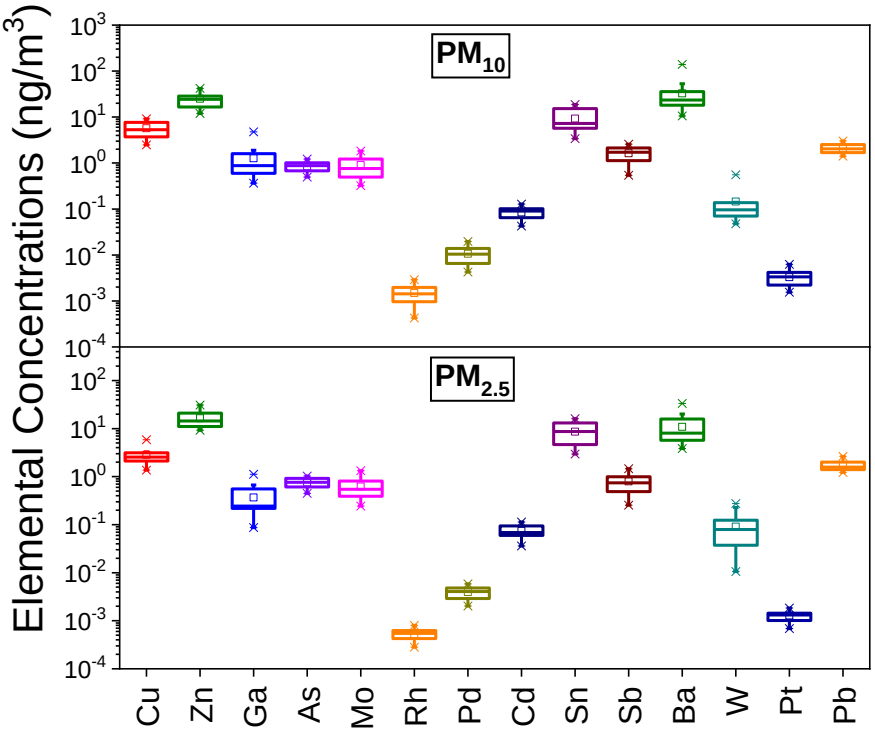

Figure C7. Ambient air concentrations of all elements typically attributed to motor vehicles based on our earlier work in the Washburn Tunnel. All concentrations values were blank subtracted. Blank concentrations are in Table C3.

C.8. Non-PGE Metal Ratios

Table C4. Comparison of elemental ratios obtained in this study to tunnel PM [21], Houston road dusts [18], upper continental crust (UCC) [210], brake wear [196, 214, 217, 354, 356, 357], tire dust [196, 217], and near-road measurements[14, 160, 217, 219, 221, 223, 224].

Ratio	Cu/Sb	Range	Cu/Zn	Range	Cu/Ba	Range	Cu/Pb	Range	Cu/As	Range	Cu/Cd	Range	Zn/Pb	Range	As/Pb	Range	Pb/Cd	Range
PM2.5 (this study)	3.8 ± 0.9	2.2-5.8	0.18 ± 0.05	0.11-0.27	0.33 ± 0.17	0.08-0.79	1.6 ± 0.4	0.9-2.6	3.7 ± 1.2	2.5-7.4	38 ± 8	23-52	9.3 ± 2	6-13.3	0.45 ± 0.08	0.31-0.61	25 ± 6	14-42
PM10 (This study)	3.6 ± 0.9	2-5.6	0.24 ± 0.09	0.11-0.49	0.22 ± 0.08	0.06-0.41	2.7 ± 0.9	1.3-5.2	6.6 ± 1.7	4.2-10.6	67 ± 16	44-109	9.3 ± 2	6-13.3	0.45 ± 0.08	0.31-0.61	26 ± 5	17-36
Tunnel PM2.5	6.2 ± 0.1	6.1-6.3	1.91 ± 0.17	1.74-2.07	0.67 ± 0.02	0.65-0.69	39.8 ± 8.6	31.2-48.4	35.4 ± 0.2	35.2-35.5	238 ± 59	179-297	20.7 ± 2.7	17.9-23.4	1.13 ± 0.25	0.88-1.38	5.94 ± 0.2	5.74-6.14
Tunnel PM10	6.6 ± 0.3	6.3-6.9	0.62 ± 0.04	0.59-0.66	0.65 ± 0.12	0.52-0.77	15.83 ± 2.38	13.45-18.2	17.33 ± 1.97	15.36-19.3	195 ± 15	180-210	25.3 ± 2.4	22.9-27.6	0.94 ± 0.24	0.7-1.18	12.46 ± 0.91	11.55-13.37
Tunnel road dust1	10.0 ± 1.5		0.21 ± 0.02		0.11 ± 0.02		0.65 ± 0.26		23.61 ± 2.79		136.48 ± 34.43		3.13 ± 1.12		0.03 ± 0.01		210.5 ± 107.1	
Houston road dust1	19.8 ± 9.0	16.3 – 25.4	0.05 ± 0.03		0.1 ± 0.12		0.94 ± 0.54		9.87 ± 5.05		89.17 ± 63.6		18.07 ± 9.35		0.09 ± 0.04		95.3 ± 63.2	
Upper continental crust	83.3		0.28		0.03		1.28		8.08		183.64		4.62		0.16		143.64	
Houston soil	22.5 ± 3.8	16.8-27.4	0.17 ± 0.15	0.02-0.37	0.06 ± 0.01	0.04-0.07	0.51 ± 0.1	0.4-0.66	3.97 ± 1.28	2.61-6.07	67.0 ± 22.6	45.5-105.0	12.67 ± 11.1	1.1-26.4	0.13 ± 0.02	0.11-0.15	128.2 ± 19.4	108.6-158.2
Brake Wear/ Tire, Exhaust and oil Profiles																		
Schauer 2006 (Dynamometer-exhaust)	54.5 ± 22.1	212.6-88.7	0.43 ± 0.18	0.22-0.69	0.11 ± 0.08	0.03-0.27	25.66 ± 15.98	8.5-60.35	29.23 ± 10.96	13.35-49.08	62.26 ± 28.35	15.46-102.24	0.98 ± 0.63	0.17-2.45	0.98 ± 0.63	0.17-2.45	18.25 ± 13.69	2.36-49.25
Schauer 2006 (Brakes)	4.8 ± 3.6	0.9-16.2	1.41 ± 1.19	0.02-3.93	0.49 ± 0.66	0.02-2.11	1739 ± 5383	16-21152	423 ± 1065	0.29-3709	360.1 ± 265.8	64-710	990.8 ± 1853.5	46.13-7473	15.73 ± 21.89	0.07-58.75	0.17 ± 0.08	0.07-0.25
Schauer 2006 (Tire)	7.8 ± 5.1	2.7-12.9	0.23 ± 0.31	0.01-0.83	21.21 ± 34.9	0.79-61.5	45.95 ± 65.6	4.1-121.55	7.22 ± 11.82	0.24-20.87			218.18 ± 66.7	146.73-278.8	19.6 ± 3.54	17.1-22.1		
Tire Dust (Hildemann 1991)	0.5		1.14		1.3		3.1		>1000				2.7					
Stout et al 2018 (used engine oil)									12									
Miller et al 2007 (lubrication oil)			0.02				3						146					
Hjortenkrans 2007 (Brake)	5.15 ± 1.33	3.43-6.67	4.62 ± 1.46	3.38-6.67			152.86 ± 68.78	100-250			93882 ± 85000	30000-240000	28.14 ± 7.34	16.92-37.5			724.25 ± 222.38	461.54-960
Hjortenkrans 2007 (Tire)	9.6 ± 0.6	8.57-10	0 ± 0	0-0			1.42 ± 0.01	1.41-1.43			11.15 ± 0.14	10.91-11.28	1135.59 ± 24.94	1115.38-1176.47			7.84 ± 0.06	7.73-7.88
Hulskotte 2014 (Brake)	4.14		2.38				86.2						36.2					
Near Roadway measurements																		
Licaos et al 2012 (Los Angeles PM2.5)	5.6 ± 0.09	5.5-5.7	2.7 ± 0.4	2.3-3.1	0.5 ± 0.2	0.3-0.7	839.8 ± 737.5	102.3-1577.3	238.6 ± 0	238.6-238.6	883.7 ± 167.8	715.9-1051.5	352.2 ± 319	33.2-671.3	2339.1 ± 2191.7	147.4-4530.8	3.8 ± 3.2	0.7-7
Dabek-Zlotorzynska et al 2019 (Canadian PM2.5)	7.9 ± 1.4	6.5-9.8	0.7 ± 0.4	0.2-1.3	0.6 ± 0.2	0.4-0.8												
Hays et al 2011 (Raleigh, NC -PM)	3.3 ± 0.8	2.4-4.2	0.7 ± 0.1	0.6-0.8	0.4 ± 0	0.4-0.4	4.5 ± 1.7	2.8-6.3	46.5 ± 36.8	9.8-83.3	173.8 ± 76.3	97.5-250	6.2 ± 1.6	4.6-7.8	10.2 ± 3.8	6.4-14	37.5 ± 2.5	35-40
Shauer 2006 (Milwaukee Tunnel PM10)	5.6 ± 1.6	3.5-8.7	0.9 ± 0.7	0-2.8	0.4 ± 0.2	0-0.8	6.4 ± 4.7	0.6-17.1	209.7 ± 193.2	4.2-650	555.8 ± 432.4	54.1-1228.6	7.6 ± 8.3	0-31.9	17.9 ± 17.5	1.9-56.7	101.5 ± 87.7	0-293.3
Shauer 2006 (Milwaukee Tunnel PM2.5)	5.7 ± 2.0	3.7-10.7	1.4 ± 1.4	0-5.1	0.4 ± 0.3	0-0.9	8.6 ± 5.7	1.4-17.3	74.9 ± 93.1	0-290	267.3 ± 224.8	0-620	6.6 ± 5.9	0-20.7	18.4 ± 15	2.7-51.7	41.8 ± 24	0-84.3
Grieshop 2005 (Pittsburg Tunnel PM2.5	4.7 ± 0.9	3.7-5.8	4.7 ± 0.9	3.7-5.8	0.9 ± 0.8	0-2.1			6.6 ± 4.4	2.2-11					31 ± 15.7	15.3-46.7	14.6 ± 9.1	5.6-23.7
Song et al 2011 (New Jersey highway	11.5 ± 1.7	8.7-13.1	1.7 ± 0.4	1.4-2.1			10.5 ± 0.6	9.9-11.1			321.3 ± 68.8	252.5-390	6.3 ± 1	5.3-7.3			30.4 ± 4.9	25.5-35.3
Lough et al 2005 (Tunnel PM10)	6.2 ± 1.4	5.1-8.8	0.8 ± 0.4	0.3-1.4	0.4 ± 0.1	0.3-0.6	6.2 ± 5.1	0.9-13.5	211.3 ± 159.8	15.6-415	490.9 ± 256.1	55.6-830	8.8 ± 8.7	1.6-25.7	18.9 ± 18.1	1.9-44.6	135.2 ± 109.7	37-321.4

C.9. Collinearity between LDV and HDT Profiles

CMB cannot potentially separate LDVs from HDTs due to collinearity in source profiles that only consider metal(loid)s like in this manuscript [14, 201, 202]. Previous studies have shown that parameters like elemental carbon, organic carbon, alkanes, hopanes, and other VOCs are necessary to separate gasoline-powered LDVs from diesel-powered HDTs while performing source apportionment via receptor models [199, 200, 358-361]. Our attempt to use both LDV and HDT elemental source profiles [14, 160, 196, 201] caused collinearity problems precluding a satisfactory solution. Collinearity in elemental profiles is demonstrated in this section by making scatter plots of literature LDV and HDT data that report metallic composition. As seen in Figure C8, LDV and HDT elemental profiles are highly correlated ($R^2 > 0.90$) in all cases [14, 160, 201] necessitating non-elemental tracers to individually obtain their contributions to ambient PM. Note that we have not considered a paper from Prof. Lynn Hildemann's group [196] in this section since they reported only a few metal(loid)s above the detection limit.

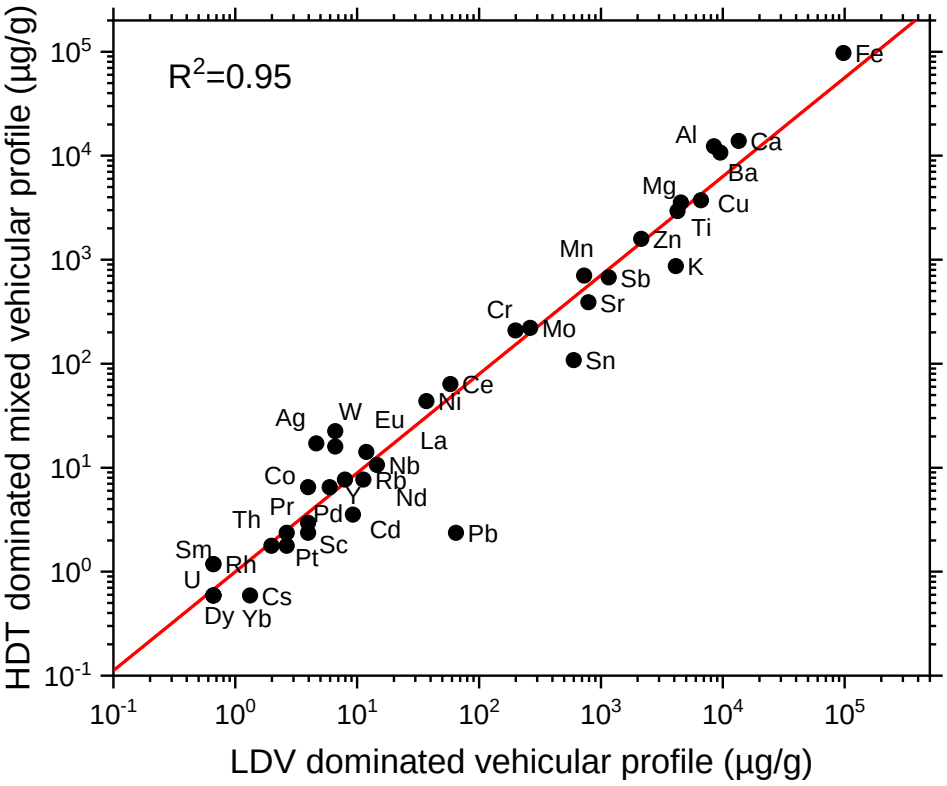
R2=0.95
HDT dominated mixed vehicular profile (µg/g)
LDV dominated vehicular profile (µg/g)
Fe
Al
Ca
Ba
Mg
Cu
Ti
Zn
Mn
K
Sb
Sr
Cr
Mo
Sn
Ce
Ni
Ag
W
Eu
La
Nb
Co
Rb
Y
Nd
Th
Pr
Pd
Cd
Pb
Sm
Sc
Pt
Rh
U
Cs
Dy
Yb

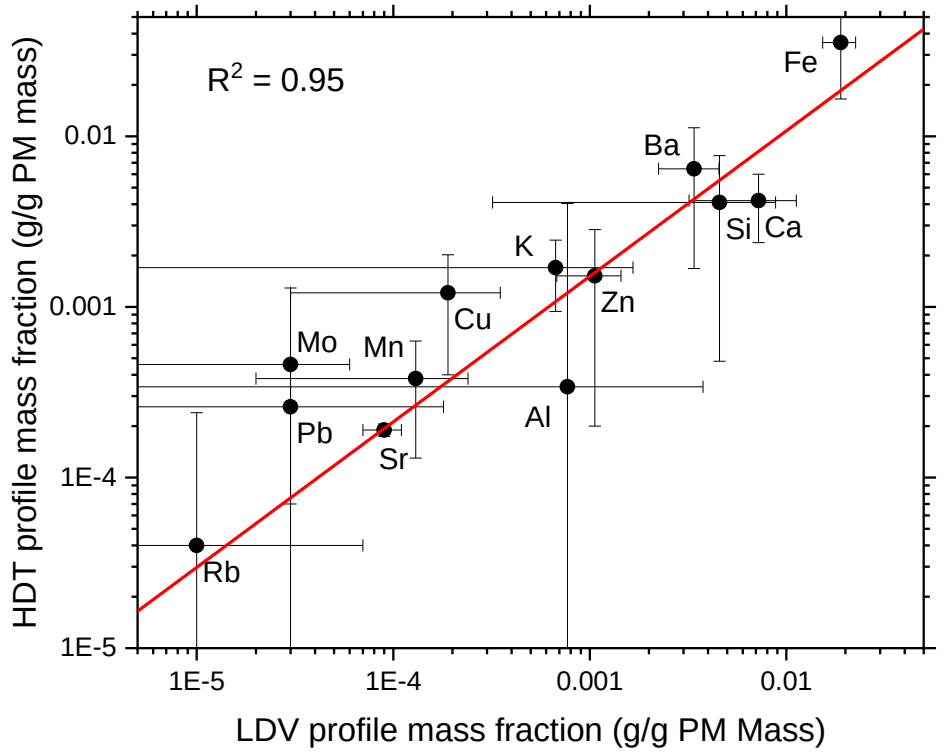
R2 = 0.95
HDT profile mass fraction (g/g PM mass)
LDV profile mass fraction (g/g PM Mass)
Fe
Ba
Si
Ca
K
Zn
Cu
Mo
Mn
Al
Pb
Sr
Rb

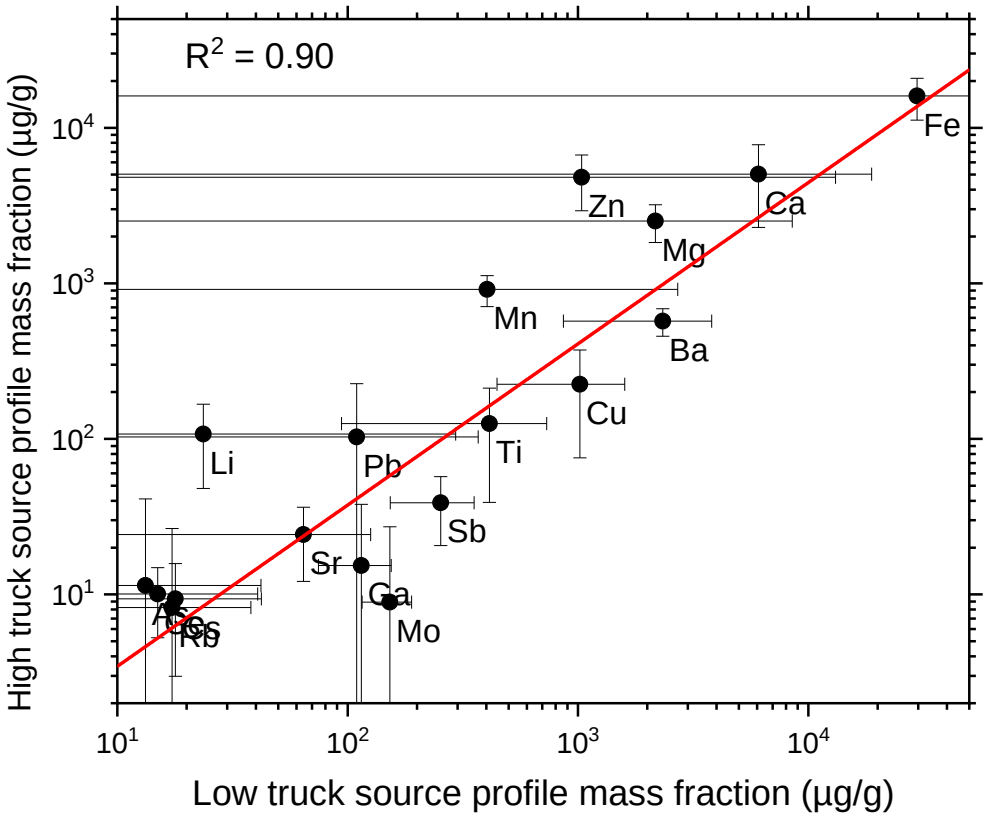

Figure C8. Similarity in HDT and LDV profiles manifests as strong correlations in the plots shown above. Profiles from (a) [160] (b).[201], and (c).[14] are shown above. Collinear profiles are not separated well during chemical mass balance modelling resulting in HDTs "interfering" with LDV source apportionment values reported.

C.10. Source apportionment results for light-duty vehicles

CMB calculations of motor vehicles' contributions to PM_{10} and $PM_{2.5}$ are depicted below. Details in the main manuscript.

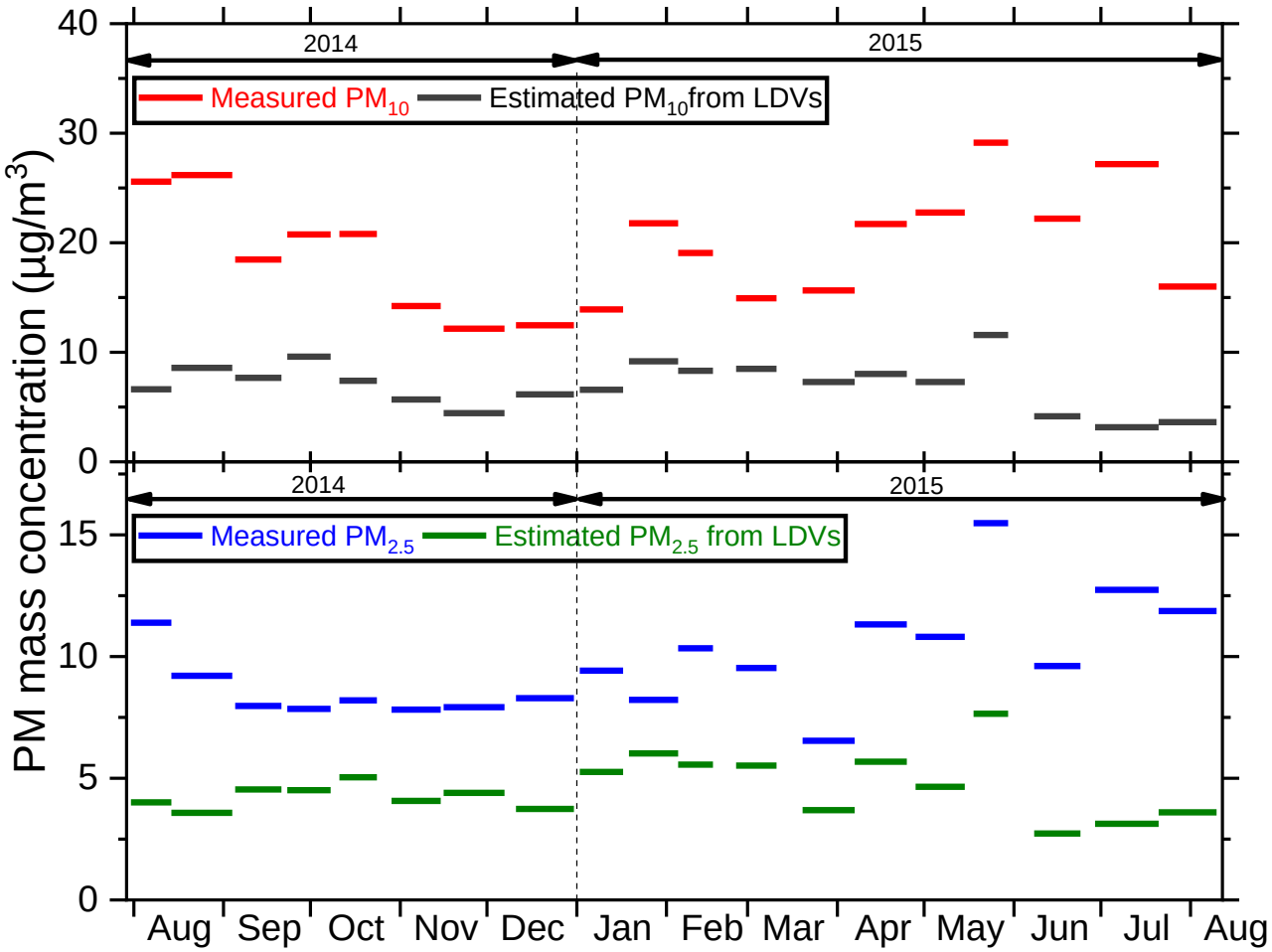

Figure C9. Time series of CMB model estimates for direct vehicular contribution to the mass for PM_{10} (top) and $PM_{2.5}$ (bottom) compared to the total measured PM.

Table C5. Statistics for best-fit lines plotted in Figure IV-4 of the main article. None of them had statistically significant intercept values as their upper confidence limit (UCL) and lower confidence limit (LCL) includes the origin.

	$PM_{2.5}$								
Elements	R^2	Slope	Std. error	95% LCL	95% UCL	Intercept	Std. error	95% LCL	95% UCL
Rh	0.89	1.32E-03	1.14E-04	1.08E-03	1.56E-03	-7.80E-03	5.73E-03	-1.99E-02	4.29E-03
Pd	0.79	1.06E-02	1.34E-03	7.80E-03	1.34E-02	-9.12E-02	6.71E-02	-2.33E-01	5.05E-02
Pt	0.77	2.99E-03	3.93E-04	2.16E-03	3.82E-03	-8.63E-03	1.97E-02	-5.03E-02	3.30E-02
Sb	0.61	2.88E+00	5.61E-01	1.69E+00	4.06E+00	-5.27E+01	2.82E+01	-1.12E+02	6.82E+00
Cd	0.67	1.97E-01	3.37E-02	1.26E-01	2.69E-01	-1.60E+00	1.69E+00	-5.17E+00	1.98E+00
Cu	0.52	8.79E+00	2.04E+00	4.50E+00	1.31E+01	-1.19E+02	1.02E+02	-3.35E+02	9.67E+01
Pb	0.59	3.76E+00	7.55E-01	2.16E+00	5.35E+00	2.81E+00	3.80E+01	-7.73E+01	8.29E+01
As	0.65	1.55E+00	2.76E-01	9.65E-01	2.13E+00	5.95E+00	1.39E+01	-2.33E+01	3.52E+01
Zn	0.29	3.26E+01	1.23E+01	6.70E+00	5.85E+01	1.56E+02	6.16E+02	-1.14E+03	1.46E+03
Ba	0.13	1.81E+01	1.17E+01	-6.76E+00	4.30E+01	1.67E+02	5.84E+02	-1.07E+03	1.41E+03
Mo	0.63	2.38E+00	4.48E-01	1.44E+00	3.33E+00	-4.75E+01	2.25E+01	-9.58E+01	7.28E-01
Ga	0.08	7.24E-01	5.98E-01	-5.39E-01	1.99E+00	5.37E+00	3.01E+01	-5.80E+01	6.88E+01
Sn	0.21	1.64E+01	7.78E+00	-5.20E-02	3.28E+01	9.94E+01	3.91E+02	-7.26E+02	9.25E+02
W	0.32	3.12E-01	1.13E-01	7.34E-02	5.50E-01	-6.29E+00	5.71E+00	-1.84E+01	5.82E+00

	PM_{10}								
	R^2	Slope	Std error	95% LCL	95% UCL	Intercept	Std error	95% LCL	95% UCL
Rh	0.83	2.66E-03	2.96E-04	2.03E-03	3.28E-03	2.00E-02	1.20E-02	-4.40E-02	3.70E-03
Pd	0.75	1.99E-02	2.78E-03	1.40E-02	2.58E-02	-1.69E-01	1.08E-01	-3.96E-01	5.83E-02
Pt	0.71	5.22E-03	8.03E-04	3.52E-03	6.91E-03	-1.98E-02	3.11E-02	-8.54E-02	4.59E-02
Sb	0.65	2.68E+00	4.84E-01	1.66E+00	3.70E+00	-1.09E+01	1.88E+01	-5.05E+01	2.86E+01
Cd	0.55	1.09E-01	2.40E-02	5.84E-02	1.60E-01	4.65E-01	9.32E-01	-1.50E+00	2.43E+00
Cu	0.57	8.70E+00	1.84E+00	4.82E+00	1.26E+01	-1.84E+01	7.13E+01	-1.69E+02	1.32E+02
Pb	0.37	2.22E+00	7.00E-01	7.41E-01	3.69E+00	3.20E+01	2.71E+01	-2.53E+01	8.92E+01
As	0.52	8.34E-01	1.95E-01	4.23E-01	1.24E+00	1.38E+01	7.54E+00	-2.16E+00	2.97E+01
Zn	0.12	1.61E+01	1.06E+01	-6.21E+00	3.84E+01	7.41E+02	4.10E+02	-1.24E+02	1.61E+03
Ba	0.23	2.29E+01	1.08E+01	-1.48E-03	4.59E+01	4.46E+02	4.13E+02	-4.34E+02	1.33E+03
Mo	0.44	1.35E+00	3.18E-01	6.78E-01	2.02E+00	-3.17E+00	12.3E+01	-2.92E+01	2.28E+01
Ga	0.11	8.90E-01	6.39E-01	-4.64E-01	2.24E+00	2.18E+01	2.46E+01	-3.04E+01	7.41E+01
Sn	0.11	8.10E+00	5.73E+00	-3.98E+00	2.02E+01	1.95E+02	2.22E+02	-2.73E+02	6.63E+02
W	0.05	1.17E-01	1.27E-01	-1.51E-01	3.86E-01	3.12E+00	4.93E+00	-7.29E+00	1.35E+01

APPENDIX D

SUPPORTING INFROMATION FOR CHAPTER V

D.1. SAMPLING INFORMATION

Figure D1. Map showing the location of our sampling site, a busy and populated area of Houston, to capture typical urban air.

D.2. DRC-Q-ICPMS settings and QAQC

Table D1. Instrumental settings and operating parameters for DRC-q-ICP-MS.

Instrument	Perkin Elmer NexION 300
Nebulizer	Concentric (Meinhard) [Type A0.5]
Spray chamber	Baffled quartz cyclonic
Torch injector	Quartz
Auto lens	On
RF power	1600 W
Gas flow rates	
Plasma	18 L min^{-1}
Nebulizer	0.96-1.18 L min^{-1}
Auxiliary	1-1.2 L min^{-1}
Interface	Platinum cones
Sampler	1.1 mm in diameter
Skimmer	0.9 mm in diameter
Measurement parameters	
Scanning mode	Peak hopping
Sweeps/reading	20
Readings/replicate	1
Replicates	3
Dwell time	50 ms (standard mode); 100 ms (DRC mode)
Sampling parameters	AS-93 plus auto-sampler
Sample flush time	45 s
Sample flush pump speed	20 rpm
Read delay	65 s
Read delay pump speed	24 rpm
Wash time	60 s
Wash pump speed	24 rpm
DRC parameters	
Cell gas	NH_3 (0.2-1.0 mL min^{-1})
RPq	0.25-0.75
RPa	0

Table D2. Method detection limits (MDL) and average blank concentrations. BDL = Below detection limit

Element	m/z	MDLs (µg/L)	Average Blank (µg/L)	Element	m/z	MDLs (µg/L)	Average Blank (µg/L)
Li	7	0.03	BDL	La	139	0.02	BDL
Be	9	0.03	BDL	Ce	140	0.02	BDL
Mg	25	0.4	0.59±0.19	Pr	141	0.02	BDL
Al	27	0.61	2.6±0.64	Nd	146	0.02	BDL
Si	29	35	BDL	Sm	152	0.02	BDL
K	39	1.2	BDL	Eu	153	0.02	BDL
Ca	44	11.5	102±41.2	Gd	158	0.02	BDL
Ti	47	0.22	BDL	Tb	159	0.02	BDL
V	51	0.79	BDL	Dy	164	0.03	BDL
Cr	52	0.1	BDL	Ho	165	0.03	BDL
Mn	55	0.03	BDL	Er	166	0.03	BDL
Fe	57	1.7	BDL	Yb	174	0.02	BDL
Ni	58	0.03	BDL	Lu	175	0.02	BDL
Co	59	0.05	BDL	W	184	0.04	BDL
Cu	65	0.08	BDL	Pt	195	0.02	BDL
Zn	66	0.22	BDL	Pb	208	0.05	BDL
Ga	69	0.05	BDL	Th	232	1.2	BDL
As	75	0.04	BDL	U	238	0.02	BDL
Se	82	0.11	BDL				
Rb	85	0.04	BDL				
Sr	88	0.04	BDL				
Y	89	0.03	BDL				
Zr	90	0.04	BDL				
Mo	96	0.04	BDL				

Rh	103	0.03	BDL				
Pd	105	0.06	BDL				
Cd	113	0.04	BDL				
Sn	118	0.04	BDL				
Sb	121	0.04	BDL				
Cs	133	0.03	BDL				
Ba	138	0.22	BDL				

Table D3. Recovery of elements measured post acid dissolution in DRC-q-ICPMS.

Element	m/z	Abundance in NIST SRM 1648a			Abundance in BCR-723		
		Certified Values	Measured	Recovery	Certified Values	Measured	Recovery
		µg g^{-1}	µg g^{-1}	%	µg g^{-1}	µg g^{-1}	%
Na	23	4240	4062	95.8			
Mg	24	8130	8521	104.8			
Al	27	34300	36048	105.1	37500	38550	102.8
Si	29	128000	137404	107.4			
K	39	10560	11426	108.2			
Ca	44	58400	62666	107.3			
Ti	47	4021	3957	98.4	2580	2571	99.7
V	51	127	136	107.1	74.9	73	97.5
Cr	52	402	382.5	95.2	440	440	100
Mn	55	790	754	95.4	1280	1269	99.1
Fe	57	39200	38457	98.1	32900	32209	97.9
Co	59	17.93	16.6	92.6	29.8	30.6	102.7
Ni	60	81.1	88.15	108.7	171	177	103.5
Cu	63	610	637.3	104.5			
Zn	66	4800	4820	100.4	1660	1613	97.2
As	75	115.5	132.5	114.7			
Se	82	28.4	29.2	102.8			
Rb	85	51	50.8	99.6	75	77	102.7
Sr	88	215	232	107.9	254	240	94.5
Y	89				12.5	14	112
Mo	96				40	37	92.5
Rh	103				0.0128	0.0117	91.4
Pd	105				0.0061	0.0054	88.5
Cd	113	73.7	74.2	100.6	2.5	2.3	92

Sn	118						
Sb	121	45.4	42.9	94.5	28.2	26	92.2
Cs	133	3.4	3.5	103.8			
Ba	138				460	453	98.5
La	139	39	37	94.9			
Sm	147	4.3	4.7	110.2			
Hf	179				2.2	2.1	95.5
W	184	4.6	5.2	112.2			
Pt	196				0.081	0.075	92.4
Pb	206	6550	6499	99.2	866	841	97.1
Th	232				0.48	0.43	89.6

D.3. RMMM calculation and elemental evidence of mineral mass

Table D4. Metal oxide to metal mass ratio used in this study to calculate the RMMM.

Element	Oxide	Oxide/Metal Ratio
Al	Al_2O_3	1.89
Si	SiO_2	2.14
Ca	CaO	1.40
Ti	TiO_2	1.67

Houston is surrounded by agricultural lands and biomass burning from the neighboring area, states, and other countries (Central America) is expected to elevate the PM concentrations. These aerosols being potassium-rich is likely to interfere in RMMM calculations including K and its oxides. Therefore, we modify our RMMM equation as:

RMMM = (Al*1.89 +Si*2.14 + Ca*1.40 + Ti*1.67)/0.75

The oxide-equivalent mass of these four elements accounts for almost ~75 % of the total mass [29] hence, the oxide mass is divided by 0.75 to estimate the total crustal mass. Since motor vehicles can also contribute significantly to Al, Si, Ca, and Ti specifically in coarse size PM (around 20% [21]), we corrected model estimates of crustal PM_{10} by adding 20% of vehicular apportioned PM_{10}.

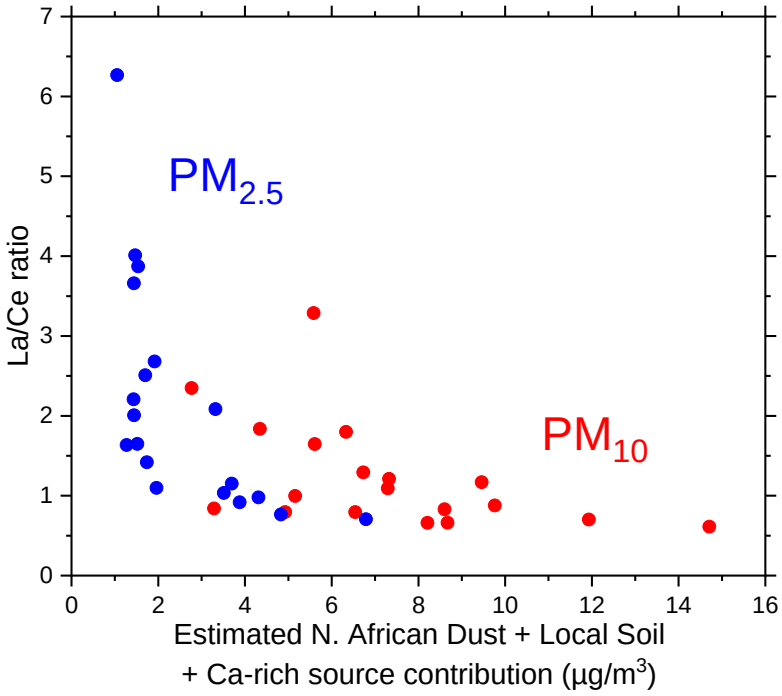

Figure D2. La/Ce ratio negatively correlated with estimated crustal mass, inferring crustal mass influencing lanthanides in ambient PM.

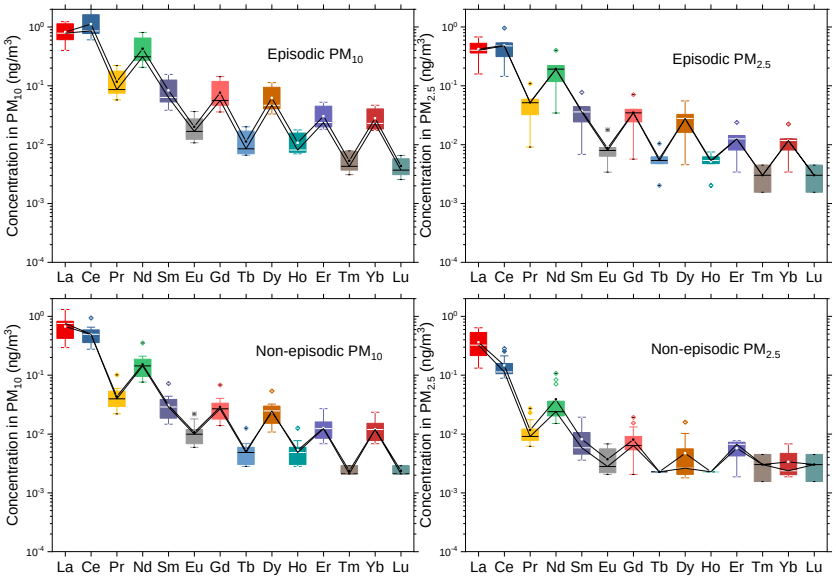

Figure D3. Lanthanide abundances during North African dust episodic days and non-episodic showing a clear change in a pattern in $PM_{2.5}$ (right; top and bottom panels). PM_{10} has less influence from FCC emission and more from mineral dust and shows relatively less deviation.

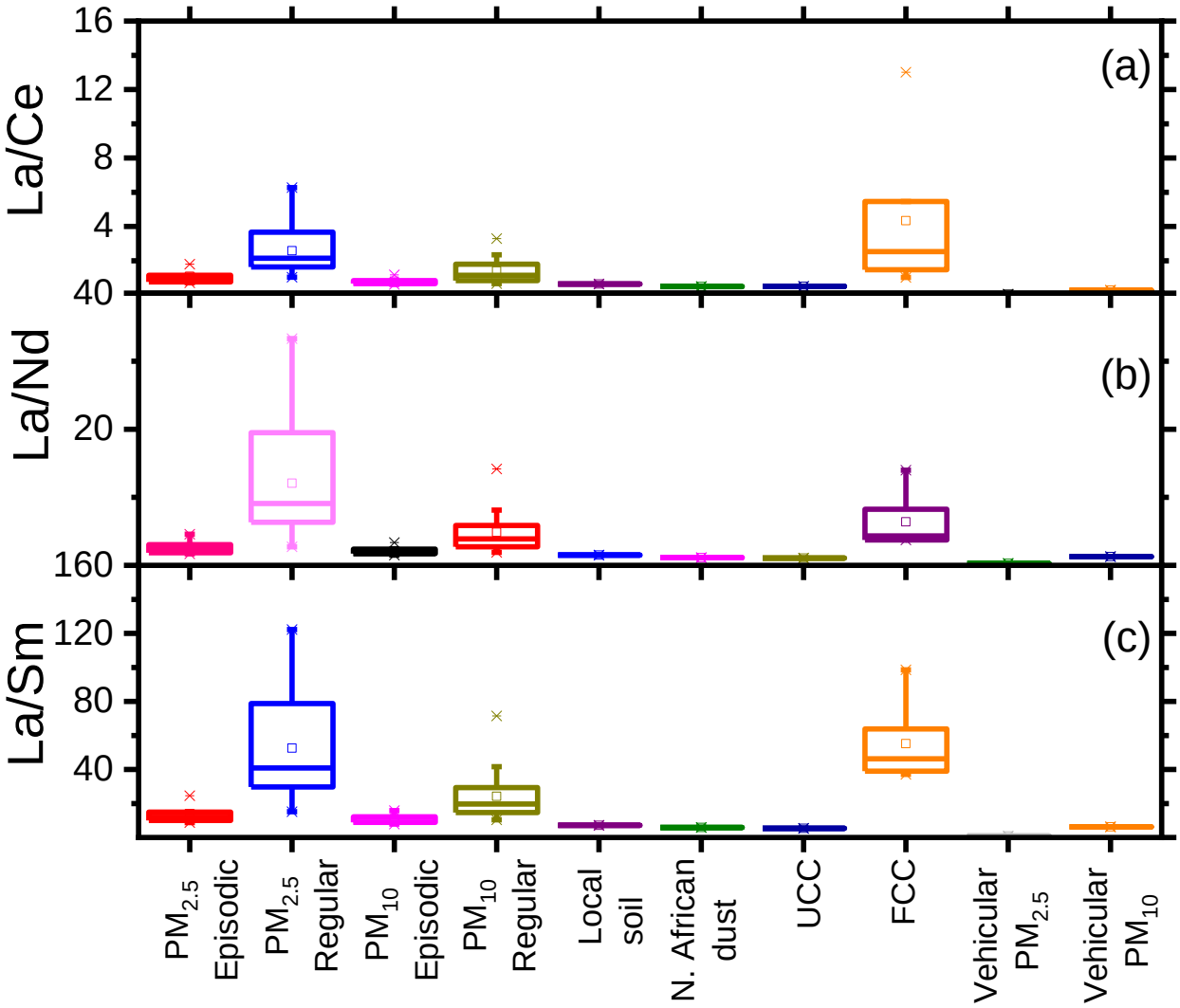

Figure D4. Elemental ratios of Lanthanides in PM_{10} and $PM_{2.5}$ during episodes and non-episodes of Saharan dust intrusion. Ratios tend to be closer to crustal profiles in dust episodic days whereas non-episodic days show resemblance to catalytic cracking profile (FCC)[86] indicating Lanthanides are influenced mainly by FCC activities and oil-burning during non-episodic days. Tunnel and Road dust[18] (T&R dust), Upper Continental Crust [120](UCC), Local soil [18], Saharan dust [29], Light Duty Vehicles particulate matter (LDV PM) profiles are compared to demonstrate the contrast in Lanthanide ratios indicating that FCC activities were the primary source of lanthanides when Saharan dust intrusion was low or negligible.

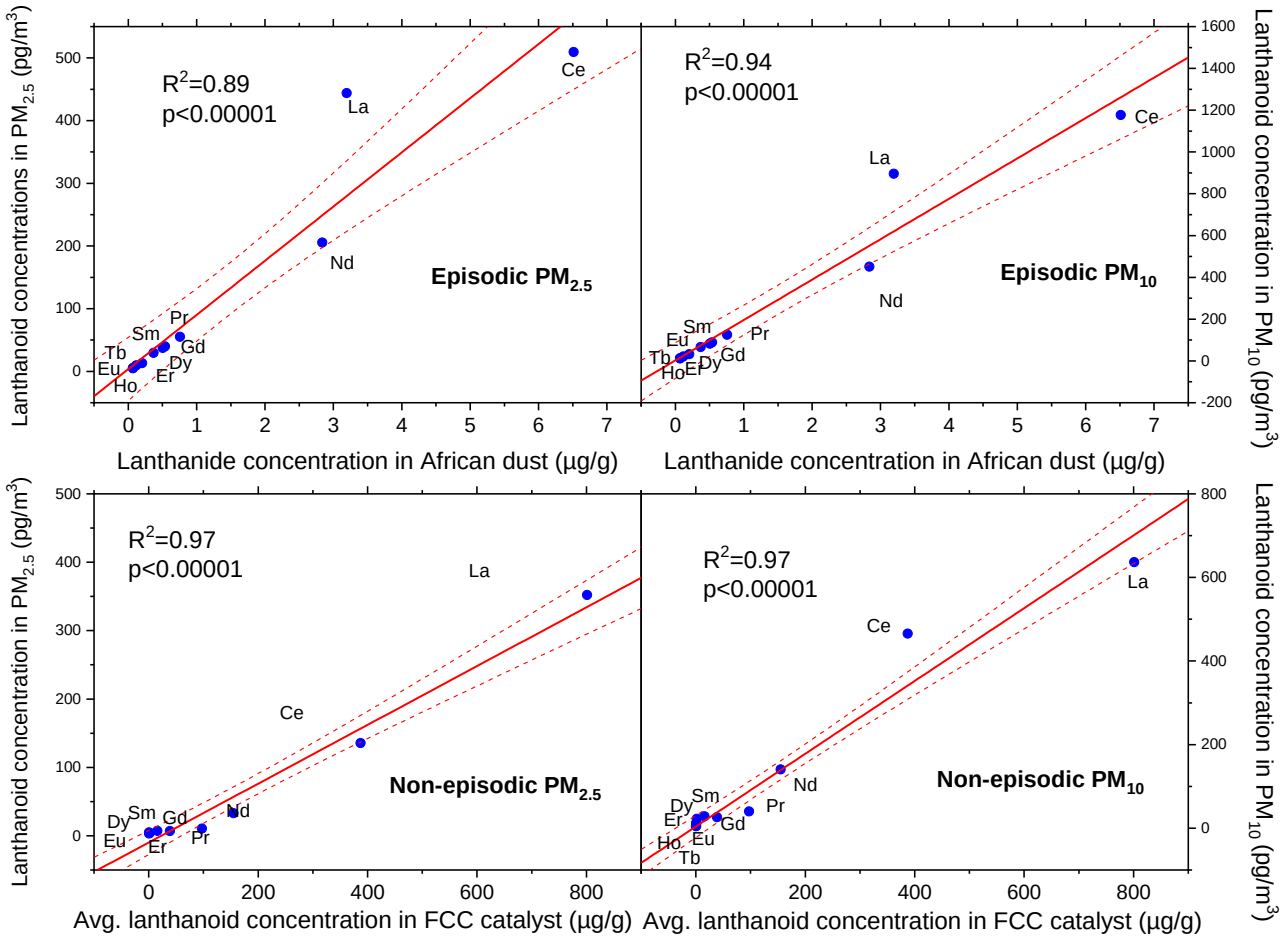

Figure D5. Lanthanide abundances correlate more towards African dust, collected at Barbados [29], on episodic days (panel (a) and (b)), whereas on other days it resembles more like FCC catalysts [86] (panel (c) and (d)) indicating African dust dominating lanthanides contribution while FCC dominates on other days.

D.4. Satellite and aerosol model evidence of long-range PM transport

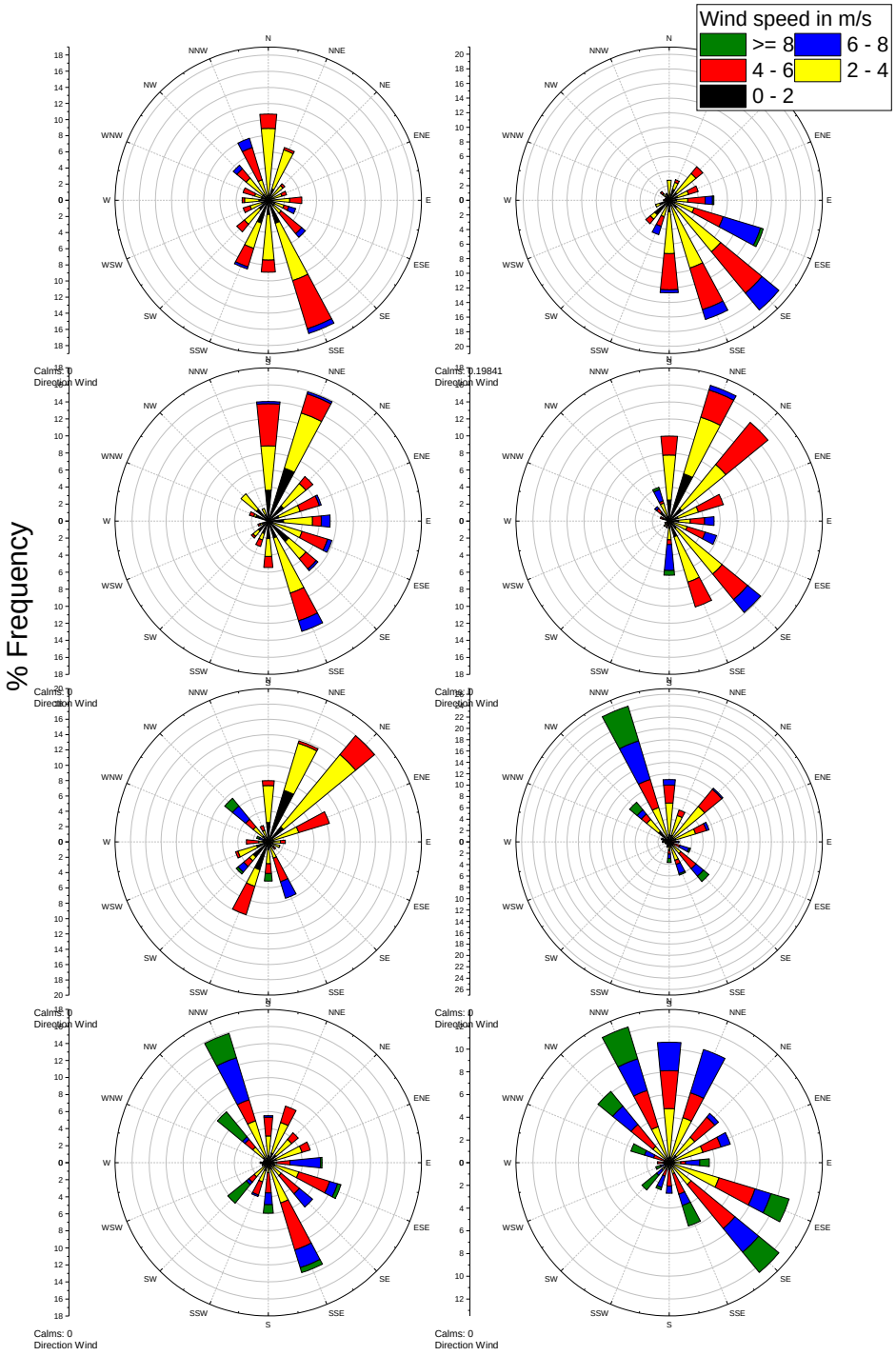

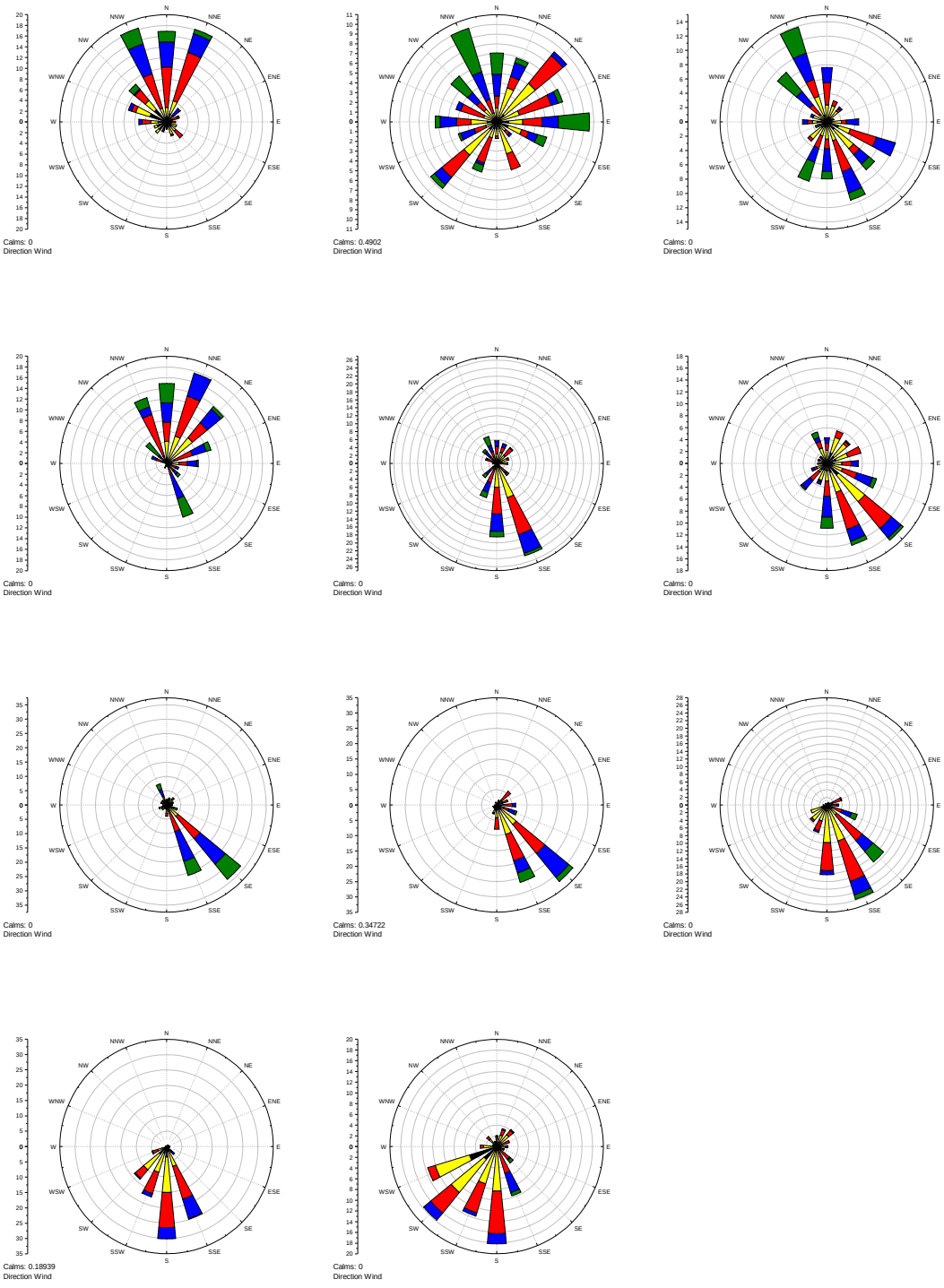

Figure D6. Windrose diagrams for all samples.

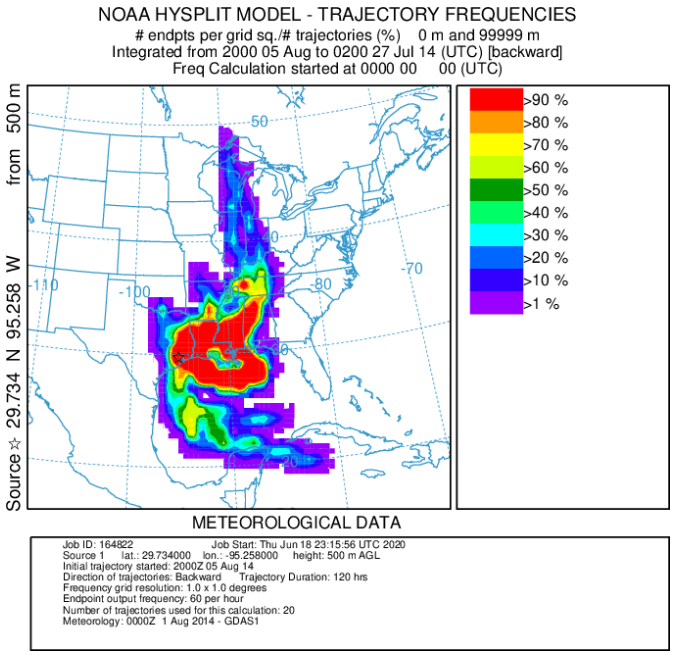

Figure D7. 8/4/14-8/5/14: Back trajectories (frequency) during a Canadian smoke episode in Aug 2014.

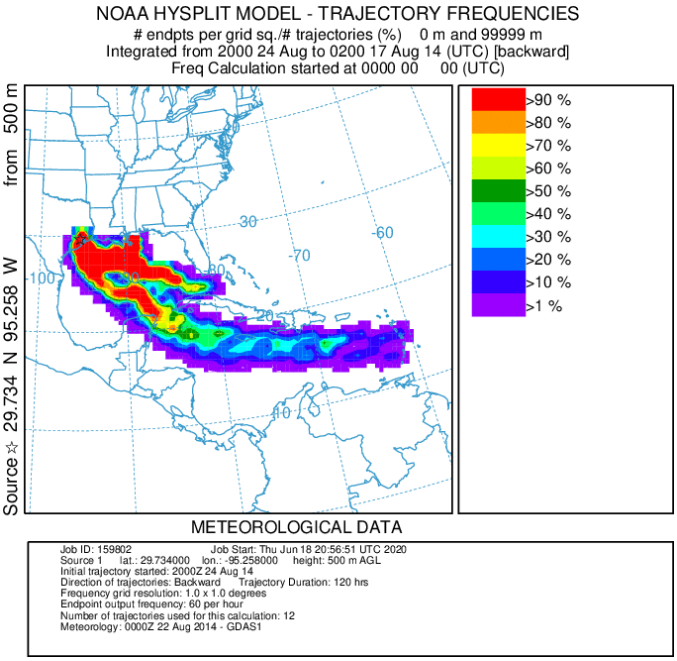

Figure D8. 8/17/14-8/24/14: Back trajectories (frequency) during a North African dust outbreak event in August 2014.

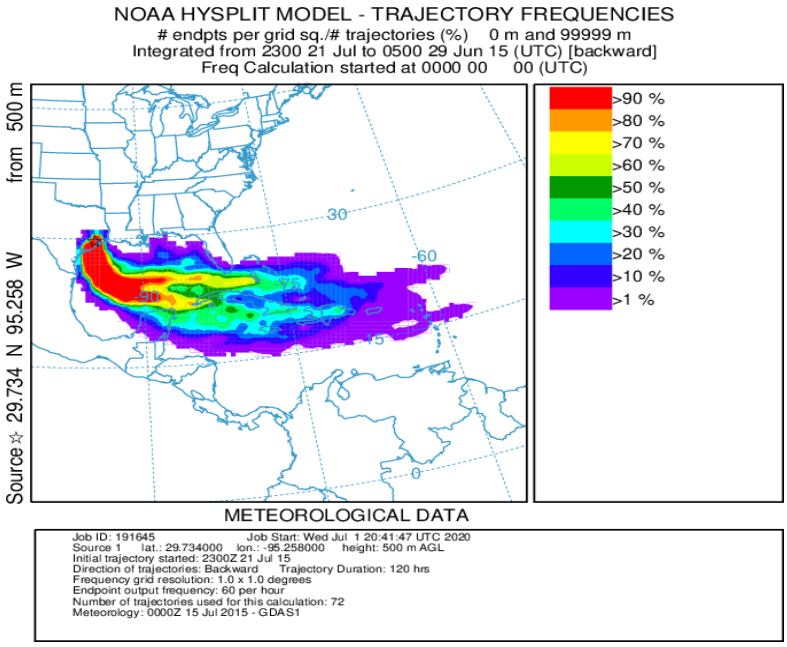

Figure D9. Back trajectories (frequency) for days when African dust mass intrusion was the highest.

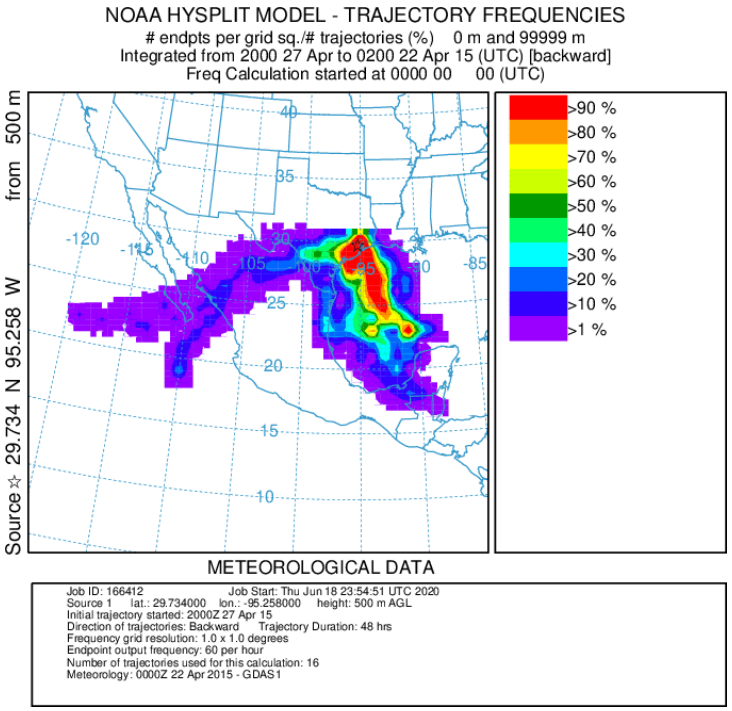

Figure D10. 4/22/2015-4/27/2015: Windrose diagram during peak Central American smoke event in Apr 2015.

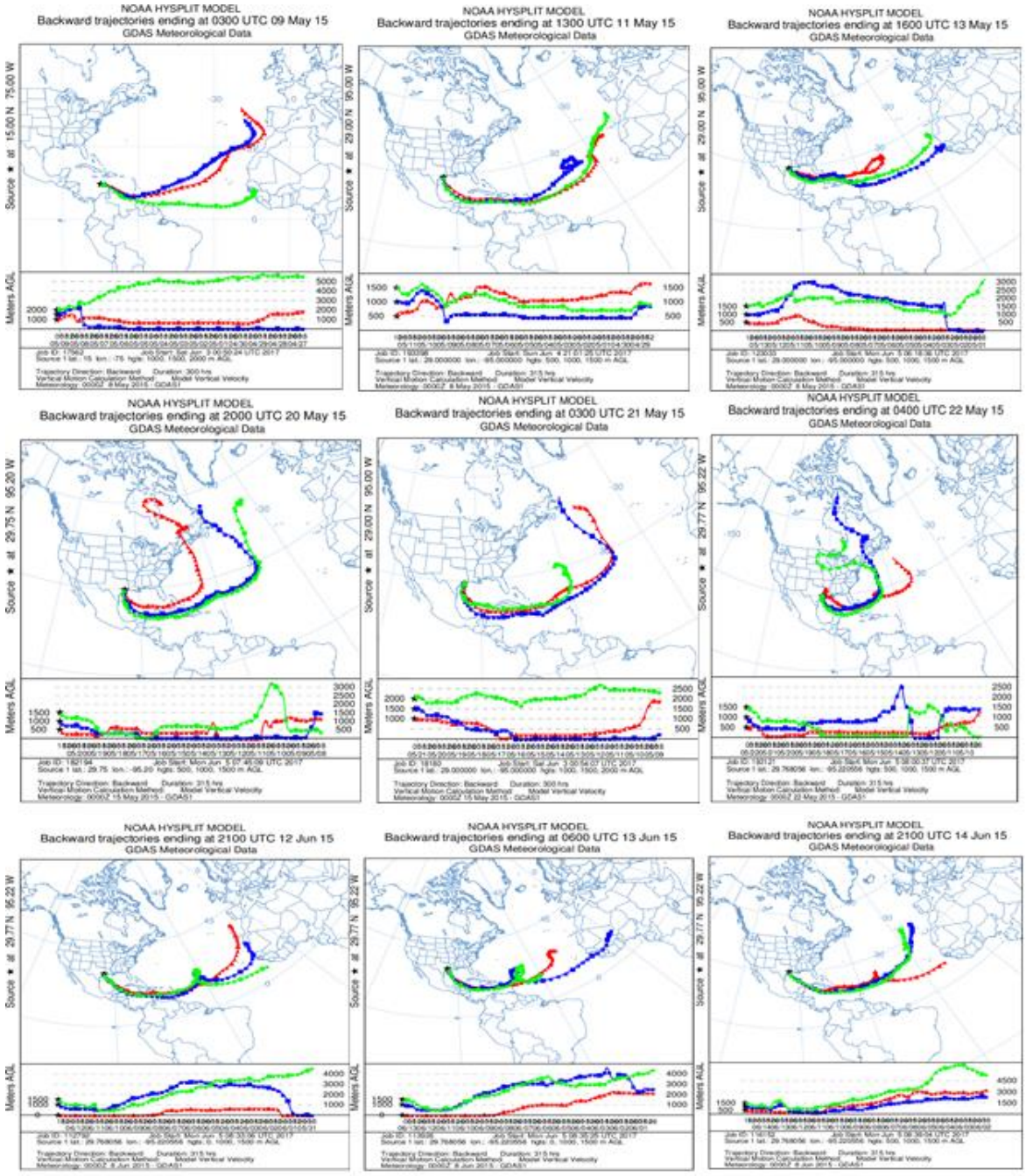

Figure D11. Images of back trajectories modeled by HYSPLIT [133, 362], show origins of the air mass in May and June. The top 3 images show the start of heavy intrusion from North African regions. Mid 3 images show diversion of trajectories, justifying the lack of influence in our PM_{10} and $PM_{2.5}$. The last 3 images show the reoccurring heavy intrusion in early June 2015.

Acknowledgment

The authors gratefully acknowledge the NOAA Air Resources Laboratory (ARL) for the provision of the HYSPLIT transport and dispersion model and/or READY website (http://www.ready.noaa.gov) used in this publication.

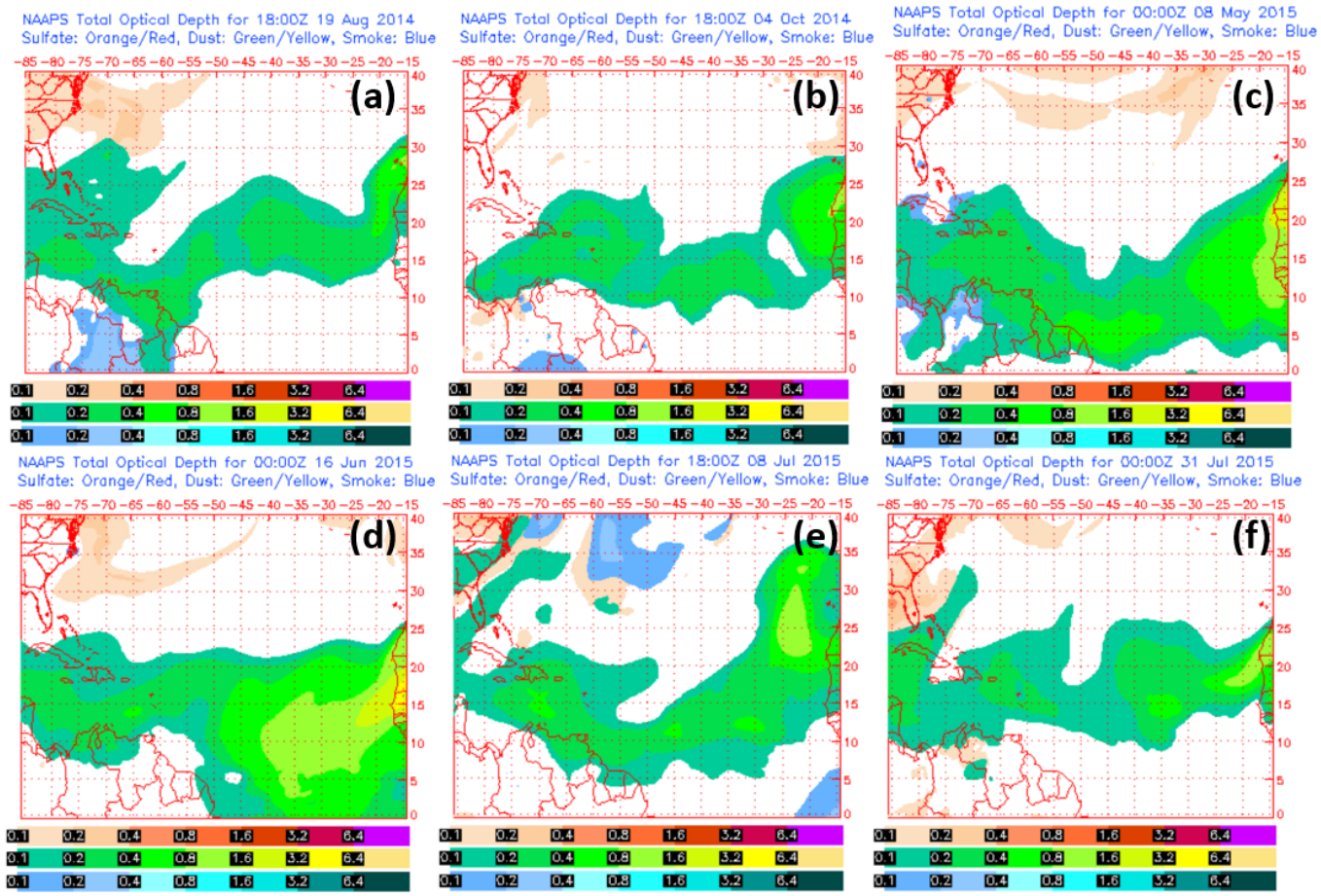

Figure D12. Images produced by NAAPS model [254] for aerosol optical depth over the tropical Atlantic. Images clearly show the presence of aerosol over the Atlantic region from May to August, however an unusual dust intrusion in October 2015 (b) was obsreved which was additioanlly confirmed from TCEQ predictions [136]

D.5. SATELLITE IMAGES FOR POTENTIAL SOURCE AREAS (PSAs)

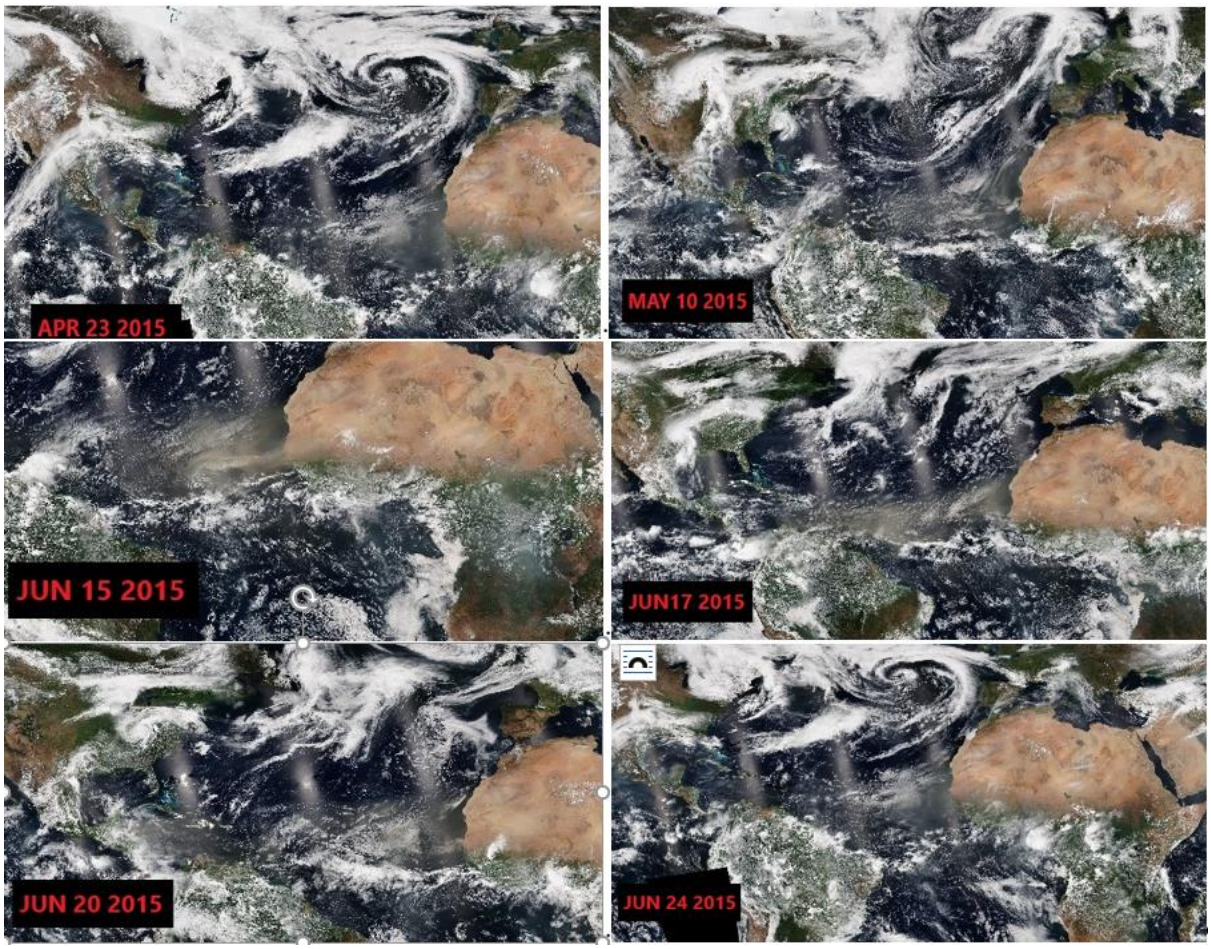

Figure D13. Satellite images show the heavy transport of Aerosol. Plume can be seen to be originating from Northern Africa in April and gradually traveling over the Atlantic region and reaching Houston. Trails of dust transport can be seen in May and June too. Image source - NASA Earth Observations (NEO)[363].

Image Credits

Imagery by Reto Stockli, NASA's Earth Observatory, using data provided by the MODIS Atmosphere Science Team, NASA Goddard Space Flight Center.

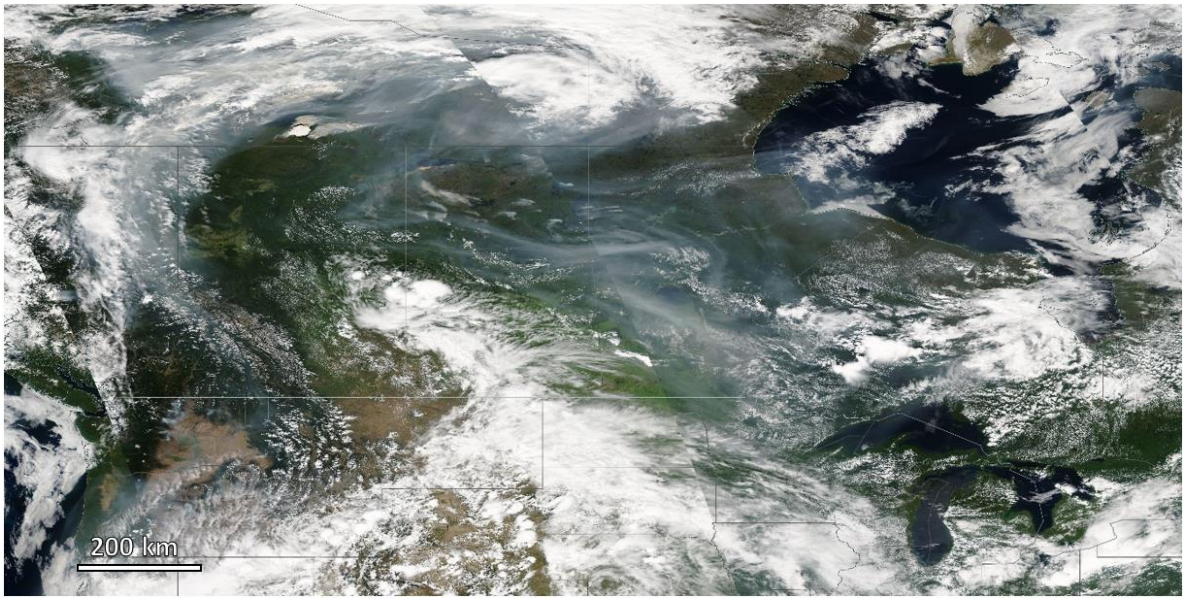

Figure D14. A satellite world view of the hazy atmosphere over Canadian skies showing the presence of smoke particles after forest fire events in 04-05August 2014.

Figure D15. A satellite world view of multiple smoke emissions spread over the south-east Unites States showing smoke emitted from multiple fire events (possibly agricultural burns) on 22-23 October 2014.

Image Credits: Imagery from WorldView by EOSDIS (https://worldview.earthdata.nasa.gov).

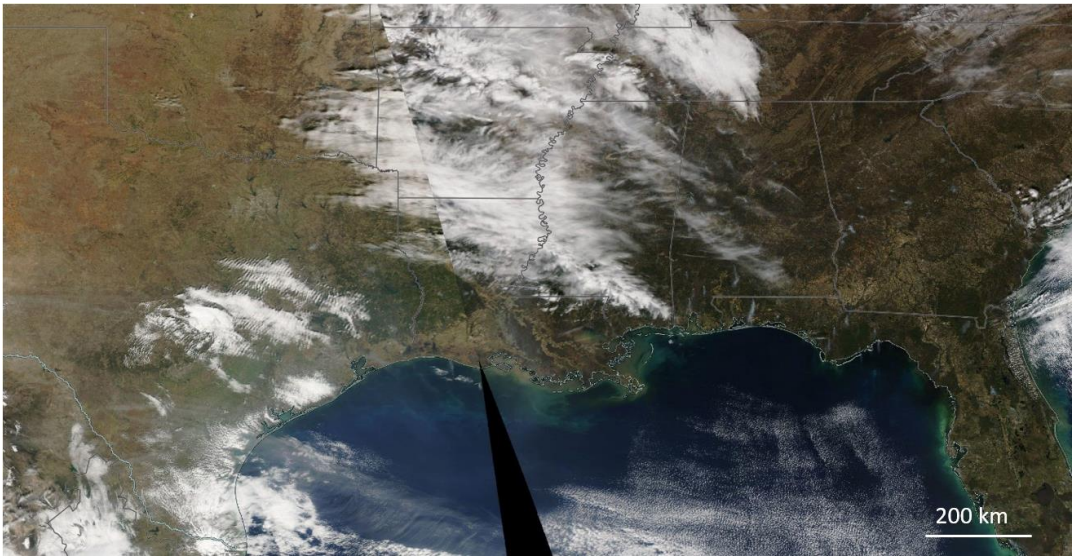

Figure D16. A satellite world view of the hazy atmosphere over South-east Unites States showing smoke emitted from multiple fire events (possibly agricultural burns) on 13-14 February 2015.

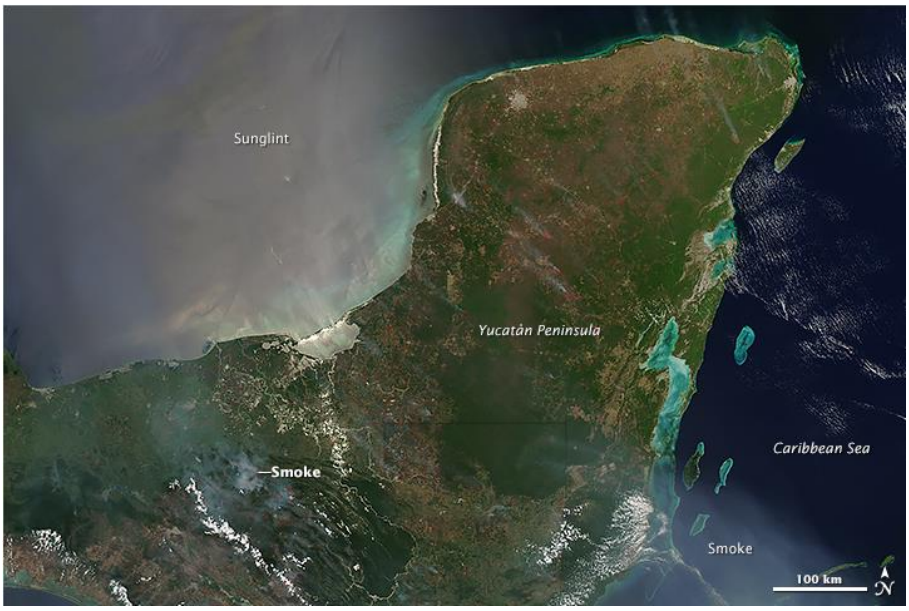

Figure D17. A satellite world view of the hazy atmosphere over South-east Unites States showing smoke emitted from multiple fire events (possibly agricultural burns) on 26 April 2015.

Image Credits: Imagery from WorldView by EOSDIS (https://worldview.earthdata.nasa.gov).

D.6. NAVY AEROSOL ANALYSIS AND PREDICTION SYSTEM (NAAPS)

CANADIAN SMOKE TRANSPORT

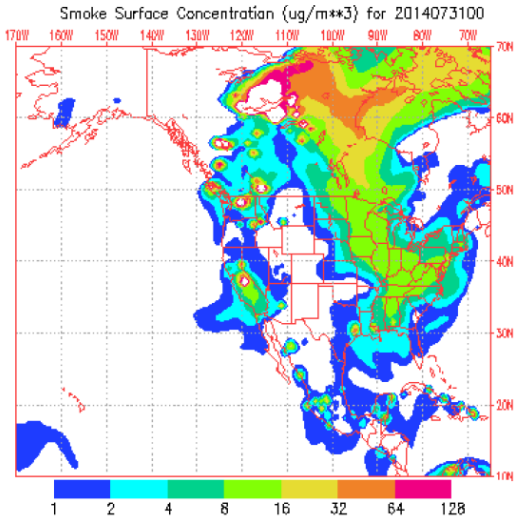

Figure D18. Smoke particles were detected from Canada to Texas indicating transport from forest fires.

OCTOBER AGRICULTURAL FIRES

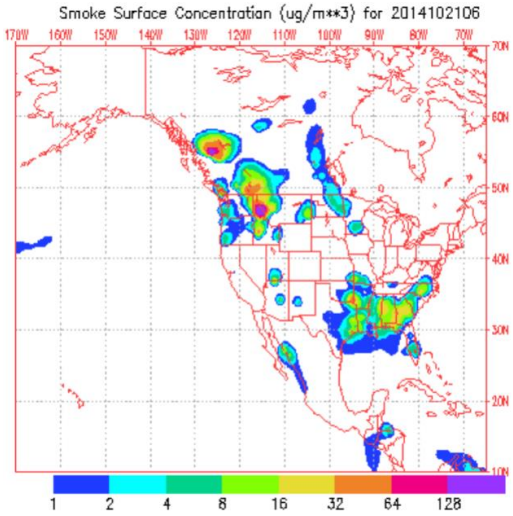

Figure D19. Smoke particles were detected from south-eastern states of USA to Houston in October 2014.

FOREST FIRE INCIDENT

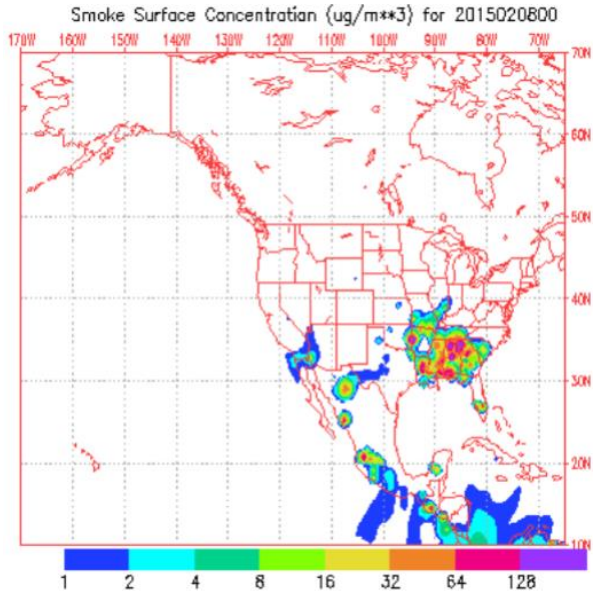

Figure D20. Smoke particles were detected from several forest fires in south-eastern states of USA to Houston in October 2014.

CENTRAL AMERICAN SMOKE

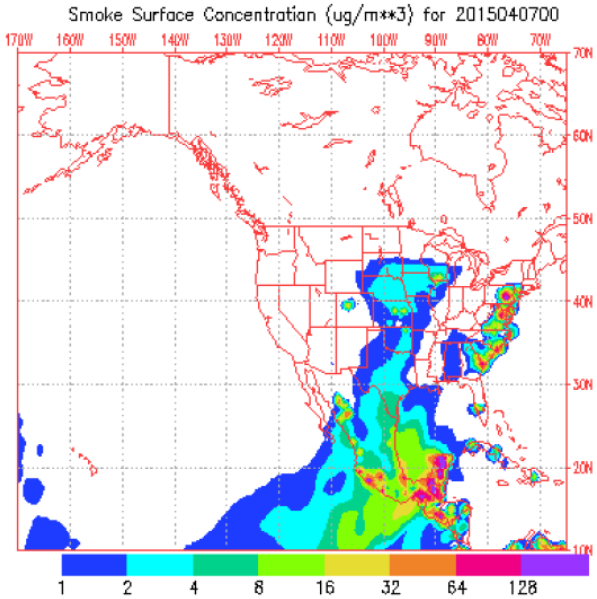

Figure D21. Smoke particles were detected from several forest fires in south-eastern states of USA to Houston in October 2014.

D.7. AOD DATA FROM AERONET DATABASE FOR BACKGROUND SITE

CANADIAN SMOKE TRANSPORT

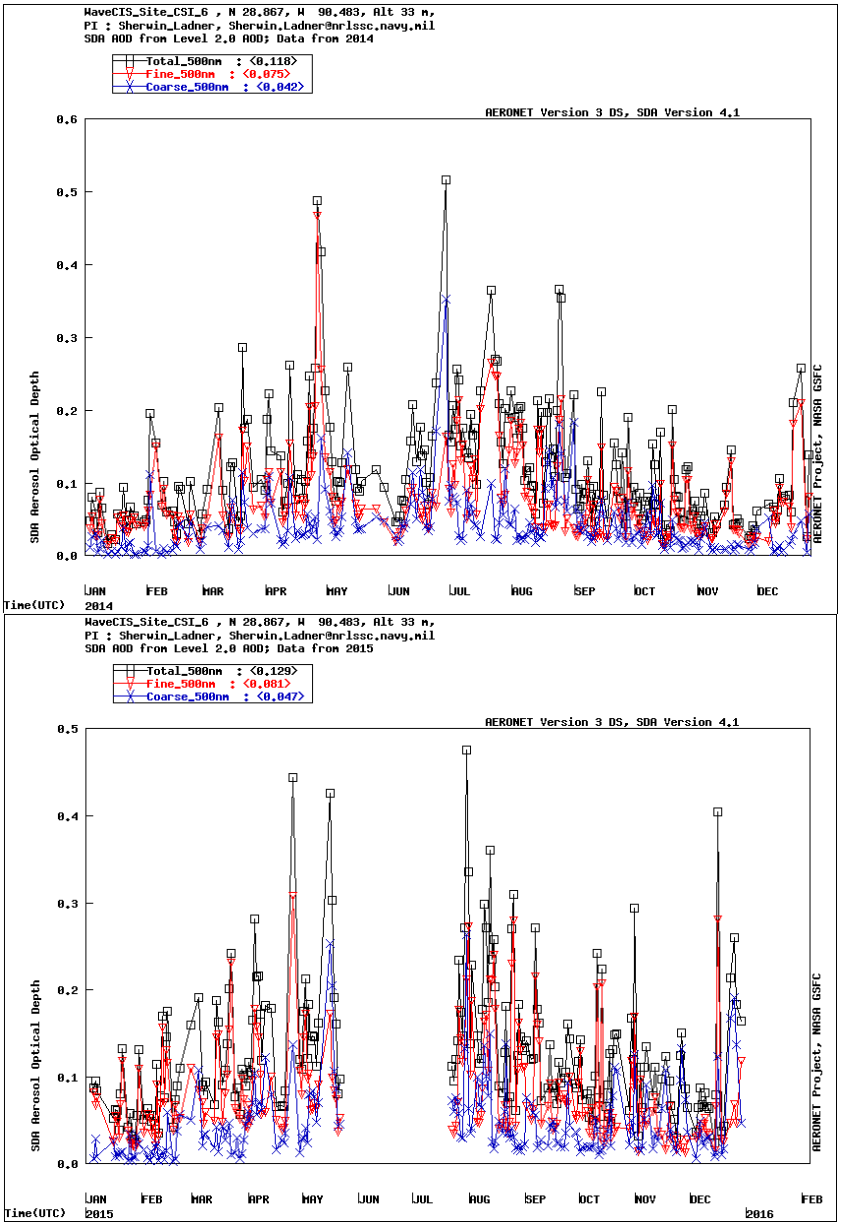

Figure D22. Fine and coarse particles reported from AERONET's AOD database show coarse and fine aerosol spikes during North African dust outbreaks.

Image credits: Aerosol Robotic Network (AERONET) (https://aeronet.gsfc.nasa.gov)

D.8. FIRE MAPS FROM FIRMS DATABASE (MODIS OBSERVATION)

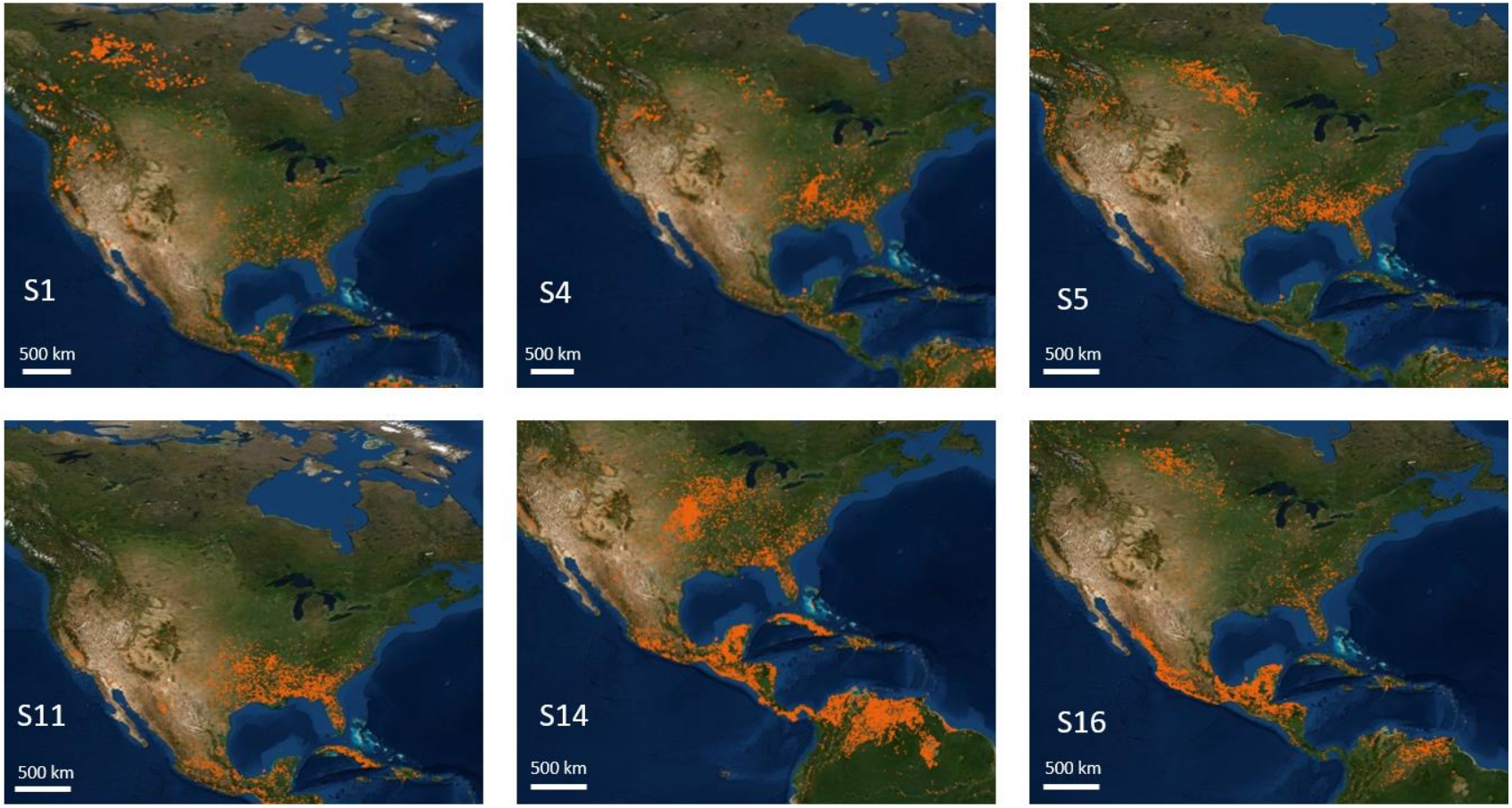

Figure D23. Fire maps generated from NASA FIRMS database (MODIS). Fire maps were integrated over each sample duration (sample ID labeled for each map)

D.9. SUPPLEMENTARY GRAPHS DISTINGUISHING CRUSTAL SOURCES

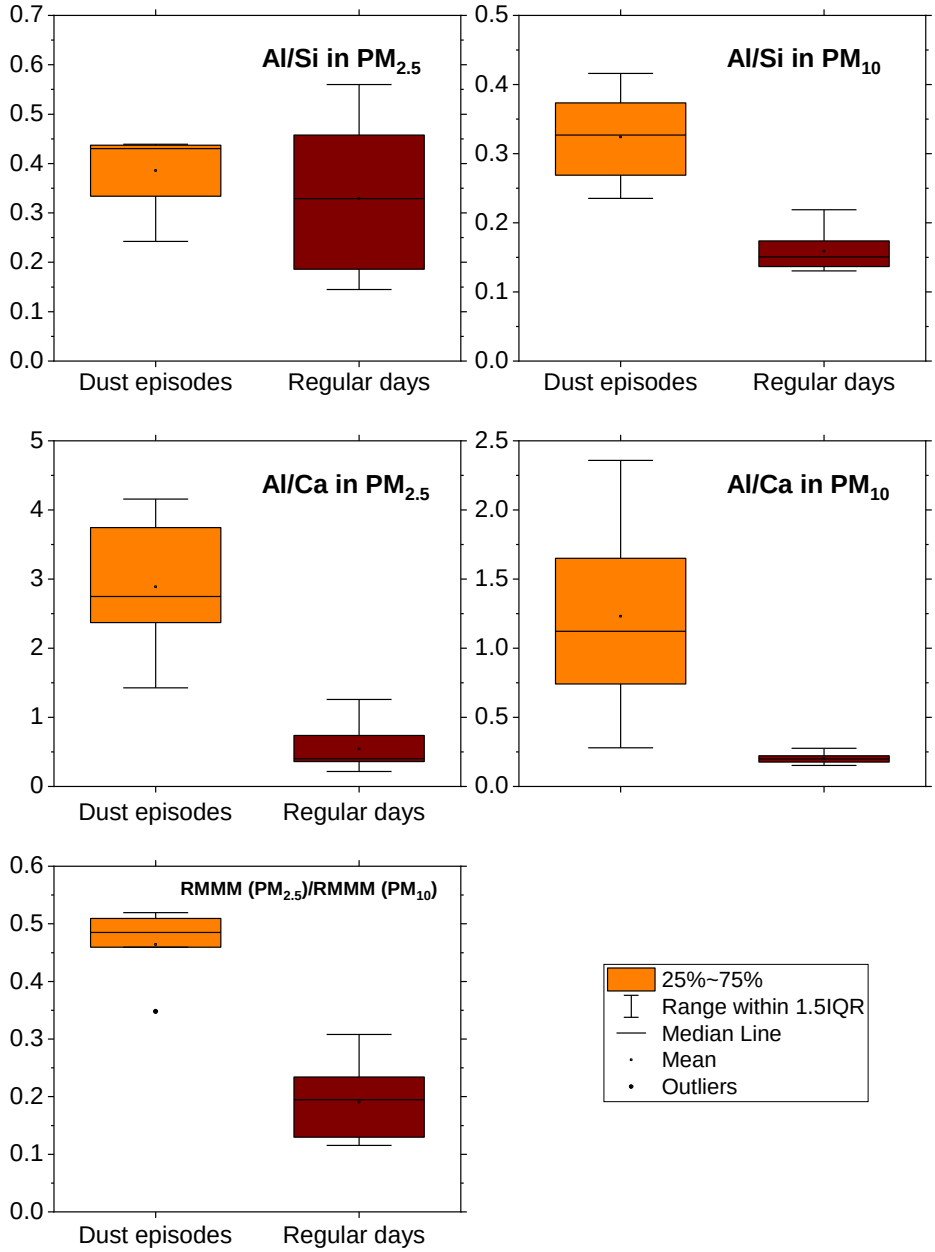

Figure D24. Elemental ratios Al/Si, Al/Ca and RMMM ratio in $PM_{2.5}$ to PM_{10} during episodes vs regular days.

D.10. NON-MINERAL POTASSIUM CALCULATION

Potassium from biomass burning PM can be calculated by removing mineral potassium

$$K_{nm} = K_{ambient} - (K_{crustal} + K_{Concrete} + K_{Coal})$$

$$K_{nm} = K_{ambient} - Al_{crustal} \times \left(\frac{K}{Al}\right)_{crustal} - Ca_{concrete} \times \left(\frac{K}{Ca}\right)_{concrete} - Se_{coal} \times \left(\frac{K}{Se}\right)_{Coal}$$

Since crustal sources dominate the ambient Al and Si and Ca are contributed by both crustal and concrete, we further expand Ca from concrete dust into crustal and non-crustal components. Ca/Si is similar between local soil and Sharan dust therefore we use Ca/Si to separate

$$Ca_{concrete} = Ca_{ambient} - Ca_{crustal}$$

$$Ca_{concrete} = Ca_{ambient} - Si_{crustal} \times \left(\frac{Ca}{Si}\right)_{crustal}$$

$$K_{nm} = K_{ambient} - Al_{crustal} \times \left(\frac{K}{Al}\right)_{crustal} - Ca_{concrete} \times \left(\frac{K}{Ca}\right)_{concrete} - Se_{coal} \times \left(\frac{K}{Se}\right)_{Coal}$$

So, replacing $Al_{crustal} = Al_{ambient}$ and $Se_{coal} = Se_{ambient}$

$$K_{nm} = K_{ambient} - Al_{ambient} \times \left(\frac{K}{Al}\right)_{crustal} - \left[Ca_{ambient} - Si_{ambient} \times \left(\frac{Ca}{Si}\right)_{crustal}\right] \times \left(\frac{K}{Ca}\right)_{concrete} - Se_{ambient} \times \left(\frac{K}{Se}\right)_{Coal}$$

Replacing $\left(\frac{K}{Al}\right)_{crustal} = 0.22$; $\left(\frac{Ca}{Si}\right)_{crustal} = 0.29$; $\left(\frac{K}{Se}\right)_{Coal} = 1.27$

$$K_{nm} = K_{ambient} - 0.22 \times Al_{ambient} - 0.11 \times Ca_{ambient} + 0.032 \times Si_{ambient} - 1.27 \times Se_{ambient}$$

Since all are parameters are measured for ambient PM, we can simply write

$$K_{nm} = K - 0.22 \times Al - 0.11 \times Ca + 0.032 \times Si - 1.27 \times Se$$

D.11. NON-MINERAL LANTHANUM AND VANADIUM

$$La_{nm} = La_{ambient} - La_{mineral}$$

Due to stable Y abundance in all sources, La from sources other than FCC can be separated with $(La/Y)_{mineral}$ ratio and $Y_{mineral} \sim= Y_{ambient}$

$$La_{nm} = La_{ambient} - \left(\frac{La}{Y}\right)_{mineral} \times Y_{ambient}$$

$$La_{nm} = La_{ambient} - 1.6 \times Y_{ambient}$$

Similarly, replacing La/Y with V/RMMM we get an equation for non-mineral vanadium:

$$V_{nm} = V_{ambient} - 5 \times 10^{-5} \times RMMM$$

D.12. Sb/Cu ratio graph and Ca/Al

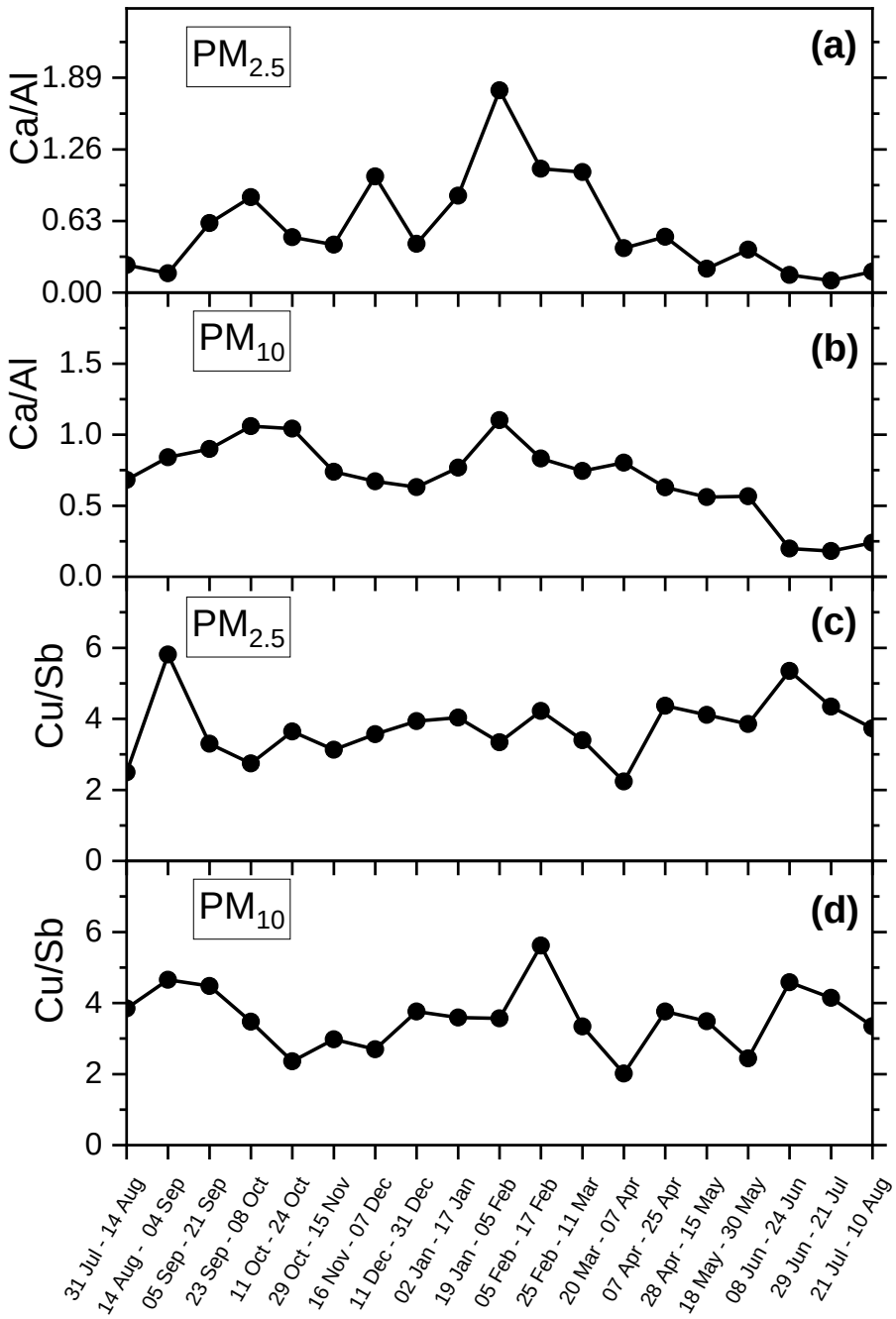

Figure D25. Ca/Al shows low Ca enrichment in both a) $PM_{2.5}$ and b) PM_{10} indicating the limited influence of cement/concrete dust. Cu/Sb consistently remains less than 6 in both c) $PM_{2.5}$ and d) PM_{10} demonstrating exclusivity of Cu and Sb to vehicular PM.

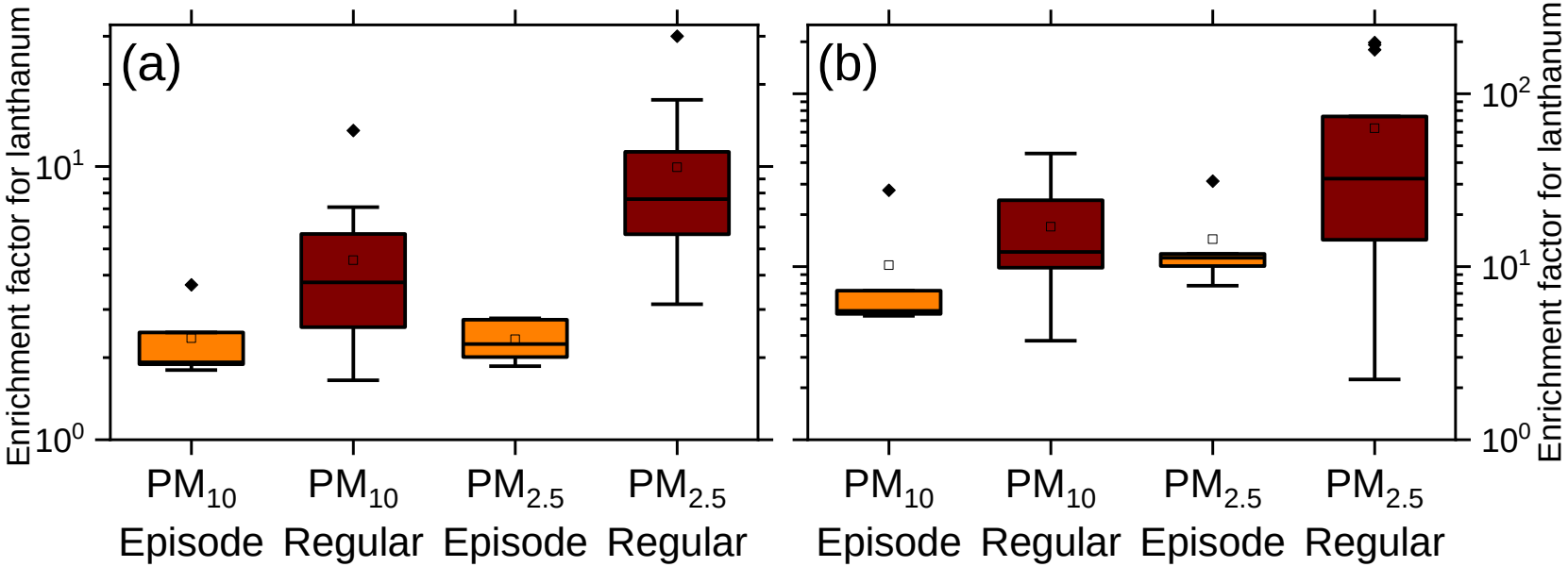

Figure D26. A comparison of enrichment factors (EF) for a) La and b) V in PM_{10} and $PM_{2.5}$ during mineral dust episodes and regular days showing dilution of anthropogenic lanthanoid and vanadium with crustal lanthanides and vanadium respectively.

D.13. SOURCE APPORTIONMENT DETAILS

CMB apportioned 84 ± 10% of PM_{10} and 78 ± 9 % of $PM_{2.5}$ mass to several sources and the unapportioned mass is attributed to secondary aerosols, which is a known PM component in Houston [9, 10, 23] as summarized in Appendix Figure D27. Amongst natural (crustal) sources, North African dust contributed an annual average of 2.7 µg m^{-3} to PM_{10} and 1.1 µg m^{-3} to $PM_{2.5}$, accounting for 12% and 11% of the mass respectively. Contributions from local soil were higher resulting in an annual average of 4.9 µg m^{-3} to PM_{10} and 0.85 µg m^{-3} to $PM_{2.5}$, accounting for 12% and 11% of the mass respectively. Amongst anthropogenic sources, motor vehicles contributed the most with an annual average of 7 µg m^{-3} to PM_{10} and 4.6 µg m^{-3} to $PM_{2.5}$. Primary aerosols from biomass burning contributed an annual average of 0.77 µg m^{-3}, accounting for 7% of $PM_{2.5}$ and a similar amount to PM_{10} (annual average of 0.90 µg m^{-3} or 4.6%). Since our focus was on classifying local and distal sources, biomass burning PM during satellite-detected large-scale fire episodes were considered distal and on other days were considered local. With this classification, distal sources (biomass burning + Saharan dust) annually contributed 1.4 µg m^{-3} (16%) and 3.1 µg m^{-3} (16%) to $PM_{2.5}$ and PM_{10} burden respectively as summarized in Appendix Figure D28.

Table D5. Ambient concentrations and African dust contributions during Saharan episodes (S2, S5, S15, S17 – S19) and on regular/ background days.

	Average mass concentrations in samples with episodic African dust influence (μg m^{-3})	Mass concentrations on regular or background days not impacted by African dust (μg m^{-3})
Total $PM_{2.5}$ concentration	11.6 (9.2-15.5)	8.8 (6.5-11.4)
Estimated African dust in $PM_{2.5}$	3.5 (1.5-5.8)	0.07 (0-0.5)
Total PM_{10} concentration	23.9 (16.0-29.1)	17.8 (12.2-25.6)
Estimated African dust in PM_{10}	7.9 (2.9-12.5)	0.2 (0-1.6)

Table D6. Ambient PM concentrations and biomass burning contributions to $PM_{2.5}$ and PM_{10} during episodes (S1, S4, S5, S11, S14, S16) and regular days.

	Average concentration during episodic biomass burning intrusions	Average concentration on regular days
Total $PM_{2.5}$ concentration (μg m^{-3})	10.6 (7.8-15.5)	9.2 (6.5-11.9)
$PM_{2.5}$ from biomass burning (μg m^{-3})	1.3 (0.8-2.1)	0.48 (0-0.9)
Total PM_{10} concentration (μg m^{-3})	20.7 (12.5-29.1)	19.2 (12.2-26.2)
PM_{10} from biomass burning (μg m^{-3})	1.4 (0.8-2.3)	0.6 (0-1.1)
Total K in PM_{10} (ng m^{-3})	241 (212-273)	191 (93-356)
K_{nm} in PM_{10} (ng m^{-3})	92 (67-122)	45 (0-95)
Total K in $PM_{2.5}$ (ng m^{-3})	122 (99-164)	84 (36-200)
K_{nm} in $PM_{2.5}$ (ng m^{-3})	92 (69-133)	44 (17-83)

Table D7. Ambient concentrations and individual local source contribution estimates for $PM_{2.5}$ and PM_{10}.

	January-March	April-June	July-September	October-December
Units	μg m^{-3}	μg m^{-3}	μg m^{-3}	μg m^{-3}
$PM_{2.5}$ concentration for the duration	8.8 (6.5-10.3)	11.8 (9.6-15.5)	10.6 (8-12.7)	8 (7.8-8.3)

$PM_{2.5}$ contribution by anthropogenic activities	5.4 (4.3-6.4)	5.5 (3-8)	3.9 (3.3-4.8)	4.7 (4.3-5.2)
Motor vehicle	5.2 (3.7-6)	5.2 (2.7-7.7)	3.8 (3.1-4.5)	4.4 (3.7-5)
Oil combustion	0.04 (0-0.14)	0.12 (0-0.27)	0.06 (0-0.11)	0.21 (0-0.41)
FCC activities	0.07 (0-0.13)	0.14 (0-0.56)	0.02 (0-0.1)	0.12 (0.04-0.35)
Coal combustion	0.05 (0-0.13)	0.01 (0-0.02)	0.04 (0-0.1)	0.02 (0-0.06)
Cement and construction	0.03 (0-0.13)	0.01 (0-0.05)	0.02 (0-0.08)	0.01 (0-0.03)
$PM_{2.5}$ contribution by windblown soil	0.9 (0.6-1.4)	0.6 (0.1-0.8)	1.1 (0.5-1.8)	0.7 (0.4-1)
PM_{10} concentration for the duration	17.1 (13.9-21.8)	24 (21.7-29.1)	22.7 (16-27.2)	16.1 (12.2-20.8)
PM_{10} contribution by anthropogenic activities	9 (6.5-13.5)	8 (3.3-12)	6.8 (2.4-10.8)	7.3 (4.1-11.5)
Motor vehicle	8 (6.6-9.2)	7.8 (4.2-11.6)	6.5 (3.2-9.6)	6.7 (4.4-9.6)
Oil combustion	0.03 (0-0.17)	0.06 (0-0.11)	0.18 (0-0.31)	0.16 (0-0.29)
FCC activities	0.05 (0-0.27)	0.03 (0-0.11)	0.04 (0-0.11)	0.04 (0-0.17)
Coal combustion	0.69 (0.09-1.42)	0.09 (0-0.26)	0.21 (0.03-0.68)	0.3 (0.02-0.95)
Cement and construction	0.23 (0-0.85)	0.03 (0-0.1)	0.46 (0-1.46)	0.12 (0-0.58)
PM_{10} contribution by windblown soil	5.8 (4.6-7.7)	3.7 (1.1-7.3)	4.5 (3.2-8.1)	5.4 (4-7.2)

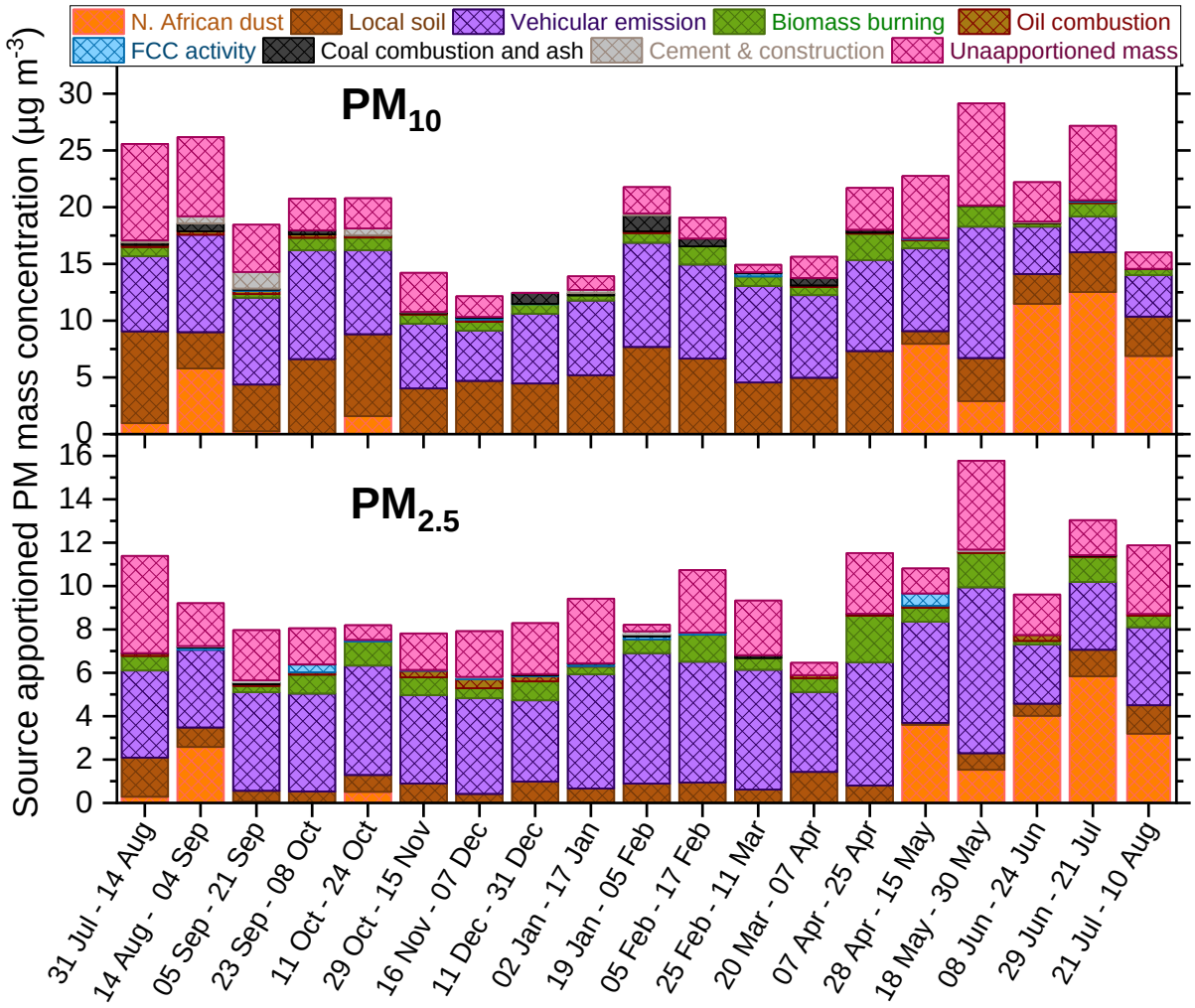

Figure D27. A complete summary of source contribution estimated for PM_{10} (top) and $PM_{2.5}$ (bottom) in this study

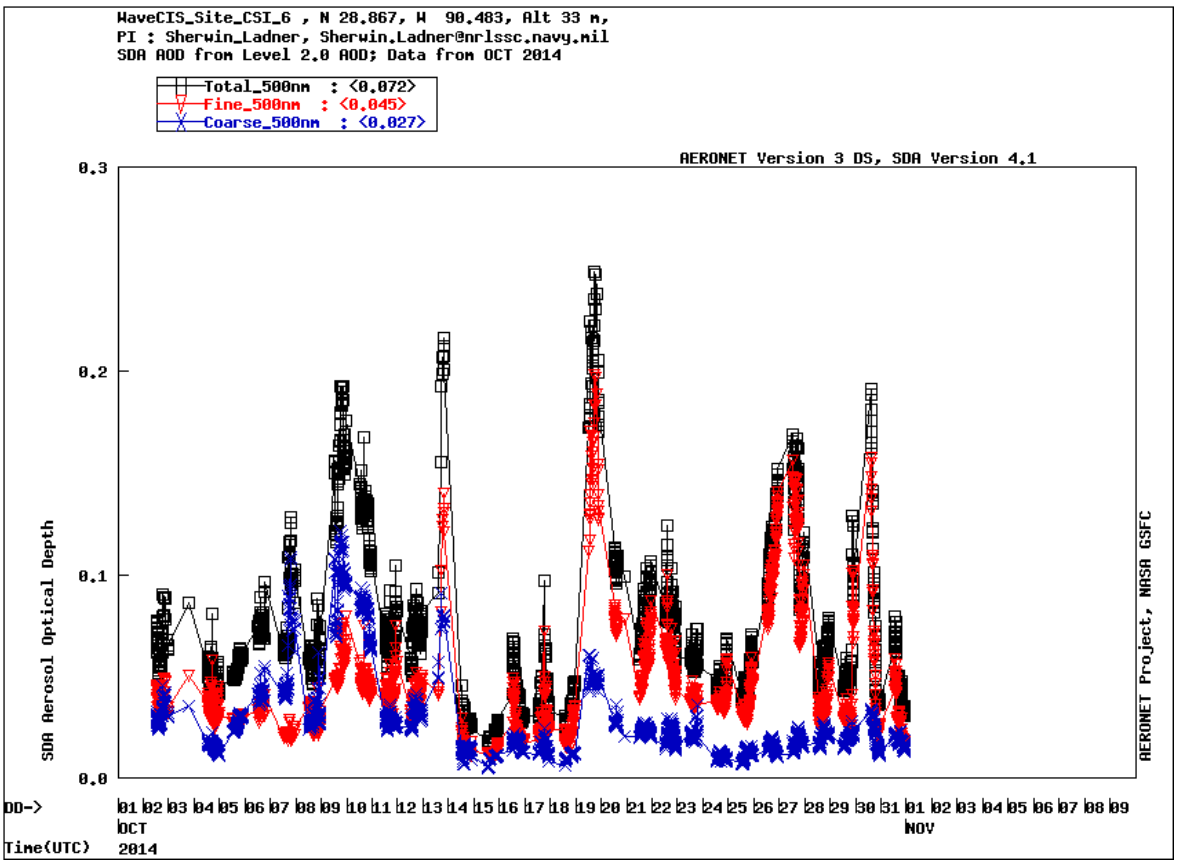

Figure D28. Aerosol optical depth (AOD) obtained from AERONET database from an oil rig platform in the Gulf of Mexico upstream of North African dust storm (+28.86667, -90.48333W) during October 2014. Peaks in coarse size indicates North African dust intrusion.

APPENDIX E

SUPPORTING INFROMATION FOR CHAPTER VI

Table E1. PM mass concentrations and I/O ratios over the sampling period.

Sampling duration		Mass concentrations (μg m^{-3})				I/O mass concentration ratio	
		Indoor		Outdoor			
Begin	End	$PM_{2.5}$	$PM_{10-2.5}$	$PM_{2.5}$	$PM_{10-2.5}$	$PM_{2.5}$	$PM_{10-2.5}$
3/11/11	3/13/11	3.05	0.333	12.3	20.0	0.248	0.0165
3/13/11	3/15/11	2.50	0.0624	12.1	16.8	0.207	0.00357
3/17/11	3/19/11	2.50	0.780	12.1	12.7	0.207	0.0614
3/19/11	3/21/11	2.37	0.250	12.8	12.4	0.185	0.0202
3/21/11	3/23/11	3.29	0.478	13.4	33.0	0.246	0.0145
3/25/11	3/31/11	4.09	0.956	17.1	10.6	0.239	0.0906
3/31/11	4/6/11	3.59	0.148	14.0	12.3	0.256	0.0122
4/6/11	4/12/11	2.58	0.531	11.6	N.C.	0.222	N.C.
4/12/11	4/18/11	2.83	0.405	13.7	28.6	0.207	0.0143
4/18/11	4/24/11	3.24	0.231	13.9	18.8	0.233	0.0122
4/14/11	4/30/11	2.27	0.852	12.4	18.6	0.183	0.0457
4/30/11	5/5/11	3.12	0.726	13.7	17.6	0.227	0.0415
5/5/11	5/11/11	3.21	0.628	14.5	14.7	0.221	0.0429

Note one PM_{10} sample (4/6/11 – 4/12/11) was lost and is designated as “not completed.”

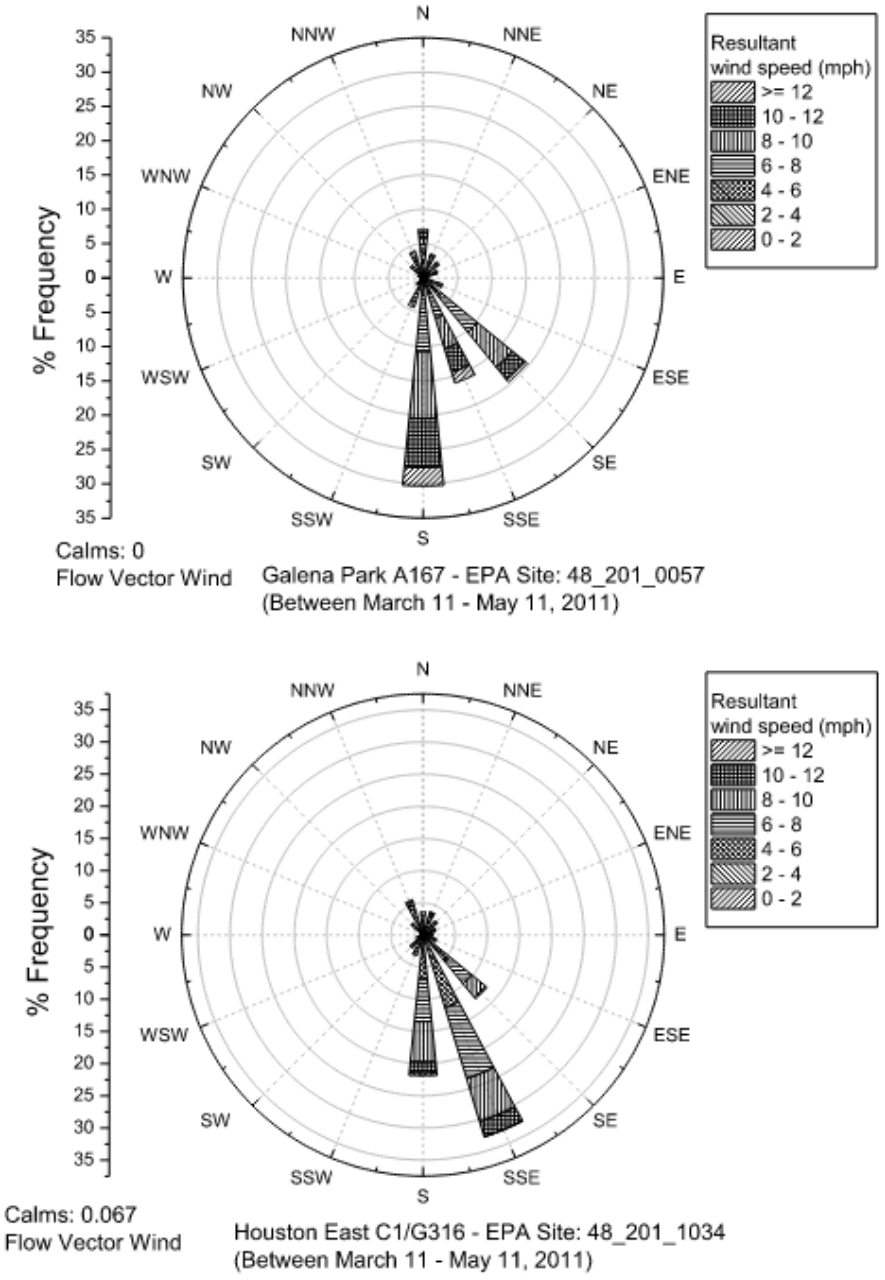

Figure E1. The frequency of wind direction covering the sampling period (March 11 – May 11, 2011) measured at TCEQ's Houston East (CAMS 1; ~2.6 miles southwest of the receptor location) and Galena Park (CAMS 1667; ~4.8 miles southwest of the receptor location) air quality monitoring sites. Filled bands indicate wind speed ranges for each direction. From Bozlaker et al. (2017)[290].

Table E2. Health Standards Used in Figure VI-3 (main manuscript) and Appendix Figure E2 (below)

μg m^{-3}	TCEQ AMCV	OSHA 8 h	EPA RfC	EPA/ATSDR MRL	CAL Non-Cancer REL	CAL 8 h	CAL Cancer
Li							
Be		2	0.02		0.007		0.00417
Na							
Mg							
Al-1	5	15000					
Si		15000					
K							
Ca							
Sc							
Ti							
V		500		0.1			
Cr		5	0.1	0.3	0.2		0.0000667
Mn	0.2	5000	0.05	0.3	0.09	0.17	
Fe							
Ni		1000		0.09	0.014	0.06	0.0385
Co	0.02	100		0.1			
Cu	1	100					
Zn	2						
Ga							
As		10			0.015	0.015	0.00303
Se	0.2	200			20		
Rb							
Sr							
Y		1000					
Zr		5000					

Mo	3	15000		0.4			
Cd	0.01	5		0.01	0.02		0.00238
Sn	2	100					
Sb	0.5	500		0.3			
Cs							
Ba	0.5	500					
La							
Ce			0.9				
Pr							
Nd							
Sm							
Eu							
Gd							
Tb							
Dy							
Ho							
Er							
Tm							
Yb							
Lu							
Hf		500					
W							
Pb		50					0.833
Th							
U				0.8			

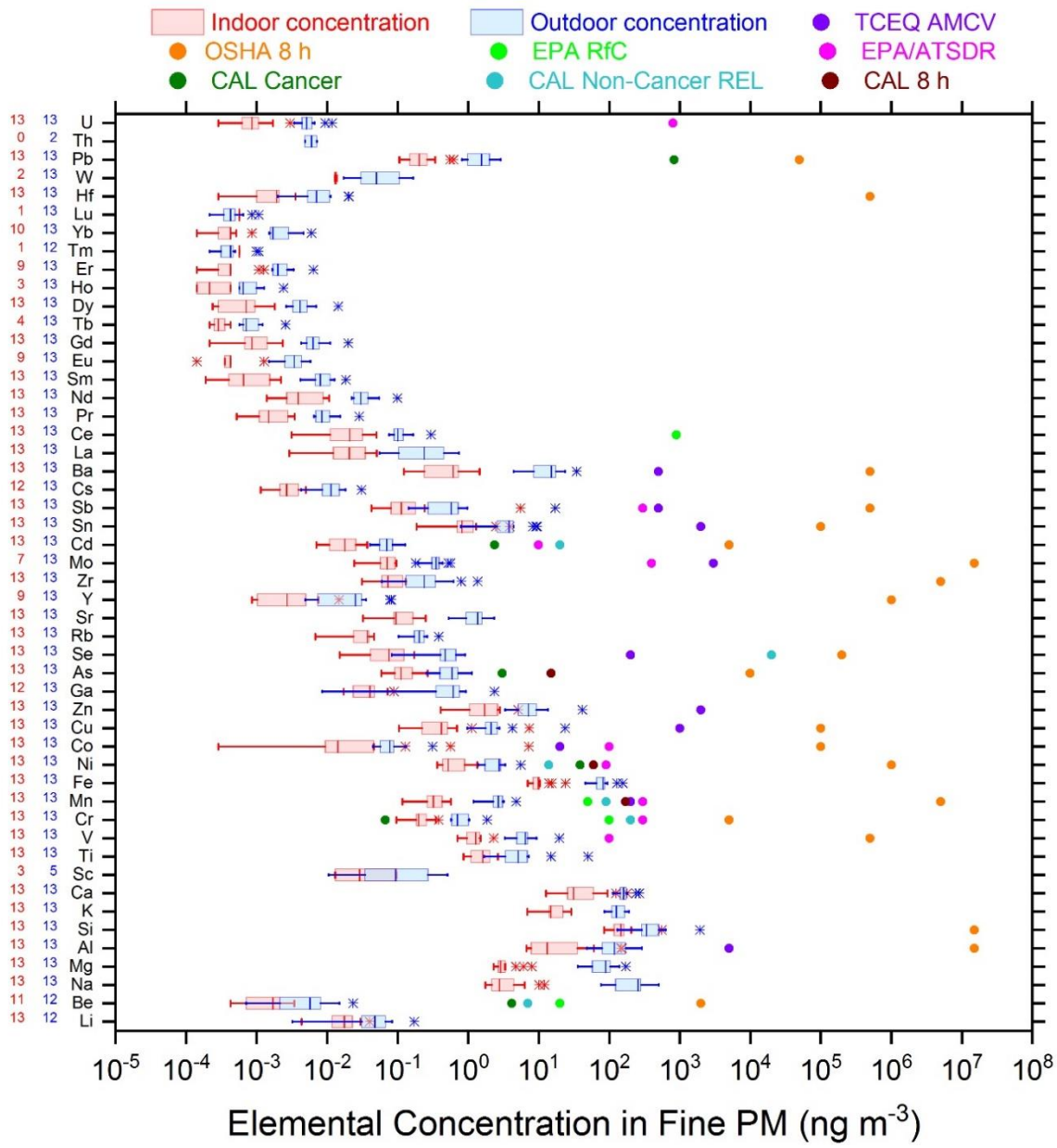

Figure E2. Fine PM indoor and outdoor elemental concentrations compared to metal HAP/TAC health standards. The red and blue colored boxplots indicate indoor and outdoor air concentrations, respectively. The box covers the interquartile range, the median represented as a solid line within the box, and outliers are depicted as asterisks with this color code. The number of samples above detection limit are shown directly to the left of each element (blue color for outdoor and red color for indoor). The colored circles indicate associated regulatory or health-based standards designated by various governing bodies as denoted in the legend.

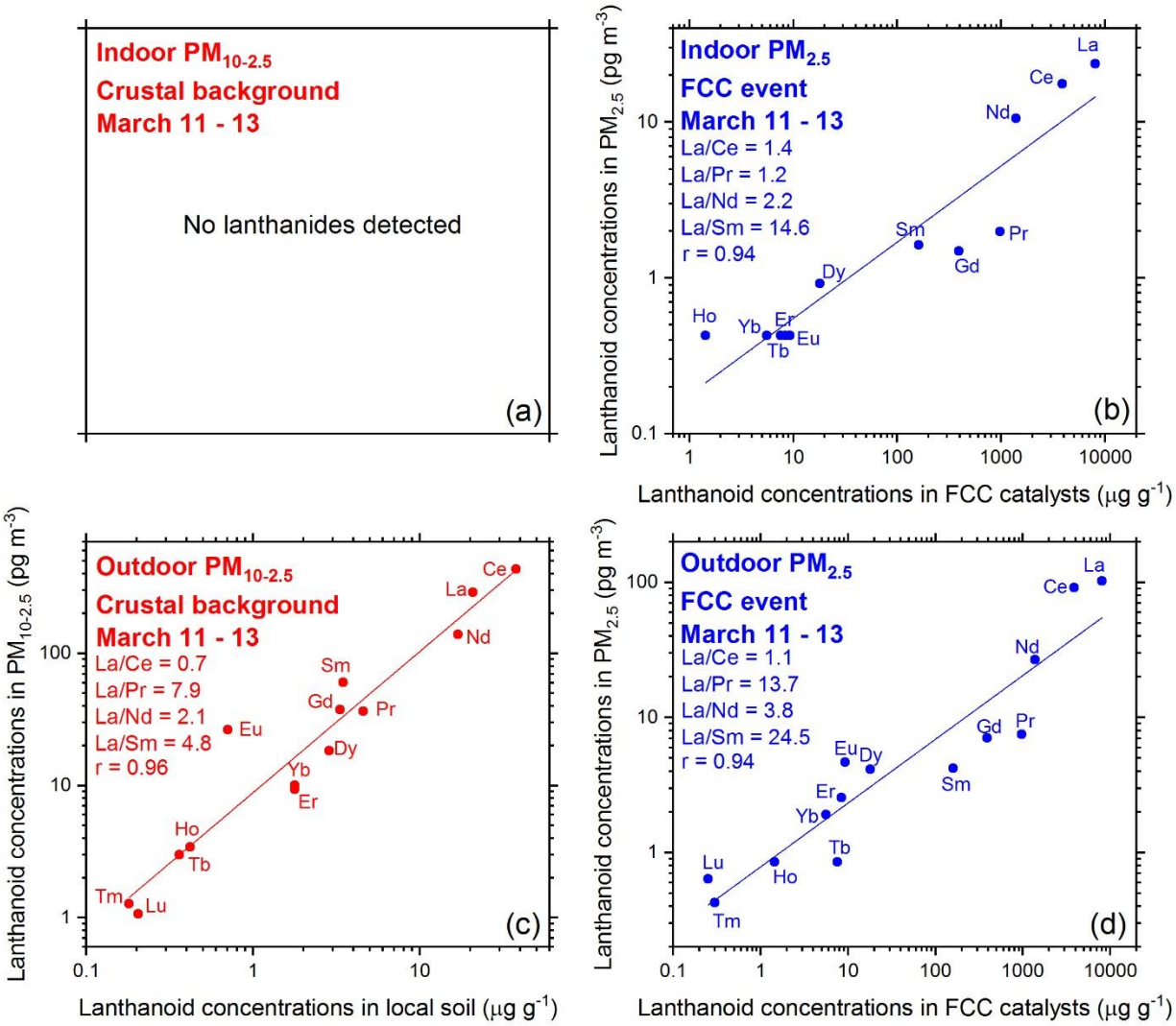

Figure E3. Correlations utilized in FCC event and background sample determinations for the March 11-13 sampling period. Panel (a) represents concentrations for indoor coarse PM, panel (b) represents concentrations for indoor fine PM (Tm and Lu are below detection limit), panel (c) represents concentrations for outdoor coarse PM, and panel (d) represents concentrations for outdoor fine PM.

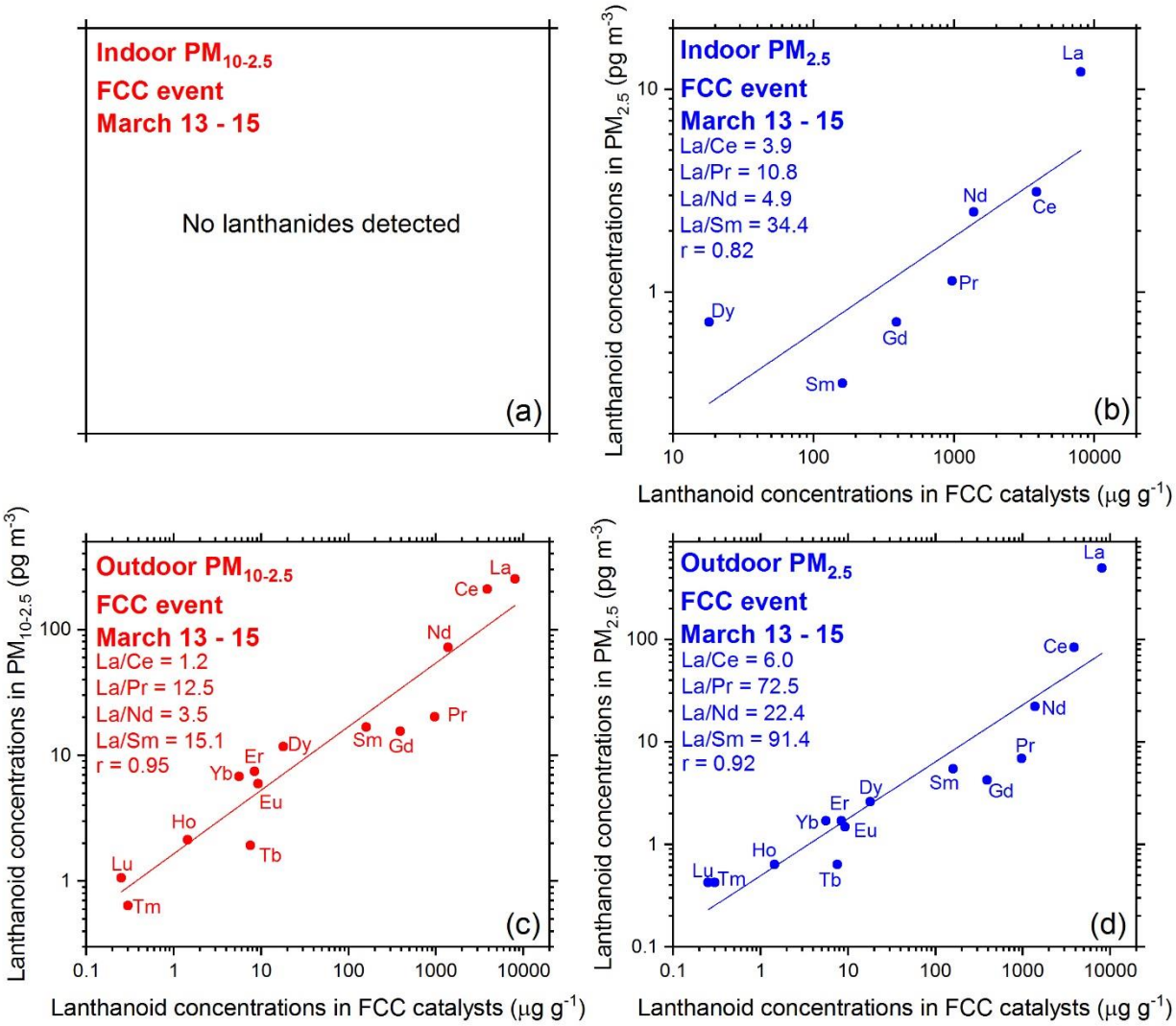

Figure E4. Correlations utilized in FCC event and background sample determinations for the March 13-15 sampling period. Panel (a) represents concentrations for indoor coarse PM, panel (b) represents concentrations for indoor fine PM (Eu, Tb, Ho, Er, Tm, Yb, and Lu are below detection limit), panel (c) represents concentrations for outdoor coarse PM, and panel (d) represents concentrations for outdoor fine PM.

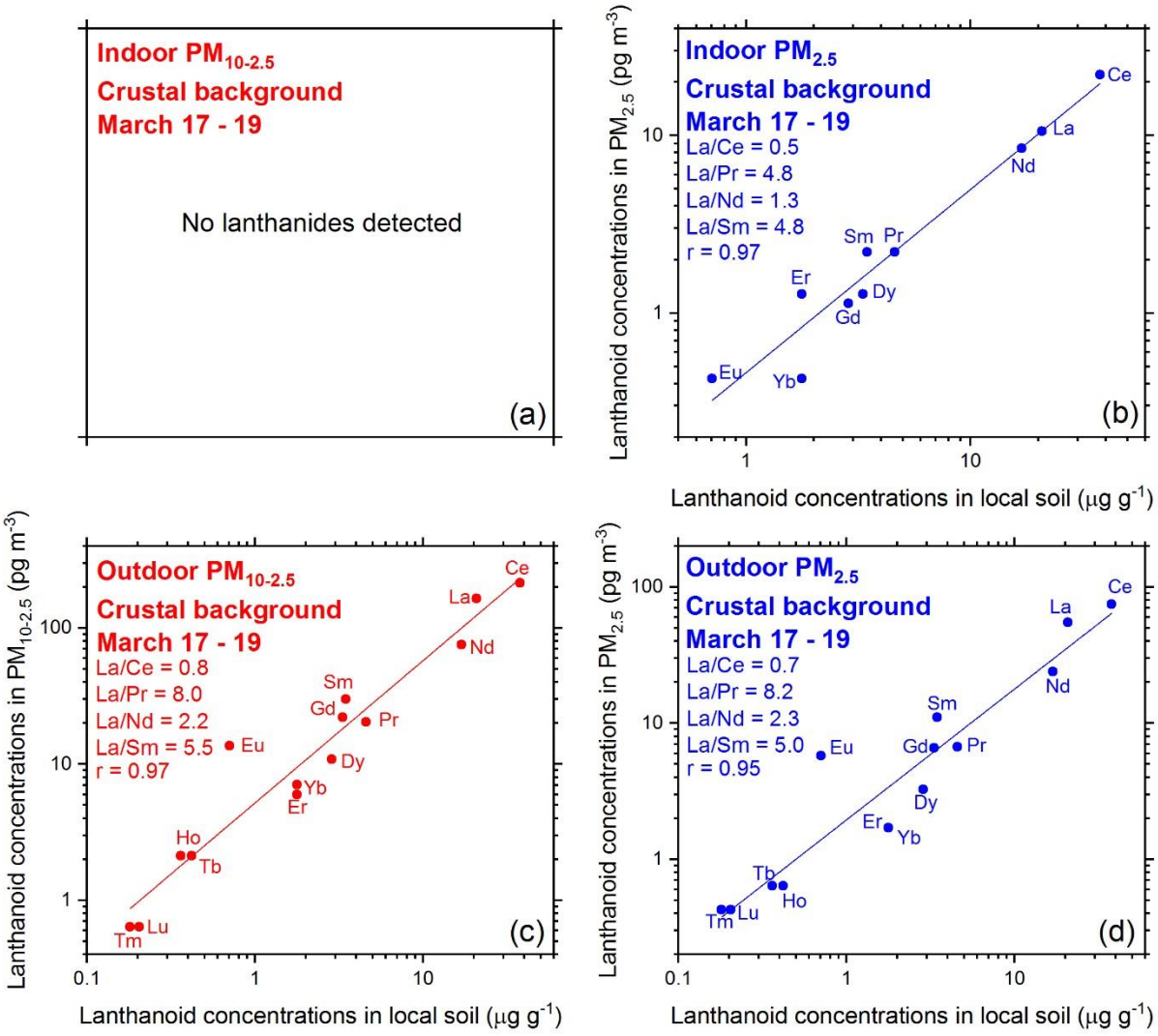

Figure E5. Correlations utilized in FCC event and background sample determinations for the March 17-19 sampling period. Panel (a) represents concentrations for indoor coarse PM, panel (b) represents concentrations for indoor fine PM (Tb, Ho, Tm, and Lu are below detection limit), panel (c) represents concentrations for outdoor coarse PM, and panel (d) represents concentrations for outdoor fine PM.

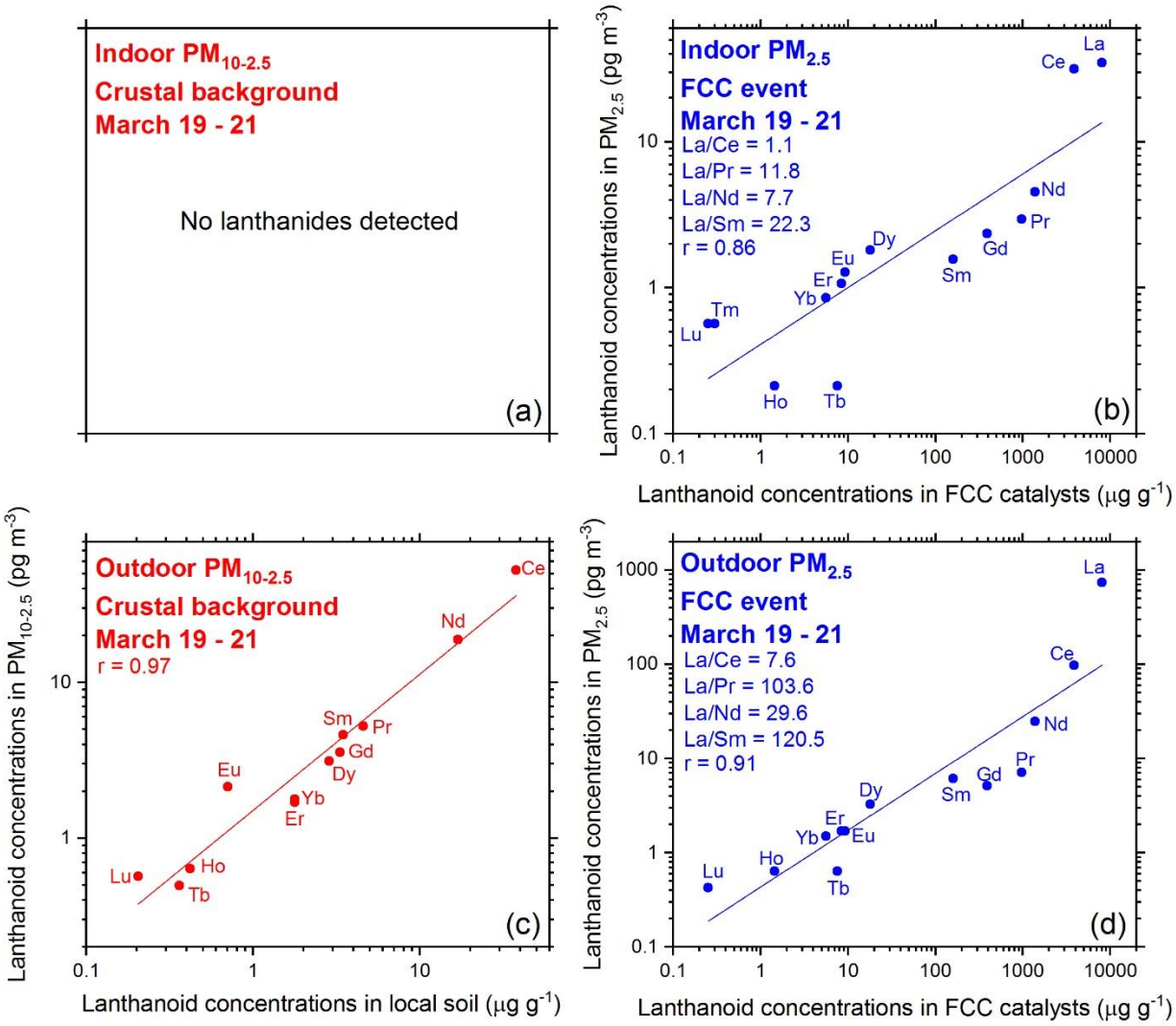

Figure E6. Correlations utilized in FCC event and background sample determinations for the March 19-21 sampling period. Panel (a) represents concentrations for indoor coarse PM, panel (b) represents concentrations for indoor fine PM, panel (c) represents concentrations for outdoor coarse PM (La and Tm are below detection limit), and panel (d) represents concentrations for outdoor fine PM (Tm is below detection limit).

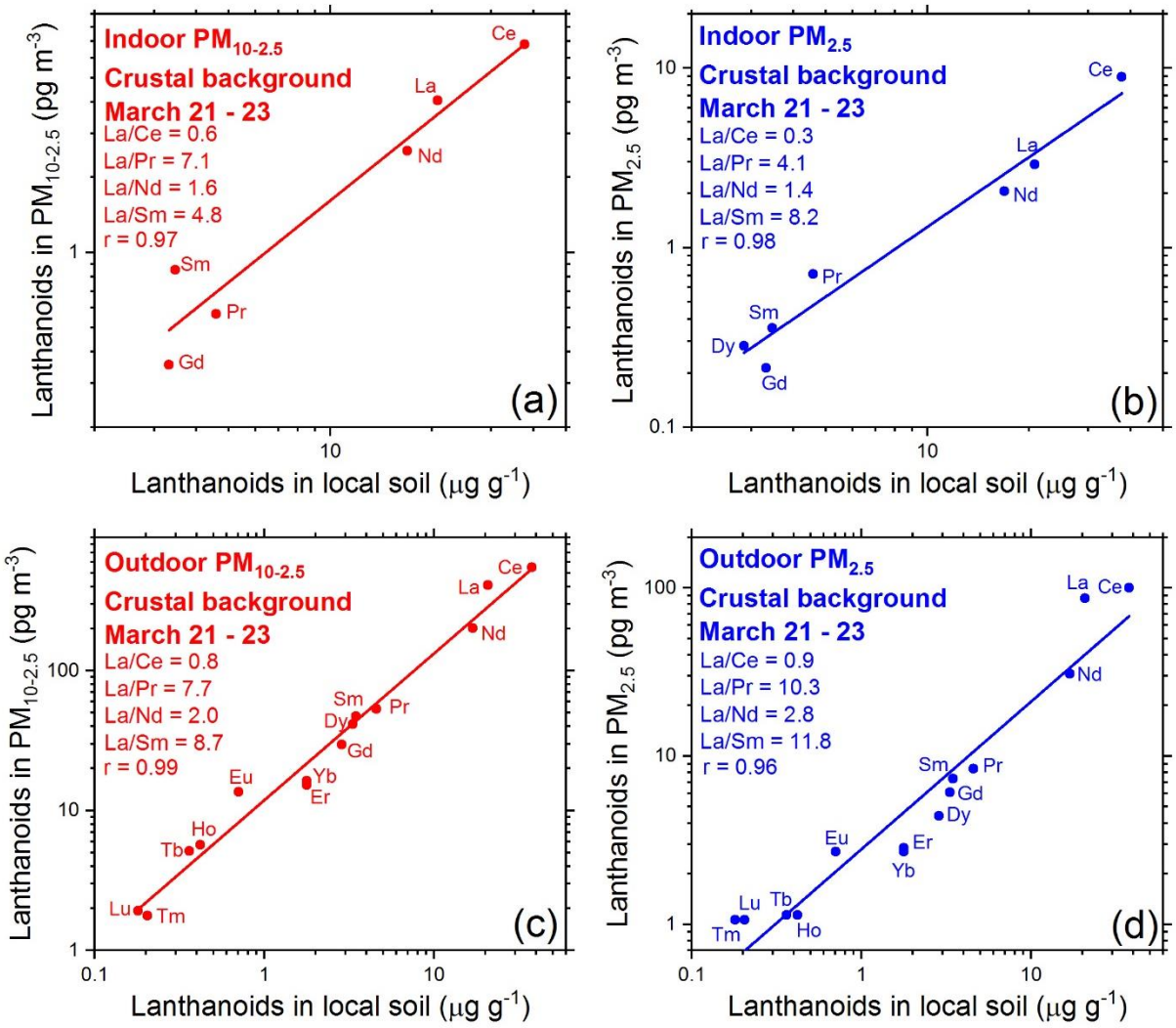

Figure E7. Correlations utilized in FCC event and background sample determinations for the March 21-23 sampling period. Panel (a) represents concentrations for indoor coarse PM, panel (b) represents concentrations for indoor fine PM, panel (c) represents concentrations for outdoor coarse PM, and panel (d) represents concentrations for outdoor fine PM.

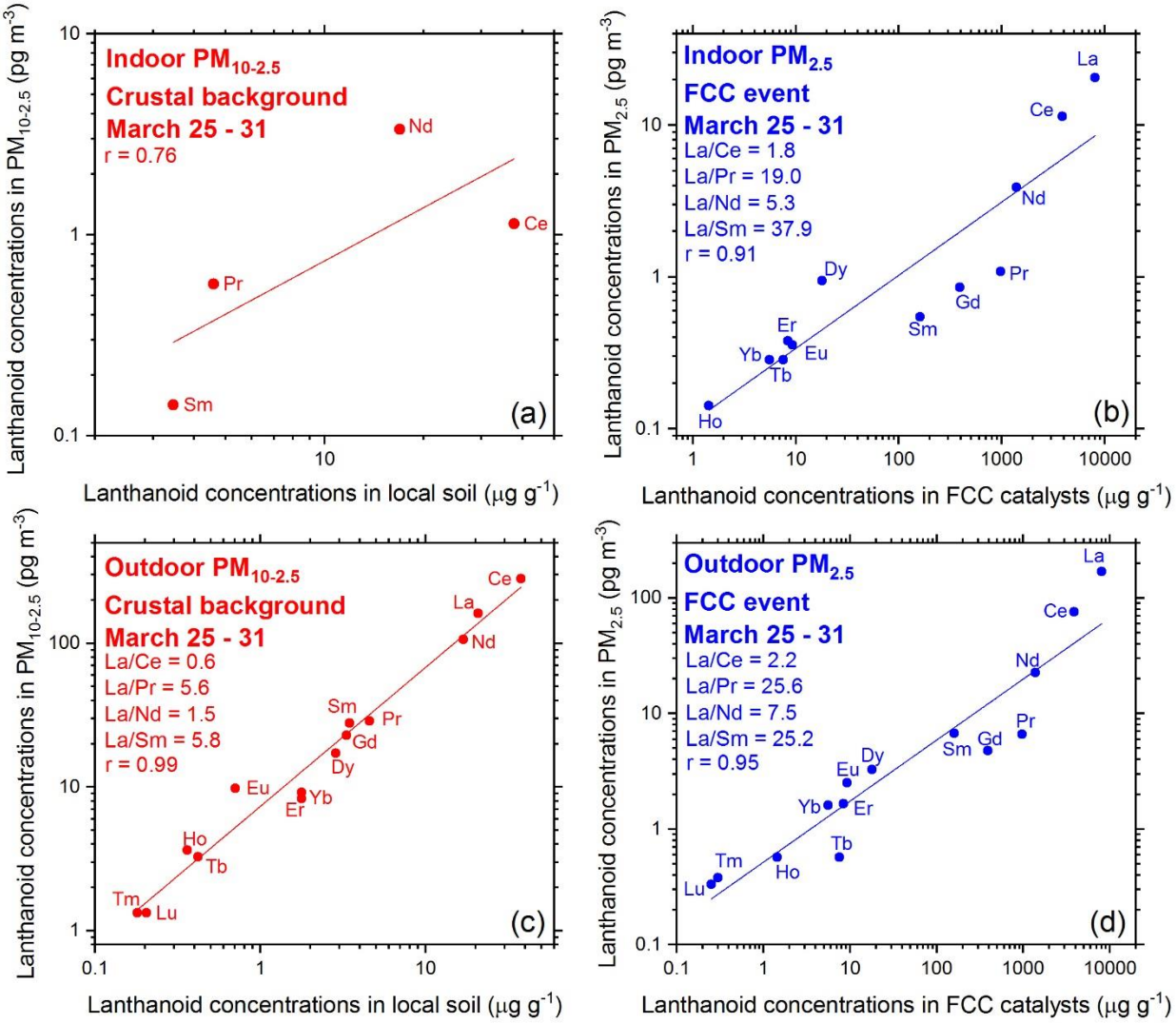

Figure E8. Correlations utilized in FCC event and background sample determinations for the March 25-31 sampling period. Panel (a) represents concentrations for indoor coarse PM (La, Eu, Gd, Tb, Dy, Ho, Er, Tm, Yb, and Lu are below detection limit), panel (b) represents concentrations for indoor fine PM (Tm and Lu are below detection limit), panel (c) represents concentrations for outdoor coarse PM, and panel (d) represents concentrations for outdoor fine PM.

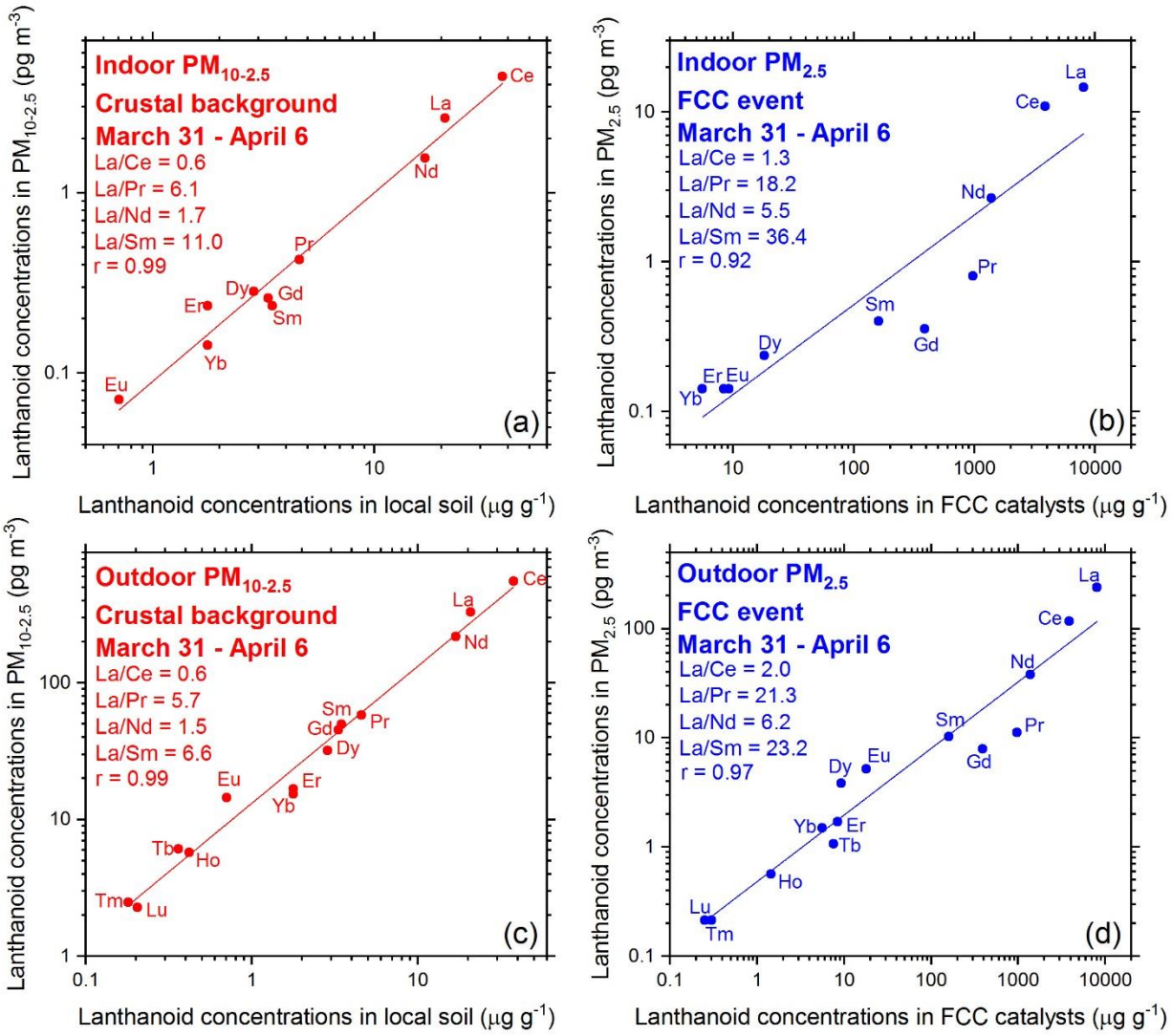

Figure E9. Correlations utilized in FCC event and background sample determinations for the March 31-April 6 sampling period. Panel (a) represents concentrations for indoor coarse PM (Tb, Ho, Tm, and Lu are below detection limit), panel (b) represents concentrations for indoor fine PM (Tb, Ho, Tm, and Lu are below detection limit), panel (c) represents concentrations for outdoor coarse PM, and panel (d) represents concentrations for outdoor fine PM.

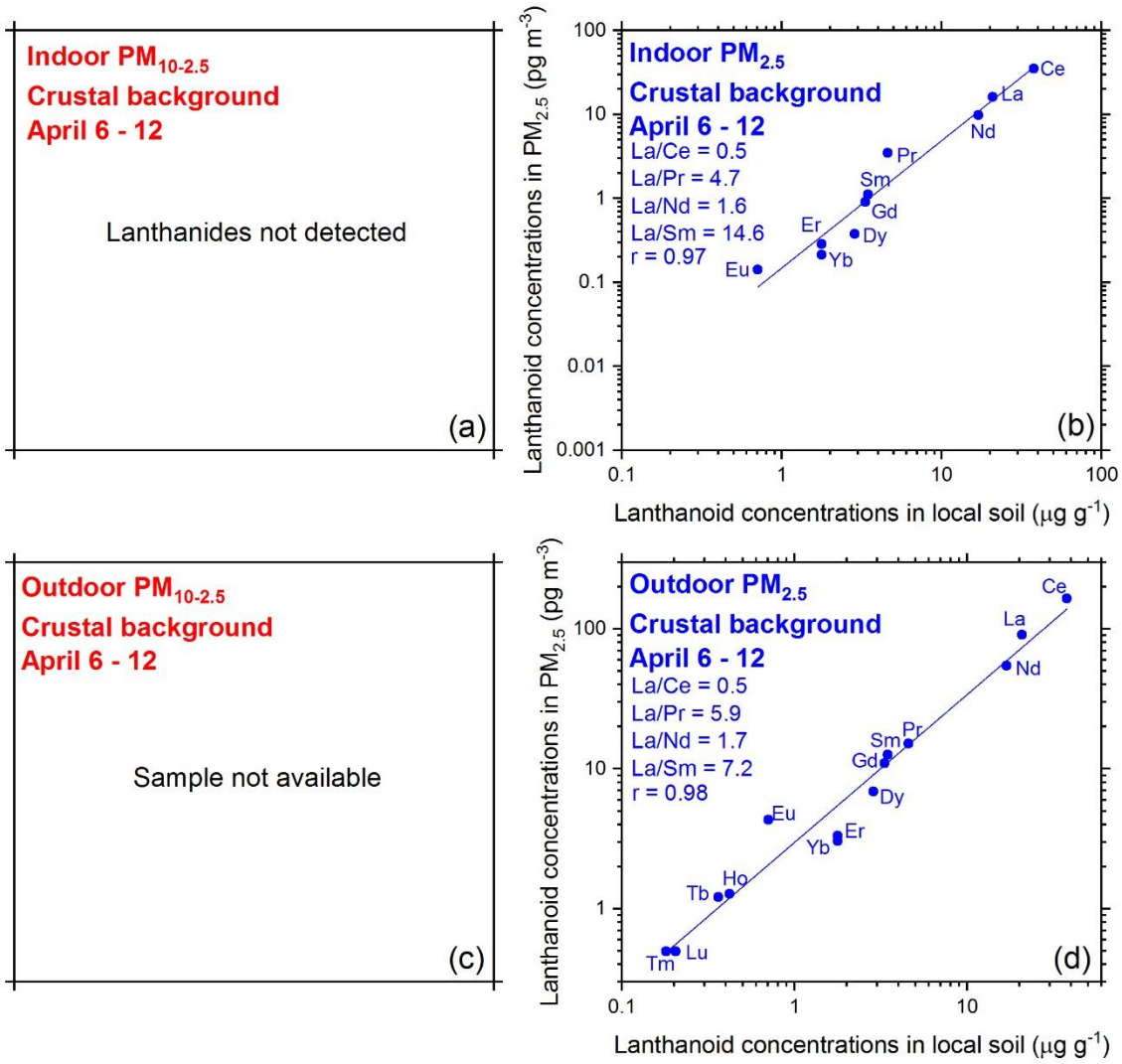

Figure E10. Correlations utilized in FCC event and background sample determinations for the April 6-12 sampling period. Panel (a) represents concentrations for indoor coarse PM, panel (b) represents concentrations for indoor fine PM (Tb, Ho, Tm, and Lu are below detection limit), panel (c) represents concentrations for outdoor coarse PM, and panel (d) represents concentrations for outdoor fine PM.

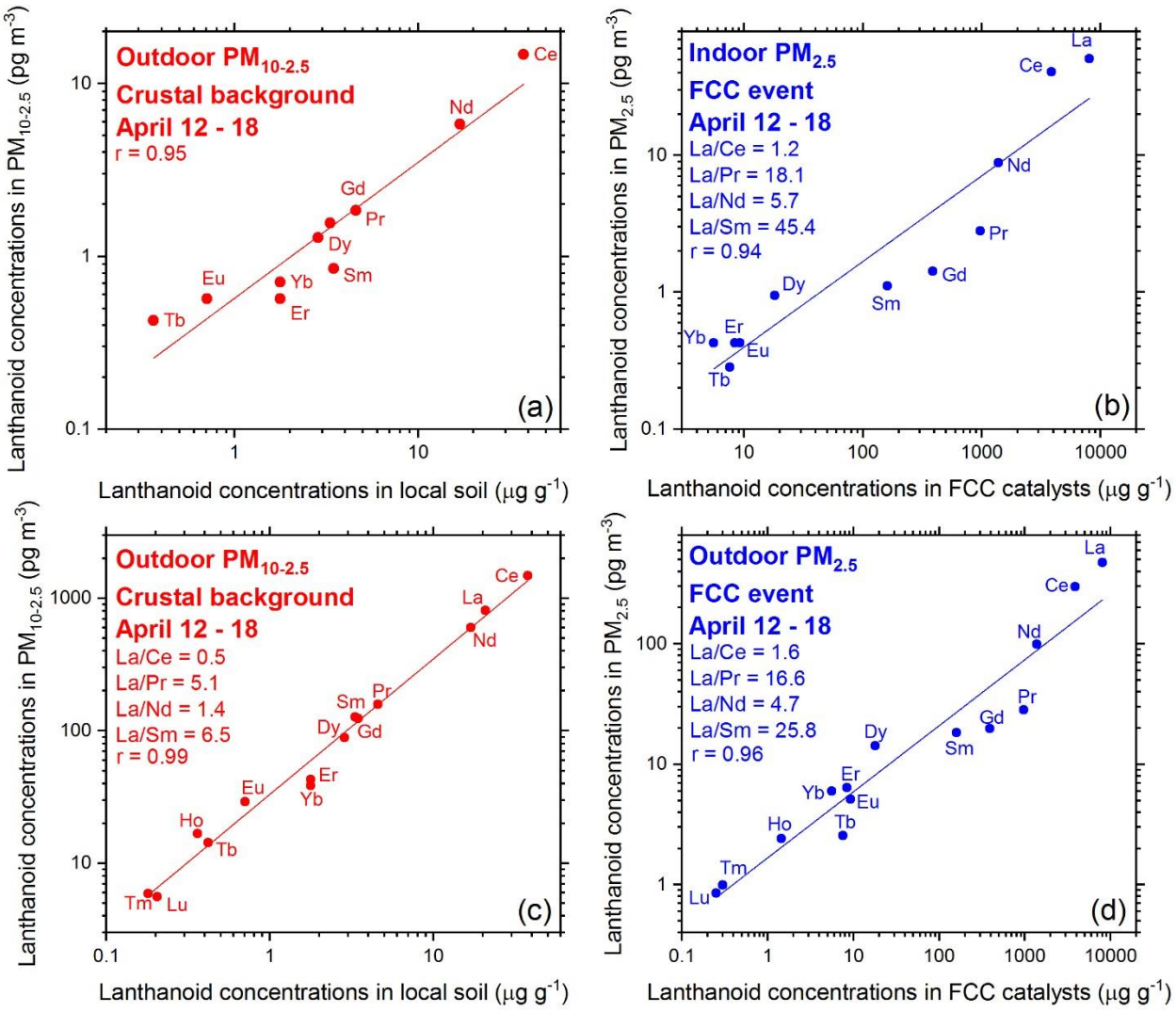

Figure E11. Correlations utilized in FCC event and background sample determinations for the April 12-18 sampling period. Panel (a) represents concentrations for indoor coarse PM (La, Ho, Tm, and Lu are below detection limit), panel (b) represents concentrations for indoor fine PM, panel (c) represents concentrations for outdoor coarse PM, and panel (d) represents concentrations for outdoor fine PM.

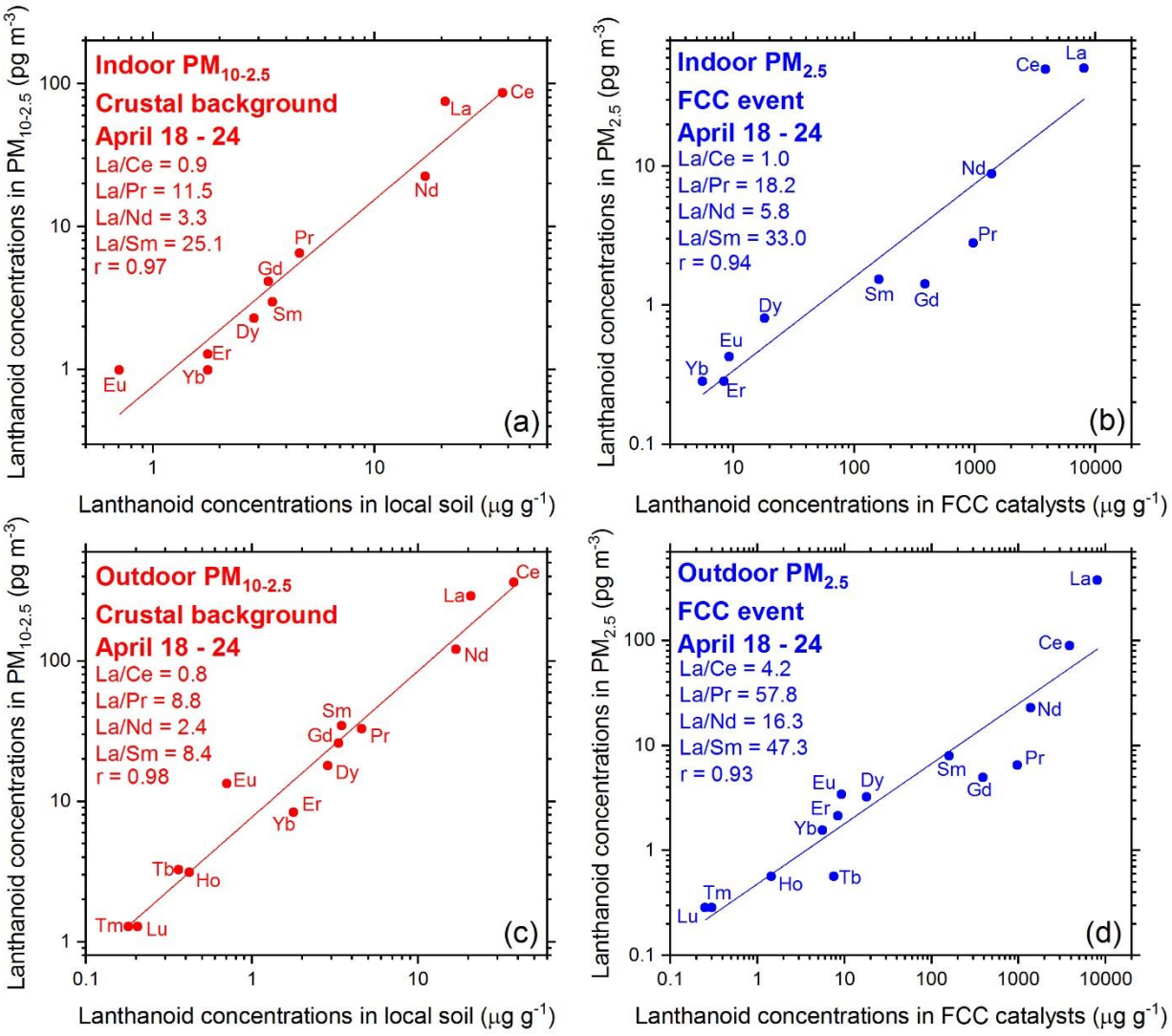

Figure E12. Correlations utilized in FCC event and background sample determinations for the April 18-24 sampling period. Panel (a) represents concentrations for indoor coarse PM (Tb, Ho, Tm, and Lu are below detection limit), panel (b) represents concentrations for indoor fine PM (Tb, Ho, Tm, and Lu are below detection limit), panel (c) represents concentrations for outdoor coarse PM, and panel (d) represents concentrations for outdoor fine PM.

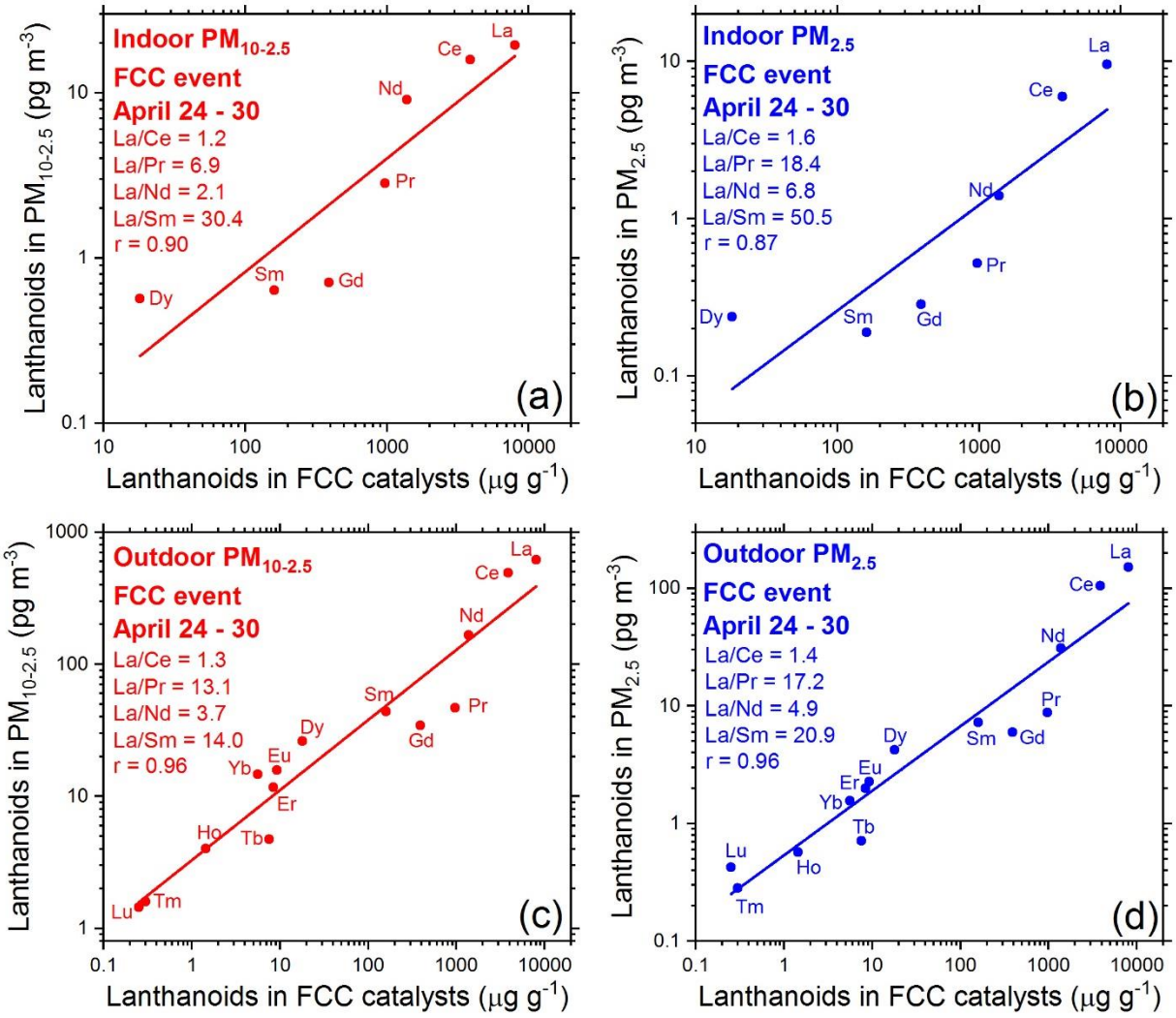

Figure E13. Correlations utilized in FCC event and background sample determinations for the April 24-30 sampling period. Panel (a) represents concentrations for indoor coarse PM, panel (b) represents concentrations for indoor fine PM, panel (c) represents concentrations for outdoor coarse PM, and panel (d) represents concentrations for outdoor fine PM.

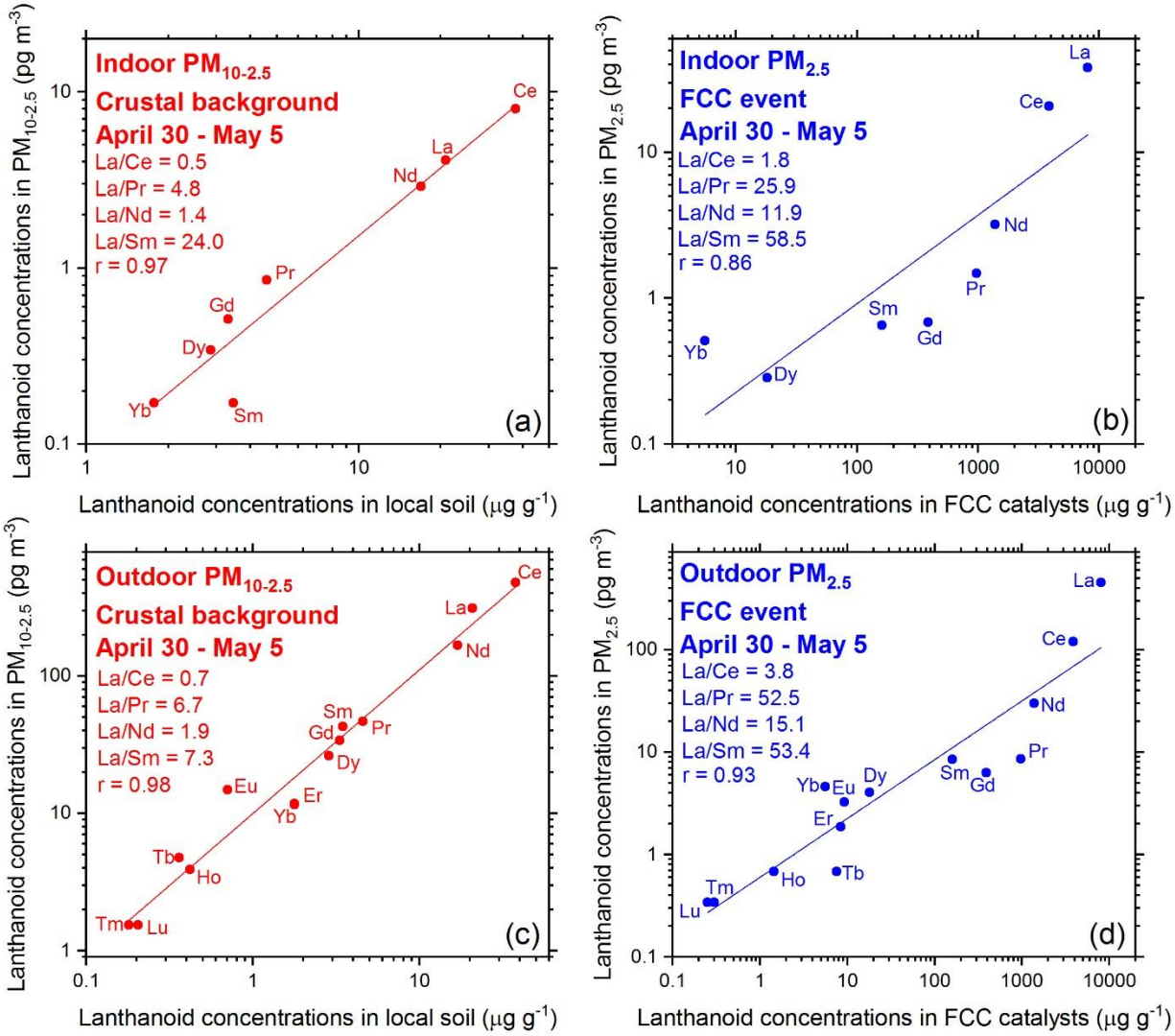

Figure E 14. Correlations utilized in FCC event and background sample determinations for the April 30-May 5 sampling period. Panel (a) represents concentrations for indoor coarse PM (Eu, Tb, Ho, Er, Tm, and Lu are below detection limit), panel (b) represents concentrations for indoor fine PM (Eu, Tb, Ho, Er, Tm, and Lu are below detection limit), panel (c) represents concentrations for outdoor coarse PM, and panel (d) represents concentrations for outdoor fine PM.

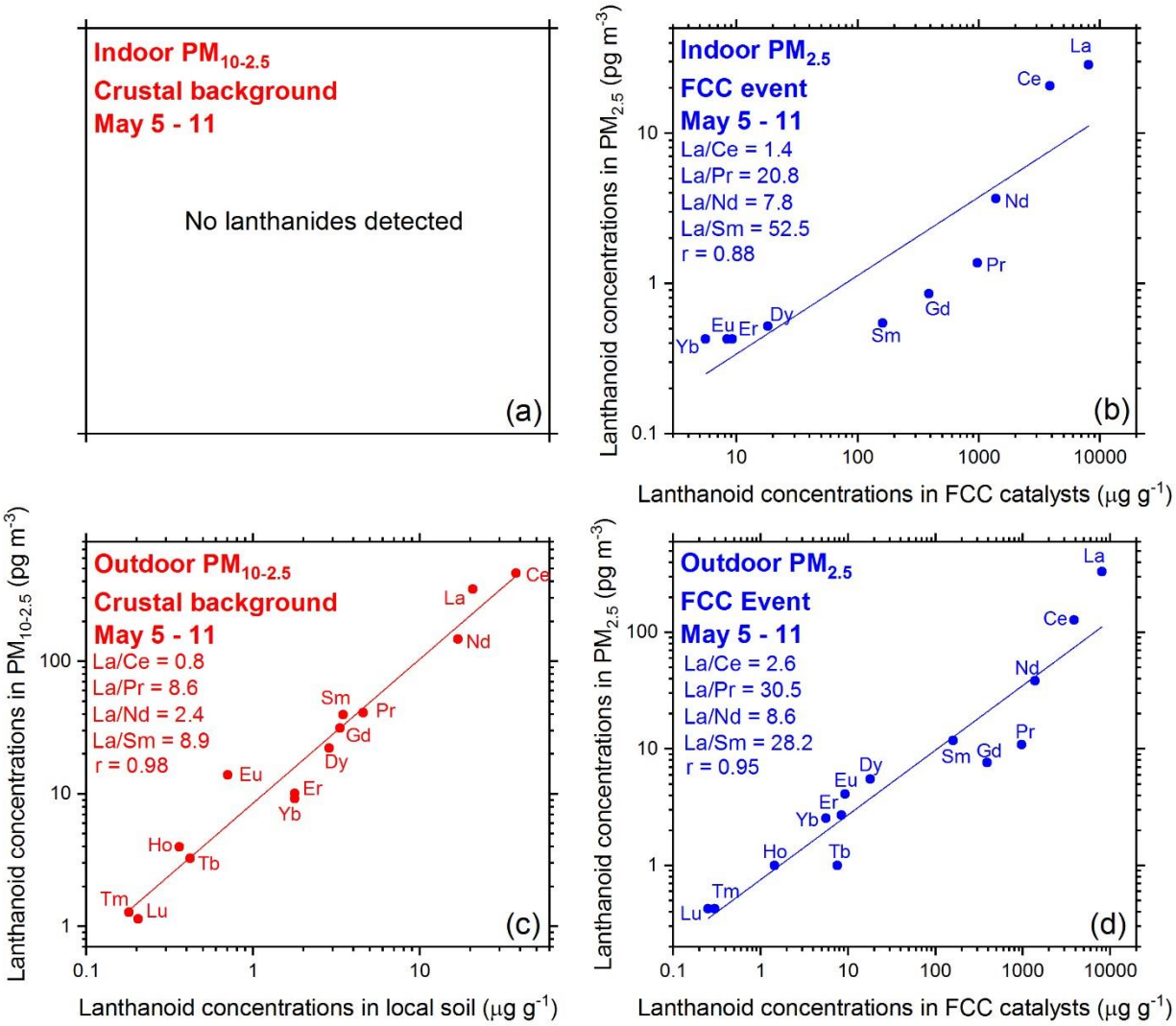

Figure E15. Correlations utilized in FCC event and background sample determinations for the May 5-11 sampling period. Panel (a) represents concentrations for indoor coarse PM, panel (b) represents concentrations for indoor fine PM (Tb, ho, Tm, and Lu are below detection limit), panel (c) represents concentrations for outdoor coarse PM, and panel (d) represents concentrations for outdoor fine PM.

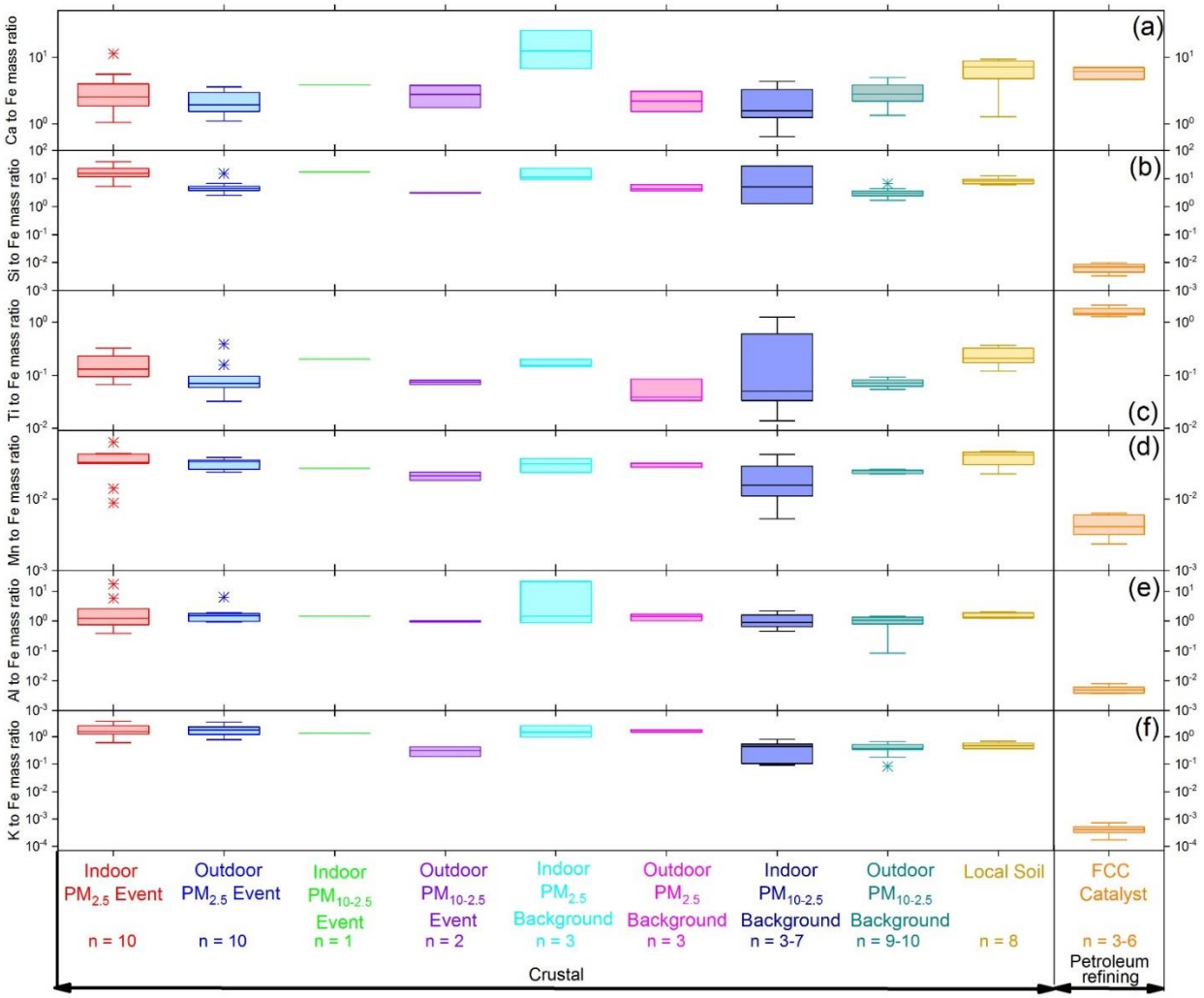

Figure E16. Ca/Fe, Si/Fe, Ti/Fe, Mn/Fe, Al/Fe, and K/Fe ratios utilized to determine the influence of local soil outdoor source in coarse PM and fine PM. The number of samples is located at the bottom of the figure.

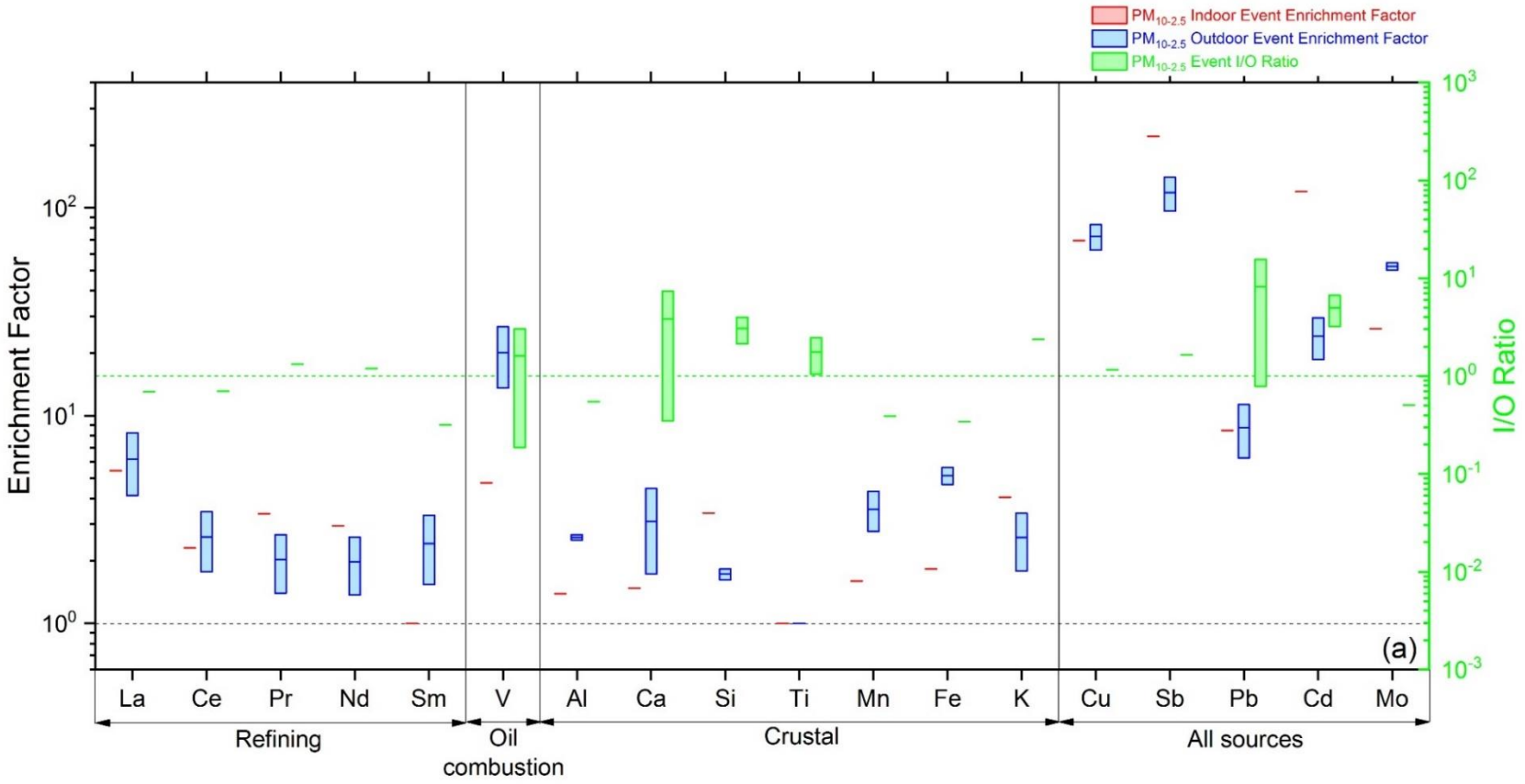

Figure E17. Indoor and outdoor enrichment factors with respect to soil (Ti) and I/O concentration ratios for event sample coarse PM categorized by outdoor source.

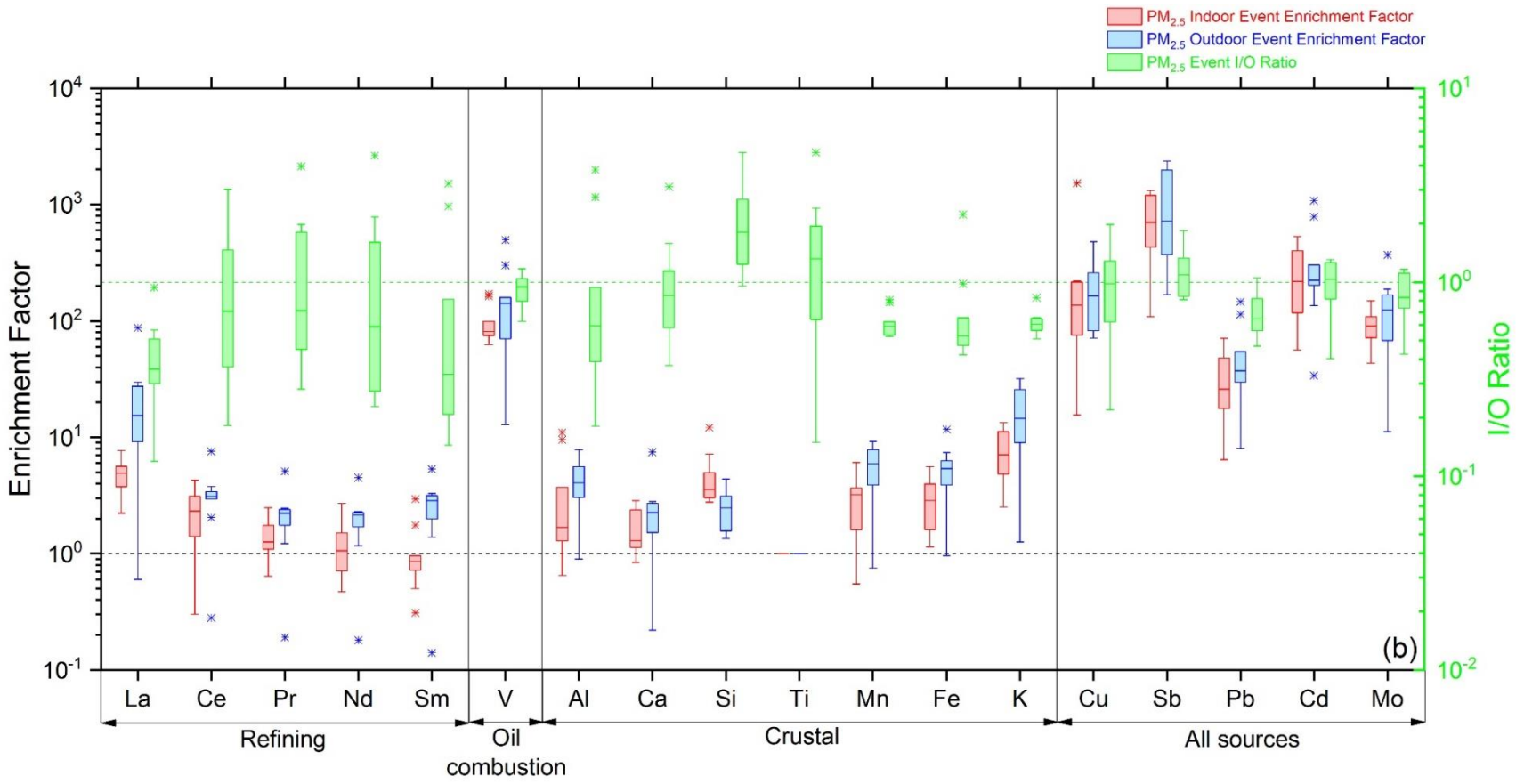

Figure E18. Indoor and outdoor enrichment factors with respect to soil (Ti) and I/O concentration ratios for event sample fine PM categorized by outdoor source.

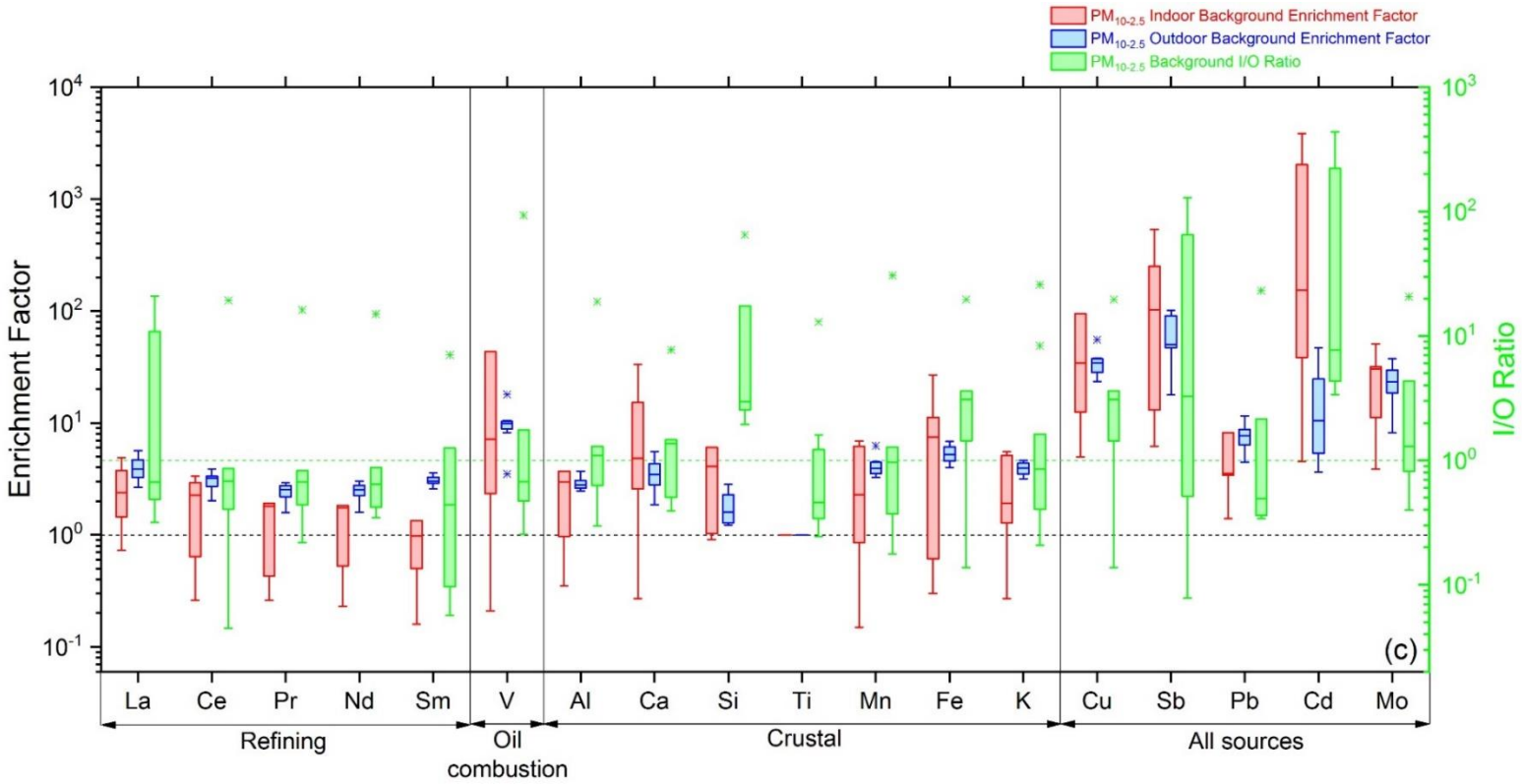

Figure E 19. Indoor and outdoor enrichment factors with respect to soil (Ti) and I/O concentration ratios for background sample coarse PM categorized by outdoor source.

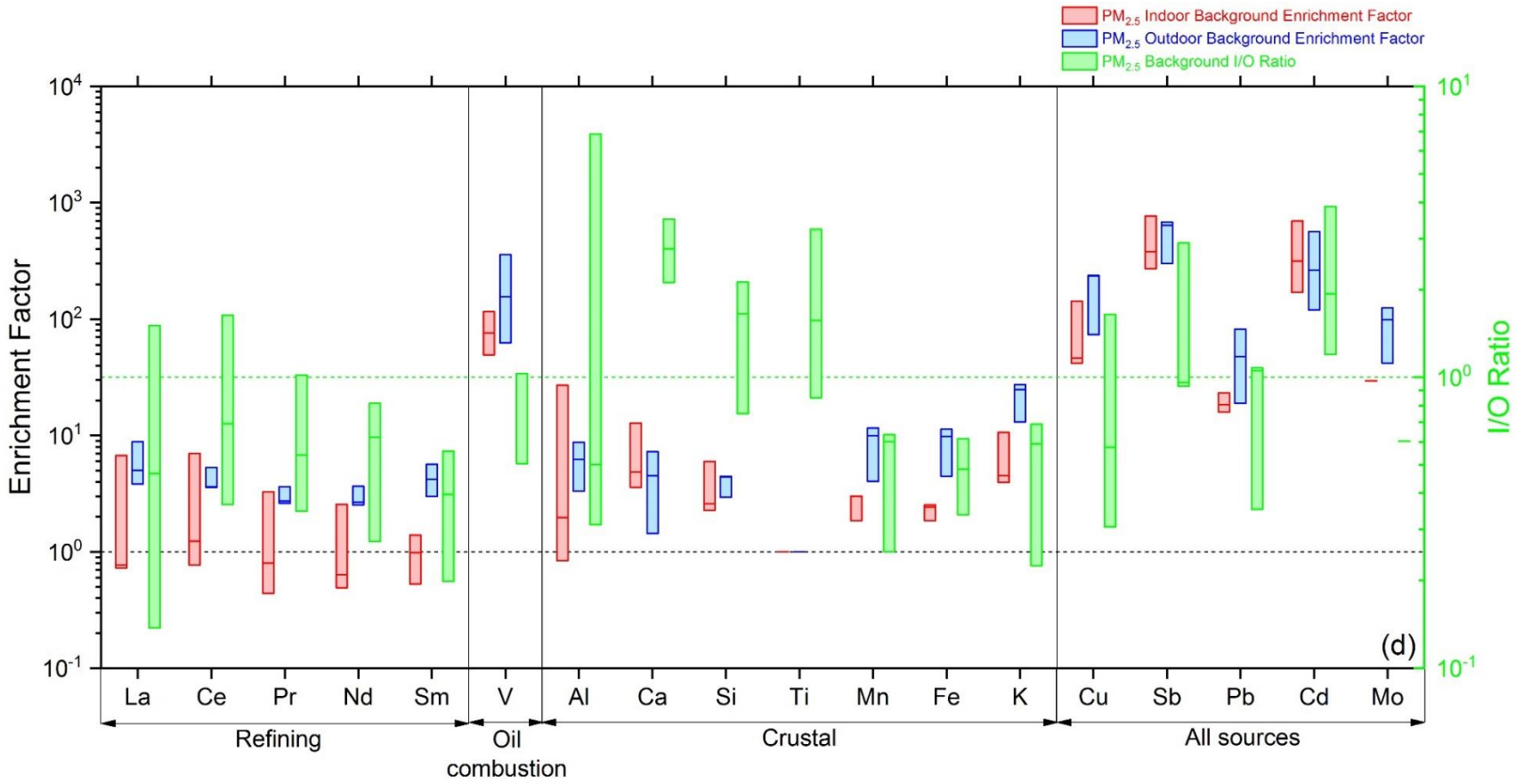

Figure E20. Indoor and outdoor enrichment factors with respect to soil (reference element – Ti) and I/O concentration ratios for background sample fine PM categorized by outdoor source

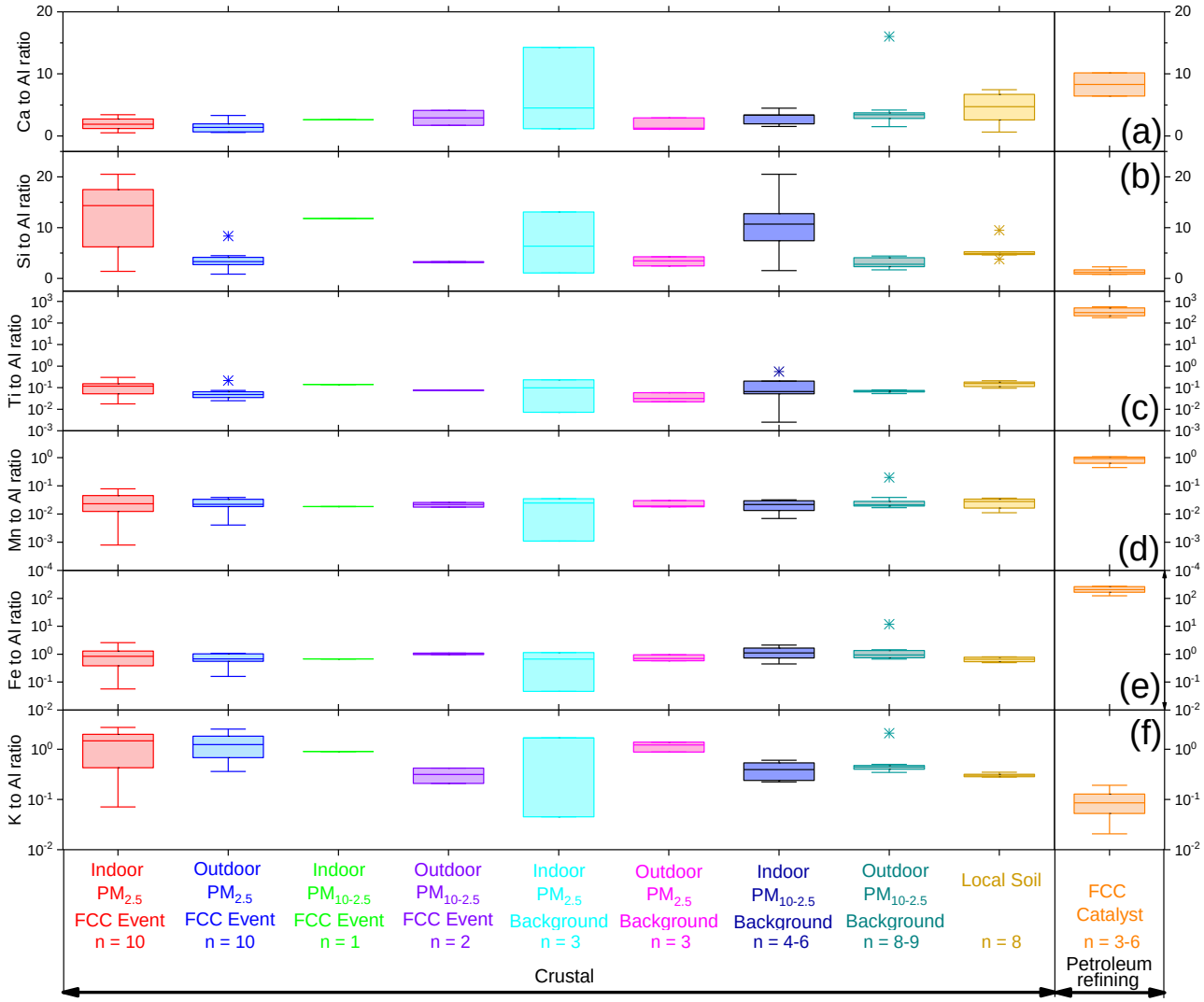

Figure E21. Ca/Al, Si/Al, Ti/Al, Mn/Al, Fe/Al, and K/Al ratios to separate the influences of crustal resuspension and FCC emissions. The number of samples for each box is shown at the bottom of the figure. Note top two panels (Ca/Al and Si/Al) are in arithmetic scale whereas all other panels are in log-scale.

Appendix Figure E21 above summarizes major element ratios; Ca/Al, Si/Al, Ti/Al, Mn/Al, Fe/Al, and K/Al, which also illustrate crustal material resuspension (similar to REE analysis in the main manuscript). In all cases, ratios for all PM samples overlap with those of local soil and are separated from FCC catalysts demonstrating that crustal material is the dominant source of these

elements in aerosols [86, 87]. Further supporting analyses may be found in SI Figures S3-15 that depict rare earths.

Another important PM source at this location is motor vehicles, especially since 435,000 vehicles daily traverse major roadways surrounding the school on average as described in methods section and Figure VI-1 of the main manuscript. To identify vehicular influence we specifically focused on tracers such as Cu/Sb, Pb/Cu, Sb/Cd, and Mo/Cd ratios [21, 52, 54]. As shown in Appendix Figure E22, these trace elemental ratios in ambient PM generally overlapped with both FCC catalysts, aerosols in a vehicular tunnel, and even the local soil. Hence, even though metals depicted in Appendix Figure E22 are typically associated with motor vehicles [54], our results herein do not distinguish them from crustal and FCC sources.

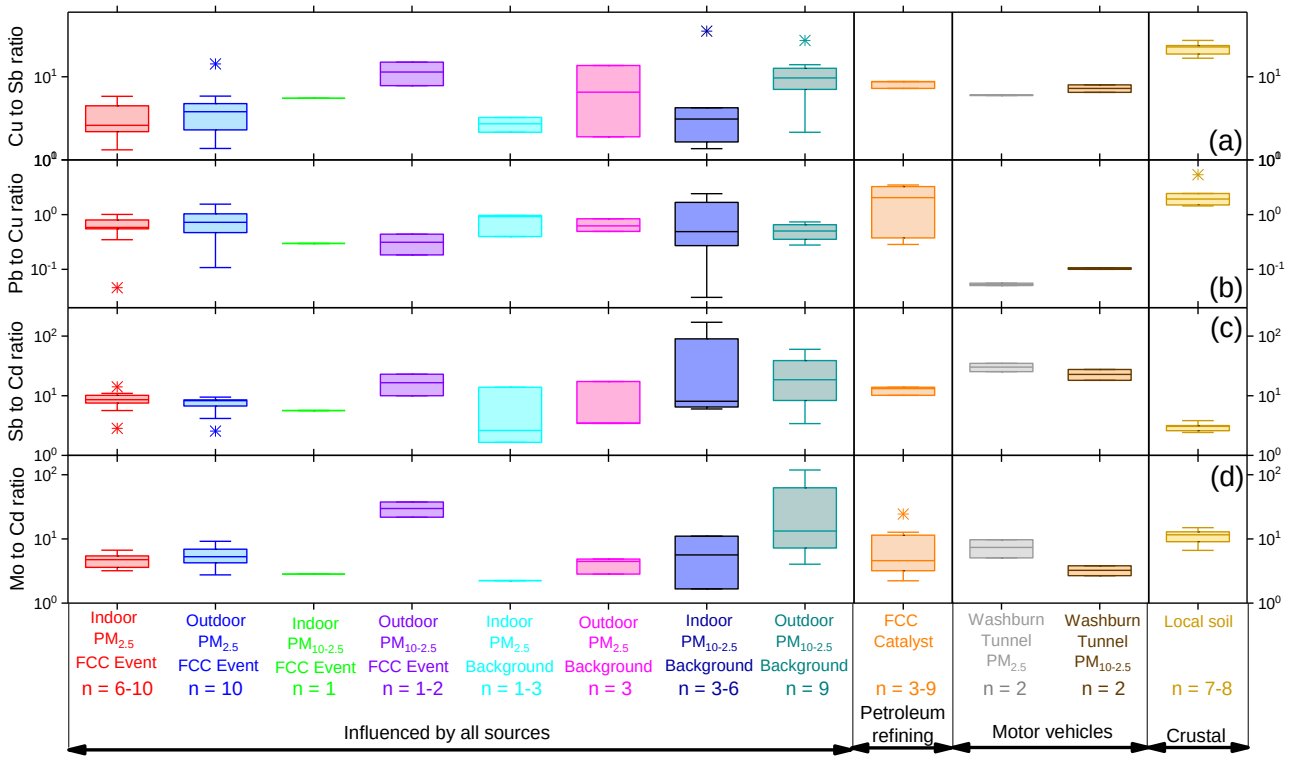

Figure E22. Cu/Sb, Pb/Cu, Sb/Cd, and Mo/Cd ratios utilized to determine the influence of motor vehicles and petroleum refining operations outdoor sources in coarse PM and fine PM. The number of samples is shown at the bottom of the figure below each box.

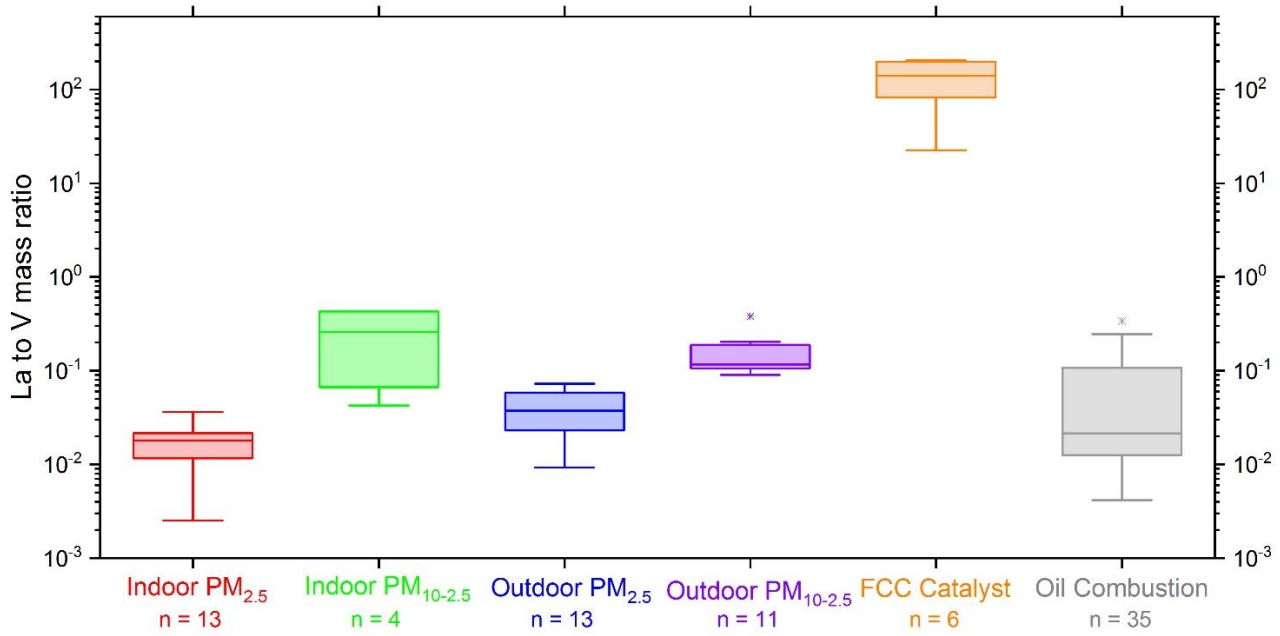

Figure E23. La/V ratio to separate petroleum refining and oil combustion sources. The number of samples is shown at the bottom of the figure below each box. Note that La was detected in only four indoor coarse PM samples.

Appendix Figure E23 depicts the La/V ratio, which is useful to discriminate aerosols that may have been influenced by oil combustion and shipping. Aerosols influenced by these sources are characterized by a low La/V ratio [52, 256, 331, 332] compared to FCC emissions where this ratio is substantially higher. As observed, La/V of all fine and coarse PM samples overlap with oil combustion (gray box on the right hand side), showing that they were enriched in V indicating that this metal did not directly originate from catalysts but likely from concommitant high temperature processes (e.g. FCC regeneration).